An Approach to Challenging Pebble Accretion

using THz Spectroscopy

Doctoral Dissertation
Linus Leo Stöckli

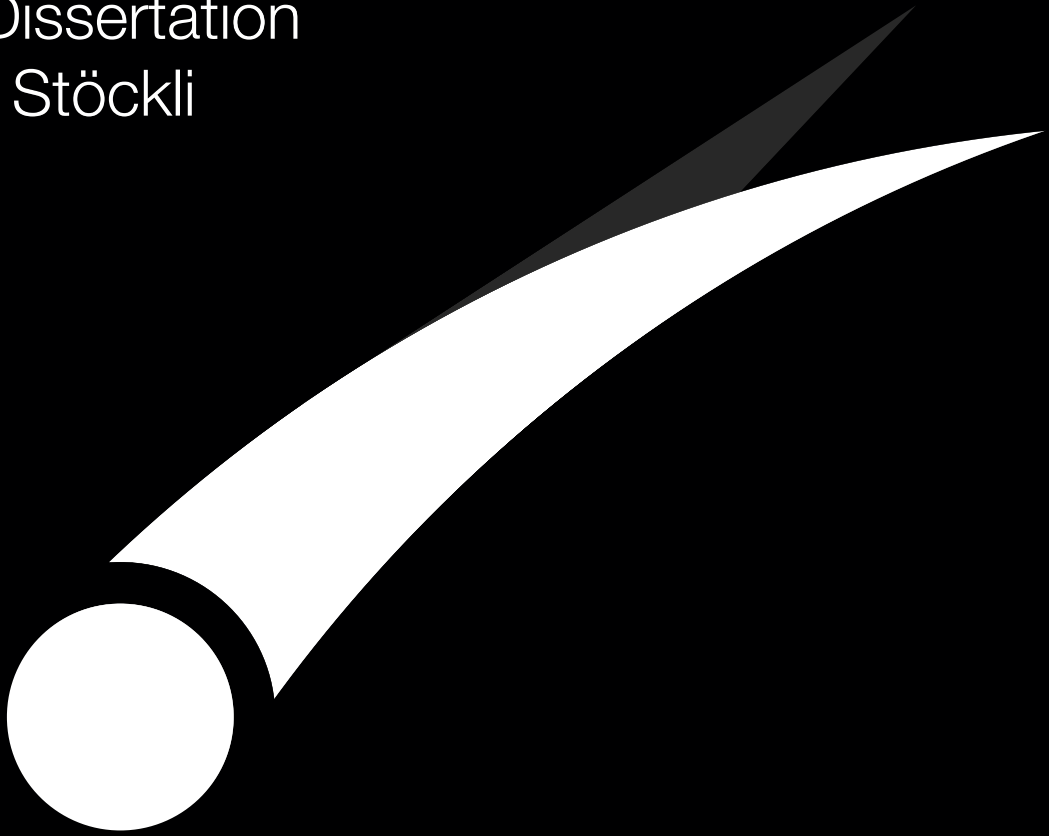

Bern, 2026

Supervised by Prof. Dr. Nicolas Thomas
Physikalisches Institut der Universität Bern

This work is licensed under the Attribution-NonCommercial-NoDerivatives 4.0 International License. To view a copy of this license, visit https://creativecommons.org/licenses/by-nc-nd/4.0/ or send a letter to Creative Commons, PO Box 1866, Mountain View, CA 94042, USA.

... für di.

“*I don’t know, but I want to know.*”

…

University of Bern - Faculty of Science - Physikalisches Institut

Abstract

An Approach to Challenging Pebble Accretion using THz-Spectroscopy

by Linus Leo Stöckli

Understanding how planets formed from the protoplanetary disk requires access to primordial material that has remained largely unaltered since the earliest stages of Solar System evolution. Comets, preserved in distant reservoirs such as the Kuiper Belt and Oort Cloud and exposed to significant solar heating only during brief perihelion passages, are among the most pristine remnants of planetesimal formation. Their internal structure and composition therefore provide key constraints for testing competing models of planetary growth, including classical hierarchical accretion and pebble-based formation scenarios.

Previous spacecraft missions have relied primarily on infrared spectroscopy for surface characterization and ground-penetrating radar for probing the interior. While radar instruments like CONSERT have demonstrated the ability to explore subsurface layers, their spatial resolution is intrinsically limited by meter-scale wavelengths. Conversely, infrared techniques offer fine spatial detail but lack the ability to penetrate below the surface. Terahertz time-domain spectroscopy (THz-TDS) occupies an intermediate regime, capable of providing centimeter-scale penetration while achieving millimeter-scale spatial resolution, and additionally offers spectroscopic sensitivity to key molecular species, such as amino acids, through characteristic absorption features in the THz band.

This thesis investigates the feasibility of THz-TDS as a novel method for in-situ subsurface analysis of cometary nuclei. To this end, we developed COCoNuT (Characteristic Observation of Cometary Nuclei using THz-spectroscopy), a laboratory facility that integrates a commercial THz time-domain spectrometer within a thermal-vacuum environment to simulate cometary surface and subsurface conditions. Using a suite of cometary analog materials, we perform proof-of-concept experiments to evaluate penetration depth, spatial resolution, data interpretation techniques, and the detectability of embedded structures and molecular signatures. The outcomes of this work establish the potential of THz-TDS as a complementary tool for future missions aimed at characterizing the internal structure and composition of small bodies in the Solar System.

Acknowledgements

First and foremost, I would like to express my sincere gratitude to Prof. Dr. Nicolas Thomas for the opportunity to join the Planetary Imaging Group, for entrusting me with this project, and for his continued support and guidance throughout.

Mathias Brändli played a central role in this work. He led the design and assembly of COCoNuT. I am sincerely grateful for his dedicated efforts and his continued support throughout the past four years.

I am also deeply thankful to Dr. Antoine Pommerol for his invaluable support and insight during the laboratory work.

A special thanks goes to Rafael Ottersberg, whose support in the lab and multifaceted contributions have been instrumental to this work.

Thank you Lukas Schneider for proof reading this document.

I feel truly fortunate to have crossed paths with so many talented, supportive, and caring colleagues and friends. This thesis has been made possible thanks to your dedication and encouragement.

Annabella Drewanowski
Axel Murk
Caroline Haslebacher
Claudio Zimmermann
Dominik Belousov
Hervé Girard
Iljadin Manurung
Jonas Lauener
Kimberley Mason-Piercy
Lea Klaiber
Lukas Gasser
Marie Azevedo
Matthew Read
Nico Haslebacher
Niels Ligterink
Patrick Robinson
Quinten Jenny-Groenveld
Ruben Tandon
Sebastian Wolf
Sophie Emberger
Valentin Bickel
Antoine Pommerol
Beda Berner
Céline Walker
Daniele Piazza
Hanna Unger
Harald Mischler
Johannes Lade
Jonathan Grone
Kristina Kipfer
Liliane Burkhard
Lukas Schneider
Martin Rubin
Michael Gensch
Nicola Gadola
Nora Hänni
Philipp Huber
Rafael Ottersberg
Sacha Häusler
Sébastien Hayoz
Stefano Spaddaccia
Valentin Meier
Arnaud Demion
Brigitte Kunz
Christoph Mordasini
David Linder
Hannes Imboden
Ignatius Argadestya
Jonas Hosch
Joseph Moerschell
Lea Höfliger
Liurong Lin
Marc Nicollerat
Mathias Brändli
Miguel Dias Almeida
Nicolas Thomas
Omar Mokhtari
Pius Stöckli
Reto Heimann
Salome Heilig
Silvan Zahno
Susanne Wampfler
Yannick Zwirner

... and many more!

Contents

Abstract **v**

Acknowledgements **vii**

1 Introduction **1**
- 1.1 Planetary Formation . . . 1
  - 1.1.1 Classical Hierarchical Growth . . . 3
  - 1.1.2 Pebble Accretion . . . 6
- 1.2 Comets . . . 9
  - 1.2.1 Exploration . . . 10
  - 1.2.2 Composition and Structure . . . 11
- 1.3 THz Time-Domain Spectroscopy . . . 15

2 Design and Commissioning of a THz Time Domain Spectro-Goniometer in a Cryogenic Comet Simulation Chamber **21**
- 2.1 Introduction . . . 22
- 2.2 Principles . . . 22
- 2.3 Requirements . . . 23
- 2.4 Design . . . 24
  - 2.4.1 Thermal Subsystem . . . 27
  - 2.4.2 Vacuum Subsystem . . . 30
  - 2.4.3 Optical Subsystem . . . 31
  - 2.4.4 Scanning Subsystem . . . 31
  - 2.4.5 Electronics Subsystem . . . 32
- 2.5 Commissioning . . . 34
  - 2.5.1 Pressure . . . 34
  - 2.5.2 Temperature . . . 35
  - 2.5.3 Beam Shape . . . 35
  - 2.5.4 Imaging Resolution . . . 36
- 2.6 Results . . . 38
- 2.7 Conclusion . . . 40
- Acknowledgements . . . 42
- Addendum: Reflections and Future Directions . . . 42

3 Frequency-Dependent Deconvolution for Enhanced THz-TDS Scans: Accounting for Beam Width Variations in Time Traces **45**
- 3.1 Introduction . . . 46
- 3.2 Beam Measurements . . . 46
- 3.3 Beam Shape Estimation . . . 49
  - 3.3.1 Generalities about PSFs . . . 49
  - 3.3.2 A Simple Approach with the Fourier Transform . . . 50

3.3.3 Overcoming the Effects of Low SNR with FIR Filtering . . . 51
3.4 Reconstructing the Underlying Time Traces . . . 53
3.4.1 In the Fourier Domain . . . 53
3.4.2 Via the FIR Filters . . . 55
3.4.3 Results . . . 55
3.4.4 Limitations . . . 58
3.5 Conclusion . . . 58
Acknowledgements . . . 59

4 THz Image Explorer - An Interactive Cross-Platform Open-Source THz Image Analysis Tool 61
4.1 Introduction . . . 62
4.2 Statement of Need . . . 62
4.3 Structure . . . 63
4.4 Usage . . . 63
4.4.1 Optical Properties Calculation . . . 63
4.4.2 Interactive 3D Viewer . . . 64
4.4.3 Filtering Pipeline . . . 65
4.5 Summary . . . 66
Acknowledgements . . . 66

5 Resolving Sub-Surface Ice Pebbles in Cometary Simulants using THz Time-Domain Spectroscopy 67
5.1 Introduction . . . 68
5.2 Setup . . . 69
5.3 Method . . . 69
5.3.1 Surface Extraction . . . 71
5.3.2 Pebbles . . . 74
5.3.3 Dust . . . 76
5.4 Results . . . 81
5.4.1 Surface Extraction . . . 81
5.4.2 Layer Detection . . . 85
5.4.3 Resolving Pebbles . . . 86

6 Discussion 91

7 Conclusion and Outlook 93
7.1 THz Time-Domain Spectroscopy in Space . . . 93
7.2 Outlook . . . 93
7.2.1 Future Mission . . . 94

A Cryo Cooler Performance 97

B Spectroscopic Analysis of Amino Acids, Salts and Minerals 99

C Electronics 111

D Open Source Contributions 115

E Internal Documentation 117

F Improvements in the Lab 119

G Metal Substrate PCBs as Low-Cost, Robust Temperature Sensor Mounts for Cryogenic Thermometry 123

H Title Page Design 135

Bibliography 137

Curriculum Vitae 153

List of Publications 155

Peer Review Contributions 157

Conference Contributions 159

Colophon 161

Declaration of the use of AI-based Tools 163

Declaration of Originality 165

List of Figures

1.1 The Oort Cloud (light blue), Kuiper Belt (dark blue) outside of Neptune's orbit and Asteroid Belt (red) between the orbits of Mars and Jupiter in our Solar System with a logarithmic radius scale. The sun (orange) is at the center. One fourth is cut away from the Oort cloud for illustration purposes. 3
1.2 Schematic illustration of Classical Hierarchical Growth: a planetesimal forms via successive sticking collisions of micrometer-sized dust particles. 4
1.3 Classical Hierarchical Growth scenario for a Jupiter-like giant planet and a smaller terrestrial planet: Micrometer-sized dust grains in the protoplanetary disk collide and stick, forming larger aggregates. These grow into pebbles, boulders, and eventually kilometer-scale planetesimals through continual collisions. Over time, these planetesimals accrete more material via sticking collisions and merge into planetary embryos and planets. The planetesimals that have not formed planets are now known as asteroids or comets (KBO, OCO). 5
1.4 Gravitational collapse of two pebble clouds. After the rapid collapse, two kilometer-sized planetesimals form. 6
1.5 Pebble accretion illustrated in a possible formation scenario of a Jupiter-like gas giant and a smaller terrestrial planet. Initially, pebbles form via sticking collisions of micrometer-sized dust grains. Outside the snow line, ice condenses onto the pebbles. Through streaming instability, dense pebble clumps collapse into planetesimals. These planetesimals then accrete more icy pebbles drifting inward, eventually forming massive planetary cores. If the core exceeds the critical mass, gas accretion begins, forming a gas giant. Unaccreted planetesimals may survive as comets or asteroids (e.g., in the Kuiper Belt or Oort Cloud). 7
1.6 Comet 67P/Churyumov-Gerasimenko photographed by the Navigation Camera (NAVCAM) of Rosetta on 3 February 2015 from a distance of 28.7 km from the comet center. The activity is clearly visible, as the ejected dust is illuminated by the sun. Credit: ESA/Rosetta/NAVCAM – CC BY-SA IGO 3.0 . 9
1.7 "Rubble Pile" structural model of a comet nucleus (a), illustrating a loosely bound aggregate of ice-rich (light blue) and refractory-rich (gray) debris, held together primarily by self-gravity, with significant porosity and minimal cohesive strength. The "Icy Glue" (b) model introduces volatile ices that act as a binding agent, providing moderate cohesion between constituent materials. A dust layer has been added to the surface. 12
1.8 The structural model of a homogeneous comet (a). A comet that formed from the gravitational collapse of a pebble cloud (b) would also appear homogeneous on large scales, but on small scales the centimeter sized pebbles become apparent. Both models are based on a 50/50 dust-to-ice ratio, a porosity of about 70% and include a dust layer on the surface. 13
1.9 The electromagnetic spectrum with the THz region (THz-gap) indicated. . . . 15

1.10 The working principle of a THz time domain spectrometer with photo-conductive antennas (PCA) and a pulsed laser. The Slow Delay Line (SDL) is usually configured only once for the optical setup to match the optical path of the laser to the once of the THz pulse. The Fast Delay Line (FDL) is continuously moving back and forth during data acquisition. 16
1.11 Photo-Conductive Antennas (PCA) are made of an InGaAs substrate with electrodes that is attached to a hyper-hemispherical Si lens. A pulsed femtosecond laser is focused on the substrate of the transmitter (Tx) and creates charge carriers (violet). These charge carriers are accelerated by the electric field $\vec{E}$ (orange) induced by the bias voltage U_{bias} between the two electrodes and thus emit radiation at THz frequencies. A second laser is delayed such that it arrives at the exact same time at the receiver (Rx). The laser again creates charge carriers which are this time moved by the electric field of the incoming THz pulse (blue). This flow of charge carriers results in a current I that can be measured with an ADC. This is a simplified diagram of a dipole antenna. 17
1.12 Direct acquisition of the full THz waveform is not feasible with current ADCs, as this would require sampling at THz rates. Instead, a widely used method involves reconstructing the waveform by delaying the laser pulse and sampling within a predefined time window. The sampling instants are denoted as t_i. Using this approach, each waveform is effectively assembled from multiple THz pulses. 18
1.13 The COCoNuT (Characteristic Observations of Cometary Nuclei using THz-spectroscopy) experimental setup in the laboratory. The instrument was designed in 2022 and 2023 and assembled and commissioned in 2023 and 2024 at the University of Bern. Its purpose is to simulate physical conditions relevant to cometary environments in order to assess the feasibility of in-situ terahertz time-domain spectroscopy measurements on comets. 19

2.1 Principle of time domain THz spectroscopy using photo-conductive antennas (PCA) and a pulsed laser. 23
2.2 The time trace (a) and the corresponding spectrum (b) obtained by the spectrometer. As the measurement was taken at ambient conditions, the water vapor absorption lines are well visible in the spectrum. Above 5 THz, the noise floor dominates. 24
2.3 Technical drawing of COCoNuT. The Main Chamber (1), Load-Lock Chamber (2), Primary Pump (3), Turbo Molecular Pump (4), Electronics Unit (5), Solar Simulator (6), and Optical Setup (7), which is discussed in more detail in Figure 2.5, are highlighted. 25
2.4 Sample holder carrier as viewed from the front. The sample-holder carrier (2) with heating cartridge (3) and temperature sensors (4) is pushed by the springs (7) onto the cryo-cooler interface (5). The shield (6) and insulator (8) isolate the cold parts from the ambient surroundings. The circular sample holder (1) is then positioned exactly in the focal point of the THz beam. 26
2.5 Two rotating arms (2) with antennas (6) and parabolic mirrors (1) are mounted on the gear assembly (3) which is actuated by the motors (4). The complete goniometer is mounted on the scanning stage (5). The sample holder can be placed at the center of the two arms. 27

2.6 Thermal simulation of the sample holder carrier and cryo-cooler interface (described in detail in the technical drawing in Figure 2.4) in equilibrium. All values are given in Kelvin. The heater is turned off, hence we observe the lowest possible temperature of $\approx 50\,\mathrm{K}$ on the sample holder and $\approx 80\,\mathrm{K}$ of the solid sample. Sample temperature increases significantly with sample porosity. The cryo-cooler interface is modeled according to the cooling power, the mounting point in the back is fixed at 298 K, hence the large gradient across the insulator. 29
2.7 Schematic diagram of the vacuum system. The main valve (V1), load-lock valve (V2), gate valve (V3) and venting valve (V4) are shown in their positions between the chambers and the pumps. The sample translator (ST) is indicated. 30
2.8 Setup of the 2” gold plated parabolic mirrors and the PCAs. The two mirror pairs are each mounted on a rotatable arm, the sample can be placed in the focal point. The coordinate system, as implemented in the scanning routines, is indicated. 32
2.9 The transmitter arm with the electromagnetic field indicated when the antenna is mounted in its normal position. Each antenna on each optical arm can be rotated freely around its own axis, allowing polarization studies in future experiments. 33
2.10 The goniometer seen from the front in reflection and transmission mode. The minimal angle is 32° due to geometrical constraints of the structure. The transmitter arm is colored in red, the receiver arm in blue. The blind spot is indicated in the figure on the right. 34
2.11 The accuracy and precision of the PID controller for different set temperatures are shown using a box plot.The box spans from the first to the third quartile, while the circles represent the outliers. These outliers are mostly recorded shortly before reaching steady-state. For some cases an overshoot can occur, this highly depends on the thermal load of the sample and has not been included in this analysis. An empty sample holder was heated according to a temperature profile, after stabilizing, the temperature was recorded for 30 minutes. 36
2.12 The normalized pulse intensities for knife edge scanning in x and y direction. . 36
2.13 Normalized beam shape profile of THz-beam in the focus point, with a FWHM of $\Delta x = 1.42\,\mathrm{mm}$ and $\Delta y = 1.44\,\mathrm{mm}$. The measurements are compared to a simulation conducted with ***Zemax*** (Ansys®, 2019), assuming an ideal Gaussian beam. 37
2.14 The optical setup in reflectance mode with the beam indicated in red. When acquiring an image of the full area, part of the beam is blocked by the sample holder walls when scanning close to the edges, since the incident and reflecting beam are aligned in the y direction, resulting in elliptical borders. . . 38
2.15 Design of the COCoNuT resolution target v0.2A/B 2024 (a). The 60 mm by 60 mm scan (b) was performed in transmission mode with a pixel size of 0.5 $\times$ 0.5 mm^2. For each pixel a THz time trace has been recorded and the intensity is plotted, with high intensity being shown as red and a low intensity as blue. As the sample-holder and the bars in the resolution target are made of metal, they block the beam and lead to a low intensity. The scan indicates a spatial resolution of 0.3 lp/mm. 39

2.16 Four band-pass filters applied in the Fourier space to the resolution target measured in transmission mode. In transmission mode, the signal is blocked on the metal-bars (blue) and can pass through the substrate material (red) in high intensity. Frequencies above 1 THz get absorbed by the substrate material. With the lowest filter (upper left), we are not able to resolve any line pairs in the resolution target. The two middle filters (upper right and lower left) yield spatial resolutions of about 0.39 and 0.45 lp/mm. The highest filter only extracts frequencies that are completely absorbed, thus no information about the sample can be retrieved. 39
2.17 Four band-pass filters applied in the Fourier space to the resolution target measured in reflection mode. In reflection mode, the signal gets reflected in high intensity on the metal bars (red) and is scattered or absorbed on the substrate material or the sample-holder (blue). The two middle filters yield spatial resolutions of about 0.39 and 0.45 lp/mm. The highest filter gives the maximum spatial resolution of 0.56 lp/mm. The images are not completely circular due to the geometry of the incoming and reflecting beam. 40
2.18 The optical properties of the CZ silicon window extracted from the spectrum are compared to HRFZ (High-Resistance Float Zone) silicon. CZ is less expensive to manufacture but contains more impurities (mostly oxygen), thus leading to a higher absorption coefficient. The shaded areas are not considered to be accurate, as the signal is dominated by noise. 41
2.19 Two pulse traces of a solid H_2O ice slab in the time domain, measured in reflection mode. One part was covered with cometary analogue dust, consisting of 10% charcoal and 90% SiO_2. The upper plot shows the covered region, where the dust leads to diffuse scattering on the surface, thus lowering the overall signal. The lower plot shows the region where ice is exposed on the surface, leading to a stronger signal. The pulse at location I is caused by the reflection on the surface and the pulses at II and III are caused by the reflections of the two sides of the sapphire bottom of the sample holder. The temporal shift of I between the two measurements is caused by an uneven surface, whereas the shift of II and III is likely due to the refractive index of the dust. 41
2.20 Sketch of the alternative design approach for COCoNuT, where the assembly is flipped by 180° and the cold-head (blue) is attached to the slider. The goniometer is supported by an additional bearing (red). 43

3.1 Two renders of the scanning setup. The goniometer with the two photo conductive antennas (PCA) is shown in transmission and reflectance mode (38°). The beam is indicated in red. The scanning axes of the xy imaging stage are indicated. 47
3.2 Scanning path for a 11 × 11 pixel 2D image. For each pixel a THz time-trace is recorded. This results in a 3D dataframe. The meander scan is optimized for speed. For the beam width measurement scan, only one dimension is scanned across a knife-edge. 47
3.3 Setup indicating the knife edge scan along the y axis. A semi-circular metal plate is placed in the sample holder to obstruct half of the area. The pulse intensity is recorded as the beam moves across this ”knife edge”. 48
3.4 The normalized pulse intensities for knife edge scanning in x and y direction. The slight asymmetry is due to minor misalignments in the optical path. . . . 48

3.5 Beam widths w_x and w_y as a function of frequency. Numerous spikes are likely fitting errors due to poor SNR at certain frequencies. The y-axis of this graph has been limited to the interval $[0, 15]$. 51

3.6 Example of frequency responses of linear phase FIR filters $\boldsymbol{b}_\xi$. For the sake of clarity, the total bandwidth has been split in only 5 filters for this plot. 52

3.7 A THz time trace (a) that has been filtered with FIR band-pass filters centered around 0.15 THz (b), 0.34 THz (c) and 0.54 THz (d). Note: For panels (b), (c), and (d), the scale has been adjusted to a shorter range due to signal filtering, which reduces the energy content significantly. 53

3.8 Beam shape fitting by frequency: this figure shows the fit of the normalized power function P_n to measurement data filtered at two different frequencies: 0.34 THz (panels (a), (b)) and 1.32 THz (panels (c), (d)). Panels (a) and (b) illustrate the beam profile fits along the x-axis and y-axis at 0.34 THz, with fitted beam widths $w_x = 2.49$ mm and $w_y = 2.63$ mm, respectively. Panels (c) and (d) show the corresponding fits at 1.32 THz, where the beam is narrower, yielding $w_x = 0.68$ mm and $w_y = 0.72$ mm. The measured data (solid blue line) is compared to the fit (dashed blue line), and the derivative, dP_n/dy, is shown in red to highlight the true beam profile. The data has been normalized by the maximum beam power P_{max}. 54

3.9 Widths of the beam as a function of frequency. The fits are cleaner than with the FFT based method. 100 FIR filters are used. 54

3.10 CAD drawing of the COCoNuT resolution target v0.2 2024 (Stöckli et al., 2025). As the sample-holder and the bars in the resolution target are made of metal, they block the beam and lead to a low intensity in transmission and reflect the beam, thus showing up as bright high intensity spots in reflection. . 56

3.11 Comparison of deconvolution techniques. The scans have been acquired with 0.5 mm × 0.5 mm pixels. The full image is 60 mm × 60 mm in size. The first column (a,e) shows the original scans. The second column (b,f) shows the results of the simple Richardson-Lucy algorithm. The third (c,g) and fourth (d,h) columns show the results of our method using the Richardson-Lucy and the Wiener deconvolution algorithms. The deconvolved images have been clipped to match the average luminance of the original images (a) and (e). We chose clipping over normalization because the deconvolution process causes a few spots of the image to gain really large luminance values. Choosing the clipping values to retain the same average luminance as the original images allows better comparison of the results. 57

4.1 THz Image Explorer icon. 62
4.2 THz Image Explorer screenshot. 62
4.3 Software Architecture. 64
4.4 The convoluted envelope of the signal. All datapoints below the indicated threshold are treated as transparent. 65

5.1 A THz cube acquired by scanning across the x and y axis. Each stack is a THz waveform/pulse measured in time domain. The time axis can be converted to the z axis. The THz waveform (A-Scan) is indicated for the blue shaded stack in (a). B-, C-, and D-Scans for a hemispherical object are indicated in (b), due to graphic simplicity, the scans are drawn outside of the cube, whereas they are actually slices through the cube along the corresponding axes. 69

5.2 The focus in this setup is set on the reference layer with a total path length of $2l$. When a sample is placed with a thickness d, the pulse is reflected earlier and since the incidence and emission angle are not equal, the setup is slightly out of focus. Due to diffuse reflection of the pulse, the receiver (Rx) is still able to capture the pulse with a path length of $l - h + a$. 70
5.3 The signal in time domain is shown in the left subplot. The envelop of the signal is binned in the right subplot and Log Norm functions are fit to the multimodal distribution. The first Log-Norm component corresponds to the noise distribution, the second Log-Norm component represents a superposition of the pulses. 71
5.4 Different 3D printed resolution targets. (a) shows a USAF 1951 target in 3D, (b) shows 10 mm half-spheres, and (c)–(f) are random Gaussian surface targets with different average feature sizes. The cutout is for alignment and focusing purposes. 72
5.5 Measurement setup to detect spherical pebbles – either solid or composed from porous ice – under a CoDA-T3 dust layer. The two sample holders are made of copper and cooled below 100 K. The dust layer varies between 1 and 2 mm due to minor out-gassing activity of the ice, which leads to shifting of dust during the pump down phase. In the transmission setup, only a half-sphere was used and placed on a 2 mm thick HRFZ silicon window. In the reflection setup, the spherical pebble was placed on a thick dust layer to move the back-reflections on the bottom of the sample holder outside of the acquisition window. 74
5.6 Pebble simulants before being placed in the vacuum chamber. The solid ice pebble has a density of $\rho_{\text{Ice}} = (0.901 \pm 0.016)\,\text{g/cm}^3$, the SPIPA-B ice pebble has a density of $\rho_{\text{SPIPA-B}} = (0.519 \pm 0.020)\,\text{g/cm}^3$ 75
5.7 Microscopic views of various dust mixtures. Large amounts of particles smaller than 500 µm tend to boil off in our setup. Charcoal does not stick well to SiO_2, but it inhibits the bonding of silicon dioxide particles by acting as a spacer in-between. 77
5.8 Optical properties of different dust components measured with pellets. The absorption of CoDA-T3 is slightly higher than CoDA-T2 which is likely caused by an overcompensation of spillage when mixing the samples. 79
5.9 Top view of the CAD representation of the COCoNuT resolution target v0.2 (2024) (Stöckli et al., 2025), modified for a 3D implementation in which the bars are extruded into cuboids with identical width and height. 81
5.10 Point-clouds of the extracted surface from the 3D resolution targets, color coded according to the distance of each point to the closest point on the 3D mesh of the scanned object. 82
5.11 Point-clouds of the extracted surface from the 10 mm spheres target, color coded according to the distance of each point to the closest point on the 3D mesh of the scanned object. 82
5.12 Point-clouds of the extracted surface from the Gaussian surface samples, color coded according to the distance of each point to the closest point on the 3D mesh of the scanned object. 83
5.13 Binned distances of all points of the point-cloud to the closest point on the 3D mesh of the scanned object, including a Gaussian fit and FWHM. 84

5.14 B-Scans of a 10 mm × 10 mm × 10 mm COC cube covered with CoDA-T3 dust. The depth depends on the refractive index n and is given as Optical Path Length (OPL). The top surface of the cube is indicated with a blue rectangle, the bottom surface with a red rectangle. The extracted surface of the dust is indicated with a black line, the rims of the sample holder are marked with a lower saturation. 85
5.15 B-Scans of a 10 mm × 10 mm × 10 mm COC cube covered with CoDA-T3 dust. The depth depends on the refractive index n and is given as Optical Path Length (OPL). The top surface of the cube is indicated with a blue rectangle, the bottom surface with a red rectangle. The extracted surface of the dust is indicated with a black line, the rims of the sample holder are marked with a lower saturation. 85
5.16 Pebble simulant made of solid ice, before and after being covered with CoDA-T3. The picture to the left was taken outside of the vacuum chamber at ambient pressure and the picture to the right was taken inside the vacuum chamber shortly before the scan began, hence the larger amount of frost on the cold surfaces in the left picture. 86
5.17 Raw (a,c,e) and filtered (b,d,f) B-Scans of the solid ice pebble and SPIPA-B ice pebble as well as the empty control scan. The raw plots show the absolute value of the recorded signal. The filtered plots show the data after a band-pass of 0.2 THz to 0.5 THz, de-convolution, downsampling and a ball-kernel smoothing is applied. The extracted surface is indicated as a black line. . . . 87
5.18 A mask with a threshold of 0.08 is applied to the data do extract sub-surface pebbles. A B-Scan is shown on the left side with the extracted surface indicated as a black line. To the left, the 3D plots show the extracted surface and the extracted sub-surface features. Solid ice presents itself as a void inside the 3D voxel plot, due to the lack of interfaces and thus lack of reflected pulses. SPIPA-B is virtually indistinguishable from pure dust sample, due to the comparable amount of interfaces. 88
5.19 Refractive Index maps of two circular ice pebbles measured in transmission. The white spots around the pebble are invalid values due to strong scattering of the pulse at the edge. The refractive index was calculated for a thickness of 11.5 mm (radius of the spherical pebble). 89

6.1 The 3D resolution target imprinted in CI dust. Minor imperfections due to walls collapsing when removing the stamp can be seen. 91

7.1 Concept of the instrument with one mirror and a window inside the drill. The optical setup and antennas are decoupled from the drill. 95

A.1 The temperature dependent cooling power of the CH-104 cryo-cooler by *SHI Cryogenics Group* as specified in the data-sheet. 97

B.1 Optical properties extracted from the pellets from batch # 1 using EMT. . . . 101
B.2 Optical properties extracted from the pellets from batch # 2 using EMT. . . . 101
B.3 Optical properties extracted from the pellets from batch # 3 using EMT. . . . 102
B.4 Thickness range for each pellet of the batch # 1. 102
B.5 Thickness range for each pellet of the batch # 2. 103
B.6 Thickness range for each pellet of the batch # 3. 103
B.7 Refractive indices and absorption coefficients of different dust samples. . . . 104
B.8 Refractive indices and absorption coefficients of different dust analogues. . . 105

B.9 Refractive indices and absorption coefficients of different amino acid and NH_4Cl samples. 106

C.1 An overview of the PCBs developed as part of this work. 111
C.2 The ELU consists of a large main PCB as a front panel to which many extension boards can be connected in the back using PCB finger connectors. This design is flexible and easily upgradable. The front panel also contains a vacuum display diagram and a touchscreen. 112

F.1 The structure of an encrypted message packet. The initialization vector (IV) contains the current timestamp (TS) and a random number (RN). The message is padded to be a multiple of 128 bit as the AES-128 block size is 128 bits. If the message is longer than 128 bits, a second block is attached to the packet. 120
F.2 High-Level encrypted communication protocol between the client (user) and the host (TCP server running on the Raspberry Pi). Messages in blue are always encrypted, messages in red are not encrypted by default to save computational resources on the host side, but can also be encrypted for maximum security. The connection is left open until either side actively closes it. 121
F.3 Screenshot of the COCoNuT remote control GUI. Certain controls have been mapped to buttons but there is a dedicated field for general commands that get relayed to the ELU. 122

G.1 General overview of the sensor mount with robust AWG24 wires attached and a bolt in place. 125
G.2 Drawing of the sensor mount PCB showing the dimensions of the traces and layer thickness. Units are given in [mm]. 126
G.3 A Thermal simulation run with Ansys Mechanical. The sensor is connected to a sink object (sample) with fixed temperature of 23.15 K. Four simplified AWG24 wires with length of 100 mm are connected to the solder pads and the other end is at a fixed temperature of 300 K. To simplify the simulation, radiation has not been considered. 127
G.4 Simulations run for multiple object temperatures with the temperature offset of the cable pads and the sensor. Four AWG24 copper wires with a length of 100 mm and connected to ambient temperature of 300 K were simulated. The large increase in the offset of the sensor at around $T = 20$ K is mainly caused by the increased thermal conductivity of copper at these temperatures (Bradley & Radebaugh, 2013). 128
G.5 Side-view of the setup with two sensors screwed down on a copper adapter which is attached to a cryo-cooler. During the measurements the cryo-cooler was turned off, such that the copper block can be assumed to be in thermal equilibrium with no temperature gradient across. Units are given in mm. . . . 129
G.6 Thermal contact of a Pt1000 on our sensor mount compared to an epoxied Pt1000 with EPO-TEK H20E. It is important to note that we observe the net thermal conductance which is composed of all different materials (Pt, Cu, Insulator, Al_2O_3) and not the characteristic curve of one single material. The measurements were averaged over four runs. 130

G.7 The Difference of the measured temperature to that of the reference Lake Shore Cryotronics, Inc. DT-670 silicon diode. The Average was taken for four Pt1000 and Pt100 sensors and two thermal cycles each. The result show reproducible and comparable results to a Pt1000 epoxied with EPO-TEK 20 and the cables taped down with aluminum tape for thermal grounding. The thermal grounding with aluminum tape was not required for our sensor mounts. Durable AWG24 wires were used. The simulation discussed in the previous section agrees with the measurements taken. 131
G.8 An adapted design with longer signal traces to decrease further the amount of heat flowing from the wire-pads to the sensor. The four-wire readout is extended up to the pads where the sensor is mounted. 132

H.1 The design of the title page is based around the Fibonacci spiral. It depicts a comet, with its two tails, approaching the Sun. 135

List of Tables

1.1 Classification of comet types with typical orbital periods and origin regions. . . 10

2.1 Specifications of COCoNuT. 28
2.2 Power budget obtained from the simulation, assuming the sample is at 100 K and the surrounding at 298 K. 28
2.3 PID parameters. The proportional factor k_p, integral k_i and derivative k_d are temperature dependent. 29
2.4 The gold-plated off-axis parabolic mirror specs. The A-type mirrors are placed directly in front of the antennas, and the B-type mirrors are placed directly in front of the sample. The mirrors were manufactured by *Thorlabs*. 31
2.5 Expansion card slots on the back of the ELU. 33
2.6 Pressure performance of the chamber. The pressures are recorded in steady-state. During measurements, the sample can be heated, which in turn increases the pressures due to sublimation. 35
2.7 Temperature performance of the chamber after reaching steady state, no heating applied. 35
2.8 COCoNuT resolution target v0.2A/B 2024, based on the USAF 1951 resolution target. The resolution is given in line-pairs per mm (lp/mm). 37

3.1 Main symbols used in this article. 49
3.2 COCoNuT resolution target v0.2 2024, based on the USAF 1951 resolution target. Element numbers are marked to the left/right of the individual elements on the target and group numbers above/below of the respective groups. The resolution is given in line-pairs per mm (lp/mm). 56
3.3 GLCM Features and blur effect (transmission scan) 57
3.4 GLCM Features and blur effect (reflectance scan) 57

5.1 Filtering parameters for surface extraction. 71
5.2 Filtering parameters for pebble extraction. 75
5.3 CoDA-T0 contents with C/Si = 0.55 and a bulk density of approximately $\rho = 0.25\,\mathrm{g/cm^3}$ 80
5.4 CoDA-T1 contents with C/Si = 5.5 and a bulk density of approximately $\rho = 0.42\,\mathrm{g/cm^3}$ 80
5.5 CoDA-T2 contents with C/Si = 5.5, bulk density of approximately $\rho = 0.43\,\mathrm{g/cm^3}$ 80
5.6 CoDA-T3 contents, bulk density of approximately $\rho = 0.37\,\mathrm{g/cm^3}$ 80
5.7 COCoNuT 3D resolution target based on the USAF 1951 resolution target (2D). The resolution is given in bar-pairs per mm (bp/mm). 81
5.8 Gaussian fit results for point cloud histograms. 82

B.1 Description of the individual components. 100
B.2 Pellet with 100% PTFE – Target 1.8 mm 107

B.3 Pellet with 100% PTFE – Target 2.1 mm 107
B.4 Pellet with 90% PTFE and 10% SiO2 – Target 1.8 mm 107
B.5 Pellet with 90% PTFE and 10% SiO2 – Target 2.1 mm 107
B.6 Pellet with 90% PTFE and 10% Charcoal – Target 1.8 mm 107
B.7 Pellet with 90% PTFE and 10% Charcoal – Target 2.1 mm 107
B.8 Pellet with 90% PTFE and 10% CoDA-T1 – Target 1.8 mm 107
B.9 Pellet with 90% PTFE and 10% CoDA-T1 – Target 2.1 mm 107
B.10 Pellet with 90% PTFE and 10% CoDA-T2 – Target 1.8 mm 108
B.11 Pellet with 90% PTFE and 10% CoDA-T2 – Target 2.1 mm 108
B.12 Pellet with 90% PTFE and 10% CI – Target 1.8 mm 108
B.13 Pellet with 90% PTFE and 10% CI – Target 2.1 mm 108
B.14 Pellet with 90% PTFE and 10% Forsterite – Target 1.8 mm 108
B.15 Pellet with 90% PTFE and 10% Forsterite – Target 2.1 mm 108
B.16 Pellet with 90% PTFE and 10% Fayalite – Target 1.8 mm 108
B.17 Pellet with 90% PTFE and 10% Fayalite – Target 2.1 mm 108
B.18 Pellet with 90% PTFE and 10% CoDA-T0 – Target 3.5 mm 109
B.19 Pellet with 90% PTFE and 10% CoDA-T0 – Target 3.4 mm 109
B.20 Pellet with 90% PTFE and 10% CoDA-T3 – Target 3.5 mm 109
B.21 Pellet with 90% PTFE and 10% CoDA-T3 – Target 3.5 mm 109
B.22 Pellet with 90% PTFE and 10% Juniper charcoal – Target 4.0 mm 109
B.23 Pellet with 90% PTFE and 10% Juniper charcoal – Target 3.8 mm 109
B.24 Pellet with 90% PTFE and 10% CI – Target 3.3 mm 109
B.25 Pellet with 90% PTFE and 10% CI – Target 3.3 mm 109
B.26 Pellet with 100% PTFE – Target 2.3 mm 110
B.27 Pellet with 100% PTFE – Target 2.3 mm 110
B.28 Pellet with 90% PTFE and 10% Pyrene – Target 2.4 mm 110
B.29 Pellet with 90% PTFE and 10% Anthracene – Target 3.0 mm 110
B.30 Pellet with 90% PTFE and 10% L-alanine – Target 2.1 mm 110
B.31 Pellet with 90% PTFE and 10% L-alanine – Target 2.7 mm 110
B.32 Pellet with 90% PTFE and 10% NH_4Cl – Target 2.0 mm 110
B.33 Pellet with 90% PTFE and 10% NH_4Cl – Target 2.9 mm 110

C.1 A description of the contribution in the electronics field. 113

D.1 An overview of Open Source software contributions. 116

E.1 An overview of additional internal documents that have been prepared as part of this work. 117

G.1 Specifications of the sensor mount, including the sensor, but without cables. . 126
G.2 Parameters to calculate the black body radiation of the environment onto the sensor. 127

Acronyms

ALMA Atacama Large Millimeter/Submillimeter Array. 6, 8

CI Carbonaceous chondrite simulant CI-E. 78

COC Cyclic Olefin Copolymer. 72, 74, 81, 85, 91, 92

CoCa Comet Camera. 15

COCoNuT Characteristic Observation of Cometary Nuclei Using THz-spectroscopy. 21, 24, 40, 42, 46, 63, 69, 93, 94, 111, 119

CoDA-T0 Cometary Dust Analogue for THz spectroscopy version 0. 76

CoDA-T1 Cometary Dust Analogue for THz spectroscopy version 1. 76

CoDA-T2 Cometary Dust Analogue for THz spectroscopy version 2. 76, 78, 79, 91

CoDA-T3 Cometary Dust Analogue for THz spectroscopy version 3. 78, 86, 91

DNC Dynamically New Comet. 10, 11

ELU Electronics Unit. 28, 31–33, 42, 111, 113

EMT Effective Medium Theory. 78, 99

FFT Fast Fourier Transform. 16, 22, 51, 59, 62, 99

FIR Finite Impulse Response. 52, 58, 59

GLCM Gray-Level Co-occurrence Matrix. 56–58

GPR Ground Penetrating Radar. 15, 17, 68

GUI Graphical User Interface. 62, 63, 93, 120

HRFZ High Resistivity Float-Zone. 69, 77

HTC Halley Type Comet. 10

I^{2}C Inter-Integrated Circuit. 32

InSAR Interferometric Synthetic Aperture Radar. 68

IR Infrared. 15

JFC Jupiter Family Comet. 10

JWST James Webb Space Telescope. 6, 8

LPC Long Period Comet. 10

MBC Main Belt Comet. 10

NIR Near Infrared. 76

PCA Photoconductive Antennas. 16, 23, 25, 46, 69, 94

PE Polyethylene. 76

PSF Point Spread Function. 46, 55, 59

PTFE Polytetrafluoroethylene. 69, 76–78, 99

PWM Pulse Width Modulation. 29

RL Richardson-Lucy. 53, 55, 58

RTD Resistance Temperature Detector. 30, 124, 128, 129

SNR Signal to Noise Ratio. 51–53, 55, 58, 71, 94

SPC Short Period Comet. 10

SPI Serial Peripheral Interface. 32

SPIPA-B Setup for Production of Icy Planetary Analogues B. 74, 86, 92

TCP Transmission Control Protocol. 33, 119, 120

THz-TDS THz Time-Domain Spectroscopy. 46, 58, 59, 68–70, 72, 76, 85, 92–94

ToF Time of Flight. 16, 68

UHV Ultra-High-Vacuum. 125

UV Ultraviolet. 15

VGU Vacuum Gateway Unit. 33

WEB Water-ice Enriched Block. 14, 74, 92

WGSL WebGPU Shading Language. 65

Glossary

CaSSIS *Colour and Stereo Surface Imaging System* is a high resolution stereographic imaging system on board the ExoMars Trace Gas Orbiter. 15

CIVA *Comet Infrared and Visible Analyzer* was a suite of imaging and spectroscopic instruments aboard the Philae lander of the ESA Rosetta mission, CIVA consisted of seven micro-cameras designed to capture panoramic images of the comet's surface in visible light, along with a microscope (CIVA-M) and a visible/infrared spectrometer (CIVA-V). 14

Comet Interceptor The ESA *Comet Interceptor* mission is scheduled to launch in 2029 and it will be the first mission to visit a comet coming directly from the outer reaches of the Sun's realm, carrying material untouched since the dawn of the Solar System. 11, 15

CONSERT *COmet Nucleus Sounding Experiment by Radio Transmission*, a bistatic radar instrument on the Rosetta mission, which is operating at 90 MHz. It measured radio wave propagation between the Philae lander and the Rosetta orbiter to investigate the internal structure of comet 67P/Churyumov–Gerasimenko. 13, 15, 68

Deep Impact *Deep Impact* was a NASA spaceprobe launched in 2005 to study the interior of Comet Tempel 1, by releasing an impactor into the comet. The spacecraft was repurposed for a flyby of comet Hartley 2 in 2007. 11, 13

dotTHz A standardized file format for terahertz time-domain spectroscopy data built on HDF5, designed to unify sample and reference waveforms along with essential metadata in a single, shareable container to enhance data reproducibility, interoperability, and long-term accessibility. 61, 62, 119

ExoMars TGO *The Trace Gas Orbiter* is a spacecraft part of the ESA ExoMars mission and currently in Mars orbit. It was launched in 2016 and carries among other instruments the CaSSIS stereographic camera. 15

GIADA *Grain Impact Analyzer and Dust Accumulator* was an in-situ instrument onboard the ESA Rosetta spacecraft, designed to characterize individual dust particles in the coma of comet 67P/Churyumov–Gerasimenko. 76

Giotto *Giotto* was the first space probe to perform a close flyby of a comet. Launched in 1985, it encountered comet 1P/Halley on 13 March 1986, passing within approximately 600 km of the nucleus. 11

HDF5 *Hierarchical Data Format version 5* is a file format and supports high-performance I/O, flexible data models, and memory mapping of datasets, enabling efficient access to large arrays and metadata in scientific and data-intensive applications. 61

ICE Originally launched in 1978 as *ISEE-3*, it was later renamed *International Comet Explorer*. After completing its mission studying the solar wind, it became the first spacecraft to make an in situ comet encounter, flying through the plasma tail of 21P/Giacobini–Zinner in 1985. 11

MIDAS *Micro-Imaging Dust Analysis System*, an atomic force microscope onboard Rosetta. MIDAS collected and imaged cometary dust particles at nanometer resolution, revealing their 3D morphology and aggregate structure. 76

MIRO *Microwave Instrument for the Rosetta Orbiter*, a radiometer and spectrometer, operating at 190 GHz and 562 GHz, that observed thermal emission and molecular lines from comet 67P/Churyumov–Gerasimenko. 15

MRO NASA's *Mars Reconnaissance Orbiter*, launched in 2005, which carries high-resolution instruments including SHARAD, enabling detailed studies of Martian surface morphology and subsurface structure. 68

OSIRIS *Optical, Spectrocopic and Infrared Remote Imaging System* had a wide-angle camera and narrow-angle camera that could obtain high-resolution images of the comet's nucleus. It was part of the Rosetta mission. 14, 15

Philae The lander component of the ESA Rosetta mission, designed to perform the first soft landing on a comet (67P/Churyumov–Gerasimenko). *Philae* carried ten scientific instruments for in situ analysis of the comet's surface and near-subsurface. Despite landing complications, it returned valuable data on surface composition, morphology, and activity. 11, 14, 68

Python *Python* is a high level programming language, which is widely used among scientists due to its easy access, platform independence and the large amount of libraries for various applications. 33, 116, 119, 120

ROLIS *Rosetta Lander Imaging System* was an imaging instrument aboard the Philae lander of the ESA Rosetta mission. ROLIS was designed to capture high-resolution images of the comet surface during descent and after landing. 14

Rosetta *Rosetta* was an ESA mission, launched in 2004, that flew to 67P/Churyumov-Gerasimenko. It carried the scientific imaging system OSIRIS along with the lander Philae. 11, 15, 18, 22, 68, 76

Rust *Rust* is a systems programming language that provides memory safety without garbage collection through its ownership and borrowing model. It is designed for high performance, reliability, and safe concurrency, making it suitable for both low-level systems code and large-scale applications. 33, 62, 63, 116

Stardust *Stardust* was a NASA mission that launched in 1999 and the first spacecraft to return a cometary sample. 11, 18

SWI *Submillimetre Wave Instrument*, a high-resolution heterodyne spectrometer aboard ESA's JUICE mission. Operating between 530–1275 GHz, SWI measures thermal emission and molecular lines in the atmospheres and exospheres of Jupiter and its moons. 15

Swift *Swift* is a general-purpose programming language developed by Apple. It combines strong type safety and modern language features with an emphasis on performance, readability, and ease of use. 61, 116

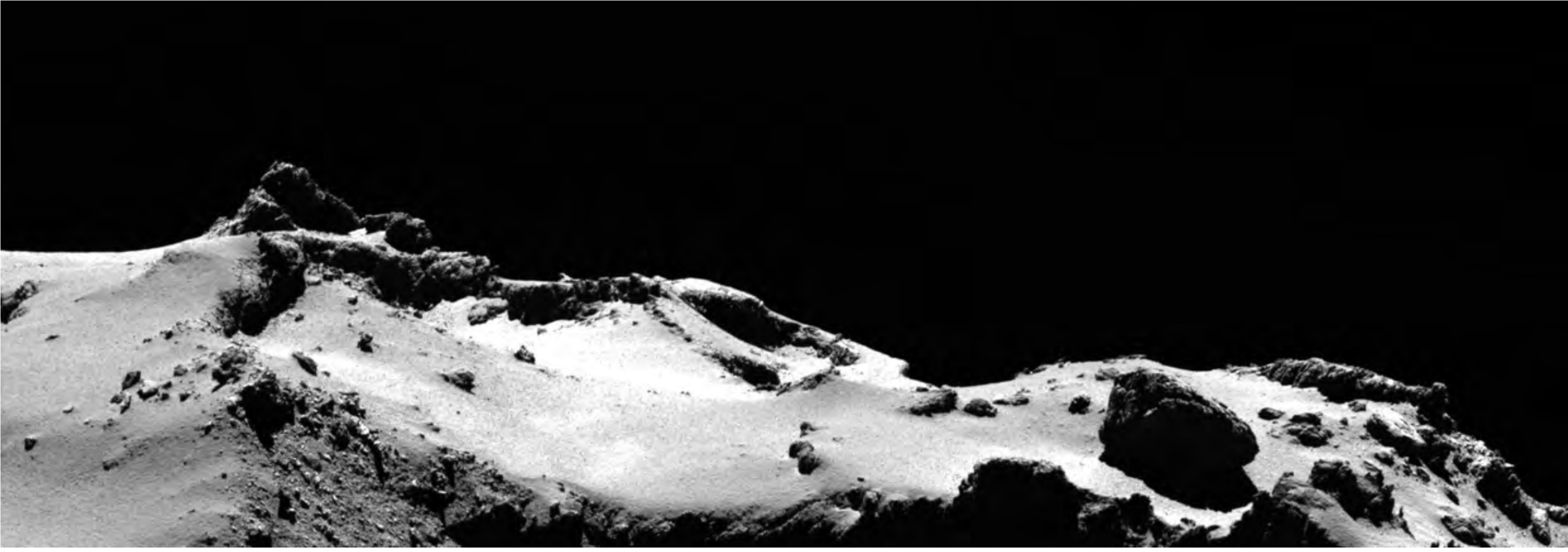

Introduction

1.1 Planetary Formation

Understanding how matter assembled into worlds requires us to trace the origins of our Solar System back to its earliest stages. Although there have been many theories about the birth and evolution of our Sun and planets (Woolfson, 1969), the most widely accepted framework for this process is the Solar Nebula Model (Armitage, 2020), which proposes that the Sun and planets formed from a rotating cloud of gas and dust, likely the remnant of a supernova explosion or the outflows of evolved stars. Gravitational instabilities within this molecular cloud initiated its collapse, forming a dense, spinning protostellar core. As the material contracted under self-gravity, conservation of angular momentum caused the infalling mass to flatten into a protoplanetary disk surrounding the emerging Sun (Williams & Cieza, 2011). This disk served as the site for subsequent planet formation, mediating the transport and growth of solid particles as well as the dissipation of gas through accretion onto the star or via outflows and winds.

The thermal and chemical structure of the disk was critical in shaping the distribution of solid materials. Temperatures varied significantly with radial distance from the Sun, and this gradient defined several key condensation fronts, or ”ice lines”. Within the silicate sublimation line, where temperatures exceeded $\sim 1500\,\mathrm{K}$ (Öberg et al., 2011), even refractory materials could not remain solid and existed in the gas phase. Outside this boundary, silicates and metals were able to condense and survive as micrometer-sized dust particles. Farther out in the disk, beyond the so-called snow line (or water ice sublimation line), typically considered to have been located around 2.7 AU in the early Solar System, the environment was cold enough for volatile species such as water, carbon dioxide, ammonia, and methane to condense into solid ices (Lecar et al., 2006). The presence of ices significantly increased the solid mass surface density in these regions, leading to the inference that giant planet cores formed more readily beyond the snow line. These rocky and icy grains constituted the primary building blocks of planetesimals and eventually planets.

Two dominant theoretical models have been developed to describe how these small grains coalesced into planetary bodies: ***Classical Hierarchical Growth*** and ***Pebble Accretion***. The classical model describes a bottom-up process in which particles gradually grow via sticking collisions, eventually forming kilometer-sized planetesimals and larger embryos through runaway and oligarchic growth. In contrast, the pebble accretion model introduces a more efficient growth pathway in which small, millimeter to centimeter sized pebbles are accreted onto planetary embryos through gravitational focusing and aerodynamic drag, drastically reducing the timescales required to form planetary cores, especially in the outer disk. Each model incorporates different assumptions about disk conditions, collisional outcomes, and dynamical stirring, leading to different predictions for the architecture and timing of planetary system formation. To evaluate and test the viability of theories of planetary formation in different disk environments, modern population synthesis models have been developed (Alibert et al., 2005; Lambrechts & Johansen, 2014; Mordasini et al., 2009). These simulations incorporate planetesimal accretion, disk evolution, gas accretion, and orbital migration in a unified framework, allowing researchers to predict statistically the diversity of observed exoplanet systems.

To better understand the physical conditions and processes that shaped the early Solar System, it is essential to investigate objects that have remained largely unchanged since their formation. Unlike the planets, which have undergone extensive thermal evolution and surface processing over billions of years, many small bodies, particularly those in the outer Solar System, retain their primordial composition and structure. These ancient planetesimals act as time capsules, preserving information about the chemical, thermal, and dynamical environment of the protoplanetary disk. Studying their physical properties, compositions, and orbital distributions provides critical constraints for testing and refining models of solar system formation and evolution. Such bodies are located today in distinct reservoirs, including the Asteroid Belt, the Kuiper Belt, the scattered disk, and the distant Oort Cloud (see Figure 1.1).

Generally, rocky planetesimals originating from the inner disk are classified as asteroids, while icy bodies from the outer disk are referred to as comets. Together, these small bodies serve as invaluable time capsules, offering a substantial link to the materials and processes that governed the birth of our planetary system.

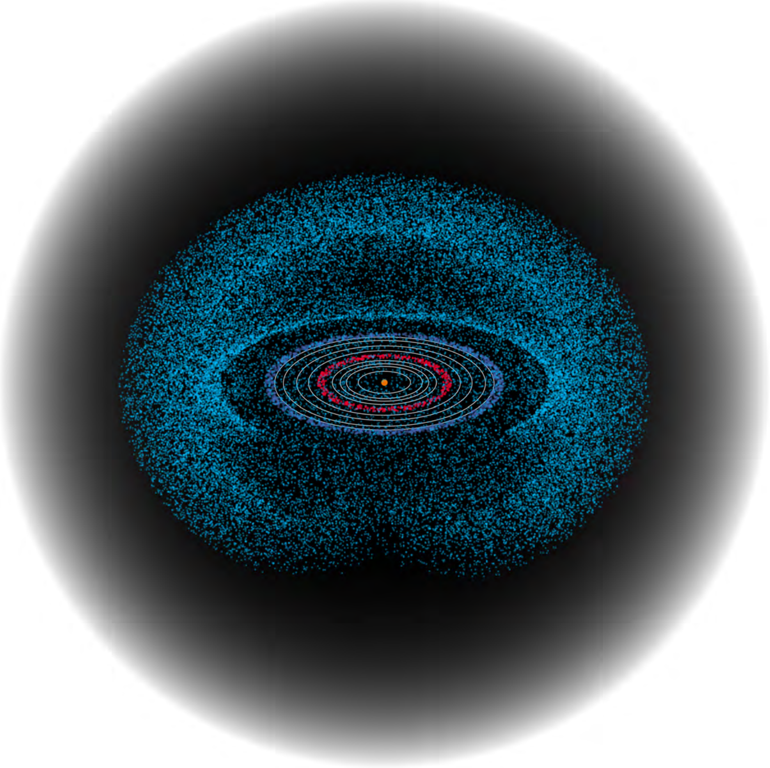

Figure 1.1: The Oort Cloud (light blue), Kuiper Belt (dark blue) outside of Neptune's orbit and Asteroid Belt (red) between the orbits of Mars and Jupiter in our Solar System with a logarithmic radius scale. The sun (orange) is at the center. One fourth is cut away from the Oort cloud for illustration purposes.

1.1.1 Classical Hierarchical Growth

The ***Classical Hierarchical Growth*** model describes planet formation as a gradual, bottom-up process that begins with sub-micrometer dust grains in the protoplanetary disk. These grains collide and adhere through short-range cohesive forces such as van der Waals interactions and electrostatic attraction, leading to the formation of larger porous aggregates. Initially, growth occurs in a relatively gentle, hit-and-stick regime, but as particles grow to millimeter and centimeter scales, collisional energies increase, leading to compaction, bouncing, and eventually fragmentation (Blum & Wurm, 2008).

Once particles grow beyond centimeter scales, gravity begins to play a dominant role. In regions of high particle density, mutual gravitational attraction between solids allows for the formation of kilometer-sized planetesimals. Safronov and Zvjagina and later Wetherill and Stewart proposed that planetesimal formation proceeds via a combination of gravitational focusing and stochastic collisions, leading to the runaway growth of larger bodies (Safronov & Zvjagina, 1969; Wetherill & Stewart, 1989). As the largest planetesimals begin to dominate their local gravitational zones, the growth transitions to an oligarchic regime, where a few large protoplanets (or planetary embryos) accrete nearby material more efficiently than their smaller counterparts. This slow, stepwise accumulation of mass is illustrated schematically in Figure 1.2.

Safronov's original model implicitly assumed that planetesimals formed through a large number of gentle, low-velocity collisions between small solid bodies. This incremental accretion process is consistent with the formation of a ***rubble pile*** structure, a loosely bound

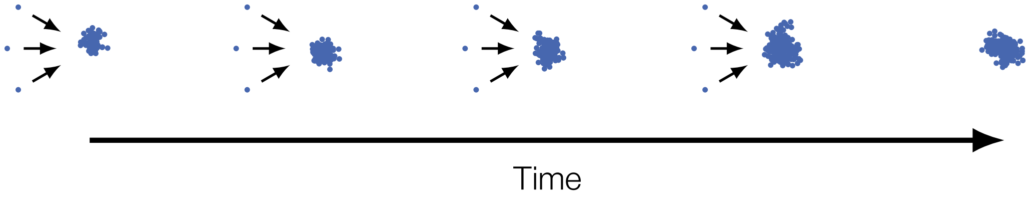

Figure 1.2: Schematic illustration of Classical Hierarchical Growth: a planetesimal forms via successive sticking collisions of micrometer-sized dust particles.

aggregate of smaller components held together primarily by self-gravity. Although Safronov did not use this term explicitly, it has become a standard interpretation of planetesimals formed via slow collisional growth. However, laboratory experiments and numerical studies suggest that, under certain conditions, collisional compaction during growth can lead to more cohesive or even monolithic internal structures (Blum & Wurm, 2008; Kataoka et al., 2013). Whether a planetesimal forms as a loosely bound rubble pile or a more cohesive monolith has significant implications for its mechanical strength, collisional evolution, and ability to retain volatiles.

The classical model provides a successful framework for understanding the formation of the inner, rocky planets. In the inner disk, where temperatures are high and only refractory materials can condense, terrestrial planets form predominantly from silicate-rich planetesimals. Through repeated impacts and mergers, these bodies grow into planetary embryos over timescales of a few million years, eventually clearing their local neighborhoods during the giant impact phase (Chambers, 2001). The formation of a rocky planet and a gas giant according to this model is shown in Figure 1.3.

A fundamental difficulty for Classical Hierarchical Growth arises from the so-called bouncing barrier, in which collisions between millimeter- to centimeter-sized dust aggregates frequently lead to bouncing rather than sticking, thereby stalling growth by simple coagulation (Johansen et al., 2014). This barrier is expected to operate throughout much of the protoplanetary disk, with its severity depending on local material properties and collision velocities. Overcoming it is therefore a necessary prerequisite for forming larger bodies.

The Classical Hierarchical Growth model encounters additional significant challenges when applied to the outer regions of the protoplanetary disk. Beyond the snow line, where temperatures are low enough for volatile compounds like water to condense into ices, the surface density of solids increases substantially. This enhancement should, in principle, favor the formation of massive planetary cores. Yet in the classical framework, where growth proceeds through incremental collisions leading up to kilometer-sized planetesimals, the timescale required to assemble a $\sim$10 Earth-mass core is often longer than the lifetime of the gaseous component of the disk, which typically dissipates within 1-10 Myr (Pollack et al., 1996). Additional processes such as the rapid inward drift of smaller solids due to gas drag and destructive collisions between planetesimals further inhibit efficient growth. As a result, classical collisional accretion alone often fails to form giant planet cores quickly enough in the outer disk, motivating the development of alternative formation mechanisms (Thommes et al., 2003).

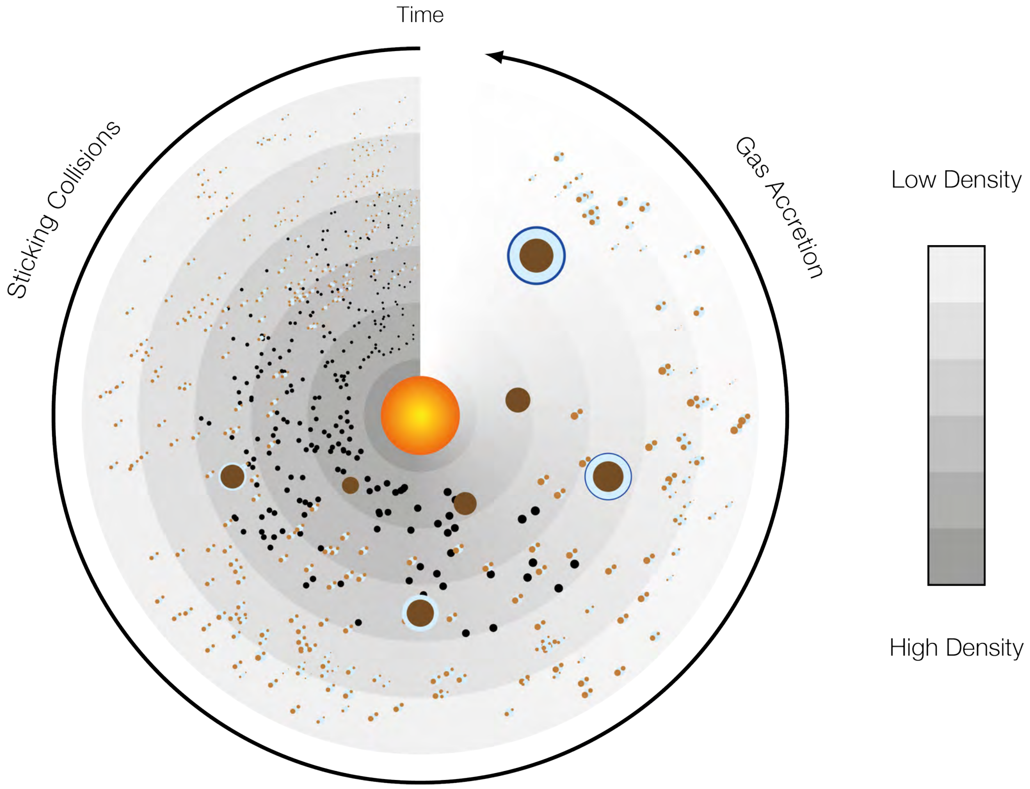

Figure 1.3: Classical Hierarchical Growth scenario for a Jupiter-like giant planet and a smaller terrestrial planet: Micrometer-sized dust grains in the protoplanetary disk collide and stick, forming larger aggregates. These grow into pebbles, boulders, and eventually kilometer-scale planetesimals through continual collisions. Over time, these planetesimals accrete more material via sticking collisions and merge into planetary embryos and planets. The planetesimals that have not formed planets are now known as asteroids or comets (KBO, OCO).

Compounding this difficulty is the meter-size barrier, which arises due to the rapid inward migration of meter-scale particles under gas drag (Blum & Wurm, 2008). As originally demonstrated by (Weidenschilling, 1977), particles of this size experience the highest drift velocities and can spiral into the central star on timescales of just hundreds of years. Consequently, alternative pathways for planetesimal formation have been proposed, such as the gravitational collapse of dense particle clumps triggered by streaming instabilities (Johansen et al., 2007; Youdin & Goodman, 2005).

1.1.2 Pebble Accretion

Pebble accretion has emerged as a leading mechanism in planet formation theory, offering a solution to the timescale bottlenecks inherent in Classical Hierarchical Growth. Like classical models, pebble accretion begins with micron-sized dust grains forming in the protoplanetary disk. These grains collide and stick together through van der Waals forces and other surface interactions, forming porous aggregates. As growth proceeds, the aggregates reach millimeter to centimeter sizes, at which point they are commonly referred to as ***pebbles***.

In the outer regions of the disk, beyond the snow line, the condensation of water ice on grain surfaces increases sticking efficiency and accelerates pebble growth. These icy pebbles are particularly abundant well beyond the snow line. Due to gas drag, pebbles experience radial drift toward the central star. However, under certain conditions, local concentrations of pebbles can become unstable to the streaming instability, a collective drag-induced process that causes clumping of solids and can trigger gravitational collapse (Wahlberg Jansson & Johansen, 2014). The rapid collapse of these pebble-rich filaments can form kilometer-sized planetesimals on timescales of hundreds to thousands of years. This process is illustrated in Figure 1.4.

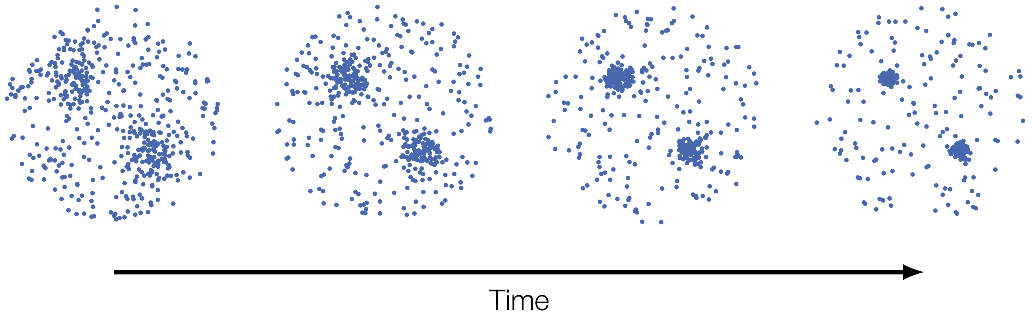

Figure 1.4: Gravitational collapse of two pebble clouds. After the rapid collapse, two kilometer-sized planetesimals form.

Once planetesimals have formed, their continued growth can be significantly accelerated by the accretion of inward-drifting pebbles, millimeter to centimeter-sized solid particles. When a planetesimal reaches a critical mass, it generates a gravitational influence (described by its Bondi or Hill sphere) large enough to efficiently capture pebbles passing through its vicinity. Gas drag slows the pebbles relative to the growing embryo, enhancing their accretion cross-section and leading to rapid mass growth (Lambrechts & Johansen, 2012; Ormel & Klahr, 2010). This process has emerged as a compelling solution to the timescale problem in classical core formation models. It allows planetary embryos, especially in the outer disk, where pebbles are more abundant and drift timescales are longer, to grow to several Earth masses within the few million years typically available before the gaseous component of the disk dissipates.

Theoretical predictions of pebble accretion are increasingly supported by high-resolution observations of protoplanetary disks. Data from the Atacama Large Millimeter/Submillimeter Array (ALMA) DSHARP survey (Andrews et al., 2018) reveal that ring-like substructures are common features in millimeter continuum emission. These rings are interpreted as dust traps or pressure bumps that act as local barriers to radial drift, allowing pebbles to accumulate (Jiang & Ormel, 2022). Such environments are ideal for both the onset of streaming instabilities, which facilitate the formation of planetesimals, and for enhancing the local efficiency of pebble accretion onto larger bodies. Complementary findings from James Webb Space Telescope (JWST) further indicate vertical grain segregation in disks: While sub-micron to micron-sized grains remain well-coupled to the gas, millimeter-sized pebbles are observed to settle toward the midplane (Duchêne et al., 2024), consistent with theoretical expectations for midplane particle concentration required for both streaming instability and pebble accretion.

The growing body of theoretical and observational evidence supports a picture in which pebble accretion contributes significantly to the growth of planetary embryos and the resulting diversity of planetary architectures. In the outer disk, where pebble fluxes can be high and growth timescales are favorable, embryos may reach the critical mass required for runaway gas accretion, enabling the formation of gas giants. In contrast, in the inner disk, smaller planetary embryos accrete pebbles relatively inefficiently, and even Earth-mass cores require comparatively high pebble fluxes in order to grow substantially (Ormel, 2017). As a consequence, core growth tends to stall at lower masses, often culminating in systems dominated by smaller, rocky planets (Lambrechts & Johansen, 2014). This radial variation in pebble-accretion efficiency is illustrated in Figure 1.5, which shows a schematic overview of pebble formation, planetesimal collapse, and planetary core growth across the protoplanetary disk.

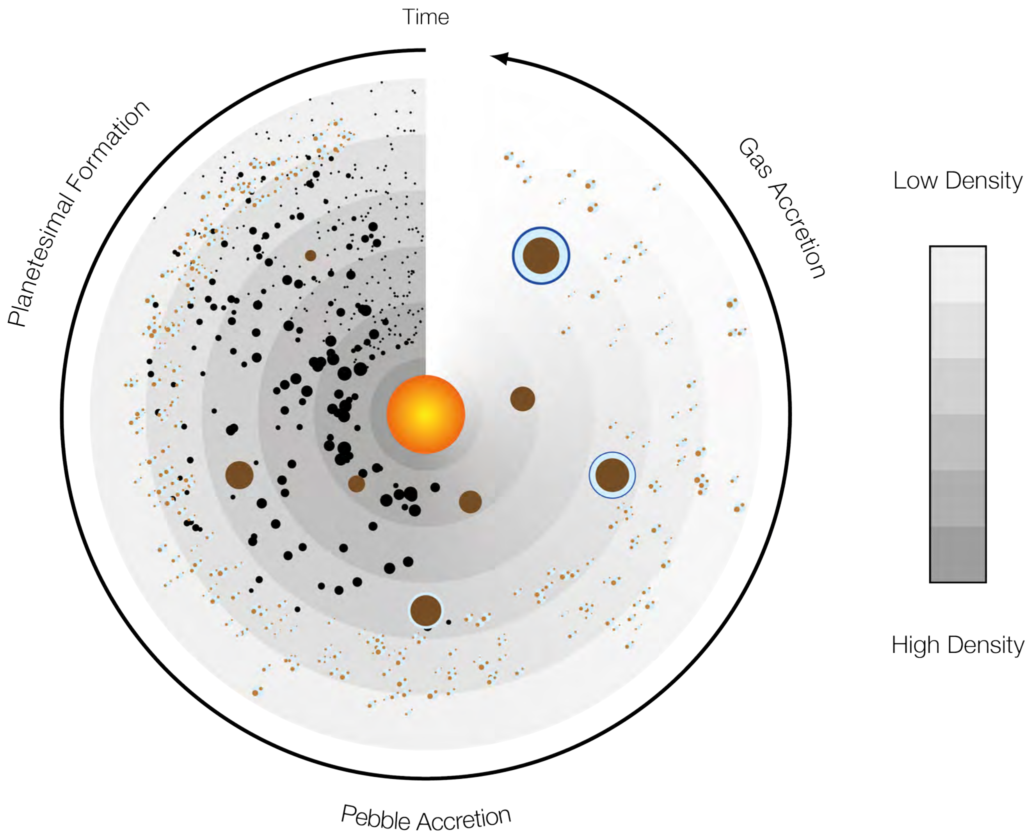

Figure 1.5: Pebble accretion illustrated in a possible formation scenario of a Jupiter-like gas giant and a smaller terrestrial planet. Initially, pebbles form via sticking collisions of micrometer-sized dust grains. Outside the snow line, ice condenses onto the pebbles. Through streaming instability, dense pebble clumps collapse into planetesimals. These planetesimals then accrete more icy pebbles drifting inward, eventually forming massive planetary cores. If the core exceeds the critical mass, gas accretion begins, forming a gas giant. Unaccreted planetesimals may survive as comets or asteroids (e.g., in the Kuiper Belt or Oort Cloud).

Despite its growing prominence, the pebble accretion paradigm is not without significant challenges and open questions. One major uncertainty lies in the availability and persistence of pebbles across the disk. Pebbles are subject to rapid inward drift due to gas drag, which may deplete the outer disk of solids before they can be efficiently accreted by growing embryos, particularly in the absence of long-lived pressure traps or disk substructures (Ormel, 2017). Moreover, the conditions required for streaming instabilities to concentrate pebbles and initiate planetesimal formation depend sensitively on local disk turbulence, metallicity, and particle size distributions, which are still poorly constrained. Observationally, while ALMA and JWST provide indirect evidence for millimeter-sized grains and vertical settling, direct confirmation of large-scale pebble populations and their spatial concentration remains elusive, limiting empirical validation of the paradigm's efficiency.

In addition, recent isotopic and dynamical analyses have raised doubts about whether the terrestrial planets themselves could have formed via pebble accretion. Morbidelli et al. argue that pebble accretion cannot simultaneously account for the compositional, chronological, and dynamical constraints of Earth and Mars, favoring instead a planetesimal-based growth scenario (Morbidelli et al., 2025). Whether pebble accretion could lead to the formation of gas giants like Jupiter is debated (Brügger et al., 2020).

These considerations highlight that while pebble accretion provides an elegant solution to the timescale problem in classical models, its applicability may be more context-dependent than initially assumed, underscoring the need for continued theoretical refinement and observational testing (Kretke & Levison, 2014).

1.2 Comets

Comets are widely assumed to be remnants of the early period of solar system formation, planetesimals that have not accreted to form planets. Their kilometer-sized nuclei are composed of refractory materials, dust, and ices. Comets are usually found on highly elliptical orbits and as they approach perihelion and experience more and more solar radiation, they heat up and their volatile compounds start to sublimate. Through this process, also known as activity, large amounts of refractory dust gets ejected from the nucleus and forms a cloud around, known as coma. Figure 1.6 shows the nucleus of comet 67P/Churyumov-Gerasimenko along with jets carrying refractory materials. Depending on how active a comet is, the coma can reach a size of millions of kilometers in diameter. As the nucleus comes closer to the sun, the dust in the coma is blown back by solar wind, which forms the tail of the comet. A second tail, much less bright, appears as the gas gets ionized by the solar radiation (Thomas, 2020).

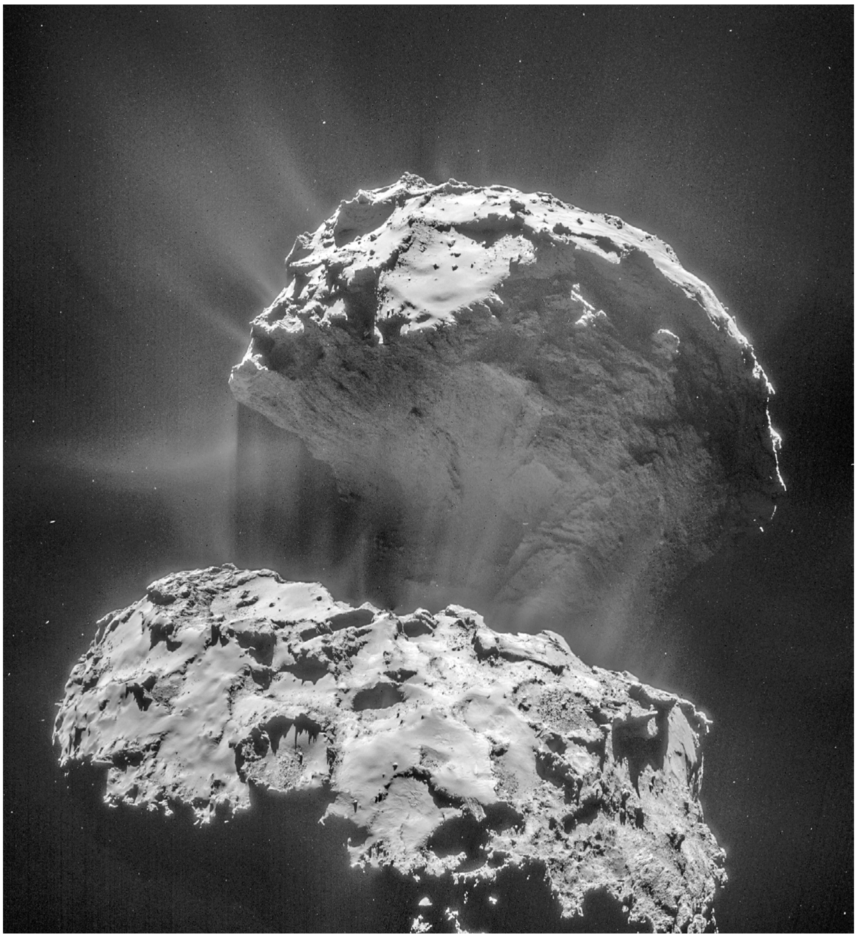

Figure 1.6: Comet 67P/Churyumov-Gerasimenko photographed by the Navigation Camera (NAVCAM) of Rosetta on 3 February 2015 from a distance of 28.7 km from the comet center. The activity is clearly visible, as the ejected dust is illuminated by the sun.
Credit: ESA/Rosetta/NAVCAM – CC BY-SA IGO 3.0

Comets have formed in the outer regions beyond the snow line where ices could condense and survive. Over time, dynamical processes – particularly the migration of the giant planets – scattered these icy bodies into distinct reservoirs. The Kuiper Belt, located beyond Neptune, is thought to be a remnant of the original protoplanetary disk, where many objects remained relatively undisturbed; it is the source of many short-period comets, particularly Jupiter Family Comet (JFC) (Gladman, 2005). In contrast, the Scattered Disk contains objects with higher eccentricities and inclinations, resulting from gravitational scattering by Neptune during its outward migration (M. J. Duncan & Levison, 1997). The Oort Cloud, a distant and nearly spherical shell of icy bodies surrounding the solar system, likely formed when planetesimals from the outer solar system were ejected outward by Jupiter and Saturn and later stabilized by galactic tides and stellar encounters (M. Duncan, 2009; Fernández, 2008). It is believed to be the source of Long Period and Dynamically New Comets (LPC, DNC). Additionally, the Main Asteroid Belt, located between Mars and Jupiter, is thought to have originally hosted both rocky and icy material. Some objects there, known as Main-Belt Comets (MBCs), may have retained subsurface ice and show comet-like activity, likely driven by sublimation (Hsieh & Jewitt, 2006). The classification of comets is shown in Table 1.1. Small bodies in the solar system are traditionally classified as asteroids or comets based on their presumed formation location relative to the snow line. However, a more refined dynamical classification can be made using the Tisserand parameter (Murray & Dermott, 2000), as defined in Equation 1.1. This parameter is conserved in the circular restricted three-body problem and is widely used to distinguish between different orbital populations:

Table 1.1: Classification of comet types with typical orbital periods and origin regions.

Type	**Orbital Period [y]**	**Typical Origin**
Main Belt Comet (MBC)	$\sim$ 3 – 6	Asteroid Belt
Jupiter Family Comet (JFC)	$<$ 20	Kuiper Belt / Scattered Disk
Halley Type Comet (HTC)	20 – 200	Scattered Disk / Oort Cloud
Short Period Comet (SPC))	$<$ 200	Kuiper Belt / Scattered Disk
Long Period Comet (LPC)	$>$ 200 (up to millions)	Oort Cloud

$$T_J = \frac{a_p}{a} + 2\sqrt{\frac{a}{a_p}(1-e^2)}\cos i \tag{1.1}$$

where a is the semi major axis, e the eccentricity, i the inclination relative to the perturbing body, a_p the semi-major axis of the perturbing body. For Jupiter, the value of T_J is classified as follows (Jewitt, 2005):

- $T_J < 2$ correspond to Halley Type Comet (HTC)
- $2 < T_J < 3$ corresponds to Jupiter Family Comet (JFC)
- $T_J > 3$ corresponds to asteroids

However, in contrast to classification of asteroids and comets at the threshold of $T_J = 3$, Jewitt and Hsieh states that there is actually a continuum and the categorization might not be as distinct as previously thought (Jewitt & Hsieh, 2024).

1.2.1 Exploration

Since some of the brighter comets are visible by the naked eye when they approach perihelion, their sightings have been documented repeatedly throughout history. Already in 1759 the return of comet 1P/Halley has been correctly predicted (Binzel, 2004). But only in the early 1950s has cometary research begun to flourish with the emergence of the ”dirty snowball” structural model of cometary nuclei by (Whipple, 1950), the proposition of a large comet reservoir, called Oort Cloud (Oort, 1950) and the insights into the plasma tail (Biermann & Lüst, 1958). Not long thereafter, space missions were planned to provide detailed observations.

The first missions to visit a comet were part of the so-called Halley Armada, comprising the Japanese Suisei and Sakigake spacecraft, the Russian Vega 1 and Vega 2 spacecraft, and ESA's Giotto mission. The Russian and Japanese spacecraft conducted coordinated observations of comet 1P/Halley, providing crucial data on its plasma environment, dust, and gas emissions. NASA also repurposed an Earth observation spacecraft, ICE, which had launched in 1978 to conduct measurements of the Sun and later performed a flyby of comet 21P/Giacobini–Zinner (Brandt et al., 1985). Giotto executed a close flyby of comet 1P/Halley in 1986, capturing the first close-up images of a comet nucleus (Keller et al., 1986).

In 1999, NASA launched the Stardust spacecraft, which flew by comet 81P/Wild 2 in 2004 and captured particles from the coma in aerogel collectors. The spacecraft returned to Earth in 2006 (Brownlee et al., 2006). Analysis of this returned comet sample has revealed that these comets preserve primitive material from the early solar system.

Deep Impact conducted a hypervelocity impact on comet 9P/Tempel 1, exposing subsurface material and revealing insights into the structure and composition of the nucleus (A'Hearn et al., 2005). After its successful encounter with comet 9P/Tempel 1 in 2005, the Deep Impact spacecraft was repurposed for an extended mission known as EPOXI, including a flyby of comet 103P/Hartley 2, known as Deep Impact Extended Investigation (DIXI). The spacecraft flew past Hartley 2 in 2010, capturing high-resolution images and compositional data of the small, active comet (A'Hearn et al., 2011).

ESA's Rosetta mission, accompanied by the Philae lander, provided the first long-term escort and surface investigation of a comet, 67P/Churyumov–Gerasimenko, yielding critical insights into cometary activity and surface evolution (Boehnhardt et al., 2017; Glassmeier et al., 2007).

To date, all cometary missions have targeted comets with periods smaller than 200 years. These objects have undergone numerous passages through the inner solar system and thus experienced repeated thermal processing, which has significantly altered the structure and composition of their surfaces. Even the Giotto mission, which flew by comet 1P/Halley, explored a Halley-type comet that, while longer-period, is not dynamically new. In contrast, it is believed that DNCs originate from the Oort Cloud and are thought to be making their first approach to the Sun, retaining more pristine, unprocessed material. No space mission has yet directly explored a DNC, leaving a major gap in our understanding of early solar system conditions.

Object like this are usually detected a couple of months before they pass perihelion. This is not enough time to launch a spacecraft. The first mission that is planned to visit a DNC is Comet Interceptor (Jones et al., 2024). It is set to launch in 2029 and will then first park at the Sun-Earth Lagrange Point SEL2 for a maximum of 4 years until a target has been selected. While launching a spacecraft in the time between detection and perihelion of a DNC is not possible, routing one from a parking orbit at SEL2 is certainly plausible. Comet Interceptor will however not accompany the comet, it will only conduct a fly-by and gather as much data as possible around closest approach.

1.2.2 Composition and Structure

We have only scratched the surface and there is still a lot left to learn about the interior structure and composition of comets. The internal structure of comets has been a topic of evolving theories since the "dirty snowball" model was first proposed by (Whipple, 1950), which envisioned comets as compact mixtures of dust and volatile ices that sublimate near the Sun.

The Giotto mission to Comet 1P/Halley in 1986 revealed a dark, low-albedo surface, suggesting a much more dust-rich composition than expected. Giotto also observed localized jets of activity rather than uniform sublimation, implying an inhomogeneous and structured nucleus (Keller et al., 1986). Later, the Deep Impact mission to Comet 9P/Tempel 1 in 2005 showed that the surface was porous and fragile, with low tensile strength and evidence of layering, inconsistent with the compactness assumed in Whipple's model (A'Hearn et al., 2005).

These findings led to the emergence of the ***rubble pile*** model, in which comet nuclei are seen as loosely bound agglomerations of larger blocks or fragments held together by weak gravity (Weissman, 1986) as displayed in Figure 1.7a. These fragments are thought to have undergone collisions and reaccumulation, making them non-primordial. To explain some cohesion between components, the ***icy glue*** model was proposed, suggesting that volatiles act as a weak cementing agent between dust grains (Gombosi & Houpis, 1986), shown in Figure 1.7b.

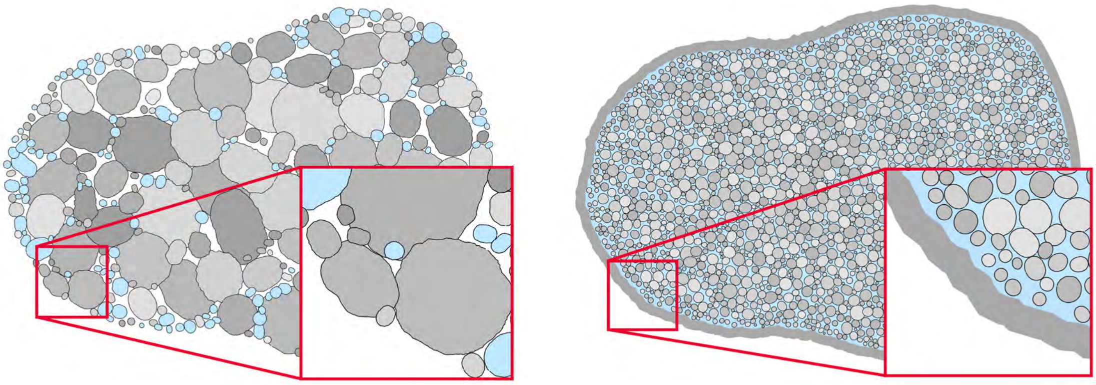

(a) Rubble Pile

(b) Icy Glue

Figure 1.7: "Rubble Pile" structural model of a comet nucleus (a), illustrating a loosely bound aggregate of ice-rich (light blue) and refractory-rich (gray) debris, held together primarily by self-gravity, with significant porosity and minimal cohesive strength. The "Icy Glue" (b) model introduces volatile ices that act as a binding agent, providing moderate cohesion between constituent materials. A dust layer has been added to the surface.

However, this idea was challenged by results from the Rosetta mission, which found that Comet 67P/Churyumov–Gerasimenko has a porosity of 72% – 74% and a bulk density of 0.533 g/cm^3 (Pätzold et al., 2016). Furthermore, (De Niem et al., 2018) shows that 67P has not encountered high-velocity collisions by large objects and 67Ps properties are consistent with primordial accretion, although this is debated (Jutzi et al., 2017). The surface was found to be dominated by dusty, non-volatile material, with ices confined to subsurface layers or isolated patches. Furthermore, the discovery of fractures, pits, and consolidated terrains indicated a complex evolutionary history (El-Maarry et al., 2019). The refractory-to-ice ratio in comets remains heavily debated. While (Pätzold et al., 2016; Rotundi et al., 2015) reported a dust-to-ice mass ratio of $\delta = 4 \pm 2$, (Fulle et al., 2016) found a higher dust-to-ice ratio of $\delta = 8.5$, a dust grain bulk density in the coma of $\rho_D = 0.795^{+0.840}_{-0.065}$ g/cm^3 and an internal macro-porosity of approximately 40%, referring to voids between larger aggregates.

CONSERT found that the interior of 67P is homogeneous at scales of tens to hundreds of meters, with no large voids or internal layering (Pätzold et al., 2016). It indicates a volumetric dust-to-ice ratio of

$$0.4 < \delta_V < 2.6$$

which translates to a dust-to-ice mass ratio of about

$$1.2 < \delta < 7.8 \quad \text{assuming the grain density} \quad \rho_{\text{dust}} \approx \rho_{\text{olivine}} \approx 3\rho_{\text{ice}}$$

This is in the same order as the previous indications, although slightly lower, which could indicate a lower ice quantity in the surface layers, possibly due to sublimation. (Kofman et al., 2020) also states that CONSERT measured different permittivity values for surface layers and the interior. Overall, the current estimations of the dust-to-ice ratio remain of low precision (Choukroun et al., 2020).

These findings support the two formation models in Section 1.1. The ***Classical Hierarchical Growth*** model predicts that comets formed through successive mergers of similarly structured, increasingly larger aggregates, resulting in a relatively homogeneous internal structure as shown in Figure 1.8a. In contrast, the ***pebble pile*** model suggests comets formed from the gentle gravitational collapse of millimeter to centimeter sized dust and ice aggregates, referred to as ***pebbles***, displayed in Figure 1.8b.

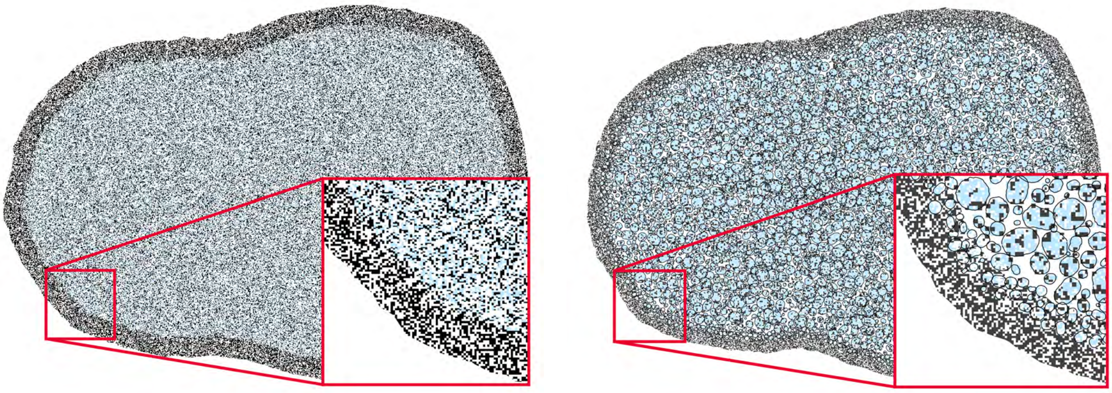

(a) Homogeneous Comet

(b) Pebble Based Comet

Figure 1.8: The structural model of a homogeneous comet (a). A comet that formed from the gravitational collapse of a pebble cloud (b) would also appear homogeneous on large scales, but on small scales the centimeter sized pebbles become apparent. Both models are based on a 50/50 dust-to-ice ratio, a porosity of about 70% and include a dust layer on the surface.

Both models would explain the observed low density, high porosity, and mechanical weakness of comets like 67P/Churyumov–Gerasimenko. The main difference lies in the expected sub-surface structure of comets; a comet formed by the gravitational collapse of a pebble cloud would possess an inhomogeneous interior with pebbles still preserved under the surface, whereas a comet formed by hierarchical growth would show a more homogeneous interior with no pebbles.

While (Davidsson et al., 2016) advocates hierarchical growth, (Blum et al., 2017, 2022; Lorek et al., 2016) argue for the possibility of a gentle collapse of a pebble cloud. The abundance of pebbles on comets is currently heavily debated.

The Deep Impact spacecraft reported the presence of centimeter to decimeter sized particles in the vicinity of the nucleus of comet 103P/Hartley 2, these are however assumed to be aggregates that have been ejected rather than primordial pebbles (Kretke & Levison, 2015). Water-ice enriched blocks (WEBs), which could be a form of ice-rich pebble agglomerates, have been proposed to be the cause of the seasonal surface blue-ing on 67P (Ciarniello et al., 2022) and are thought to be primordial, there is however no clear observational confirmation yet.

”Goosebumps”, at scales of about 3 meters, have been observed on comet 67P (Sierks et al., 2015), which were linked to primordial pebbles by Sierks et al., however, since similar structures were found all over the nucleus (Thomas et al., 2015), it is unlikely that these ”goosebumps” are an expression of primordial pebbles (Herique et al., 2019). Analysis of the Philae landing site with data from CIVA has been argued to indicate the abundance of millimeter sized pebbles which could be of primordial origin (Poulet et al., 2016), the data are, however, not conclusive. Further investigations with OSIRIS and ROLIS do not distinguish between boulders and pebbles and do not indicate primordial origin (Pajola et al., 2017). These millimeter or centimeter sized objects on the surface might well be broken debris from activity of larger objects like boulders (El-Maarry et al., 2019; Kretke & Levison, 2015).

The absence of pebbles might well challenge the pebble accretion theory for the formation of our Solar System.

1.3 THz Time-Domain Spectroscopy

In planetary science, the visual wavelength regime has been extensively explored, from early ground-based telescopes to modern in-situ imaging instruments such as CaSSIS on ExoMars Trace Gas Orbiter (ExoMars TGO) (Thomas et al., 2017), OSIRIS on the Rosetta spacecraft (Keller et al., 2007), and Comet Camera (CoCa) on the forthcoming Comet Interceptor mission (Jones et al., 2024). While visual observations can reveal detailed surface morphology, they provide only limited information about the composition of individual constituents. By extending measurements in the Ultraviolet (UV) and Infrared (IR) ranges and applying spectroscopy, it becomes possible to study absorption and emission features, enabling compositional analysis. However, the high frequencies in these wavelength ranges generally preclude access to subsurface properties. To probe internal structure and deeper layering, longer wavelengths capable of penetrating below the surface are required. Ground Penetrating Radar (GPR), widely used in terrestrial applications, operates at MHz to GHz frequencies (microwaves), offering subsurface sensitivity but typically with spatial resolutions no better than tens of centimeters. Instruments operating at comparable frequencies have also been flown on space missions, including low-MHz radar sounding of cometary interiors with CONSERT (Barbin et al., 1999), and GHz radiometry of cometary comae and planetary atmospheres with MIRO (Gulkis et al., 2007) and SWI (Fletcher et al., 2023), respectively.

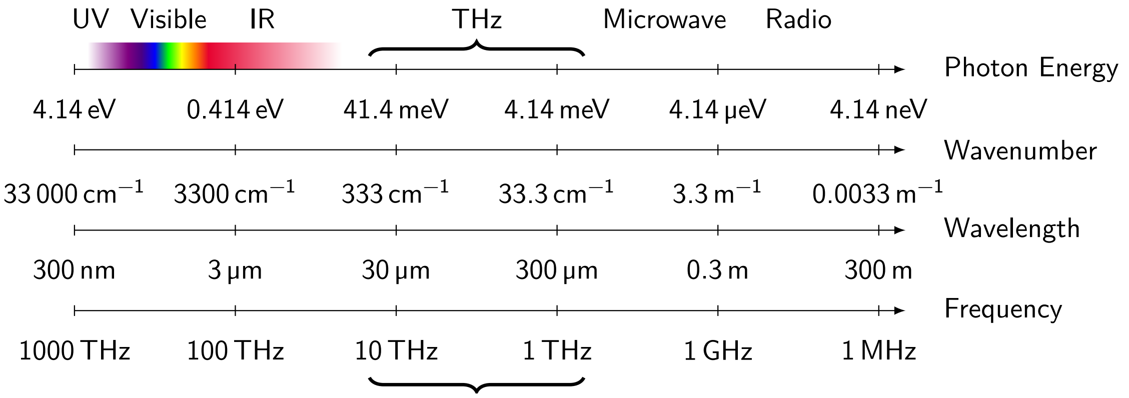

Figure 1.9: The electromagnetic spectrum with the THz region (THz-gap) indicated.

In-between IR and the microwave region lies the THz band, indicated in Figure 1.9. This band has long been called the ***THz-gap*** (Pawar et al., 2013) as it was not possible to create and detect THz radiation in an affordable way. This began to change in the late 1980s (Beard et al., 2002; van Exter et al., 1989), and THz research is gaining more and more popularity in pharmaceutical, bio-technological and industrial fields (Dhillon et al., 2017; Leitenstorfer et al., 2023; Naftaly et al., 2019; Park et al., 2015). It has also become of interest in space applications (Pearson et al., 2021), for example for lunar regolith analysis (S. Wang, 2024; S. Wang & Hiramatsu, 2024) and astrophysical ice analysis (Giuliano et al., 2019). Efforts have been made to space qualify components for future missions (Gueckstock et al., 2024). For in-situ measurements of sub-surface layers of planetary bodies, THz frequencies are located at the sweet spot of providing sub-surface penetration at the cm scale while still providing benefits of mm to cm scale resolution.

Terahertz spectroscopy is conducted using either pulsed or continuous wave (CW) radiation. CW systems generally provide higher frequency resolution and superior dynamic range, while pulsed systems operate in the time domain, offering greater flexibility and access to

broader spectral information (Karpowicz et al., 2005). Although pulsed setups are typically more complex to implement, their versatility and the richness of the data they provide make them well-suited for initial proof-of-concept studies. Consequently, we have chosen to focus on the pulsed THz time domain spectroscopy method.
A THz time domain spectrometer creates broadband THz pulses and measures them as a time trace. The setup of a common commercial THz time domain spectrometer is shown in Figure 1.10. It relies on a femtosecond pulsed laser that is directed to a beam splitter. Part of the beam is guided to the transmitter (Tx) and part, through two delay lines (SDL and FDL), to the receiver. The delay line is adjusted such that the laser pulse and the THz pulse arrive at the same time at the receiver (Rx).

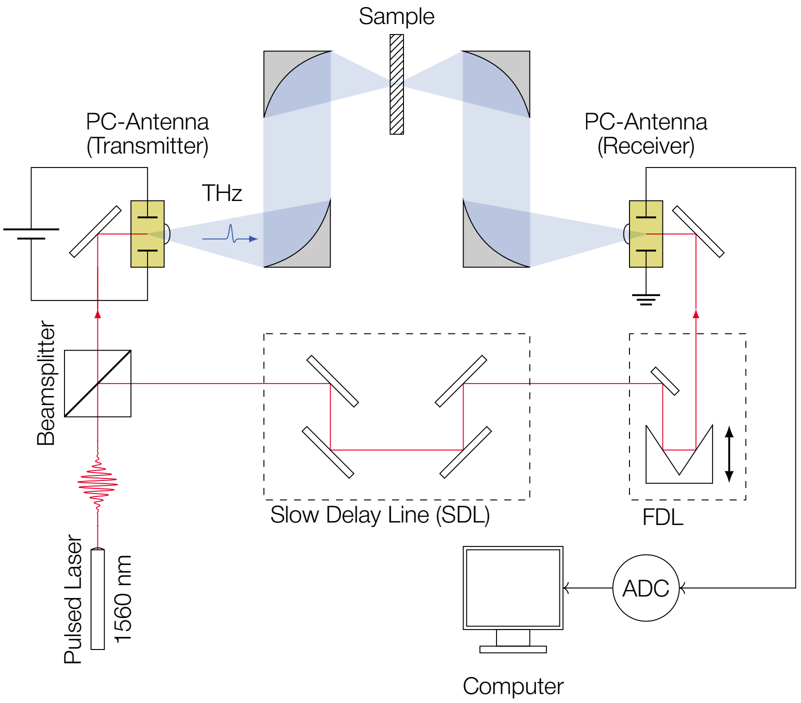

Figure 1.10: The working principle of a THz time domain spectrometer with photo-conductive antennas (PCA) and a pulsed laser. The Slow Delay Line (SDL) is usually configured only once for the optical setup to match the optical path of the laser to the once of the THz pulse. The Fast Delay Line (FDL) is continuously moving back and forth during data acquisition.

While other THz sources, e.g. spintronic emitters (Feng et al., 2021) or plasma generation sources (Roskos et al., 2007), exist, we focus solely on Photo-Conductive Antennas (PCA) (Burford & El-Shenawee, 2017). Each PCA consists of an InGaAs substrate with electrodes attached. The beam is then focused by an attached silicon lens. The working principle of PCAs is described in Figure 1.11.

To capture the pulse in time domain without needing sub-pico-second sampling, the THz waveform can be stitched together from different THz pulses. For that, the laser pulse is delayed slightly by the Fast Delay Line (FDL) for every incoming THz pulse. Scanning the signal within a predefined time window with this method is displayed in Figure 1.12.

The trace can then be used to perform Time of Flight (ToF) analysis and can also be transformed into Fourier space using the Fast Fourier Transform (FFT), thus obtaining magnitude and phase information which gives insight into the complex refractive index of the material.

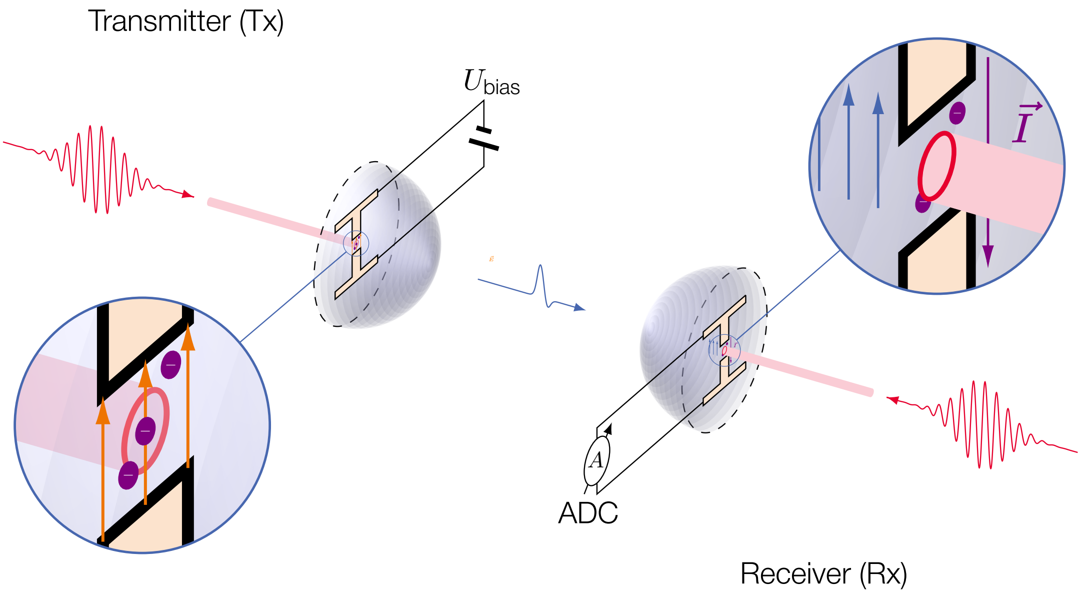

Figure 1.11: Photo-Conductive Antennas (PCA) are made of an InGaAs substrate with electrodes that is attached to a hyper-hemispherical Si lens. A pulsed femto-second laser is focused on the substrate of the transmitter (Tx) and creates charge carriers (violet). These charge carriers are accelerated by the electric field $\vec{E}$ (orange) induced by the bias voltage U_{bias} between the two electrodes and thus emit radiation at THz frequencies. A second laser is delayed such that it arrives at the exact same time at the receiver (Rx). The laser again creates charge carriers which are this time moved by the electric field of the incoming THz pulse (blue). This flow of charge carriers results in a current I that can be measured with an ADC. This is a simplified diagram of a dipole antenna.

Hence sampling THz pulses in time domain requires a complex setup including delay stages or using a dual-comb laser (Willenberg et al., 2024). The latter method does not require a delay-stage and is thus a solution without moving parts, which is especially attractive for space applications.

Operating in time domain brings along other possibilities than just spectroscopic analysis. Previous efforts were made to analyze paintings (Gomez-Sepulveda et al., 2017; Koch-Dandolo et al., 2015) to recover the original work that has been painted over. A THz time domain spectrometer can thus essentially be used as a Ground Penetrating Radar (GPR) but with higher frequencies. This is especially promising to resolve features at smaller scales which could not be resolved with common GPR instruments. Extending this technique to 3D leads to the field of THz tomography (Guillet et al., 2014; Su et al., 2023).
While THz cameras exist (Kanda et al., 2017; Zdanevičius et al., 2015), they require a very high power emission source to illuminate the sample and usually lack the ability to record the waveform in time domain. Most THz detection techniques only provide single-pixel measurements, hence a scanning mechanism is required to obtain a 2D image. We have designed and commissioned a setup to perform proof-of-concept measurements on cometary simulants in the laboratory, as described in Chapter 2. The setup is shown in Figure 1.13. Improving the spatial resolution of 2D scans was achieved through a frequency dependent deconvolution algorithm which is described in Chapter 3. To interactively analyze the obtained data, we have published an open-source cross-platform software which is presented in Chapter 4. The efforts of using THz time domain spectroscopy to resolve the sub-surface

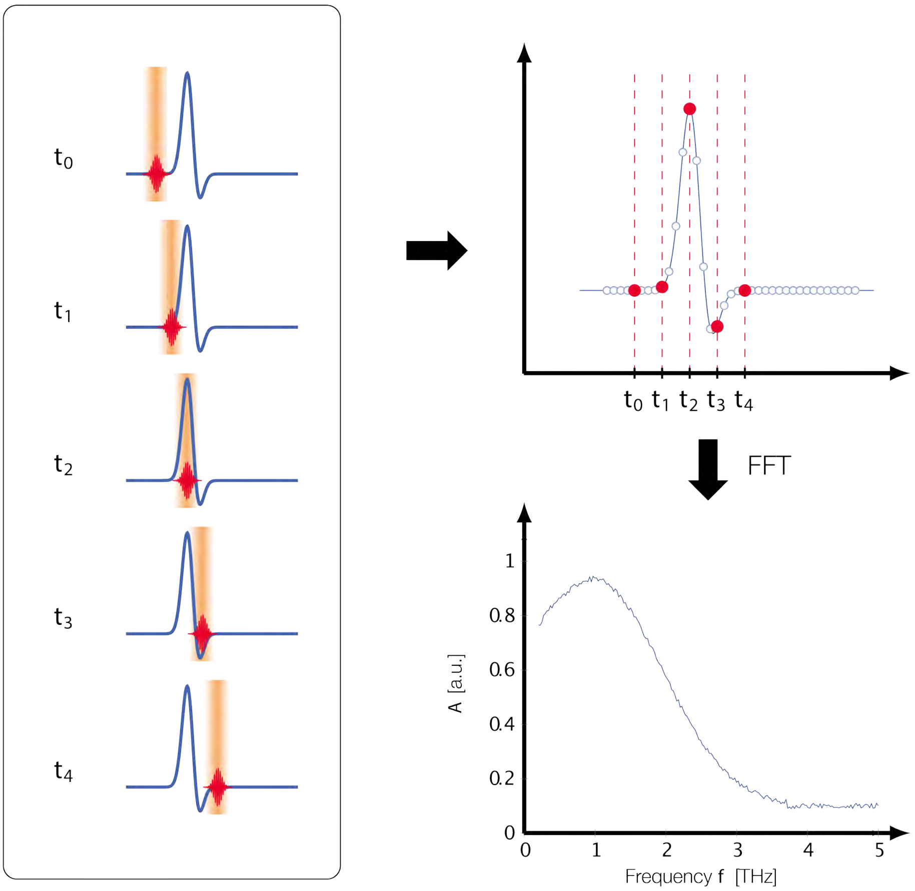

Figure 1.12: Direct acquisition of the full THz waveform is not feasible with current ADCs, as this would require sampling at THz rates. Instead, a widely used method involves reconstructing the waveform by delaying the laser pulse and sampling within a predefined time window. The sampling instants are denoted as t_i. Using this approach, each waveform is effectively assembled from multiple THz pulses.

structure of comets are documented in Chapter 5. Possible applications and implications for future investigations are discussed in Chapter 6.

Amino acids, which are known to be the building blocks of life, have been detected on comets. Specifically, Glycin and L-alanine in the Stardust samples from comet 81P/Wild 2 (Glavin et al., 2008) and glycine on comet 61P/Churyumov-Gerasimenko by Rosetta (Altwegg et al., 2016). It is also known that certain amino acids, for example L-alanine, in their crystalline form, possess distinct absorption lines at THz frequencies. We have documented our spectroscopic measurements of amino acids in Appendix B.

As part of the work conducted in the laboratories, an additional project has been completed about a novel temperature sensor mount. This component has been integrated in all our laboratory setups discussed here and is documented in Appendix G.

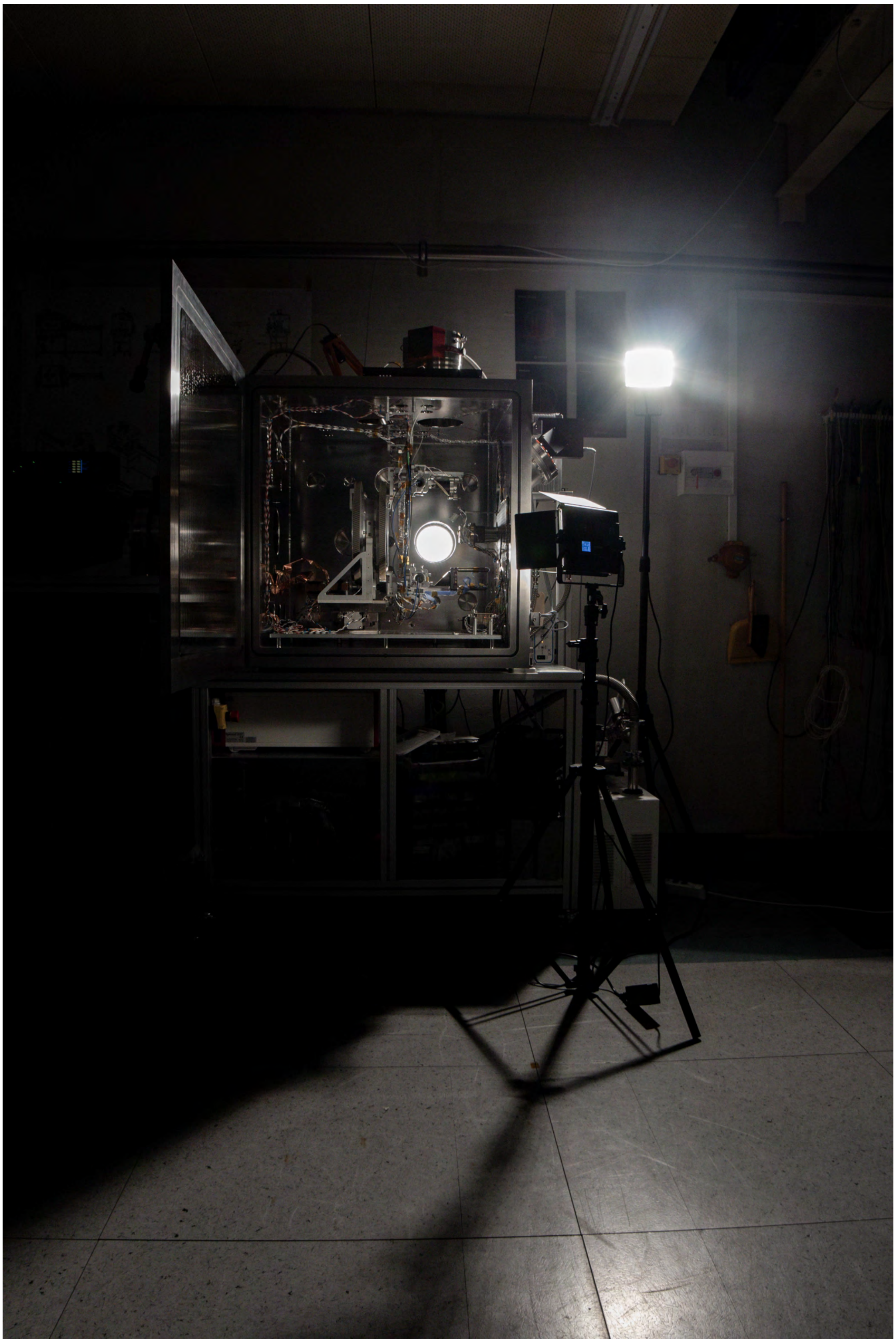

Figure 1.13: The COCoNuT (Characteristic Observations of Cometary Nuclei using THz-spectroscopy) experimental setup in the laboratory. The instrument was designed in 2022 and 2023 and assembled and commissioned in 2023 and 2024 at the University of Bern. Its purpose is to simulate physical conditions relevant to cometary environments in order to assess the feasibility of in-situ terahertz time-domain spectroscopy measurements on comets.

Design and Commissioning of a THz Time Domain Spectro-Goniometer in a Cryogenic Comet Simulation Chamber

Linus Leo Stöckli, *Mathias Brändli, Daniele Piazza, Rafael Ottersberg, Antoine Pommerol, Axel Murk, Nicolas Thomas*

Published in *Review of Scientific Instruments*, Vol. 96 (3): 034502, 2025
DOI: https://doi.org/10.1063/5.0252742

Preamble:

This chapter describes the COCoNuT setup, the core hardware part of this work, that we have developed to conduct an initial proof-of-concept analysis of performing THz spectroscopic measurements on cometary nuclei or other planetary bodies. Minor adjustments have been made to the setup after the publication of this chapter to further increase the quality of the acquired data. These improvements, along with reflections and considerations for future projects are noted in an un-published addendum at the end of this chapter.

Abstract:

We present our newly developed laboratory setup, called COCoNuT (Characteristic Observation of Cometary Nuclei using THz-spectroscopy), consisting of a THz spectro-goniometer in a vacuum chamber along with a cryo-cooler intended for cooling down samples rich in ices expected in cometary environments. This setup allows use of THz time domain spectroscopy on analogues including refractory materials in the spectral range from 0.1 THz to 5.5 THz with a spectral resolution of up to 0.005 THz. Since the optical setup is mounted on a precision controlled x/y-stage, imaging or spatial averaging can be performed. In this work, we present the design decisions and selection of components. Furthermore, the commissioning of the setup is described and the capabilities are shown. The system can reach pressures of 1×10^{-7} mbar and temperatures of 50 K. For 2D scanning a spatial resolution of 0.3 line-pair per mm is obtained.

2.1 Introduction

Comets offer a unique opportunity to gain a deeper understanding of the early evolution of our Solar System. It is widely assumed that they are remnants of the planetary formation process being proto-planetesimals that were not integrated into planets (Öpik, 1973). Support for the pebble accretion concept of planetary formation, in which cm-sized objects (pebbles) are brought together to produce the cores of gas giant planets, has been presented through analysis of images of cometary nuclei (Sierks et al., 2015), although this is controversial and disputed (Herique et al., 2019; Thomas, 2020). Comets are composed mostly of volatile ices and dust, however the exact composition is not known. To investigate the physical properties of comets in laboratory experiments, the environment can be simulated in a vacuum chamber (Binzel, 2004; Kreuzig et al., 2021; Seidensticker & Kochan, 1995) where water ice (Pommerol et al., 2019) and dust analogues (Lethuillier et al., 2022) can be analyzed. In-situ comet exploration such as that conducted using the Rosetta spacecraft (Bond, 2020) has focused on visible and infrared imaging and spectroscopy (Keller et al., 2007), radar (Barbin et al., 1999) observations and mass-spectrometry. A significant part of the electromagnetic spectrum has not yet been investigated. In particular the THz region, reaching from 100 GHz to 10 THz (3 mm - 30 μm), sitting in between infrared and microwave frequencies, is relatively unexplored. While the Doppler-resolved MIRO instrument (Gulkis et al., 2007; Rezac et al., 2019) on-board the Rosetta mission conducted extensive measurements of the comet's coma at 190 GHz and 562 GHz, relatively little is known about the nucleus outside of these narrow frequency windows. Studies of THz frequencies play an increasing role in space sciences (Siegel, 2010). We have specifically chosen THz spectroscopy, because ice is sporadically seen on the surface of comets (Sunshine et al., 2006) and THz frequencies can provide a deeper penetration into the samples than Vis-IR techniques while providing a better spatial resolution than ground penetrating radar. As it has previously been established that many ices are transparent at lower THz frequencies and only have significant absorbance at higher THz frequencies (Ioppolo et al., 2014), analyzing the nucleus with a THz spectrometer seems promising to gain knowledge about its physio-chemical structure. The non-volatile components have been shown to contain organic material (Filacchione et al., 2019; Levasseur-Regourd et al., 2007; Llorca, 2005), which can potentially be analyzed in the THz spectrum. Furthermore, as water vapor has a distinct fingerprint pattern (Cui et al., 2015), THz-spectroscopy can be used to study the sublimating gas above the surface of the comet and determine the influence of the sub-surface structure on cometary activity and the coma. While this setup is primarily focused on cometary exploration, the technology can possibly be used on any planetary exploration mission where ice is present, e.g. Mars. Here we describe a laboratory setup designed to study the feasibility of determining the composition of cometary samples using time domain THz spectroscopy. This will help to lay the foundation for a possible future instrument on an in-situ space mission, designed to help us gain a deeper insight into the composition of small bodies, possibly planets and last but not least: planetary formation.

2.2 Principles

While spectroscopy at infrared and radio wavelengths has been conducted for a long time, it has only been in the last decades that the THz gap has been closed and the possibility to investigate the properties of materials in this frequency range (Koch et al., 2023) exploited. The fundamental principle of time domain spectroscopy is to create a THz pulse and measure its transmission or reflection in the time domain. The resulting trace can then be transformed into Fourier space by using the Fast Fourier Transform (FFT) to obtain a frequency spectrum.

One option to produce THz radiation is a photoconductive antenna (Burford & El-Shenawee, 2017). An internal pulsed femto-second-laser is directed onto a photoconductor where photocarriers are generated, as shown in Figure 2.1. The applied DC voltage bias accelerates the photocarriers, producing a transient photocurrent, driving the dipole antenna and leading to a THz pulse being emitted. The pulse is then guided through a sample and onto the receiver using parabolic off-axis mirrors. A second Photoconductive Antennas (PCA) takes the role of the receiver of the THz radiation. In our setup, the laser pulse from the transmitter was split and a second beam is directed through an optical delay line with the same length as the THz path. Thus the THz pulse and the laser pulse arrive at the same time at the receiver. On the receiving PCA, the laser beam produces photocarriers which are then accelerated by the electric field of the incident THz pulse. The induced current is recorded in a specified temporal window to measure the intensity of the incoming THz pulse in the time domain.

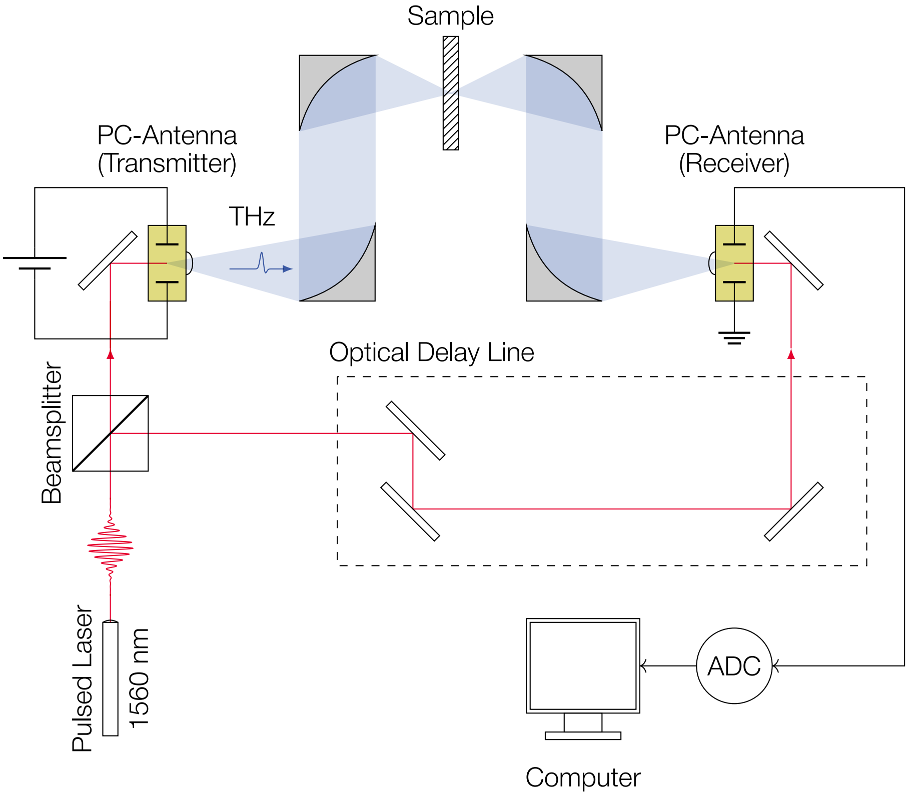

Figure 2.1: Principle of time domain THz spectroscopy using photoconductive antennas (PCA) and a pulsed laser.

In Figure 2.2 we show a single THz pulse in transmission mode in air. To obtain a THz image, an object can be scanned by recording a time trace for each pixel. To plot the image, either the peak-to-peak amplitude of the pulse or the sum of the squares of the trace can be plotted. To further analyze the image, certain windows in the time domain can be selected, corresponding to different depths of the sample (Koch-Dandolo et al., 2015). For each pixel a spectrum is available, which can help differentiating different materials by looking at specific absorption features.

2.3 Requirements

To investigate the application of THz time domain spectroscopy (TDS) we set the requirements for the setup to simulate the conditions found on comets (Thomas, 2020):

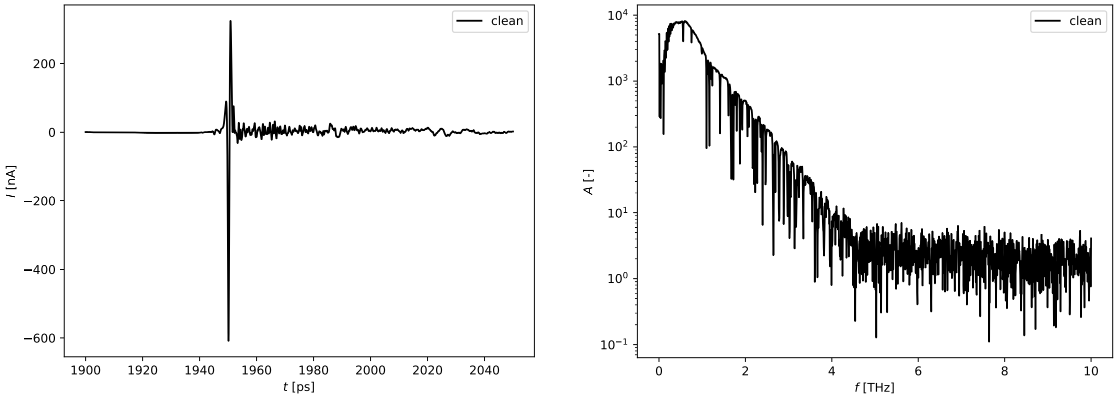

Figure 2.2: The time trace (a) and the corresponding spectrum (b) obtained by the spectrometer. As the measurement was taken at ambient conditions, the water vapor absorption lines are well visible in the spectrum. Above 5 THz, the noise floor dominates.

- Ability to reach sample temperatures ranging from 120 K to 300 K with an active temperature control to reach temperatures with an accuracy of ±2 K and a precision of ±0.5 K
- Ability to reach pressures ranging down to 1×10^{-7} mbar
- Ability to perform time domain THz spectroscopy in either reflection or transmission
- Ability to perform THz 2D imaging

2.4 Design

The main purpose of **COCoNuT** (Characteristic Observation of Cometary Nuclei using THz-spectroscopy) is to simulate the conditions found on comets. A dual-chamber design was implemented to decrease the time spent on loading the sample. This in turn decreases the time the sample is in contact with ambient air. This is especially important for ice samples produced in liquid nitrogen (LN_2) as planetary and cometary analogues. These cold samples cannot be termed as pristine when they are exposed to ambient air for a prolonged time because of rapid accumulation of frost. In addition heat and thermal gradients will lead to metamorphism of the ice.

A technical drawing showing the entire setup is shown in Figure 2.3. The main chamber has three windows for external observation and irradiation of the sample.

The dual chamber design consists of a load-lock chamber and main chamber which are separated by a gate valve. The sample can be loaded in the load-lock chamber while the main chamber is under vacuum. After pumping down the load-lock chamber, the sample can be inserted with the sample translator in the main chamber. The load-lock system is manually operated. Limit switches prevent the gate valve from closing when the sample translator is extended. The spring-loaded sample translator pushes the sample-holder-carrier onto the cryo-cooler. The sample holder itself is screwed down onto the sample holder carrier as shown in Figure 2.4.

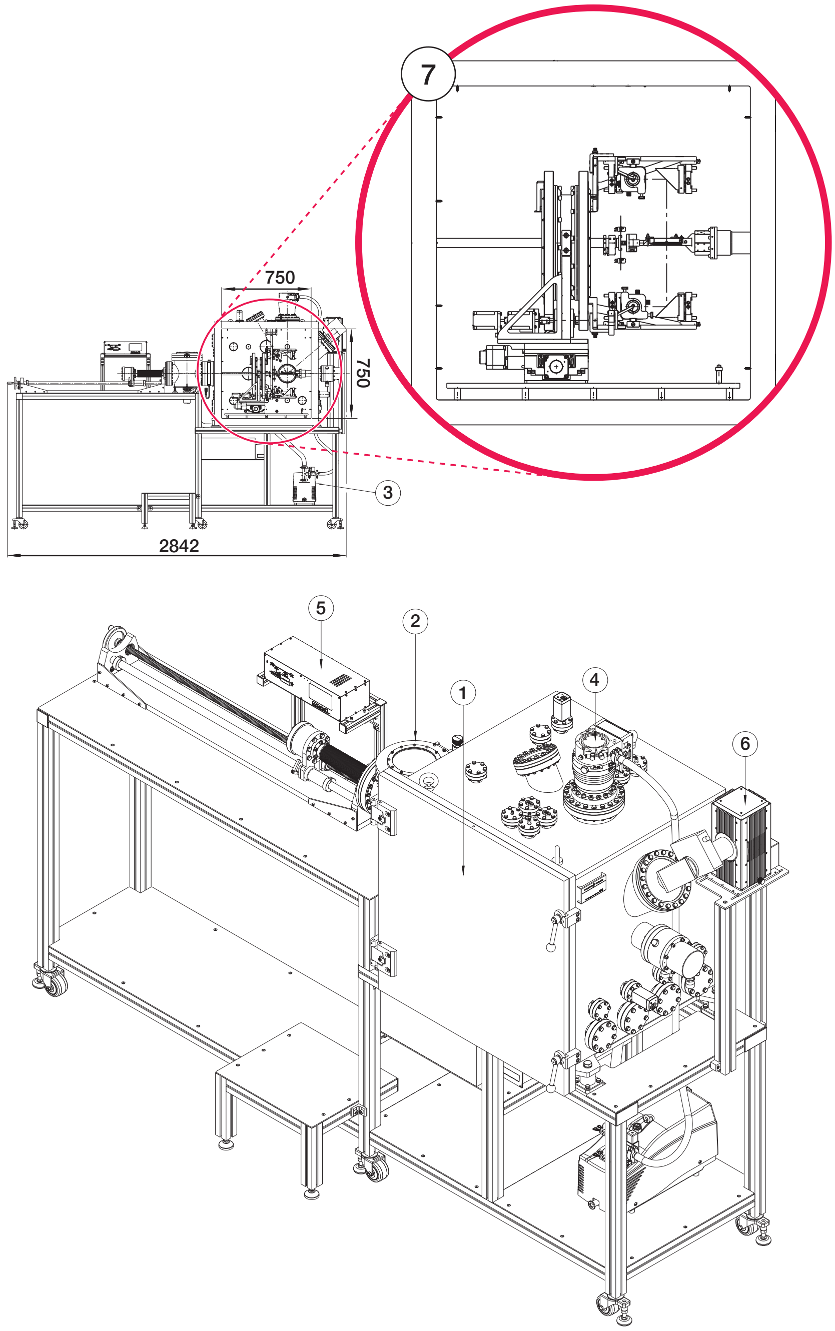

Figure 2.3: Technical drawing of COCoNuT. The Main Chamber (1), Load-Lock Chamber (2), Primary Pump (3), Turbo Molecular Pump (4), Electronics Unit (5), Solar Simulator (6), and Optical Setup (7), which is discussed in more detail in Figure 2.5, are highlighted.

The system has been designed to house the antennas of the TeraFlash THz time-domain spectrometer from ***TOPTICA Photonics AG*** (Toptica, 2014) and operates with an internal 1560 nm laser with an average pulse width of about 80 fs and a repetition rate of 80 MHz. The spectrometer is placed outside of the chamber and the laser is patched into the chamber through polarization maintaining optical fiber feed-throughs. The InGaAs/InAlAs Photoconductive Antennas (PCA) (Roehle et al., 2010) have been manufactured by the ***Fraunhofer Heinrich-Hertz-Institute (HHI)*** and provide a bandwidth of up to 5 THz, dynamic range of about 100 dB, and beam power of about 70 μW. They have been made vacuum compatible

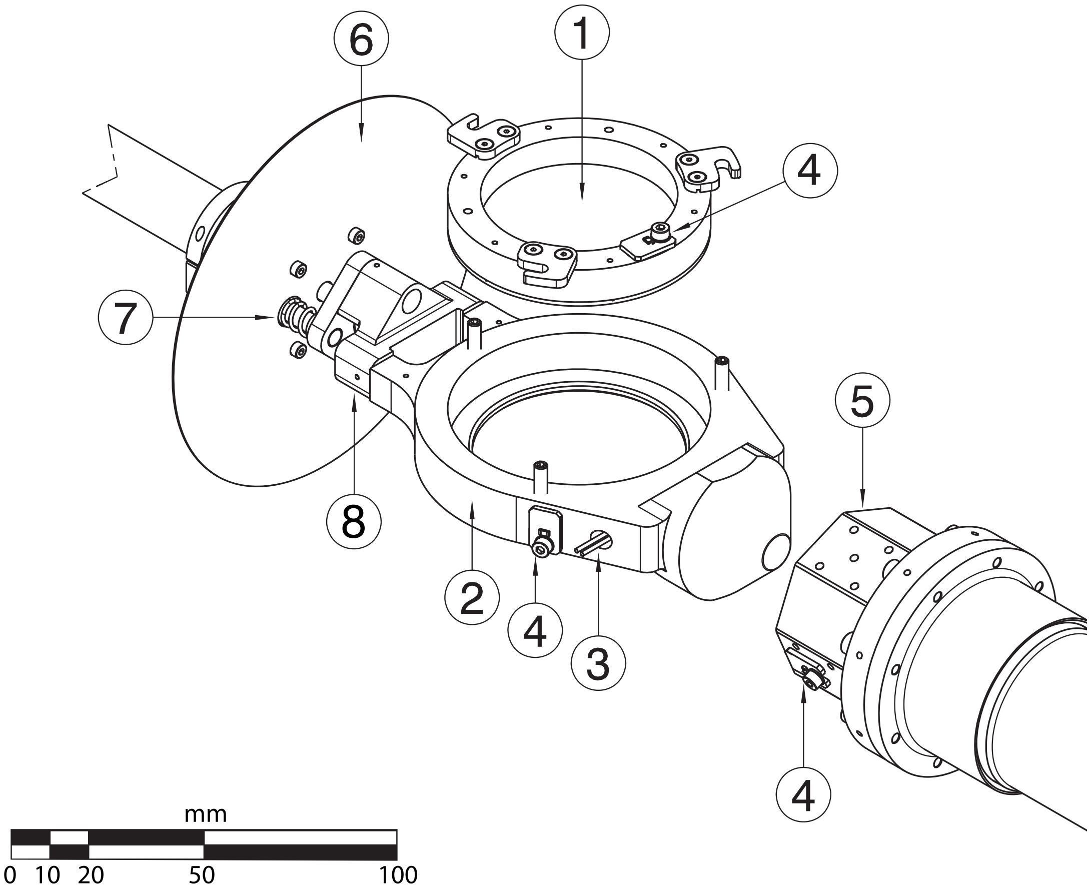

Figure 2.4: Sample holder carrier as viewed from the front. The sample-holder carrier (2) with heating cartridge (3) and temperature sensors (4) is pushed by the springs (7) onto the cryo-cooler interface (5). The shield (6) and insulator (8) isolate the cold parts from the ambient surroundings. The circular sample holder (1) is then positioned exactly in the focal point of the THz beam.

by introducing a venting hole and special tubing for the wires. The beam opening angle is 25° which is then focused on the sample using gold plated 2” parabolic mirrors. The optical setup is placed on a goniometer and scanning stage to provide measurements at different x and y coordinates and at different angles. THz goniometry has previously been used to characterize building materials (Piesiewicz et al., 2005) and measuring the dielectric properties of samples (M. Li, 2001). The setup can be upgraded with minimal effort to perform THz-ellipsometry (Mazaheri et al., 2022). The measurement head is shown in Figure 2.5. Due to the geometry of the goniometer, the minimum angle is 32°. By replacing the transmitter and receiver antenna with an optional transceiver antenna (Kohlhaas et al., 2018), measurements could be conducted at 0°. Depending on the acquisition range in the time domain, the signal can be sampled up to 20 times per second.

A summary of the specifications is shown in Table 2.1.

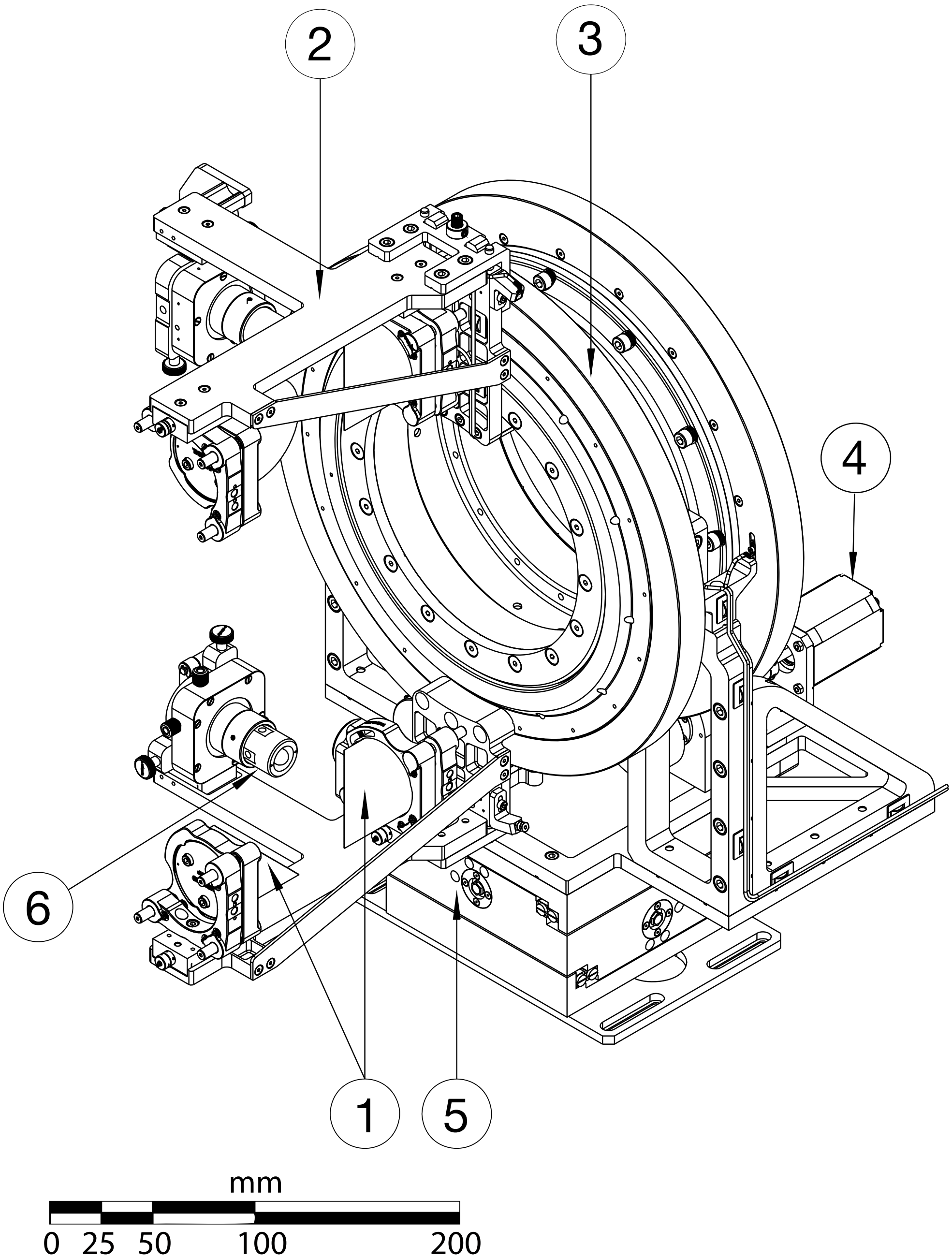

Figure 2.5: Two rotating arms (2) with antennas (6) and parabolic mirrors (1) are mounted on the gear assembly (3) which is actuated by the motors (4). The complete goniometer is mounted on the scanning stage (5). The sample holder can be placed at the center of the two arms.

2.4.1 Thermal Subsystem

The sample-holder needs to be cooled down to simulate the low temperatures down to 100 K. In general two options are used in laboratories to cool experiments down to these

Table 2.1: Specifications of COCoNuT.

Main Chamber Volume	421 304.49 cm^3
L.-L. Chamber Volume	9346.64 cm^3
Dimensions	1034 mm× 2842 mm × 1975 mm
Weight	984 kg
TMP	Pfeiffer HiPace300
Primary Pump	Pfeiffer ACP40
Pressure Gauges	Pfeiffer PKR251
Cryo Cooler	SHI Cryogenics Group CH-104
X/Y Stage Travel	104 mm × 104 mm
Goniometer Range	32° - 180° (dead angle: 71° - 120°)

temperatures: LN_2 cooling or liquid-helium cryo-coolers. While a cryo-cooler is more expensive, LN_2 is more cumbersome to operate and the temperatures are not as stable when doing measurements other than at the 77 K. Thorough simulations have been conducted using ***Ansys Mechanical*** (Ansys®, 2018) and ***Airbus Systema*** (Airbus, 2021) to dimension a cryo-cooler and the heating element. This approach was eventually chosen. The thermal simulation gives an estimate of the temperature gradient across the sample holder as well as the time required to reach thermal equilibrium. The chamber is not fitted with a cold shroud, thus thermal radiation plays a role in sample temperature. In Table 2.2 the incoming radiation value obtained by the simulation is noted. A cooled shroud would drastically decrease the incoming radiation onto the sample. The optical setup would have to be kept outside of the shroud anyways, since the antennas need to be kept at room temperature as per the manufacturers requirements. Thus, large slits would be required in the shroud to provide optical access, rendering this not a viable option. From the maximum force of the springs, $F_s = 180$ N, and the cross-sectional area, $A = 4426$ mm^2, we can determine the contact pressure of 60 kPa. Investigations (Misra & Nagaraju, 2010) show that, with this contact pressure, the thermal contact for gold plated copper surfaces in vacuum should be around 5000 W/(m^2 K). We can implement this in the simulation and arrive at the result shown in Figure 2.6. Since a cryo-cooler cannot be regulated, a heater needs to be introduced to compensate the cooling power and reach different steady state temperatures. Different options for heating elements have been simulated and finally a heating power of 100 W (230 V AC) has been chosen. To control the heating element, a proportional-integral-derivative (PID) controller (Michal & Radek, 2015) has been implemented on the Electronics Unit (ELU) according to Equation 2.1:

Table 2.2: Power budget obtained from the simulation, assuming the sample is at 100 K and the surrounding at 298 K.

	P [W]	Heat Source
Conductive	0.02	Sample holder PEEK insulator
Radiative	1.56	Chamber walls

$$u(t) = k_p\, e(t) + k_i \int_0^t e(\tau)\mathrm{d}\tau + k_d \frac{\mathrm{d}}{\mathrm{d}t} e(t) \tag{2.1}$$

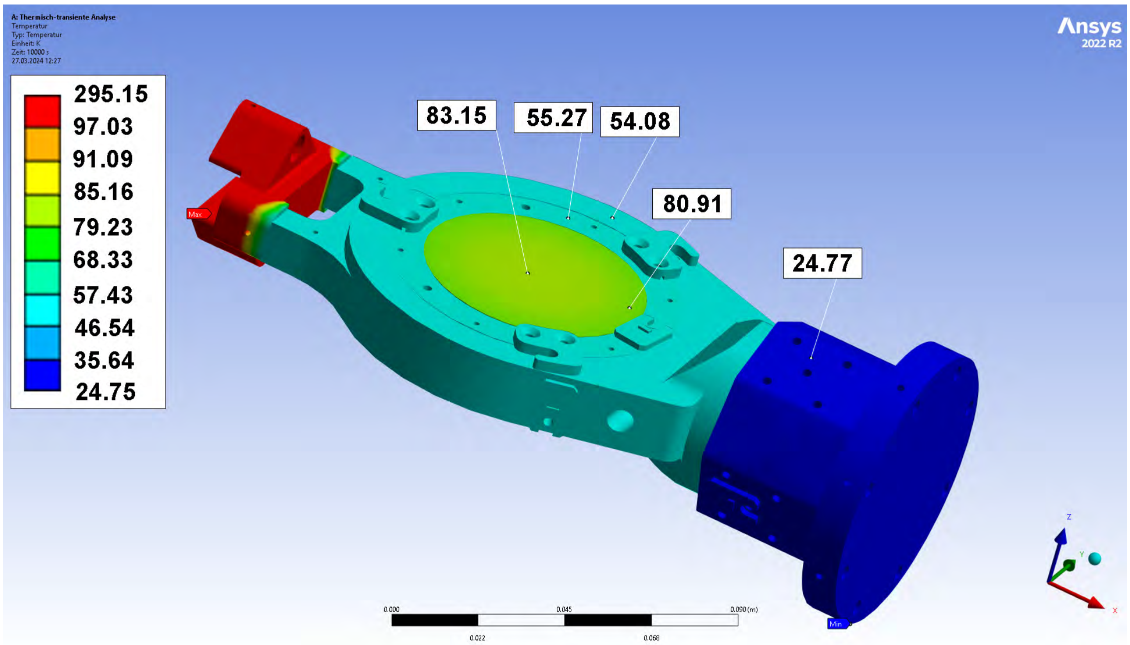
A: Thermisch-transiente Analyse
Temperatur
Typ: Temperatur
Einheit: K
Zeit: 10000 s
27.03.2024 12:27
295.15
97.03
91.09
85.16
79.23
68.33
57.43
46.54
35.64
24.75
Ansys
2022 R2
83.15
55.27
54.08
80.91
24.77
Max
Min
0.000
0.045
0.090 (m)
0.022
0.068
Z
Y
X

Figure 2.6: Thermal simulation of the sample holder carrier and cryo-cooler interface (described in detail in the technical drawing in Figure 2.4) in equilibrium. All values are given in Kelvin. The heater is turned off, hence we observe the lowest possible temperature of ≈ 50 K on the sample holder and ≈ 80 K of the solid sample. Sample temperature increases significantly with sample porosity. The cryo-cooler interface is modeled according to the cooling power, the mounting point in the back is fixed at 298 K, hence the large gradient across the insulator.

where k_p is the proportional gain, k_i is the integral gain and k_d is the derivative gain. The current deviation of the set temperature is given as $e(t) = T_{\text{set}} - T(t)$. The PID output $u(t)$ is then set as the duty cycle of a 3 Hz Pulse Width Modulation (PWM) signal controlling the heater. Since the temperature is measured on the sample holder, which lags behind the sample holder carrier where the heater is mounted, an overshoot can occur.

Since the cryo-cooler has a temperature dependent cooling power, shown in Figure A.1 in Chapter A, the controller was tuned with the temperature dependent parameters specified in Table 2.3. Temperatures are measured using Pt100, Pt1000 resistance temperature detectors (RTD) and BAS16 silicon diodes (Rijpma & Ter Brake, 2006) which are all mounted on in-house developed PCB sensor mounts (Stöckli et al., 2024). Additionally, for precise

Table 2.3: PID parameters. The proportional factor k_p, integral k_i and derivative k_d are temperature dependent.

T [K]	k_p	k_i	k_d
< 50	0.04	0.06	0.04
77	0.05	0.1	0.075
100	0.06	0.15	0.2
140	0.06	0.18	0.4
200	0.06	0.15	0.4
290	0.04	0.05	0.4
> 300	0.08	0.05	0.4

reference measurements, a ***Lake Shore Cryotronics*** DT-670 silicon diode (Courts, 2002) is used. The decision to go against thermocouples was based on the simplicity in vacuum chamber feed-through choice, as for RTDs and diodes gold plated copper feed-throughs can be used, which have very little chance of corrosion, smaller footprint and more flexibility.

Taking accurate measurements of the temperature of porous samples in vacuum is challenging, since the thermal contact of the sample and the sensor is not well defined. To mitigate this, we have implemented a contactless IR thermopile based temperature sensor (Ottersberg et al., 2025) to measure the surface temperature of the samples.

2.4.2 Vacuum Subsystem

The connection diagram of the vacuum components is shown in Figure 2.7. The main chamber has been built by ***Pfeiffer Vacuum GmbH***. The load-lock chamber was custom-made at the ***University of Bern***. To evacuate the chambers in a first stage, the ACP40 was selected as a primary pump. This brings the pressure down to the sub-mbar region. To go further down, the HiPace 300 turbo molecular pump (TMP) can be switched on. This pump is placed in-between the main chamber and the primary pump to compress the air and increase the pumping efficiency of the system for lower pressures. The load-lock chamber can be separated from the main chamber by closing the gate valve (V3). The primary pump can be disconnected from the turbo molecular pump by closing the main valve (V1) and connected by opening the load-lock valve (V2) to the load-lock chamber directly by a valve system. Two Pfeiffer PKR251 pressure gauges, rated for ranges from 5×10^{-9} mbar to 1000 mbar, are mounted on each of the chambers to monitor the pressures. When operating the chamber with a sublimating sample present, the pressure measured by the PKR251 will not represent the local pressure above the sample. To measure the local pressure, microelectromechanical systems (MEMS) Pirani sensors from ***Heimann*** were placed inside the chamber (Simon et al., 2012), which have previously been used in similar laboratory setups

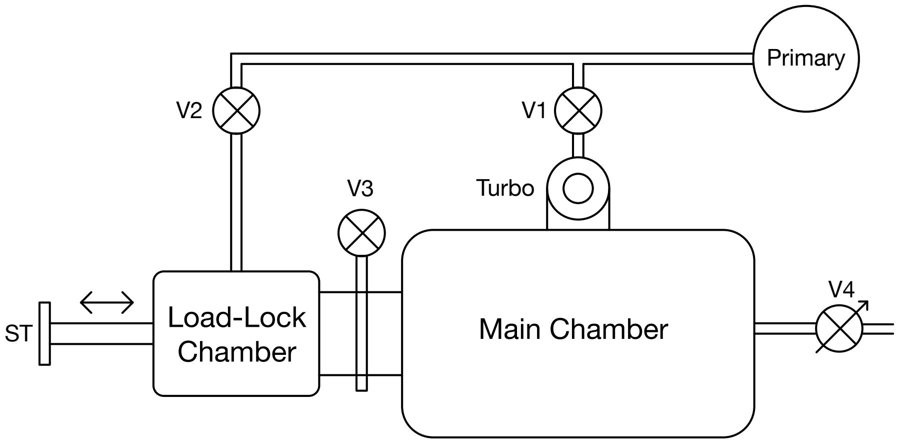

Figure 2.7: Schematic diagram of the vacuum system. The main valve (V1), load-lock valve (V2), gate valve (V3) and venting valve (V4) are shown in their positions between the chambers and the pumps. The sample translator (ST) is indicated.

for this purpose (X. Li et al., 2017). The placement of these sensors is a trade of between direct measurement and optical access to the sample.

2.4.3 Optical Subsystem

The THz spectrometer uses two photo-conductive antennas: a transmitter and a receiver, both are built in a similar way, but the electronics inside are slightly different. The emitted THz beam from the transmitter is divergent with an angle of 25° (Toptica, 2014). Gold plated parabolic mirrors, see Table 2.4, are placed to focus the beam on the sample and then again on to the receiver antenna.

Table 2.4: The gold-plated off-axis parabolic mirror specs. The A-type mirrors are placed directly in front of the antennas, and the B-type mirrors are placed directly in front of the sample. The mirrors were manufactured by *Thorlabs*.

Mirror	Focal-length	Diameter	Part number
Tx A	3”	2”	MPD239-01
Tx B	6”	2”	MPD269-01
Rx B	6”	2”	MPD269-01
Rx A	3”	2”	MPD239-01

The U-shaped beam path, as shown in Figure 2.8, adds up the imperfections of each parabolic mirror (Chopra & Lloyd-Hughes, 2023) and thus leads to an increased spot size and a more difficult alignment process. It is however more compact than a step-shape or S-shape path. Thus due to spatial constraints, we have opted for the slightly adapted U-shape path, where the antennas protrude out of the beam plane. The photo-conductive antennas emits a linearly polarized THz beam. The orientation of the electromagnetic field is indicated in Figure 2.9. The current setup displayed corresponds to transverse magnetic (TM) incidence on the sample, but the orientation can be changed.

2.4.4 Scanning Subsystem

The scanning setup consists of a custom-designed goniometer for the transmitter and receiver optics, which is mounted on a x/y-stage. Thus giving the ability to scan the sample in 2D for different phase angles and/or switch between transmission and reflection mode. The sample remains stationary and attached to the cryo-cooler, while the setup scans across a 60 mm × 60 mm area for angles from 32° to 180° (views between 71° - 120° are obstructed by the sample carrier and sample holder) as indicated in Figure 2.10. Due to the heavy weight of the arms ($\approx$ 2 kg) the counterweight can not completely balance out the load. We thus need electromagnetic brakes to offload the motors when holding the mechanism in place, as the motors would overheat in vacuum otherwise. The stage does not need brakes since the load is always perpendicular to the direction of motion. The goniometer limits are not motor independent, since moving each arm can lead to a collision if the other arm is stationary or moving in the opposite direction. Thus, there are limit switches that prevent collisions for both motors. Additional homing sensors are implemented in the transmission alignment for easy homing. The stepper motors of the goniometer provide 550 mNm of torque. The stage motors as well as the goniometer motors are controlled by TMC5160 stepper drivers in the Electronics Unit (ELU). These drivers are commonly used in 3D printers and CNC machines and are highly accurate, efficient and reliable.

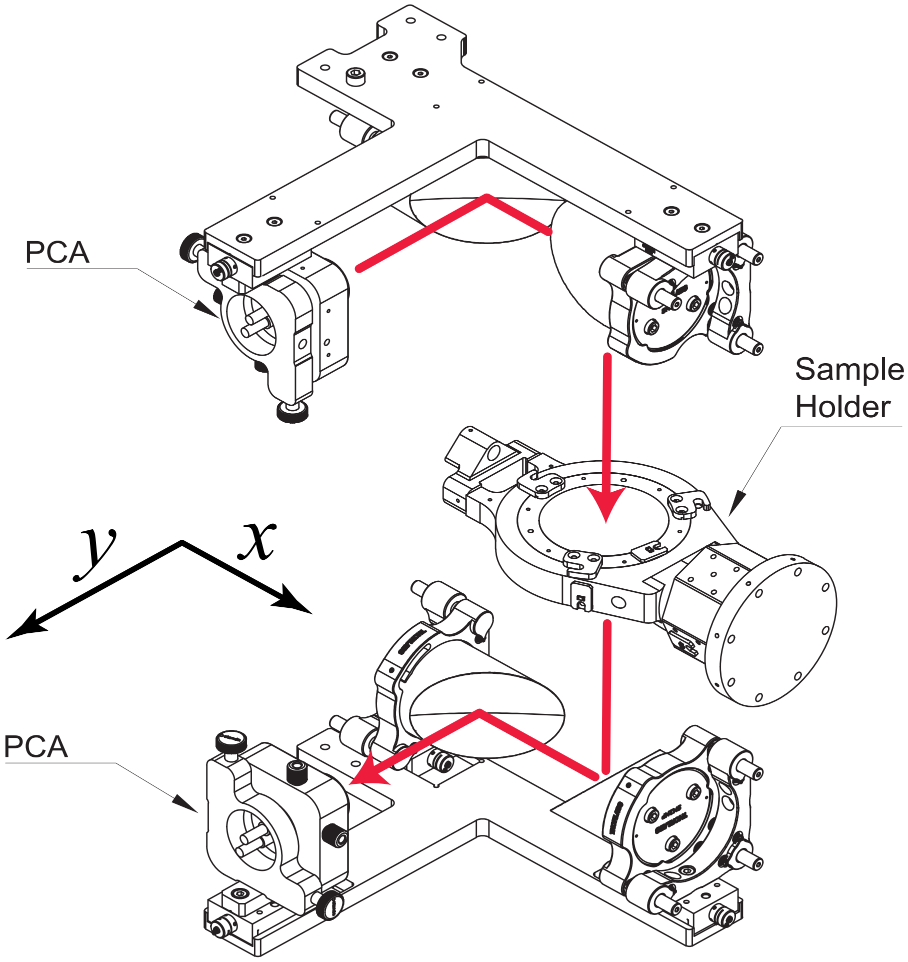

Figure 2.8: Setup of the 2” gold plated parabolic mirrors and the PCAs. The two mirror pairs are each mounted on a rotatable arm, the sample can be placed in the focal point. The coordinate system, as implemented in the scanning routines, is indicated.

2.4.5 Electronics Subsystem

To ensure safety of all components, the Electronics Unit (ELU) must monitor the state of the chamber and only under specific conditions can certain actions be allowed. On the one hand, the moving parts are equipped with end-switches to prevent collisions. On the other hand, the gate valve may only be closed when the sample translation rod is not extended and may only be opened when the turbo molecular pump is not running. Motors, cryo-compressor and pumps are controlled by the ELU over Serial Peripheral Interface (SPI), RS-232 and RS-485. Temperatures are readout over an SPI bus and an Inter-Integrated Circuit (I^2C) bus, pressure sensors are also attached to the ELU bus. The ELU is thus capable of gathering diagnostics data on these devices. Furthermore, motor and brake temperatures are also monitored alongside the sample temperatures and pressures in the chambers. Housekeeping temperatures are read out with the two-wire method, while sample temperatures are read out using the four-wires method to get a more accurate reading. The ELU is a custom system, based on an STM32F405 ARM micro-controller. Different expansion cards, as shown in Table 2.5, can be inserted in the back to allow simple replacements or

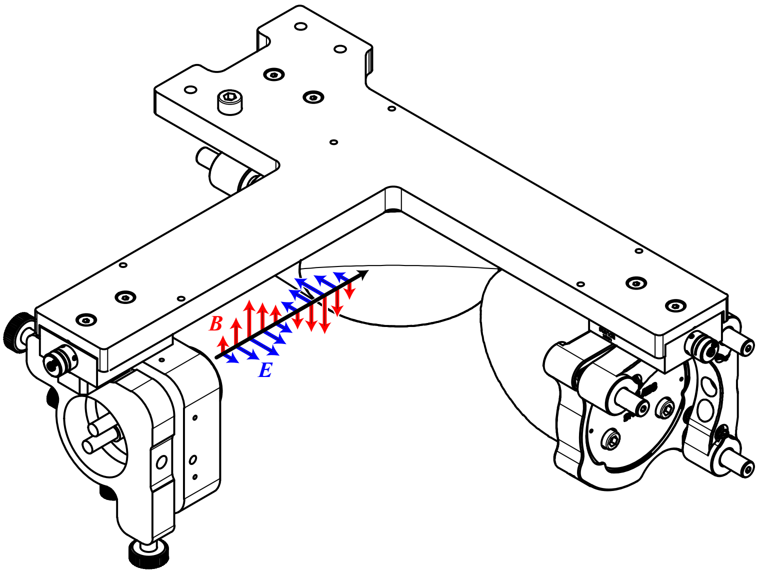

Figure 2.9: The transmitter arm with the electromagnetic field indicated when the antenna is mounted in its normal position. Each antenna on each optical arm can be rotated freely around its own axis, allowing polarization studies in future experiments.

upgrades of individual subsystems. The embedded software of the safety critical ELU is written in Rust (Sharma et al., 2024) and a wrapper for FreeRTOS (Barry, 2023). A custom Vacuum Gateway Vacuum Gateway Unit (VGU) provides the option to read out the local pressure and temperature sensors in the chamber. The ELU and VGU are connected to a Raspberry Pi through their dedicated RS-232 buses, serving as a network interface to push live housekeeping data from the ELU and VGU to a database. The THz spectrometer is connected directly to the Raspberry Pi. The Raspberry Pi runs all control logic, such as scanning procedures. The high-level multi-threaded software on the Raspberry Pi is written in Python. The spectrometer data is saved in dotTHz format (Lee et al., 2023).

Table 2.5: Expansion card slots on the back of the ELU.

Card	#	Interface	Supply [V]	Notes
RTD	4	SPI	3.3, 5	Housekeeping Temps
Serial	2	UART	3.3, 5	Comm. (RS-232, RS-485)
Diodes	2	I^2C	3.3, 5	Sample Temperatures
Pressure	2	I^2C	3.3, 5, 24	Pfeiffer Press. Gauges
Exp.	1	I^2C	3.3, 5, 24	Unused
IO	1	GPIO	3.3, 5, 24	Heater, Switches
Valves	1	GPIO	3.3, 5, 24	Valve Controls
Motors	4	SPI	3.3, 5, 24	Stepper Controls

The Raspberry Pi hosts a Transmission Control Protocol (TCP) server with an encrypted communication protocol, allowing the remote control of the complete system. The encryption is based on the Advanced Encryption Standard (AES128) (National Institute of Standards and Technology (US), 2001). Every message is encrypted using a key (shared between host and client) and an IV (initialization vector) which is built from the TS (current timestamp) plus

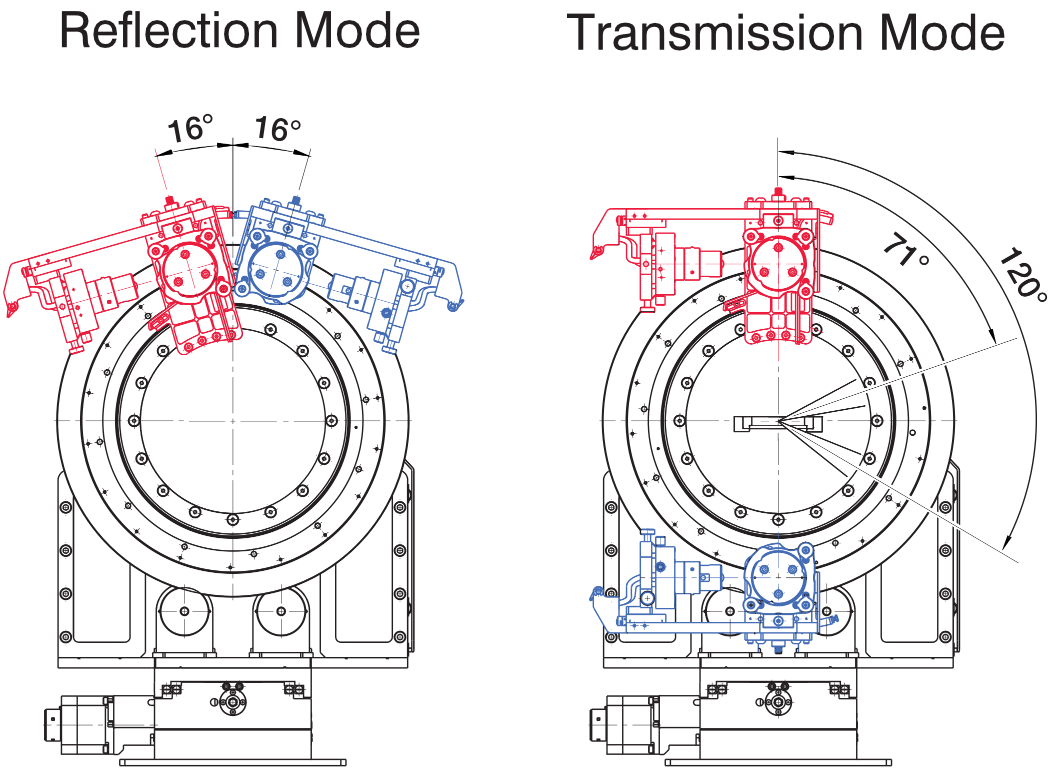

Figure 2.10: The goniometer seen from the front in reflection and transmission mode. The minimal angle is 32° due to geometrical constraints of the structure. The transmitter arm is colored in red, the receiver arm in blue. The blind spot is indicated in the figure on the right.

the RN (random number). Every received IV is added to a nonce set, to prevent replay attacks. Since the IVs contain the timestamp, they can be removed from the set once they have expired (time validity is set to 10 seconds) to reduce the memory load.

2.5 Commissioning

After the entire system had been fully assembled, a series of tests were conducted to characterize the different subsystems and verify that the requirements given in Section 2.3 are fulfilled.

2.5.1 Pressure

The steady state pressures are displayed in Table 2.6. The requirements are fulfilled. When all valves are closed and pumps turned off, the leak-rate of the system is $q_\mathrm{L} \approx 1 \times 10^{-4}$ L/s which qualifies as sufficiently tight (Rottländer et al., 2016). The ultimate operating pressure can be calculated using the pump speed $S = 260\,\mathrm{L/s}$ of the HiPace 300 turbo pump: $p_\mathrm{ult} = q_\mathrm{L}/S \approx 5 \times 10^{-5}$ mbar. By turning on the cryo-cooler, the pressure can drop below the ultimate operating pressure of the turbo pump, because of condensation of particles on the cold surfaces.

Table 2.6: Pressure performance of the chamber. The pressures are recorded in steady-state. During measurements, the sample can be heated, which in turn increases the pressures due to sublimation.

Pump Type	t	p [mbar]
Primary	1 h	$<$ 9e-1
Primary + TMP	1 h after TMP start	$<$ 9e-5
Primary + TMP + Cryo	2 h after Cryo start	$<$ 9e-7
Primary + TMP + Cryo	48 h total	$<$ 9e-8

2.5.2 Temperature

The temperatures after reaching steady state are noted in Table 2.7 and agree with the simulation within ±5 K on the structure and ±20 K on the ice sample. The heating element is strong enough to easily heat up the sample to room temperature, thus fully compensating the cryo-cooler. The heat up time is roughly equal to cool down time, which is about 1 - 2 hours, depending on the heat capacity of the sample. The PID controller reaches the temperatures with an over- or undershoot of about 1 K. After reaching steady state, the temperature usually lies within ±0.5 K, with oscillations of 0.1 K - 0.2 K as shown in Figure 2.11, fulfilling the requirements.

Table 2.7: Temperature performance of the chamber after reaching steady state, no heating applied.

	T [K]
Coldhead	25 ±2
Sample Holder Carrier	50 ±5
Sample Holder	51 ±5
Sample (Solid Ice Slab)	75 ±10

2.5.3 Beam Shape

The beam shape was measured by using the knife edge technique (Phing et al., 2015). A metal semicircle shield was placed on the center of the circular sample holder. Its straight edge was then scanned in each direction and the pulse intensity, calculated as the sum of squares, is shown in Figure 2.12. To determine the beam shape from the obtained data, the error-function given in Equation 2.2 can be fitted (De Araújo et al., 2009).

$$p(x) = A \cdot \mathrm{erf}\left(\frac{x - x_0}{\sqrt{2}\,\sigma}\right) + B \tag{2.2}$$

A Gaussian is fitted to the recorded data and compared to the simulation obtained from the ***Zemax*** model as depicted in Figure 2.13. The simulation has been conducted under the assumption of an ideal Gaussian beam with point source, thus explaining the narrower beam than in the measurements. The emitted beam power is 74.2 µW. Dynamic range of approximately 100 dB, bandwidth of 5.5 THz and spectral resolution of up to 0.005 THz can be achieved. The beam shape presented in Figure 2.13 can be used in the future to de-convolve THz images (Ahi et al., 2018; Liebendorfer, 2020; Ljubenovic et al., 2022) by mitigating the effects of the point spread function (PSF), thus increasing the sharpness and improving edge and feature detection in THz images.

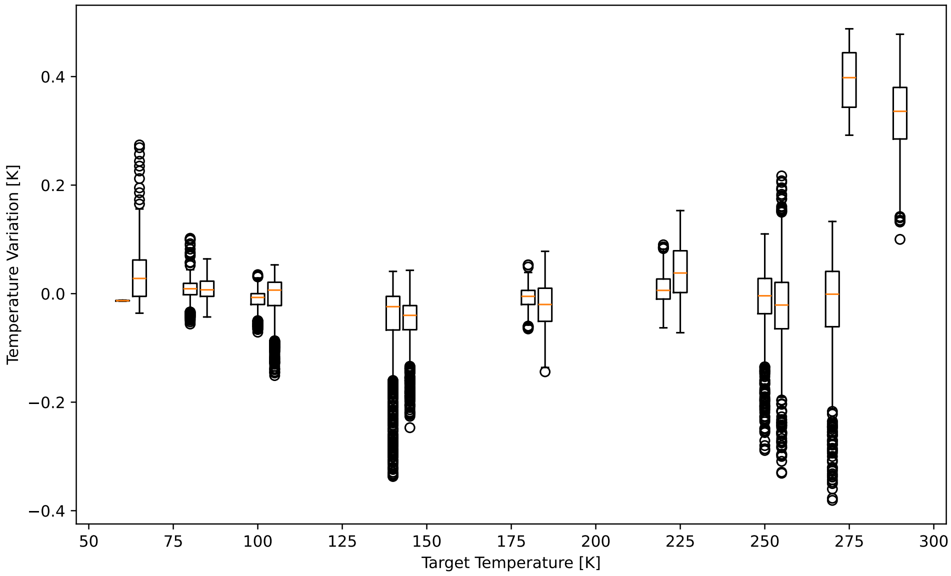

Figure 2.11: The accuracy and precision of the PID controller for different set temperatures are shown using a box plot.The box spans from the first to the third quartile, while the circles represent the outliers. These outliers are mostly recorded shortly before reaching steady-state. For some cases an overshoot can occur, this highly depends on the thermal load of the sample and has not been included in this analysis. An empty sample holder was heated according to a temperature profile, after stabilizing, the temperature was recorded for 30 minutes.

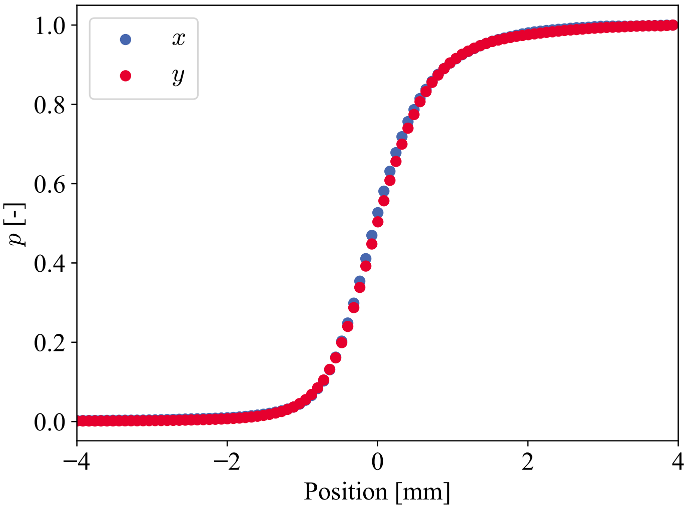

Figure 2.12: The normalized pulse intensities for knife edge scanning in x and y direction.

2.5.4 Imaging Resolution

To quantify the imaging resolution, a target has been designed and was placed in the sample holder and scanned in either transmission or reflection as shown in Figure 2.14.

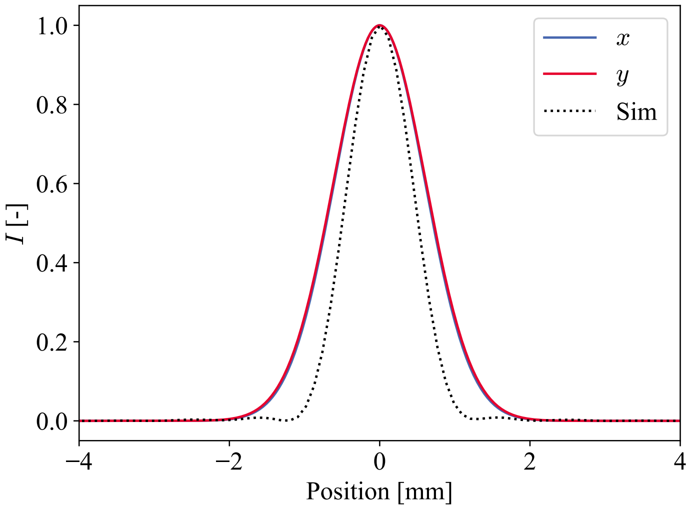

Figure 2.13: Normalized beam shape profile of THz-beam in the focus point, with a FWHM of $\Delta x = 1.42$ mm and $\Delta y = 1.44$ mm. The measurements are compared to a simulation conducted with ***Zemax*** (Ansys®, 2019), assuming an ideal Gaussian beam.

The resolution target is derived from the USAF 1951 resolution test chart (Department of Defense, 1959) and is manufactured using a printed circuit board (PCB) as displayed in Figure 2.15. The resolution is presented in Table 2.8 for each element on the target.

Table 2.8: COCoNuT resolution target v0.2A/B 2024, based on the USAF 1951 resolution target. The resolution is given in line-pairs per mm (lp/mm).

Element	**Group Number**	**Group Number**	**Group Number**
	-2	-1	0
1	0.250	0.500	1.00
2	0.281	0.561	1.12
3	0.315	0.630	1.26
4	0.354	0.707	1.41
5	0.397	0.794	1.59
6	0.445	0.891	1.78

To obtain an image from the THz scans, the intensity of each pulse is calculated and plotted as the corresponding pixel on a 2D array. The resolution is bounded by the diffraction limit and the spot size of the beam, which is obtained from the beam width measurement. The FWHM (full-width-half-maximum) is around 1.5 mm. We can set the step-size to 0.5 mm for each pixel, which will over-sample the spot size, and from the obtained scan determine the resolution. By applying a band-pass filter in Fourier space for each pixel, we can eliminate certain frequencies. Four different filters are shown in Figure 2.16 and Figure 2.17. The non-circular image in reflection mode is explained by the beam geometry in Figure 2.14. As expected, this shows that the higher frequencies give a much better spatial resolution of up to 0.56 lp/mm. However, they do not penetrate the sample as much, as the lower frequencies. This is especially visible in the transmission images, where we are barely able to identify any structure in the substrate material (fiberglass FR-4, thickness is 1.6 mm) of the resolution target PCB and frequencies above 1 THz get absorbed completely. The 2D stage

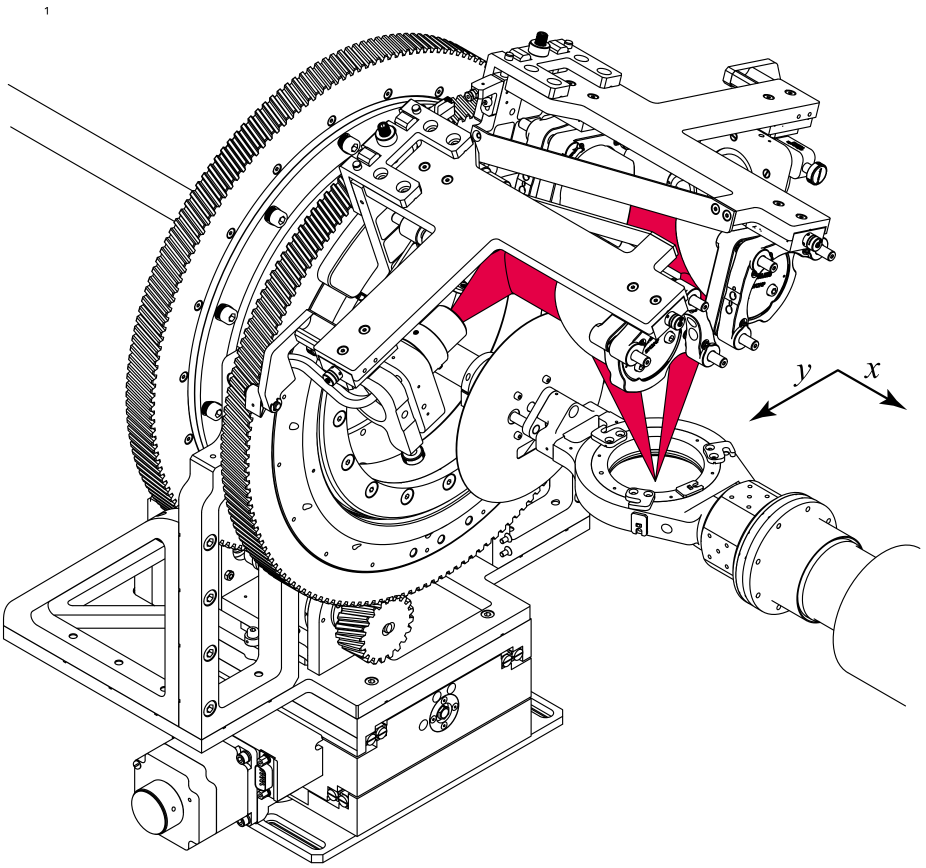

Figure 2.14: The optical setup in reflectance mode with the beam indicated in red. When acquiring an image of the full area, part of the beam is blocked by the sample holder walls when scanning close to the edges, since the incident and reflecting beam are aligned in the y direction, resulting in elliptical borders.

can be positioned with a resolution of 0.05 mm. The optical arms of the spectro-goniometer can be positioned with a resolution of 0.5°.

2.6 Results

The sample-holder can be fitted with a 2 mm Si-CZ (Czochralski) window. To obtain a reference for all samples that will be placed in this sample-holder, this window has been characterized by calculating the optical properties (Jepsen, 2019). The refractive index $n(f)$ given in Equation 2.3:

$$n(f) = \frac{c\Delta\phi(f)}{2\pi f d} + 1 \tag{2.3}$$

where $\Delta\phi(f) = \phi_{\text{ref}}(f) - \phi_{\text{sample}}(f)$ is the phase difference obtained from the FFT, d is the thickness of the sample and c is the speed of light. The absorption coefficient $\alpha(f)$ is given in Equation 2.4:

$$\alpha(f) = -\frac{2}{d}\ln\left(\frac{E_{\text{sample}}(f)}{E_{\text{ref}}(f)}\frac{(n(f)+1)^2}{4\,n(f)}\right) \tag{2.4}$$

where $E_i(f)$ are the frequency domain amplitudes.

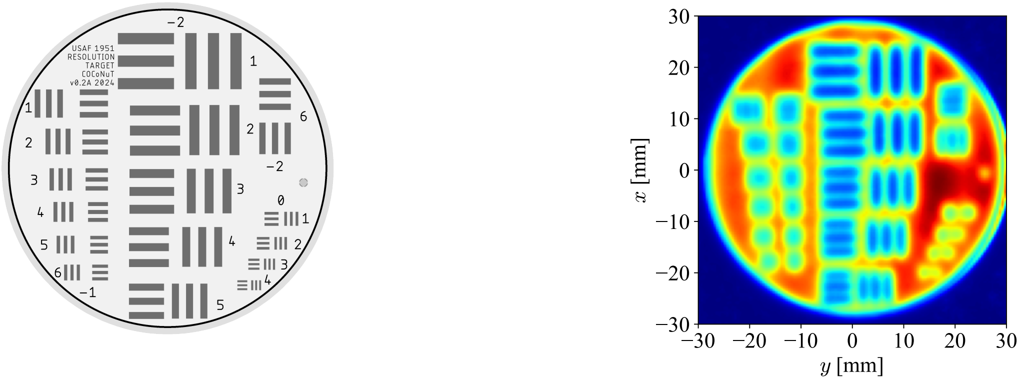

Figure 2.15: Design of the COCoNuT resolution target v0.2A/B 2024 (a). The 60 mm by 60 mm scan (b) was performed in transmission mode with a pixel size of 0.5 × 0.5 mm^2. For each pixel a THz time trace has been recorded and the intensity is plotted, with high intensity being shown as red and a low intensity as blue. As the sample-holder and the bars in the resolution target are made of metal, they block the beam and lead to a low intensity. The scan indicates a spatial resolution of 0.3 lp/mm.

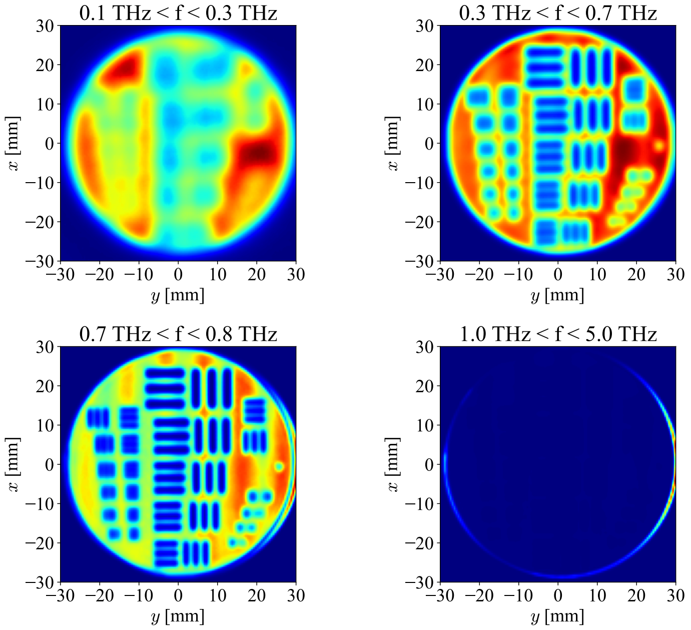

Figure 2.16: Four band-pass filters applied in the Fourier space to the resolution target measured in transmission mode. In transmission mode, the signal is blocked on the metal-bars (blue) and can pass through the substrate material (red) in high intensity. Frequencies above 1 THz get absorbed by the substrate material. With the lowest filter (upper left), we are not able to resolve any line pairs in the resolution target. The two middle filters (upper right and lower left) yield spatial resolutions of about 0.39 and 0.45 lp/mm. The highest filter only extracts frequencies that are completely absorbed, thus no information about the sample can be retrieved.

The results are discussed in Figure 2.18 and compared to the values obtained from literature (Dai et al., 2004; Rogalin et al., 2018). Alternatively, Quartz or Sapphire windows

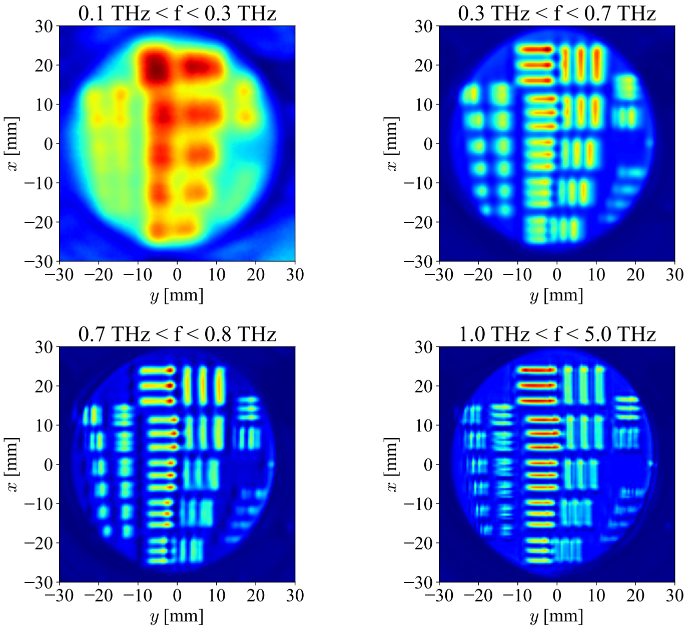

Figure 2.17: Four band-pass filters applied in the Fourier space to the resolution target measured in reflection mode. In reflection mode, the signal gets reflected in high intensity on the metal bars (red) and is scattered or absorbed on the substrate material or the sample-holder (blue). The two middle filters yield spatial resolutions of about 0.39 and 0.45 lp/mm. The highest filter gives the maximum spatial resolution of 0.56 lp/mm. The images are not completely circular due to the geometry of the incoming and reflecting beam.

can be placed into the sample holder.

Initial measurements with cometary analogues have been conducted and the comparison of water ice and charcoal-silicate dust mixture is presented in Figure 2.19. The results clearly show that information about the sub-surface structure can be extracted from the time-domain data. These measurements open up the possibility for 3D surface reconstruction by analyzing the first pulse caused by the surface reflection.

2.7 Conclusion

We have introduced our newly developed setup, which allows us to perform THz time domain spectroscopy of cometary analogues near conditions expected on comets. The setup is capable of reproducing such conditions and can be used to simulate conditions of other planetary bodies. The goniometer is capable of performing measurements at various angles, and we can easily switch between transmission and reflection mode without the need to flood the chamber and exchange the sample. The flexibility of this setup could allow to place other measurement instruments in the chamber without heavy modifications. Pressures of $<1 \times 10^{-7}$ mbar and sample temperatures of <80 K have been recorded. The system is capable of an average spatial resolution of 0.3 line-pair per mm. Our ultimate aim is to use COCoNuT to bring this instrumentation technique to at least TRL 5 (Technology Readiness Level 5 (NASA, 2007; TEC-SHS, 2008)) and therefore suitable for selection for an interplanetary mission, e.g. ORIGO (Marschall et al., 2023).

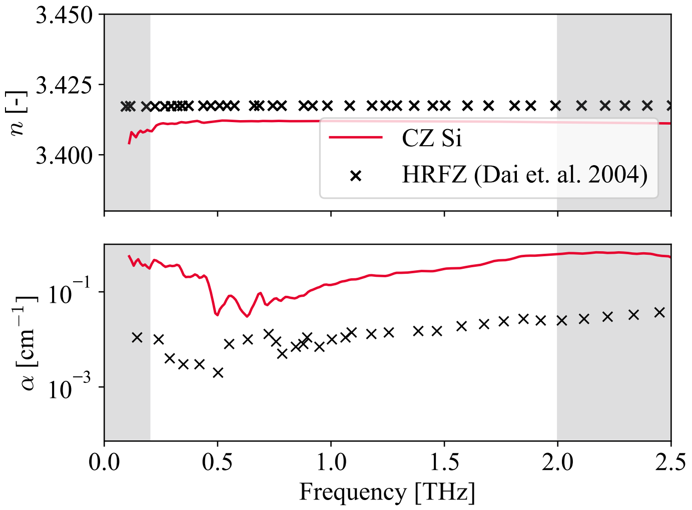

Figure 2.18: The optical properties of the CZ silicon window extracted from the spectrum are compared to HRFZ (High-Resistance Float Zone) silicon. CZ is less expensive to manufacture but contains more impurities (mostly oxygen), thus leading to a higher absorption coefficient. The shaded areas are not considered to be accurate, as the signal is dominated by noise.

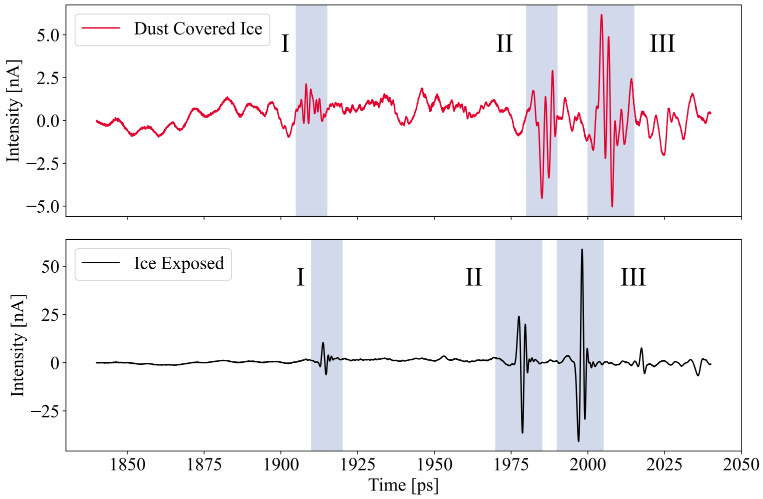

Figure 2.19: Two pulse traces of a solid H_2O ice slab in the time domain, measured in reflection mode. One part was covered with cometary analogue dust, consisting of 10% charcoal and 90% SiO_2. The upper plot shows the covered region, where the dust leads to diffuse scattering on the surface, thus lowering the overall signal. The lower plot shows the region where ice is exposed on the surface, leading to a stronger signal. The pulse at location I is caused by the reflection on the surface and the pulses at II and III are caused by the reflections of the two sides of the sapphire bottom of the sample holder. The temporal shift of I between the two measurements is caused by an uneven surface, whereas the shift of II and III is likely due to the refractive index of the dust.

Acknowledgements

This work was supported through a MARVIS (Multidisciplinary Advanced Research Ventures in Space) programme of the Swiss Department for Business, Education, and Research (SBFI) called SUBICE. SUBICE is a project of the University of Bern (UniBe), the University of Applied Sciences and Arts, Western Switzerland (HES-SO), and Thales-Alenia Space Switzerland (TASCH). The project has been partially funded by the European Space Agency (ESA) under the ESA Initial Support for Innovation (EISI) program. We acknowledge the support of the Open Space Innovation Platform (OSIP) and in particular Nicolas Thiry and Leopold Summerer. The contribution of RO and AP has been carried out within the framework of the NCCR PlanetS supported by the Swiss National Science Foundation under grants 51NF40-182901 and 51NF40-205606. The authors want to thank the Space Research & Planetary Sciences fine mechanical and electronics departments, specifically: Sacha Häusler, Sébastien Hayoz, Iljadin Manurung, Harald Mischler, Sebastian Wolf and Claudio Zimmermann for their help in constructing the setup. Furthermore, the authors want to express gratitude to Stephan Reschke for the technical support of the spectrometer. Last but not least, the authors want to thank the two anonymous reviewers, whose comments were greatly appreciated and have improved the quality of the manuscript.

Addendum: Reflections and Future Directions

Although the design presented in this chapter is of high quality and has been carefully developed, several insights have emerged during the commissioning phase that should be considered in future experimental setups.

First, rotational mechanical systems should be properly weight-balanced. This measure reduces the load on the drive motors and can eliminate the need for mechanical brakes. In the case of the COCoNuT setup, counterweights were retrofitted, but due to space limitations the system remains slightly unbalanced. Proper balancing would significantly improve the accuracy of the goniometer and remove the necessity for regular homing procedures that currently compensate for positional errors introduced by brake play.

Second, the mounting rods of the sample holder should be enlarged, and the use of linear bearings should be considered. The current design tends to tilt and jam, thereby blocking the springs that are required to ensure firm contact with the cold-head.

Third, the goniometer arms exhibit flexure under the weight of the optical components, leading to misalignment when switching between transmission and reflection modes. To address this, an auto-alignment mechanism was integrated into the collimating mirror of the Rx arm, which is most affected by mechanical deformation. This adjustment capability allows for effective compensation of the misalignment caused by flexure.

The auto-alignment mechanism consists of two vacuum grade servo motors and a two degrees of freedom kinematic mirror mount. The servo motors are controlled by an additional extension card based on an STM32F103 ARM microcontroller for the Electronics Unit (ELU). However, a more stable approach would be to mechanically stabilize the arms of the goniometer using a secondary gear system. This reinforcement would minimize flexing during operation and eliminate the need for the compensating auto-alignment mechanism that is currently required to correct for positional deviations.

An alternative design approach worth considering is to mount the entire sample holder directly onto the cryo-head and enable translation of the complete cryo-head assembly back to the load-lock chamber. Such a configuration would improve the thermal contact between the sample holder and the cryo-head, thereby enhancing cooling efficiency and reducing

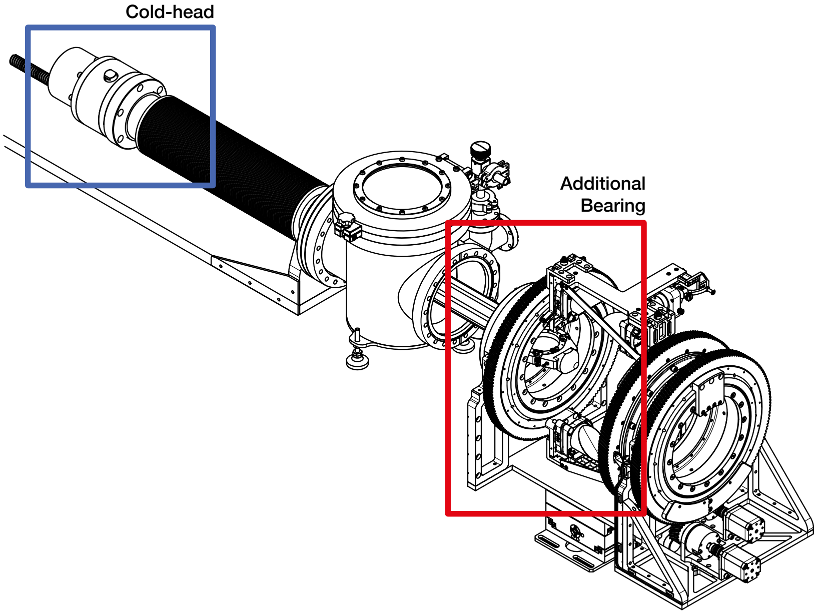

Figure 2.20: Sketch of the alternative design approach for COCoNuT, where the assembly is flipped by 180° and the cold-head (blue) is attached to the slider. The goniometer is supported by an additional bearing (red).

thermal gradients across the system. A sketch of this concept is shown in Figure 2.20.

Frequency-Dependent Deconvolution for Enhanced THz-TDS Scans: Accounting for Beam Width Variations in Time Traces

*Arnaud Demion, **Linus Leo Stöckli**, Nicolas Thomas, Silvan Zahno*

Published in *IEEE Transactions on Terahertz Science and Technology*, Vol. 15 (3): pp. 505-513, 2025
DOI: https://doi.org/10.1109/TTHZ.2025.3546756

Preamble:

This chapter focuses on a first post-processing step for THz TDS images acquired with the setup described in the previous chapter. I have contributed to this work by providing the measurements used for the characterization and by aiding with the implementation and testing of the algorithm. This work plays a core role in the data analysis in later chapters.

Abstract:

Terahertz Time-Domain Spectroscopy (THz-TDS) is a powerful tool for non-destructive testing, but the quality of scans is limited by beam spreading effects, which vary with frequency. We propose a deconvolution method that accounts for the changing beam width as a function of frequency. By incorporating frequency-specific Gaussian beam profiles, determined through the knife-edge technique, the proposed method enhances the spatial resolution of THz-TDS scans while keeping the ability to analyze the phase of the signals. Our approach significantly improves contrast and sharpness in both reflectance and transmission modes. This technique offers a more accurate and robust enhancement of THz-TDS imaging.

3.1 Introduction

THz Time-Domain Spectroscopy (THz-TDS) has gained substantial traction for applications in non-destructive testing, material characterization, and biomedical imaging due to its unique ability to penetrate various materials and provide high-resolution spectral information(Q. Wang et al., 2022; Zhang et al., 2016). However, the spatial resolution of THz-TDS imaging is inherently limited by beam spreading effects, which vary with frequency. The beam, while Gaussian in profile, changes in width with frequency due to variations in the focusing of the lenses and the radiation patterns of antennas across the THz spectrum.

Point Spread Function (PSF) deconvolution (Ding et al., 2010; Ning et al., 2019; True et al., 2021; Xu et al., 2014) like the Richardson-Lucy (RL) algorithm is a commonly used method to enhance image sharpness by mitigating the effects of the PSF. However, this approach generally assumes a frequency-independent PSF, making it better suited for narrowband sources. THz-TDS, by contrast, spans a broad frequency range, meaning that the PSF and beam profile change with frequency — a characteristic that simple image deconvolution techniques do not adequately address. Previous deconvolution approaches in THz-TDS have improved image sharpness but tend to neglect the temporal or depth information inherent in THz time-domain signals, thus limiting their utility (Ljubenovic et al., 2022).

In this study, we propose a frequency-dependent deconvolution method specifically designed to correct for beam spreading in THz-TDS time traces. By incorporating frequency-dependent Gaussian beam profiles derived from the knife-edge technique, our approach reconstructs time-domain traces with enhanced spatial resolution while preserving depth information and minimizing artifacts. Our proposed method provides a valuable tool for more accurate and refined THz-TDS imaging.

3.2 Beam Measurements

The **COCoNuT** (Characteristic Observation of Cometary Nuclei using THz-spectroscopy) setup was used to perform all the measurements (Stöckli et al., 2025). COCoNuT is a custom laboratory setup, built around a TeraFlash Pro THz time domain spectrometer (TDS) by Toptica. Its main purpose is to lay the groundwork for a possible future space exploration with a THz-TDS spectrometer on board. To simulate the conditions found on comets and other planetary bodies, a cryogenic vacuum chamber is required. COCoNuT houses a THz imaging system in a dual stage vacuum chamber. The two Photoconductive Antennas (PCA) are mounted on a goniometer, allowing switching between reflectance and transmission mode as shown in Fig. 3.1. Since this spectrometer with the photo conductive antennas can only perform single pixel measurements, all optical components must be mounted on an xy-stage to move the beam across the sample pixel by pixel. The imaging system has a spatial resolution of 0.01 mm which is a limit of the motor controller. The images can be acquired either in slow or in fast mode. In slow mode, the stage moves and stops at each pixel to then average a single trace over multiple measurements, this reduces the noise in higher frequencies. In fast mode, the stage moves along one axis and records one single measurement per pixel, when passing the corresponding position. In both slow and fast mode, the stage moves along a meander path to optimize for speed as indicated in Fig. 3.2.

The beam width was measured in transmission mode using the knife edge technique (De Araújo et al., 2009). A straight, sharp object was placed along the x axis, obstructing the beam path for all negative values on the y-axis and allowing the beam to pass through for all positive values on the y-axis. The signal was then recorded by scanning across the y-axis in discrete steps as shown in Fig. 3.3, and vice-versa for the x-axis.

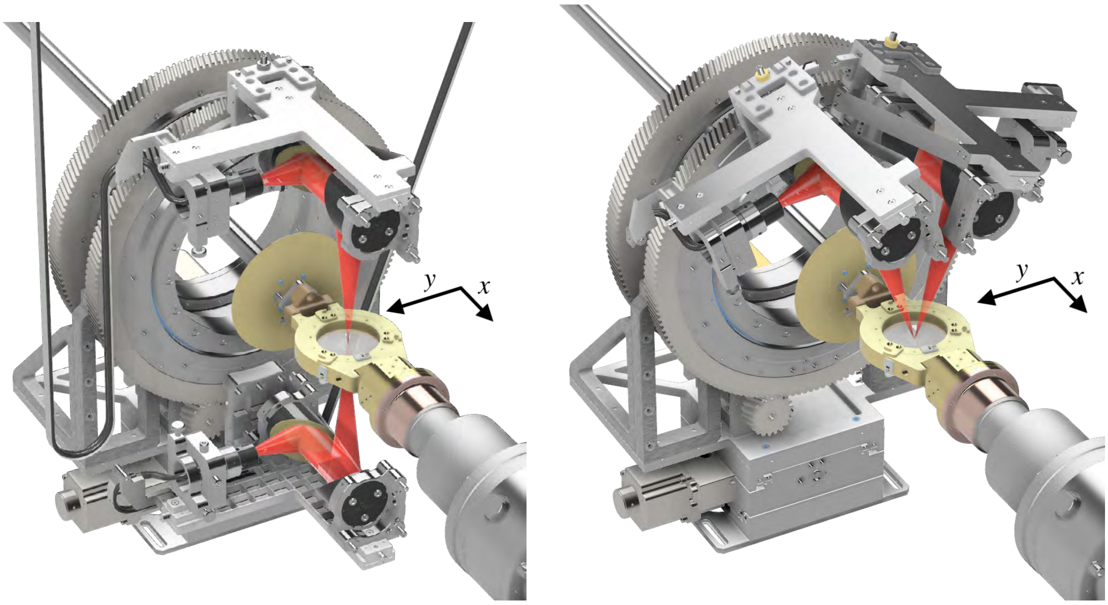

(a) Transmission

(b) Reflectance

Figure 3.1: Two renders of the scanning setup. The goniometer with the two photo conductive antennas (PCA) is shown in transmission and reflectance mode (38°). The beam is indicated in red. The scanning axes of the xy imaging stage are indicated.

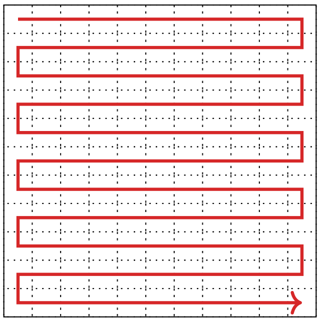

Figure 3.2: Scanning path for a 11 × 11 pixel 2D image. For each pixel a THz time-trace is recorded. This results in a 3D dataframe. The meander scan is optimized for speed. For the beam width measurement scan, only one dimension is scanned across a knife-edge.

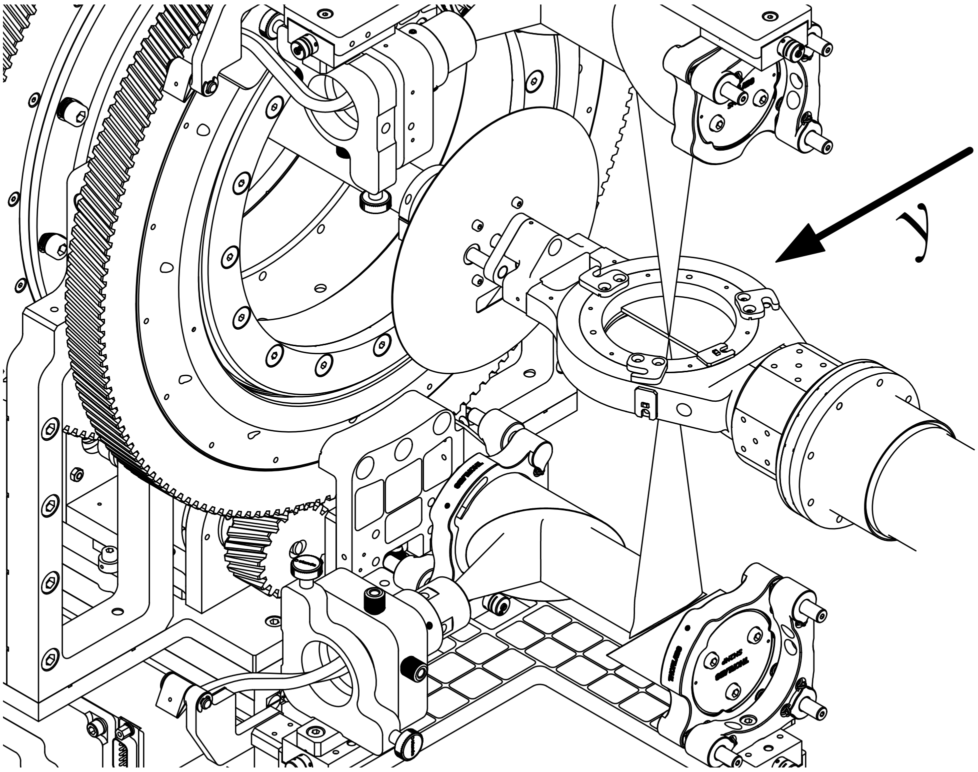

Figure 3.3: Setup indicating the knife edge scan along the y axis. A semi-circular metal plate is placed in the sample holder to obstruct half of the area. The pulse intensity is recorded as the beam moves across this "knife edge".

The resulting beam intensity, taken as the sum of squares of the time trace, follows an integrated Gaussian curve, also known as the error function, and is shown in Fig. 3.4.

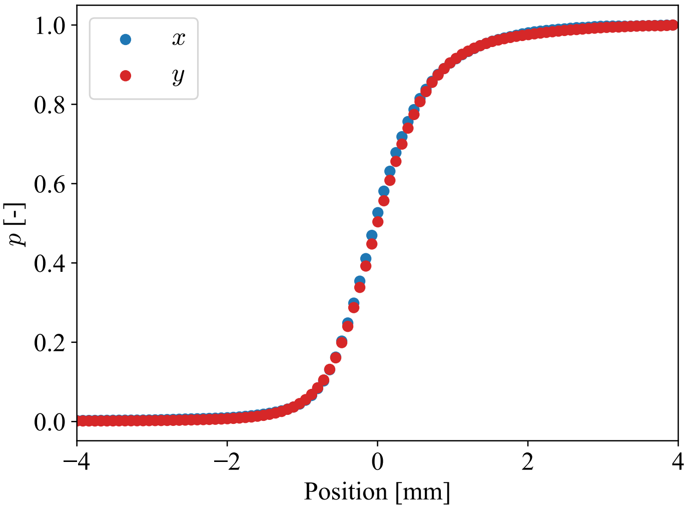

Figure 3.4: The normalized pulse intensities for knife edge scanning in x and y direction. The slight asymmetry is due to minor misalignments in the optical path.

However, if we, instead of just integrating over time, analyse each pulse in the frequency domain, we can extract the width for different frequencies.

All measurements were acquired at 1 atm and room temperature.

3.3 Beam Shape Estimation

3.3.1 Generalities about PSFs

Table 3.1: Main symbols used in this article.

Symbol	Description
$I(x,y)$	Irradiance profile of the beam
I_0	Maximum intensity of the beam
(x_0,y_0)	Center of the beam
(w_x,w_y)	Width of the beam along x and y
$\boldsymbol{s}_i$	Time trace at position i
ξ	Frequency index
$\boldsymbol{s}_{i\xi}$	Time trace at position i and filterd around the frequency ξ
$\boldsymbol{S}_i$	Fourier transform of the time trace $\boldsymbol{s}_i$
$\boldsymbol{S}_{i\xi}$	Fourier transform of the time trace $\boldsymbol{s}_{i\xi}$
$\boldsymbol{b}_\xi$	bandpass FIR filter centered around frequency ξ
P_i	Power of the beam at position i
$P_{i\xi}$	Power of the beam at position i and filtered around the frequency ξ
$P_n(x)$, $P_n(y)$	Normalized knife edge power profile along x and y
P_{max}	Maximum power of the beam
PSF(x,y)	2D Point Spread Function of the beam ($I(x,y)/P_{\text{max}}$) and deconvolution kernel
d_i	Pixel value of the scan image at position i
d_ξ	Pixel value at position i and filtered around the frequency ξ
u	Underlying image that would be observed without the beam spreading
u_ξ	Underlying frequency component of the image
$\hat{u}_\xi$	Estimated underlying frequency component of the image
$\mathcal{F}$	Fourier transform operator
$\mathcal{F}^{-1}$	Inverse Fourier transform operator

The irradiance profile of a Gaussian beam is given by the following expression,

$$I(x,y) = I_0 \cdot \text{exp}\left(-\frac{2(x-x_0)^2}{w_x^2} - \frac{2(y-y_0)^2}{w_y^2}\right), \tag{3.1}$$

where (x_0, y_0) is the center of the beam, at which the intensity is maximal and (w_x, w_y) is the width along x and y.

When measuring the beam profile using the knife-edge method, a sharp blade is placed at the focal point in the path of the beam. If the blade is positioned parallel to the y-axis and moved along the x-axis, the transmitted power can be described by integrating Eq. 3.1,

$$P(x) = \frac{I_0 \pi w_x w_y}{4}\left[1 + \text{erf}\left(\frac{\sqrt{2}(x-x_0)}{w_x}\right)\right], \tag{3.2}$$

where x is the position of the edge of the blade. The same procedure can be performed with the blade parallel to the x-axis to obtain $P(y)$.

As we are only interested on the beam width (w_x, w_y) the measurements can be normalized between 0 and 1. Writing $P_n = P/P_{\text{max}}$ with $P_{\text{max}} = I_0 \pi w_x w_y/2$, the expressions for the transmitted power become,

$$\begin{aligned} P_n(x) &= \frac{1}{2}\left[1+\mathrm{erf}\left(\frac{\sqrt{2}(x-x_0)}{w_x}\right)\right], \\ P_n(y) &= \frac{1}{2}\left[1+\mathrm{erf}\left(\frac{\sqrt{2}(y-y_0)}{w_y}\right)\right], \end{aligned} \tag{3.3}$$

and the associated beam intensity profiles along the x and y axis become,

$$\begin{aligned} I_n(x) &= \frac{\mathrm{d}P_n(x)}{\mathrm{d}x} = \sqrt{\frac{2}{\pi}}\frac{\exp\left(-\frac{2(x-x_0)^2}{w_x^2}\right)}{w_x}, \\ I_n(y) &= \frac{\mathrm{d}P_n(y)}{\mathrm{d}y} = \sqrt{\frac{2}{\pi}}\frac{\exp\left(-\frac{2(y-y_0)^2}{w_y^2}\right)}{w_y}. \end{aligned} \tag{3.4}$$

The un-normalized beam profile can be expressed as

$$I(x,y) = P_{\mathrm{max}} I_n(x) I_n(y). \tag{3.5}$$

If the beam widths w_x and w_y were the same for all frequencies, the observed image would be interpreted as the result of the following convolution,

$$d = u * P, \tag{3.6}$$

where d is the observed image, P is the PSF and u is the underlying image that would be observed without the blurring effect of the beam. However, the width of a focused Gaussian beam varies with the frequency, and it is assumed that the observed image can be expressed as a sum of convolutions by frequencies,

$$d = \sum_{\xi} d_{\xi} = \sum_{\xi} P_{\xi} * u_{\xi}, \tag{3.7}$$

where ξ is the frequency index, P_{ξ} is the PSF at frequency f_{ξ} and u_{ξ} is the underlying frequency component of the image, composed of the pixels $u_{i\xi}$.

3.3.2 A Simple Approach with the Fourier Transform

Let $\boldsymbol{s}_i = (s_{i0}, s_{i1}, \ldots, s_{ik}, \ldots, s_{iN-1})$ denote the measured time traces, where i is the position index (either for the x of y-axis, or for both in the case of a scan) and $k = 0, \ldots, N-1$ is the time index of the terahertz traces. Omitting the homogeneity factor[1], the frequency-independent PSF is reconstructed by first fitting Eq. 3.3 to the knife edge measurements in x and y directions,

$$P_i = \sum_{k=0}^{N-1} |s_{ik}|^2, \tag{3.8}$$

to find the position and width parameters, and then by multiplying the two profiles to obtain the normalized 2D PSF $\mathrm{PSF}(x,y) = I_n(x)I_n(y)$.

---

[1] We directly interpret the sum of the squared s_{ik} values as the transmitted power.

Likewise, the individual pixels d_i values of a terahertz scan image d can be simply computed with

$$d_i = \sum_k |s_{ik}|^2. \tag{3.9}$$

Using the Plancherel theorem (Plancherel & Leffler, 1910), the total energy received at a point can be expressed with the Fourier transform $\boldsymbol{S}_i = \mathcal{F}\{\boldsymbol{s}_i\}$ of the time trace $\boldsymbol{s}_i$,

$$\sum_k |s_{ik}|^2 = \sum_\xi |\mathcal{F}\{\boldsymbol{s}_i\}(f_\xi)|^2 = \sum_\xi |S_{i\xi}|^2. \tag{3.10}$$

A pixel of the scan can therefore be expressed as $d_i = \sum_\xi d_\xi = \sum_\xi |S_{i\xi}|^2$.

Instead of fitting the sum of the squared samples like in Eq. 3.8, Eq. 3.3 can be fitted to the Power Spectral Density (PSD),

$$P_{i\xi} = |\mathcal{F}\{\boldsymbol{s}_i\}_\xi|^2, \tag{3.11}$$

for each ξ of the Fourier Transform of the THz traces.

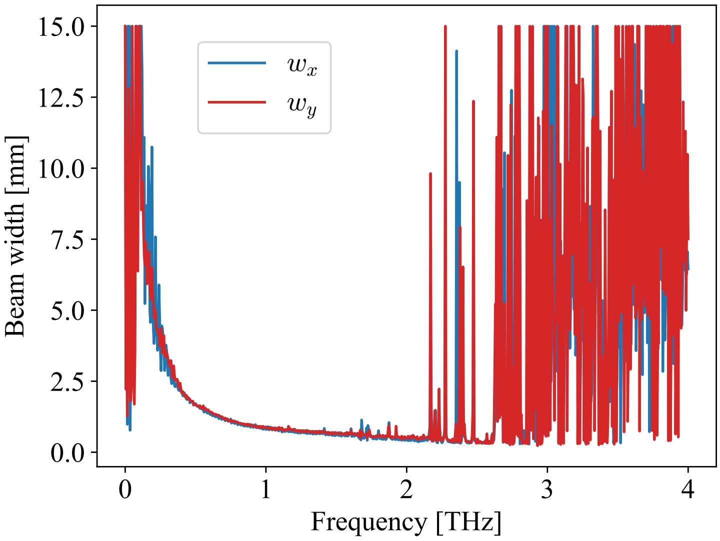

Figure 3.5: Beam widths w_x and w_y as a function of frequency. Numerous spikes are likely fitting errors due to poor SNR at certain frequencies. The y-axis of this graph has been limited to the interval $[0, 15]$.

The problem with this method becomes obvious when plotting the results in Fig. 3.5, where numerous spikes appear due to frequency points with low Signal to Noise Ratio (SNR). Indeed, the spectrum of a terahertz trace that came through air containing water vapor is not a smooth curve and presents absorption bands (Drs et al., 2019; Slocum et al., 2013) where the magnitude becomes really low. The two extremities of the spectrum ($f < 0.25$ THz and $f > 2$ THz) where the magnitude of the Fast Fourier Transform (FFT) becomes dominated by noise also show a large amount of artifacts.

3.3.3 Overcoming the Effects of Low SNR with FIR Filtering

To average closely spaced frequencies when estimating the beam widths, the time traces are filtered using windowed Sinc filters or brickwall filters. These filters are non-causal, preserving phase, and are sharp enough with an adequate length. Sinc filters, being Infinite Impulse

Response (IIR) filters, are multiplied by a Kaiser window to dampen the Gibbs oscillations that occur when truncating their responses to create Finite Impulse Response (FIR) filters. The first and last filters are a low-pass and high-pass filter, respectively, to cover the entire spectrum. The high-pass filter includes all frequencies above 4 THz, where the SNR is too low to fit the beam widths reliably. In Fig. 3.6 we show an example of the frequency responses of such filters. Splitting the total bandwidth into $M = 100$ segments from 0.15 THz to 4 THz results in band-pass filters with a bandwidth of 0.039 THz, which provides sufficient resolution to analyze beam widths without introducing artifacts from poor SNR.

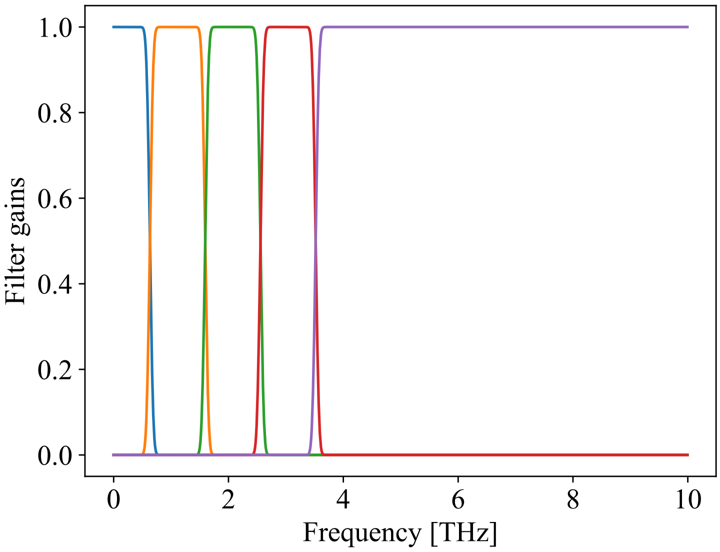

Figure 3.6: Example of frequency responses of linear phase FIR filters $\boldsymbol{b}_\xi$. For the sake of clarity, the total bandwidth has been split in only 5 filters for this plot.

In Fig. 3.7, the effect of the convolution by the filters on a time trace is shown. The filters are designed to not introduce any distortion, such that,

$$\begin{aligned} \boldsymbol{s}_i &= \sum_{\xi=0}^{M-1} \boldsymbol{s}_{i\xi} \\ &= \sum_{\xi=0}^{M-1} \boldsymbol{b}_\xi * \boldsymbol{s}_i, \end{aligned} \tag{3.12}$$

where $\boldsymbol{b}_\xi$ and $\boldsymbol{s}_i$ are respectively the FIR filters and the time traces. $\xi = 0, \ldots, M-1$ is the index of the filter determining its center frequency and $\boldsymbol{s}_{i\xi}$ is the filtered time trace.

Eq. 3.3 are then fitted onto the following data,

$$\begin{aligned} P_{i\xi} &= \sum_{k=0}^{N-1} \left| s_{i\xi k} \right|^2, \\ &= \sum_{k=0}^{N-1} \left| (\boldsymbol{b}_\xi * \boldsymbol{s}_i)_k \right|^2, \end{aligned} \tag{3.13}$$

for each ξ, like in Eq. 3.11. The $s_{i\xi k}$ are the samples of the filtered time traces recorded during the knife edge measurements. Examples of fits are shown in Fig. 3.8.

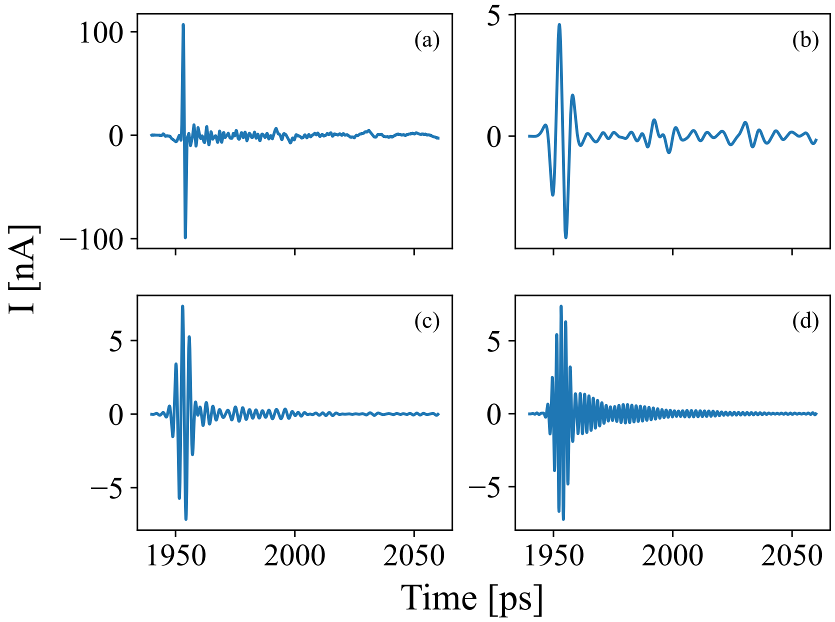

Figure 3.7: A THz time trace (a) that has been filtered with FIR band-pass filters centered around 0.15 THz (b), 0.34 THz (c) and 0.54 THz (d). Note: For panels (b), (c), and (d), the scale has been adjusted to a shorter range due to signal filtering, which reduces the energy content significantly.

The results are shown in Fig. 3.9. The curves obtained for the beam widths w_x and w_y are smoother compared to the ones obtained with the method based on the Fourier transform. No spikes caused by a low SNR are visible.

3.4 Reconstructing the Underlying Time Traces

3.4.1 In the Fourier Domain

In Eq. 3.7, the underlying frequency component u_ξ of a scan image d is defined. The pixels are given by $u_{i\xi} = |\boldsymbol{S}'_{i\xi}|^2$, where $\boldsymbol{S}'_i$ is the Fourier transform of the underlying time trace $\boldsymbol{s}'_i$. An estimation $\hat{u}_\xi$ of u_ξ can be computed using various deconvolution algorithms, such as the Wiener filter or the Richardson-Lucy (RL) algorithm. The 2D RL algorithm is defined as,

$$\hat{u}_\xi^{(t)} = \hat{u}_\xi^{(t-1)} \cdot \frac{d_\xi}{\hat{u}_\xi^{(t-1)} * \mathsf{PSF}_\xi} * \mathsf{PSF}^*_\xi, \tag{3.14}$$

where PSF_ξ is the 2D PSF, $\mathsf{PSF}^*_\xi(x, y) = \mathsf{PSF}_\xi(-x, -y)$ is the flipped 2D PSF and t is the iteration number. The 2D Wiener deconvolution is defined as,

$$\hat{u}_\xi = \mathcal{F}^{-1} \left\{ \left(|\mathcal{F}\{\mathsf{PSF}_\xi\}|^2 + \mathsf{SNR}^{-1} \right)^{-1} \mathcal{F}\{P_\xi\}^\dagger \mathcal{F}\{d_\xi\} \right\}, \tag{3.15}$$

where SNR^{-1} is a Signal to Noise Ratio dependent damping factor that is generally replaced by a regularization term(Orieux et al., 2010; Šroubek et al., 2019). The symbol † denotes the complex conjugate.

In the following, the symbol ˆ denotes a quantity estimated through a deconvolution technique.

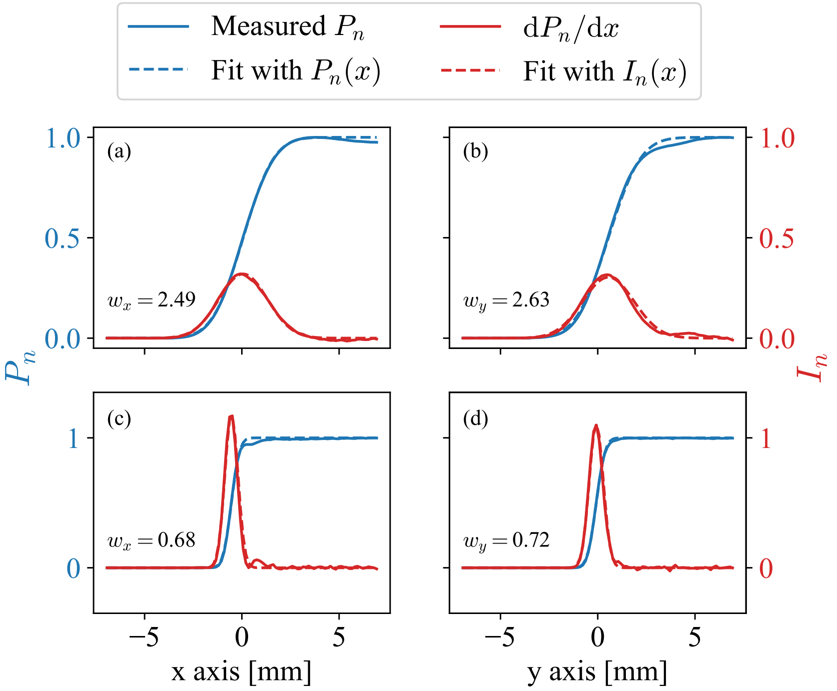

Figure 3.8: Beam shape fitting by frequency: this figure shows the fit of the normalized power function P_n to measurement data filtered at two different frequencies: 0.34 THz (panels (a), (b)) and 1.32 THz (panels (c), (d)). Panels (a) and (b) illustrate the beam profile fits along the x-axis and y-axis at 0.34 THz, with fitted beam widths $w_x = 2.49$ mm and $w_y = 2.63$ mm, respectively. Panels (c) and (d) show the corresponding fits at 1.32 THz, where the beam is narrower, yielding $w_x = 0.68$ mm and $w_y = 0.72$ mm. The measured data (solid blue line) is compared to the fit (dashed blue line), and the derivative, dP_n/dy, is shown in red to highlight the true beam profile. The data has been normalized by the maximum beam power P_{max}.

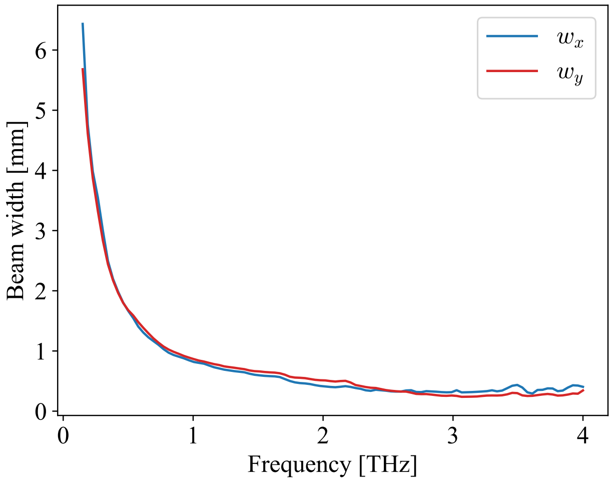

Figure 3.9: Widths of the beam as a function of frequency. The fits are cleaner than with the FFT based method. 100 FIR filters are used.

Assuming that the estimated signal $\hat{\boldsymbol{s}}'_i = \mathcal{F}^{-1}\{\hat{S}'_i\}$ and the measured signal $\boldsymbol{s}_i$ both have the same phase content, we can write,

$$\begin{aligned}\hat{S}'_{i\xi} &= |\hat{S}'_{i\xi}|e^{i\,\arg S_{i\xi}},\\ &= \sqrt{\hat{u}_{i\xi}}e^{i\,\arg S_{i\xi}}.\end{aligned} \tag{3.16}$$

In practice this method requires to get a frequency-dependent PSF with a good resolution in frequency, and as we saw earlier in this article, the estimation of the frequency-dependent PSF through the Fourier Transform can suffer from a poor SNR.

3.4.2 Via the FIR Filters

Another straightforward way to compute the estimated time traces is to use the filters that were already used in the estimation of the PSF. The estimated time traces are then given by the following sum,

$$\begin{aligned} \hat{\boldsymbol{s}}'_i &= \sum_{\xi=0}^{M-1} \hat{\boldsymbol{s}}'_{i\xi}, \\ &= \sum_{\xi=0}^{M-1} g_{i\xi} \cdot \boldsymbol{b}_\xi * \boldsymbol{s}_i, \\ &= \sum_{\xi=0}^{M-1} g_{i\xi} \cdot \boldsymbol{s}_{i\xi}, \end{aligned} \tag{3.17}$$

where $g_{i\xi}$ is a gain factor for the frequency range ξ at the position i in the scan.

Using the definition of the gains $g_{i\xi}$ in Eq. 3.17 and that of the pixel value in Eq. 3.9, the estimation of the underlying filtered pixel intensity $\hat{u}_{i\xi} = |\hat{\boldsymbol{s}}'_{i\xi}|^2$ can be rewritten as,

$$\hat{u}_{i\xi} = g_{i\xi}^2 \cdot d_{i\xi}. \tag{3.18}$$

Therefore, the gains can be computed with the output $\hat{u}_{i\xi}$ of the deconvolution algorithm applied on the filtered data using the frequency dependent PSF,

$$g_{i\xi} = \sqrt{\frac{\hat{u}_{i\xi}}{d_{i\xi}}}. \tag{3.19}$$

3.4.3 Results

We used a custom resolution target to quantify the maximal resolution of scans. This resolution target is based on the USAF 1951 resolution target (Department of Defense, 1959).

Our adapted design has been manufactured as a Printed Circuit Board (PCB) where the bars are made of thin copper strips that are laminated to a 1.6 mm thick dielectric glass-reinforced epoxy laminate (FR-4) substrate, which is transparent at THz frequencies. It is shown in Fig. 3.10. The resolution for the different size elements can be extracted from Table 3.2.

Fig. 3.11 shows the visual results of the deconvolution of the transmission and reflectance scans. The results are compared to the original scans and to the scans deconvolved with the RL algorithm using the frequency-independent PSF. The simple RL deconvolution improves image sharpness but also introduces artifacts. In the transmission scan, edge ripples are visible along the inner periphery of the target, while numerous ripples appear throughout the reflectance scan. The deconvolutions using the frequency-dependent PSF effectively remove these artifacts, sharpening the images. The target edges are better defined, and the contrast is enhanced, whether using the RL or Wiener method.

The number of iterations of the simple RL deconvolution algorithm was set to 100. In the case of the frequency-dependent RL algorithm, the number of iterations depends on the

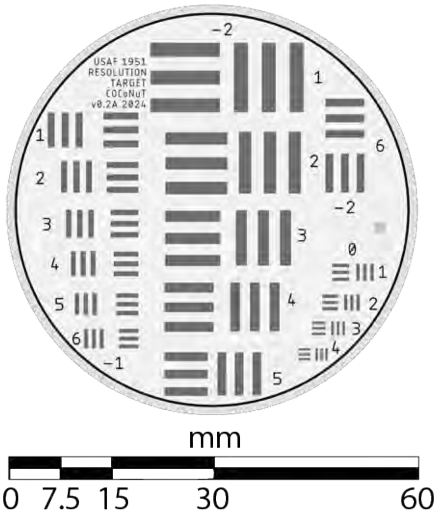

Figure 3.10: CAD drawing of the COCoNuT resolution target v0.2 2024 (Stöckli et al., 2025). As the sample-holder and the bars in the resolution target are made of metal, they block the beam and lead to a low intensity in transmission and reflect the beam, thus showing up as bright high intensity spots in reflection.

Table 3.2: COCoNuT resolution target v0.2 2024, based on the USAF 1951 resolution target. Element numbers are marked to the left/right of the individual elements on the target and group numbers above/below of the respective groups. The resolution is given in line-pairs per mm (lp/mm).

Element	**Group Number**	**Group Number**	**Group Number**
	-2	-1	0
1	0.250	0.500	1.00
2	0.281	0.561	1.12
3	0.315	0.630	1.26
4	0.354	0.707	1.41
5	0.397	0.794	1.59
6	0.445	0.891	1.78

beam width and goes from 1 to $\text{iter}_{\text{max}} = 500$,

$$\text{iterations}_{\xi} = \frac{\max(w_{x\xi}, w_{y\xi}) - w_{\text{min}}}{w_{\text{max}} - w_{\text{min}}}(\text{iter}_{\text{max}} - 1) + 1, \tag{3.20}$$

such that, the wider the beam is at a certain frequency index ξ, the more iterations are needed to deconvolve the image. w_{min} and w_{max} are the overall minimum and maximum beam widths, respectively. In the case of the Wiener deconvolution, the regularization term was set to $\lambda = 0.1$.

Tables 3.3 and 3.4 present a quantification of the improvement in image quality through different deconvolution methods. The Gray-Level Co-occurrence Matrix (GLCM) features are used to quantify the contrast and correlation of the unclipped images. The GLCM features are computed for the original scans and the deconvolved scans. Contrast measures the local variations in the image, while correlation indicates the linear dependency between pixel intensities. A higher contrast highlights a greater difference in luminance values, while

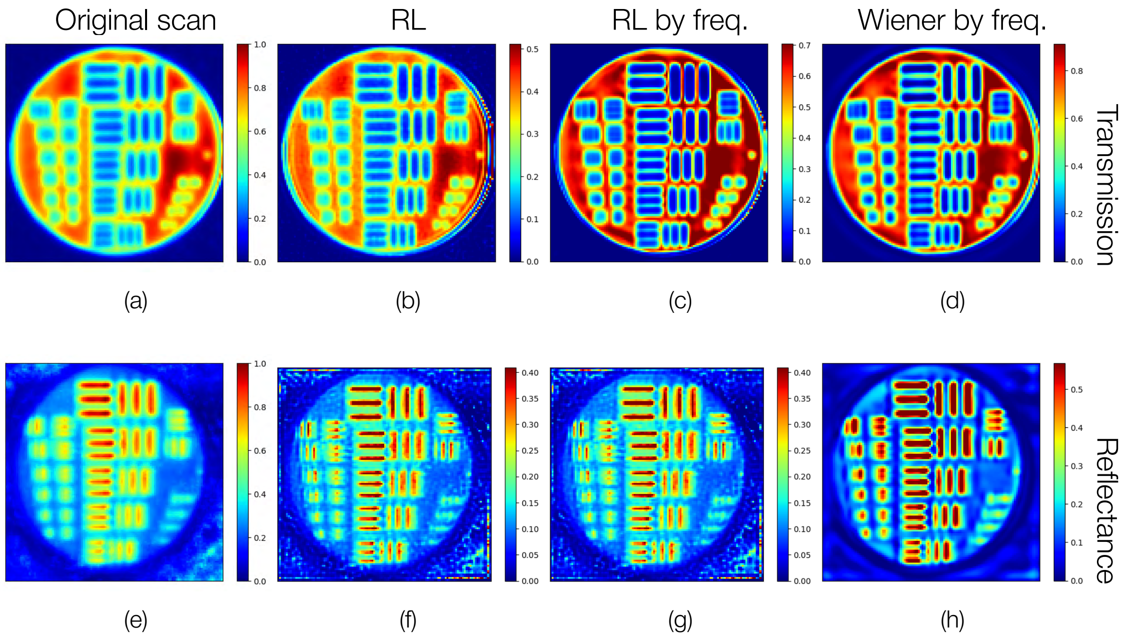

(a) (b) (c) (d)

(e) (f) (g) (h)

Figure 3.11: Comparison of deconvolution techniques. The scans have been acquired with 0.5 mm × 0.5 mm pixels. The full image is 60 mm × 60 mm in size. The first column (a,e) shows the original scans. The second column (b,f) shows the results of the simple Richardson-Lucy algorithm. The third (c,g) and fourth (d,h) columns show the results of our method using the Richardson-Lucy and the Wiener deconvolution algorithms. The deconvolved images have been clipped to match the average luminance of the original images (a) and (e). We chose clipping over normalization because the deconvolution process causes a few spots of the image to gain really large luminance values. Choosing the clipping values to retain the same average luminance as the original images allows better comparison of the results.

Table 3.3: GLCM Features and blur effect (transmission scan)

	Contrast						**Correlation**						**Blur Effect**	**Resolution [lp/mm]**
(d,α)	**(1,0)**	**(1,45)**	**(1,90)**	**(5,0)**	**(5,45)**	**(5,90)**	**(1,0)**	**(1,45)**	**(1,90)**	**(5,0)**	**(5,45)**	**(5,90)**		
Original	194.76	310.46	132.98	2604.31	3182.45	2160.36	0.98	0.97	0.99	0.75	0.69	0.79	0.48	0.354
RL	385.57	416.72	101.78	1094.02	1354.41	945.55	0.88	0.87	0.97	0.66	0.57	0.71	0.38	0.397
RL by freq.	642.57	898.86	357.95	4170.58	5297.15	3311.38	0.93	0.9	0.96	0.53	0.39	0.62	0.32	0.500
Wiener by freq.	628.29	998.92	415.86	6181.06	7942.82	5078.27	0.95	0.93	0.97	0.54	0.4	0.62	0.34	0.500

Table 3.4: GLCM Features and blur effect (reflectance scan)

	Contrast						**Correlation**						**Blur Effect**	**Resolution [lp/mm]**
(d,α)	**(1,0)**	**(1,45)**	**(1,90)**	**(5,0)**	**(5,45)**	**(5,90)**	**(1,0)**	**(1,45)**	**(1,90)**	**(5,0)**	**(5,45)**	**(5,90)**		
Original	102.39	220.28	127.2	1144.91	1721.47	1115.32	0.98	0.96	0.98	0.79	0.69	0.8	0.41	0.397
RL	107.6	230.86	146.91	369.87	591.92	396.68	0.91	0.81	0.88	0.69	0.5	0.67	0.27	0.561
RL by freq.	200.38	438.2	250.97	1132.08	1823.68	1068.13	0.91	0.81	0.89	0.53	0.25	0.55	0.28	0.561
Wiener by freq.	245.54	484.39	244.79	1907.42	3001.37	1628.23	0.94	0.88	0.94	0.52	0.26	0.59	0.3	0.561

high correlation suggests a less random texture. The GLCM features are computed for two distances $d = 1, 5$ (in pixels) and three angles $\alpha = 0, 45, 90$ (in degrees). An improvement in the sharpness of the images is reflected by an overall increase in contrast for every distance and angle. The correlation, however, should remain high at a short distance, and neither too high nor too low at long distances[2], as excessively high correlation would indicate a smooth

---

[2] Around 0.5, but not close to 0 or 1.

(blurry) texture, and too low would indicate a random (noisy) texture. The contrast and correlation features provide a good indication of the quality of the deconvolution process, which must enhance sharpness without introducing excessive noise.

To complement the GLCM features, the blur effect (Crété-Roffet et al., 2007) has also been computed. The blur effect is a no-reference perceptual metric that quantify the blur annoyance in images. It ranges from 0 to 1, where 0 indicates no blur and 1 indicates a high level of blur.

While the simple RL method gives moderate improvements in terms of contrast—and even worse in the reflectance case – there is a clear increase in contrast for both the transmission and reflectance scans with the frequency – dependent deconvolution methods. They are also better at keeping the correlation at a high level at a short distance, while lowering it at a longer distance.

The blur effect metric confirms the same trend, with the frequency-dependent deconvolution methods showing a lower blur effect than the simple RL method in the transmission case, and roughly the same value in the reflectance case, at the expense of a lot of ripples in the image.

3.4.4 Limitations

In its current form, the method presented in this paper applies only to Gaussian beam profiles. However, in some cases, the beam profile may be more complex, such as when the beam is clipped by an aperture or in far-field measurements (Jin et al., 2006; Rasmussen et al., 2023). In these situations, the Gaussian approximation and corresponding beam profile estimation are no longer valid.

A more refined approach to beam profile measurement, for instance, using radial and azimuthal knife-edge techniques (Strohaber et al., 2011), could enable the characterization of beams exhibiting higher-order modes, such as Laguerre-Gaussian or Hermite-Gaussian beams. In principle, the deconvolution method presented in this paper could be extended to such beam profiles, as the deconvolution kernel does not necessarily need to be Gaussian.

We also assume that the SNR is sufficiently high in the frequency domain of interest of the scans, as deconvolution processes inherently amplify noise. The FIR filters used to estimate the beam widths and centers are designed to minimize the impact of noise, but the deconvolution process itself can introduce artifacts. Lowpass and highpass filters can be used to remove noise at the extremities of the spectrum, where the SNR is low.

3.5 Conclusion

We have demonstrated the ability to correct THz-TDS scans for beam shape directly in the time domain using a frequency-dependent PSF. The presented algorithms enhance the xy-resolution of the scans while preserving the time dimension for further analysis, such as the application of Wiener deconvolution to retrieve the reflection coefficients of a sample along its z-axis (Chen et al., 2010; Jiang et al., 2021; Mei et al., 2020, 2021; Walker et al., 2012). Our approach outperforms the simple RL deconvolution algorithm, as evidenced by the GLCM features and blur effect metric. The resolution extracted from the USAF 1951 chart does not show a significant improvement of the frequency method over the pure RL at first glance. However, it is not trivial to differentiate the true bars in the scan from the artifacts that occur during signal processing with the pure RL algorithm. The RL by frequency method produces a higher image quality with little to no artifacts, allowing to even see the circular shape of the sample holder around the resolution target. Additionally, the frequency-dependent deconvolution methods provide better control over the deconvolution process, allowing the number of iterations to be adjusted according to the beam width at each frequency, thus minimizing the risk of over-fitting.

The FFT-based method can be combined with the frequency-dependent PSF obtained through FIR filters to further enhance the quality of the deconvolution, by interpolating the beam widths and centers between frequencies. These methods are applicable to any scanning THz-TDS system and can improve scan quality for a wide range of applications, including material characterization and medical imaging.

Acknowledgements

This work was supported through a MARVIS (Multidisciplinary Advanced Research Ventures in Space) programme of the Swiss Department for Business, Education, and Research (SBFI) called SUBICE. SUBICE is a project of the University of Bern (UniBe), the University of Applied Sciences and Arts, Western Switzerland (HES-SO), and Thales-Alenia Space Switzerland (TASCH). The project has been partially funded by the European Space Agency (ESA) under the ESA Initial Support for Innovation (EISI) program. We acknowledge the support of the Open Space Innovation Platform (OSIP) and in particular Nicolas Thiry and Leopold Summerer. The authors want to thank the Space Research & Planetary Sciences (UniBe) fine mechanical and electronics departments, specifically: Mathias Brändli, Sacha Häusler, Sébastien Hayoz, Iljadin Manurung, Harald Mischler, Daniele Piazza, Sebastian Wolf and Claudio Zimmermann for their help in constructing the setup.

THz Image Explorer - An Interactive Cross-Platform Open-Source THz Image Analysis Tool

Linus Leo Stöckli*, Arnaud Demion, Nicolas Thomas*

Published in *Journal of Open Source Software*, 10(115), 8754, 2025
DOI: https://doi.org/10.21105/joss.08754

Preamble:

Software in the scientific domain often lacks the availability to the community. To circumnavigate this problem, we have decided to open-source our interactive THz image analysis software which also includes a high-performance implementation of the algorithm described in the previous chapter. The main advantage of open-sourcing projects like this is the increased lifespan as other developers can easily report bugs and add new features. The software is set up in a way that users can develop and add new filters by just creating one single rust file without having to do adjustments to the rest of the code-base. This lowers the bar for contributions since a deep understanding of the application is not required. This application has proven to be very valuable for browsing through measurements and performing minor filtering. To further improve the workflow of browsing through THz measurement files, I have developed a QuickLook plugin for the macOS Finder application, which allows the user to quickly look at the meta data of a dotTHz file without opening it with a full analysis tool. Since the dotTHz standard is solely a wrapper for the HDF5 standard, two separate versions of the plugin have been developed and published, both are written in Swift.
The software is published on GitHub: https://github.com/unibe-icelab/thz-image-explorer

4.1 Introduction

THz time-domain spectroscopy (TDS) is a fast-growing field with applications to perform non-destructive studies of material properties (Neu & Schmuttenmaer, 2018). This involves measuring the interaction of pulses of radiation with a sample, where the pulses are measured after either passing through (transmission spectrum) or being reflected by (reflection spectrum) the sample. Through Fourier analysis (FFT), we can investigate the complex refractive index and absorption coefficient of the sample. By placing either the sample or the optical setup on a moving stage, the sample can be imaged in 2D.

Figure 4.1: THz Image Explorer icon.

We developed an interactive Graphical User Interface (GUI), written in Rust (Matsakis & Klock II, 2014), to aid in investigating acquired 2D scans. The application implements the dotTHz standard (Lee et al., 2023) and is platform independent and open-source, thus making it easier to maintain and increasing its reach.

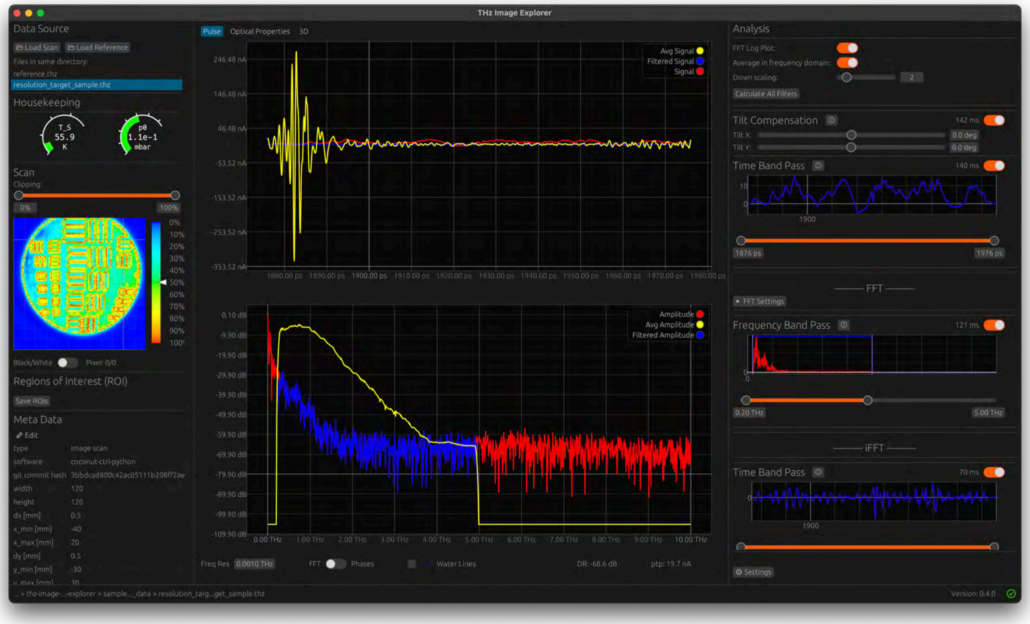
THz Image Explorer
Data Source
Load Scan
Load Reference
Files in same directory:
reference.thz
resolution_target_sample.thz
Housekeeping
T_S
55.9
K
p0
1.1e-1
mbar
Scan
Clipping:
0%
100%
0%
10%
20%
30%
40%
50%
60%
70%
80%
90%
100%
Black/White
Pixel: 0/0
Regions of Interest (ROI)
Save ROIs
Meta Data
Edit
Pulse
Optical Properties
3D
246.48 nA
146.48 nA
46.48 nA
-53.52 nA
-153.52 nA
-253.52 nA
-353.52 nA
1880.00 ps
1890.00 ps
1900.00 ps
1910.00 ps
1920.00 ps
1930.00 ps
1940.00 ps
1950.00 ps
1960.00 ps
1970.00 ps
1980.00 ps
Avg Signal
Filtered Signal
Signal
0.10 dB
-9.90 dB
-19.90 dB
-29.90 dB
-39.90 dB
-49.90 dB
-59.90 dB
-69.90 dB
-79.90 dB
-89.90 dB
-99.90 dB
-109.90 dB
0.00 THz
1.00 THz
2.00 THz
3.00 THz
4.00 THz
5.00 THz
6.00 THz
7.00 THz
8.00 THz
9.00 THz
10.00 THz
Amplitude
Avg Amplitude
Filtered Amplitude
FFT
Phases
Water Lines
Analysis
Calculate All Filters
Tilt Compensation
Time Band Pass
10
0
1900
1876 ps
1976 ps
FFT
FFT Settings
Frequency Band Pass
0
0
0.20 THz
5.00 THz
iFFT
Time Band Pass
0
1900
Settings
... > thz-image-...-explorer > sample..._data > resolution_targ...get_sample.thz

type image scan
software coconut-ctrl-python
git commit hash 3bbdcad800c42ac05111b208ff2ae
width 120
height 120
dx [mm] 0.5
x_min [mm] -40
x_max [mm] 20
dy [mm] 0.5
y_min [mm] -30
y_max [mm] 30

Freq Res 0.0010 THz
DR: -68.6 dB
ptp: 19.7 nA

FFT Log Plot:
Average in frequency domain:
Down scaling: 2
Tilt Compensation 142 ms
Tilt X: 0.0 deg
Tilt Y: 0.0 deg
Time Band Pass 140 ms
Frequency Band Pass 121 ms
Time Band Pass 70 ms
Version: 0.4.0

Figure 4.2: THz Image Explorer screenshot.

4.2 Statement of Need

Interactive analysis tools for THz spectroscopy are essential to browse through images and analyse different regions of interest efficiently. Commercial suppliers (e.g., Menlo Systems) provide closed-source analysis tools where the code cannot be adapted by the user, which is often essential in research environments and can extend the maintainability of the code. Solutions published by the scientific community are not available on all platforms, are only applicable on single pixel measurements, and/or are not focused on an interactive workflow (Loaiza et al., 2024; Peretti et al., 2019). With this application, we provide a high-performance solution written in Rust that allows an interactive analysis of 2D THz scans with multiple filters and a 3D viewer. The work is open-source, and pre-built bundles are provided for Linux, macOS, and Windows, ensuring broad accessibility for the scientific community.

4.3 Structure

The application is multithreaded with two main threads:

- GUI thread
- Data thread

The GUI uses `egui`, an immediate-mode GUI library for Rust. The structure of the software is shown in Figure 4.3.

4.4 Usage

A sample scan (of a resolution target) is available in the `sample_data` directory. The measurement has been acquired using the COCoNuT setup (Stöckli et al., 2025).

4.4.1 Optical Properties Calculation

The user can select a source and reference scan in the drop-down menu, after which the refractive index n and absorption coefficient α are computed according to Jepsen (Jepsen, 2019).

$$n(\omega) = 1 + \frac{c\Delta\phi(\omega)}{\omega d},$$
$$\alpha(\omega) = -\frac{2}{d}\ln\left(\frac{(n+1)^2}{4n}\cdot\frac{A_{\text{sample}}(\omega)}{A_{\text{reference}}(\omega)}\right),$$

where

- $\Delta\phi(\omega) = \phi_{\text{sample}}(\omega) - \phi_{\text{reference}}(\omega)$ is the phase difference
- $A_{\text{sample}}(\omega)$ and $A_{\text{reference}}(\omega)$ are the amplitude spectra
- c is the speed of light
- $\omega = 2\pi f$ is the angular frequency
- d is the sample thickness

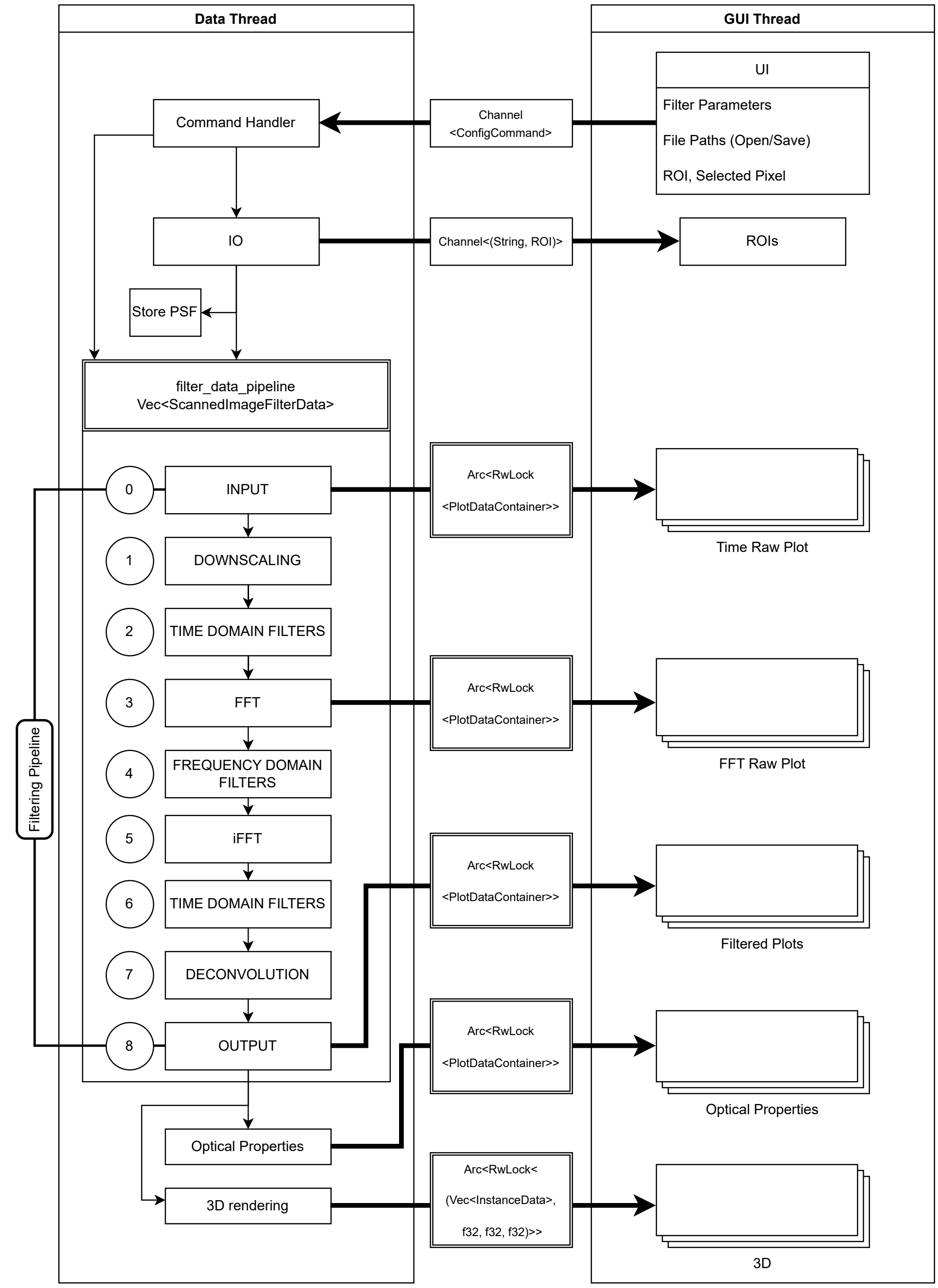
Data Thread
GUI Thread
UI
Filter Parameters
File Paths (Open/Save)
ROI, Selected Pixel
Command Handler
Channel
<ConfigCommand>
IO
Channel<(String, ROI)>
ROIs
Store PSF
filter_data_pipeline
Vec<ScannedImageFilterData>
Filtering Pipeline
0
INPUT
1
DOWNSCALING
2
TIME DOMAIN FILTERS
3
FFT
4
FREQUENCY DOMAIN FILTERS
5
iFFT
6
TIME DOMAIN FILTERS
7
DECONVOLUTION
8
OUTPUT
Optical Properties
3D rendering
Arc<RwLock
<PlotDataContainer>>
Time Raw Plot
FFT Raw Plot
Filtered Plots
Optical Properties
Arc<RwLock<
(Vec<InstanceData>,
f32, f32, f32)>>
3D

Figure 4.3: Software Architecture.

4.4.2 Interactive 3D Viewer

A THz time domain scan produces a 3D data array with dimensions $n_x \times n_y \times n_t$, where (n_x, n_y) represent the spatial coordinates and n_t represents the time axis.

Scans performed in reflection can be visualized in 3D. First, we transform each time trace into an intensity value by computing the squared amplitude and applying a Gaussian envelope function

$$I(x, y, t) = |s(x, y, t)|^2 * G_\sigma(t),$$

where $G_\sigma(t)$ is a normalized 1D Gaussian kernel with standard deviation $\sigma = 6.0$ and radius of 12 samples, applied via convolution to smooth the squared signal and extract the envelope as shown in Figure Figure 4.4.

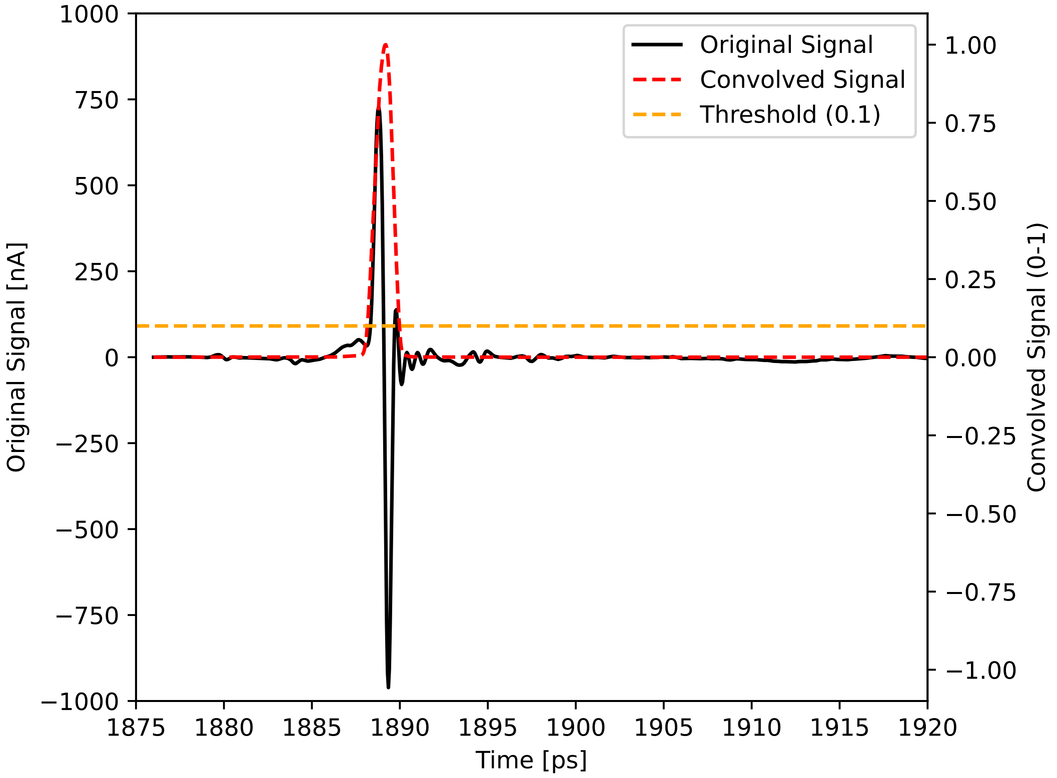

Figure 4.4: The convoluted envelope of the signal. All datapoints below the indicated threshold are treated as transparent.

The time axis is converted to a spatial distance coordinate by assuming a refractive index of $n = 1$ and using the relation $z = ct/2$, where c is the speed of light and the factor of 2 accounts for the signal's round-trip. This transformation yields a 3D intensity cube $I(x, y, z)$.

Each element (voxel) in this cube represents the THz signal intensity at a specific point in 3D space, enabling visualization of reflections from internal interfaces and sub-surface structures. The computed intensities are mapped to voxel opacity values; regions with high intensity appear opaque while low-intensity regions become transparent.

The 3D viewer is implemented using the `bevy` game engine (Bevy Contributors, 2025) with a custom WebGPU Shading Language (WGSL) shader, available as a separate crate under the name `bevy_voxel_plot`.

4.4.3 Filtering Pipeline

he filtering process is a simple linear pipeline, where the output of one filter is the input of the next filter. Filters can be placed in the following specific domains:

- Time Domain Before FFT - Frequency Band Pass Filter - Time Domain After FFT

Band-pass filters are already implemented in the application for each domain. The band-pass filter in time domain before FFT can be used to trim off trailing pulses. By selecting a slice in time domain after FFT, it is possible to scan through the z-axis of the scan and analyse sub-surface layers (Koch-Dandolo et al., 2015).

Deconvolution

The deconvolution filter is an implementation of the Frequency-dependent Richardson – Lucy algorithm described in (Demion et al., 2025).

Custom Filters

The code-base can easily be extended with custom filters. The user needs to create a custom file in the `src/filters` directory with a struct that implements the `Filter` trait.

4.5 Summary

THz Image Explorer primarily serves as a high-performance data analysis tool for THz 2D images. Its main focus lies on preliminary browsing of measurements, rough analysis of scans and identifying regions of interest in each scan. It is designed in a modular way to allow possible implementation of more thorough analysis features in the future.

Acknowledgements

This work was supported through a MARVIS (Multidisciplinary Advanced Research Ventures in Space) programme of the Swiss Department for Business, Education, and Research (SBFI) called SUBICE. SUBICE is a project of the University of Bern (UniBe), the University of Applied Sciences and Arts, Western Switzerland (HES-SO), and Thales-Alenia Space Switzerland (TASCH). The project has been partially funded by the European Space Agency (ESA) under the ESA Initial Support for Innovation (EISI) program. We acknowledge the support of the Open Space Innovation Platform (OSIP) and in particular Nicolas Thiry and Leopold Summerer.

Resolving Sub-Surface Ice Pebbles in Cometary Simulants using THz Time-Domain Spectroscopy

Linus Leo Stöckli*, Hervé Girard, Rafael Ottersberg, Dominik Belousov, Arnaud Demion, Antoine Pommerol, Marc Nicollerat, Valentin Meier, Joseph Moerschell, Axel Murk and Nicolas Thomas*

In prep, 2025

Preamble:

In this chapter we provide the significant results that build heavily on the work presented in the preceding chapters. We focus on time domain tomography using a THz time domain spectrometer. This chapter is an unpublished manuscript and is intended to be published in the near future.

Abstract:

Planetary formation theories aim to explain how planets form from the proto-planetary disk through processes such as classical hierarchical growth or pebble accretion. Comets are considered primitive remnants of this early phase, bodies that never coalesced into planets and now reside in the Oort Cloud and Kuiper Belt. Investigating their internal structure provides crucial tests for competing formation models.

Previous in-situ missions have used infrared (IR) spectroscopy and ground-penetrating radar to study cometary nuclei. While radar probes below the surface but with low resolution, IR offers finer detail but limited penetration. Terahertz time-domain spectroscopy (THz-TDS) provides a promising middle ground, achieving centimeter-scale depth with millimeter-scale resolution.

We are assessing the suitability of THz-TDS for in-situ cometary exploration using COCoNuT (Characteristic Observation of Cometary Nuclei using THz-spectroscopy), a laboratory setup that simulates cometary conditions in a thermal vacuum chamber and houses a commercial THz spectrometer. Using comet analogs, we perform proof-of-concept experiments to evaluate the technique's ability to resolve subsurface structures. In particular, we demonstrate the potential to detect icy pebbles beneath a dust layer. The presence – or absence – of such pebbles could help distinguish between pebble accretion and classical hierarchical growth, challenging the pebble accretion paradigm.

5.1 Introduction

High-resolution surface and sub-surface mapping of planetary bodies such as asteroids, comets, and moons is a key objective in planetary exploration. Interferometry or Time of Flight (ToF) based techniques have been extensively used for the purpose of surface mapping and Ground Penetrating Radar (GPR) instruments for the purpose of sub-surface mapping.

Looking at surface imaging, one of the most established techniques is laser altimetry, which relies on the time of flight and phase analysis of reflected laser pulses to derive surface elevation maps. Examples include the Mars Orbiter Laser Altimeter (MOLA) aboard ***Mars Global Surveyor*** (Smith et al., 2001), the Lunar Orbiter Laser Altimeter (LOLA) on the ***Lunar Reconnaissance Orbiter*** (Smith et al., 2010), and more recently, the ***BepiColombo*** Laser Altimeter (BELA), which aims to provide high-resolution topographic data of Mercury from orbit (Thomas et al., 2021). While these systems operate from orbit to obtain detailed topographical mapping at a planetary scale, they only achieve vertical resolutions around 30 cm. Higher performance systems are plausible but over shorter ranges.

Another powerful method is Interferometric Synthetic Aperture Radar (InSAR), which utilizes phase differences between radar images acquired from slightly different viewing angles to compute surface elevations and monitor changes over time. While widely used for terrestrial applications (e.g., with Sentinel-1), InSAR was also employed on the ***Magellan*** mission to map Venus through its dense atmosphere to map the surface with a depth resolution of about 100 m (Saunders & Pettengill, 1991).

To date, most attempts to investigate the subsurface structure of planetary bodies have relied primarily on GPR techniques. For example on Mars, the SHARAD radar aboard the ***Mars Reconnaissance Orbiter*** (MRO) has provided high-resolution sounding of the planet's upper layers, revealing the internal stratigraphy of the polar layered deposits and buried glacial landforms (Seu et al., 2007). Complementing these orbital observations, the RIMFAX instrument on NASA's ***Perseverance*** rover offers in-situ GPR profiling at meter-scale resolution, enabling detailed characterization of shallow sedimentary structures within Jezero Crater (Hamran et al., 2022). Beyond Mars, the CONSERT bi-static radar experiment on the ***Rosetta/Philae*** mission demonstrated the capability of radio-wave sounding to probe the internal dielectric structure of comet 67P/Churyumov–Gerasimenko (Kofman et al., 2015, 2020). Together, these instruments illustrate the central role of radar sounding in advancing our understanding of planetary sub-surfaces. GPR instruments are limited in their spatial resolution to the meter scale due to their comparably long wavelengths, whereas THz Time-Domain Spectroscopy (THz-TDS) operates at much shorter wavelengths, enabling spatial resolutions at the millimeter scale. THz-TDS has previously been used to image objects through dust clouds in transmission (Spencer et al., 2024) and to image objects covered with flour (Herrmann & Sakai, 2000) and milk powder (Hu et al., 2021) in reflection. Spatial variations of the micro-porosity of carbonated rock samples have been successfully measured with a THz time-domain spectrometer in transmission (Bouchard et al., 2022). Other approaches have used water absorption in limestone sedimentary rock samples to estimate macro- and micro-porosity (Heshmat et al., 2017). Here, we extend these existing investigations of THz applications for sub-surface structural analysis by exploring their feasibility in the context of space-mission environments.

To determine whether imaging at THz frequencies is operationally suitable for in-situ space missions, we first characterize mineral dust for cometary analogues in the laboratory and then conduct tests aimed at resolving sub-surface pebble structures. THz pulses can penetrate a range of non-metallic materials, including regolith and ice, enabling the reconstruction of internal structures within shallow layers.

5.2 Setup

The measurements in this chapter were taken with the COCoNuT setup described in Chapter 2. The setup is based around a thermal vacuum chamber to simulate vacuum and temperature conditions relevant to cometary nuclei. The THz-TDS system uses a commercial fiber-coupled Photoconductive Antennas (PCA) emitter and detector arrangement, enabling time-domain measurements of THz pulses and derivation of amplitude and phase information.

To characterize different materials, pellets made of polytetrafluoroethylene (PTFE) were placed in a sample holder with a 2 mm thick High Resistivity Float-Zone (HRFZ) silicon window underneath and measured in transmission. To further analyze cometary analogues, the dust and ice was first placed in a sample holder with a depth of 64 mm, thus excluding any back reflections on the bottom plate. The measurement was then acquired in reflection and used to extract the surface layer and resolve sub-surface pebbles. Furthermore, pebbles were covered with dust and placed on the HRFZ silicon window and measured in transmission.

5.3 Method

Samples were scanned in x and y direction. The scans are saved as data cubes of dimensions $n_x \times n_y \times n_t$ where n_t is the dimension of the time axis, as indicated in Figure 5.1.

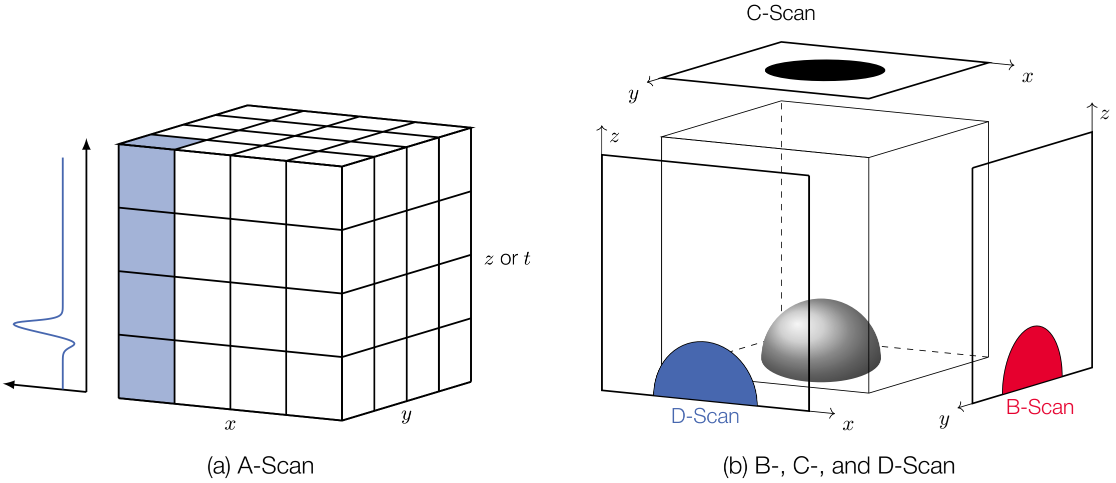

(a) A-Scan

(b) B-, C-, and D-Scan

Figure 5.1: A THz cube acquired by scanning across the x and y axis. Each stack is a THz waveform/pulse measured in time domain. The time axis can be converted to the z axis. The THz waveform (A-Scan) is indicated for the blue shaded stack in (a). B-, C-, and D-Scans for a hemispherical object are indicated in (b), due to graphic simplicity, the scans are drawn outside of the cube, whereas they are actually slices through the cube along the corresponding axes.

The THz cubes are stored in the dotTHz format along with metadata (Lee et al., 2023). The path of the beam in reflection is shown in Figure 5.2.

The travel times for the reference and sample signal are given in Equation 5.1 and Equation 5.2:

$$t_{\text{ref}} = \frac{2\,l}{c} \tag{5.1}$$

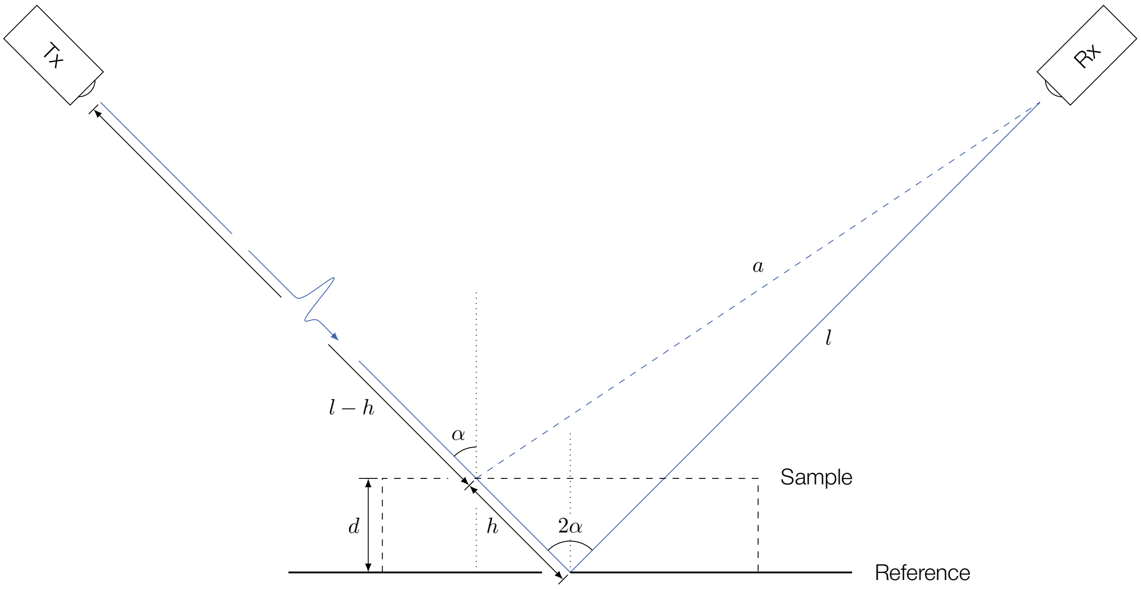

Figure 5.2: The focus in this setup is set on the reference layer with a total path length of $2l$. When a sample is placed with a thickness d, the pulse is reflected earlier and since the incidence and emission angle are not equal, the setup is slightly out of focus. Due to diffuse reflection of the pulse, the receiver (Rx) is still able to capture the pulse with a path length of $l-h+a$.

$$t_{\text{sample}} = \frac{l-h+a}{c} \tag{5.2}$$

By using basic trigonometry, we can use the time difference $\Delta t = |t_{\text{sample}} - t_{\text{ref}}|$ to calculate the distance d along the z axis using Equation 5.3:

$$d = \frac{2\,c\,l\,\Delta t - c^2 \Delta t^2}{2\,(l\,\cos(2\,\alpha) + l - c\,\Delta t)}\,\cos(\alpha) \overset{c\,\Delta t \ll l}{\approx} \Delta t \cdot \frac{c}{2\,\cos(\alpha)} \tag{5.3}$$

The normalized absolute value of the waveform for each pixel is first deconvolved using the frequency dependent deconvolution algorithm presented in Chapter 3. To map the signal current to a positive value, we apply a convolution with a Gaussian $G(x)$ where σ and r are based on the nominal pulse width $t_{\text{width}} \approx 1$ ps of THz-TDS trace and the sampling time-step $\delta t = 0.05$ ps, described in Equation 5.4 - Equation 5.6.

$$\sigma = \frac{t_{\text{width}}}{3\,\delta t} \approx 6 \tag{5.4}$$

$$r = \lfloor 3\,\sigma \rceil = 18 \tag{5.5}$$

$$G(x) = \exp\left(\frac{-x^2}{2\,\sigma^2}\right) \qquad x = \{-r, r\} \tag{5.6}$$

This yields an envelope from 0 to 1, as described in Chapter 4. Thus, the recorded value at each point along the time axis is now transformed using Equation 5.3 and the envelope maps intensity to an opacity value for the voxels of the data cube, resulting in a 3D scan.

5.3.1 Surface Extraction

To study the surface of a sample, we first deconvolve the signal as described in Chapter 3 with parameters described in Table 5.1. Since the lower frequencies penetrate deeper into the sample, we will exclude them with a bandpass filter of from 1 to 5 THz. Although the 3D plot can reveal the interfaces and internal structures of the sample, it tends to be noisy and does not always show a clean surface. A simplified way of extracting the top surface interface is to run a peak-finder with the threshold as the mean $\overline{X}_{\mathrm{LN}}$ of the Log-Norm given in Equation 5.7.

Filter	Parameter	Value	Unit
Deconvolution	`low_cut`	1.0	THz
	`high_cut`	5.0	THz
	`start_freq`	1.2	THz
	`end_freq`	4.0	THz
	`win_width`	0.5	THz
	`n_filters`	20	
	`w_max`	30	mm
1D Gaussian	`sigma`	6	

Table 5.1: Filtering parameters for surface extraction.

$$I_{\mathrm{th}} = \exp\left(\mu_1 + 0.5\,\sigma_1^2\right) \cdot \lambda = \overline{X}_{\mathrm{LN}} \cdot \lambda \tag{5.7}$$

with μ_1 and σ_1 obtained from the secondary Log-Norm component of the multi-modal signal distribution shown in Figure 5.3 and λ as an experimental parameter that is usually set to 1, but can be adjusted for different samples or laboratory setups. The value of I_{th} was empirically chosen and depends on the Signal to Noise Ratio (SNR) of the laboratory setup.

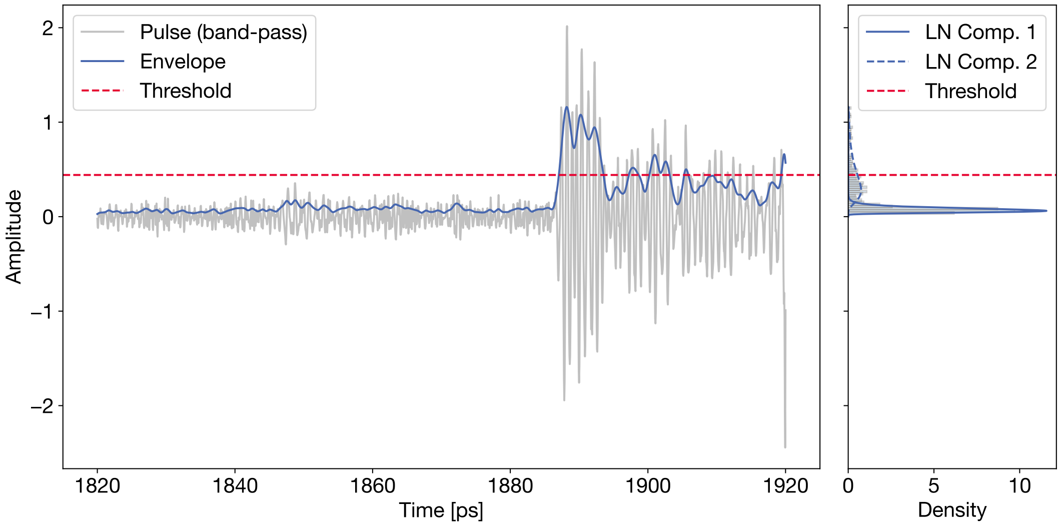

Figure 5.3: The signal in time domain is shown in the left subplot. The envelop of the signal is binned in the right subplot and Log Norm functions are fit to the multi-modal distribution. The first Log-Norm component corresponds to the noise distribution, the second Log-Norm component represents a superposition of the pulses.

The z position for the first detected peak is extracted and stored in a 2D array representing the surface layer. This process can also be used to extract additional layers by extracting the trailing peaks, if present. The extracted 2D array can optionally be smoothed to reduce noise, this will however also lead to loss of minor details. To evaluate the spatial resolution of the THz-TDS measurements, we designed several resolution targets using CAD and fabricated them via 3D printing with Cyclic Olefin Copolymer (COC) filament. Simple targets consist of a 3D version of the USAF 1951 resolution target (Department of Defense, 1959), where the bars were extruded along the z axis. To test the resolution for centimeter sized round objects, 10 mm half-spheres were printed. For a more realistic approach, samples with Gaussian surfaces were designed.

The Gaussian surface is generated to simulate a random, undulating surface on the top of a cylindrical structure. The process begins by creating a 2D grid of points, which represents the top surface of the cylinder. This grid spans a square region centered at the origin, with dimensions determined by the cylinder's outer radius and a specified resolution. A circular mask is then applied to restrict the surface to the cylinder's top face, excluding points outside the cylinder's radius. Random noise is generated using a normal distribution to create an initial random surface. This noise is smoothed using a Gaussian filter to achieve the desired feature size. The filter's standard deviation σ is calculated based on the feature size f and grid resolution r, using the formula:

$$\sigma_{\text{pixels}} = \frac{f}{2.35 \cdot r} \tag{5.8}$$

where the constant converts full width at half maximum (FWHM) to standard deviation. The smoothed surface is then scaled to achieve the desired peak-to-valley amplitude, which is equal to the feature size f. The surface is then used to create a 3D mesh of the cylinder, including the top Gaussian surface, a flat circular base, and side walls connecting the top and bottom.

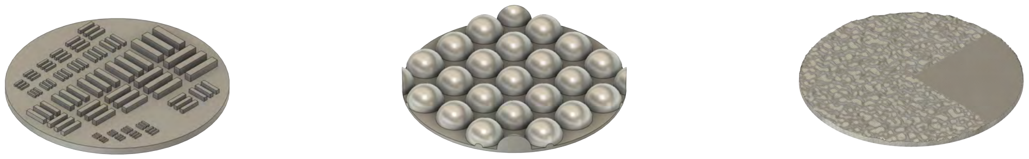

(a) USAF 1951 (b) Half-Spheres (c) 1.0 mm

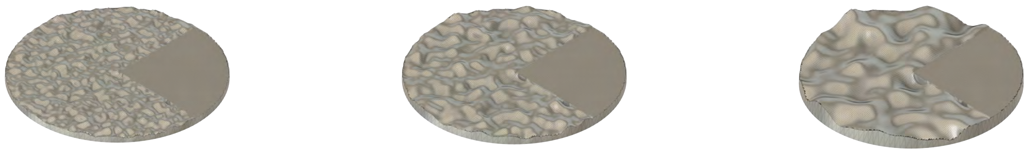

(d) 1.5 mm (e) 2.5 mm (f) 5.0 mm

Figure 5.4: Different 3D printed resolution targets. (a) shows a USAF 1951 target in 3D, (b) shows 10 mm half-spheres, and (c)–(f) are random Gaussian surface targets with different average feature sizes. The cutout is for alignment and focusing purposes.

These printed targets are shown in Figure 5.4 and were either scanned directly or gently pressed into cometary dust analogues to create negative surface impressions. The extracted surfaces from the scans were then converted into point clouds and aligned with the corresponding 3D-print mesh files using the ICP-algorithm in ***CloudCompare*** (Besl & McKay, 1992).

5.3.2 Pebbles

As an initial study, we 3D printed different shapes with a COC filament. These shapes serve as ice/icy pebble simulants. COC was chosen because of its low outgassing in high vacuum (Domingues et al., 2025), low loss at THz frequencies and because it has a refractive index of ≈ 1.5 (Kaluza et al., 2024; Kubiczek et al., 2024), which is similar to that of ice, lying at ≈ 1.8 (Tao et al., 2024). The main advantage of these 3D printed simulants is the ability to compare the measured object to a true 3D model. Additionally, there is no need to cool down the sample when working with COC as opposed to true ice samples. It has to be noted that, while both COC and water ice are fairly transparent at lower THz frequencies, COC has an absorption coefficient of only 10 % of that of solid water ice, it was thus essential to verify the scans with true ice samples. Two different sample holders were used to scan the pebbles covered with dust in reflection and transmission mode as shown in Figure 5.5. Two different centimeter-sized water ice pebbles were constructed. A solid ice sphere was used for initial scans, focusing on a very ice-rich pebble or Water-ice Enriched Block (WEB) (Ciarniello et al., 2022). The water was simply frozen in a 23 mm spherical ice tray in an ordinary freezer and then taken out and submerged in liquid nitrogen (LN_2) to cool it down further and prepare it for insertion into the vacuum chamber. This simulant is shown in Figure 5.6a. In a second run, a porous pebble was produced by putting ice produced with the Setup for Production of Icy Planetary Analogues B (SPIPA-B) (Pommerol et al., 2019) (with a mean diameter of (67 ± 31) µm and a porosity of (49.3 ± 1.4) %) into the same ice tray in an ordinary freezer. We let it sinter for 3 hours, yielding a stable but porous cubic pebble. This porous pebble was then submerged in LN_2 and placed in the vacuum chamber. This simulant is shown in Figure 5.6b.

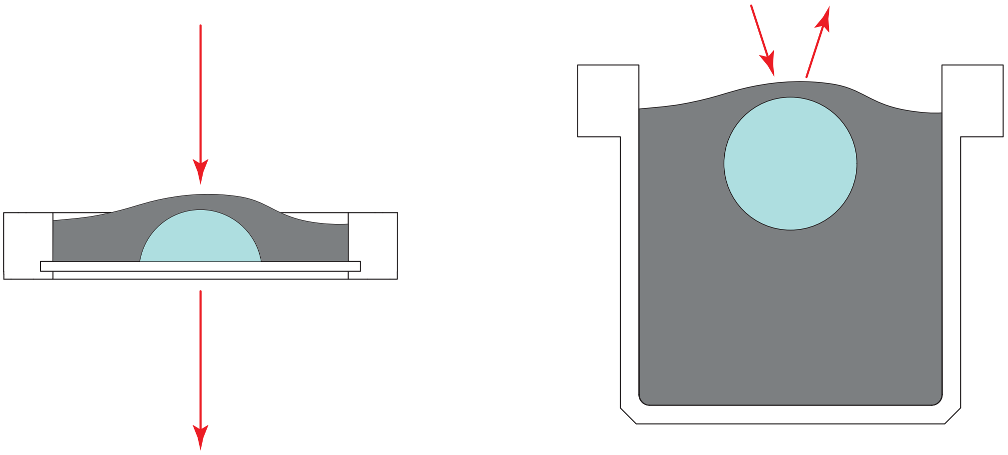

(a) Transmission

(b) Reflection

Figure 5.5: Measurement setup to detect spherical pebbles – either solid or composed from porous ice – under a CoDA-T3 dust layer. The two sample holders are made of copper and cooled below 100 K. The dust layer varies between 1 and 2 mm due to minor out-gassing activity of the ice, which leads to shifting of dust during the pump down phase. In the transmission setup, only a half-sphere was used and placed on a 2 mm thick HRFZ silicon window. In the reflection setup, the spherical pebble was placed on a thick dust layer to move the back-reflections on the bottom of the sample holder outside of the acquisition window.

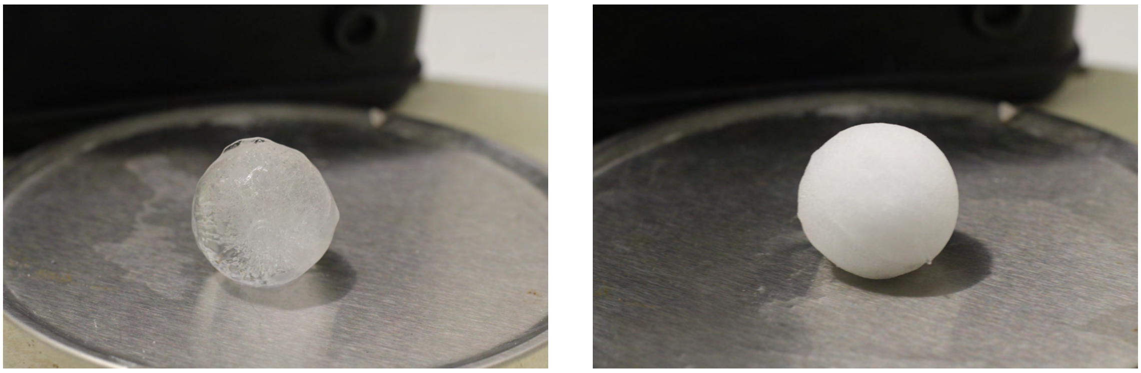

(a) Solid Ice

(b) SPIPA-B

Figure 5.6: Pebble simulants before being placed in the vacuum chamber. The solid ice pebble has a density of $\rho_{\text{Ice}} = (0.901 \pm 0.016)\,\text{g/cm}^3$, the SPIPA-B ice pebble has a density of $\rho_{\text{SPIPA-B}} = (0.519 \pm 0.020)\,\text{g/cm}^3$

The pebble extraction filtering pipeline begins with instrument deconvolution and calibration to remove system response from each trace producing corrected traces suitable for analysis. Each waveform is then processed along the axial (time/depth) axis by applying a 1D Gaussian convolution to map the signal to a positive value. The volume is then globally smoothed with a 3D Gaussian and thresholded to remove noise. Local density filtering follows: A spherical (ball) kernel is convolved with the denoised dataset and normalized to yield a local solid fraction, which is masked to extract the features. Parameter choices control the balance between noise suppression and feature preservation. The parameters for the filtering pipeline are listed in Table 5.2.

Filter	**Parameter**	**Value**	**Unit**
Deconvolution	`low_cut`	0.2	THz
	`high_cut`	0.5	THz
	`start_freq`	0.2	THz
	`end_freq`	0.5	THz
	`win_width`	0.5	THz
	`n_filters`	20	
	`w_max`	30	mm
1D Gaussian	`sigma`	6	
3D Gaussian	`sigma_smooth`	2	
Noise Threshold	`threshold`	0.08	
Local Density	`ball_kernel_radius`	20	
Masking	`threshold`	0.5	

Table 5.2: Filtering parameters for pebble extraction.

5.3.3 Dust

GIADA, the dust analyzer on the Rosetta spacecraft, found that grains close to the nucleus of 67P are composed of (15 ± 2) % ice, (5 ± 2) % of Fe-sulphides, (28 ± 5) % silicates and (51 ± 12) % hydrocarbons in average volume abundances with a microporosity of (52 ± 8) % (Pätzold et al., 2016).

The Rosetta mission found that Comet 67P/Churyumov–Gerasimenko has a porosity of 72 % – 74 % and a low bulk density of 0.533 g/cm^3 (Pätzold et al., 2016), well below that of solid water ice.

The Spitzer telescope analyzed several comets and have found that sub-micron dust tends to be dominated by amorphous carbon and sub-micron silicates tend to be dominated by amorphous silicate materials (Harker et al., 2023). These are however measurements of the coma and not the nucleus.

Findings from the Rosetta mission suggest that 67P sheds a layer of accumulated dust in the first stages of solar approach before exposing primordial dust (Schulz et al., 2015), which leads to further uncertainty on the exact composition and origin of cometary dust.

MIDAS sampled dust from Comet 67P and identified micrometer-scale, porous particles (Mannel et al., 2019). These sizes are far smaller than the wavelengths associated with THz frequencies. The observed particle sizes likely reflect fragmentation of larger aggregates during release from the nucleus or transport in the coma, rather than the intrinsic size of the original dust agglomerates.

To study THz-TDS for cometary applications, we have developed cometary dust simulants for THz spectroscopy called CoDA-Tx (Cometary Dust Analogue for THz spectroscopy version x). The samples are inspired by the work of Lethuillier et al., although the authors mainly focus on the albedo in the visible and NIR and agglomerates that form (Lethuillier et al., 2022). They favor a 60 % to 40 % SiO_2/charcoal ratio for cometary dust analogues, although an atomic C/Si ratio of around 5.5 has been observed at comet 67P (Bardyn et al., 2017; Engrand et al., 2024), which would correspond to a 48 % to 52 % Si/charcoal ratio. Agglomerate size distribution is very important for THz time domain spectroscopy, since Mie Scattering and Multiple Scattering both play a dominating role. Thus, a dust sample forming millimeter-sized agglomerates is preferred.

Our most basic mixture is called CoDA-T0 and was designed to form larger agglomerates. CoDA-T1 extends CoDA-T0 by increasing the amount of activated charcoal to achieve a C/Si ratio of 5.5. CoDA-T2 introduces forsterite[1] to simulate the Mg-rich silicates reported on comets.

At ambient conditions in the laboratory, SiO_2 is composed of spherical nano-particles (NPs) which possess hydroxyl groups on the surface, arising from the humidity in air. These will then form hydrogen bonds with adjacent NPs thus forming larger agglomerates. The Mg-rich silicate forsterite does not form agglomerates in the same way, as it is formed as a salt in a grid structure and remains as small grains. Activated charcoal, the amorphous carbon simulant, is mainly non-polar and will not form agglomerates when mixed with SiO_2.

Mixtures with a high amount with small particles tend to be difficult to handle in the lab. Experiments with CoDA-T1 and CoDA-T2 have shown that the micrometer sized charcoal grains and forsterite grains are strongly coupled to the gas and can thus be ejected from the sample holder during the pump down phase in the vacuum chamber.

To characterize the absorption behavior of cometary dust simulants at THz frequencies, we manufactured pellets with polytetrafluoroethylene (PTFE) as a matrix material. PTFE based pellets have been found to be more suitable for THz spectroscopy than polyethylene (PE) pellets due to lower porosity. A compaction pressure of $>$ 350 MPa is preferable

---

[1] Forsterite 15 microns powder, obtained from Reade Advanced Materials

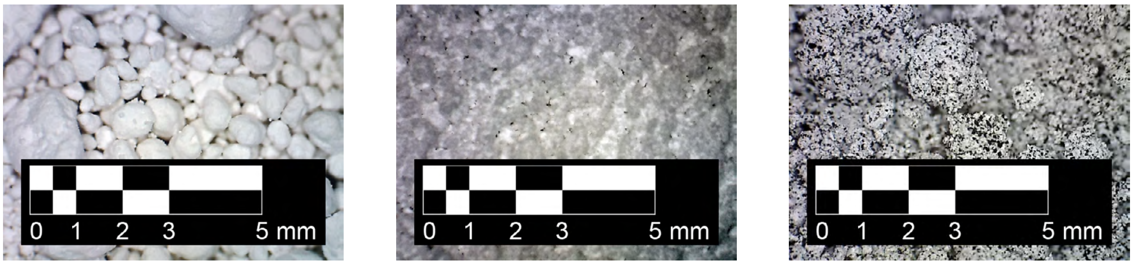

(a) SiO_2 (b) Forsterite (c) CoDA-T0

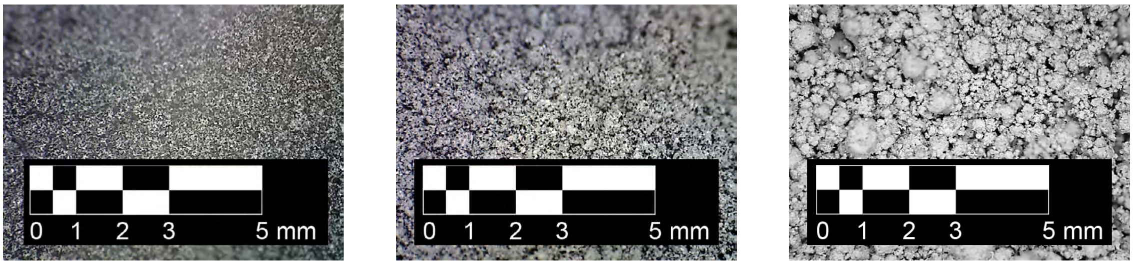

(d) CoDA-T1 (e) CoDA-T2 (f) CoDA-T3

Figure 5.7: Microscopic views of various dust mixtures. Large amounts of particles smaller than 500 µm tend to boil off in our setup. Charcoal does not stick well to SiO_2, but it inhibits the bonding of silicon dioxide particles by acting as a spacer in-between.

to prevent lamination/capping (Murphy et al., 2022). PTFE pellets are widely used in spectroscopic applications to determine the properties of different samples at THz frequencies (Garg et al., 2022; Murphy et al., 2023). Our pellets, with a diameter of 15 mm, were pressed with a maximum force of 90 kN, which equals a pressing stress of 510 MPa. The pellets are composed of 10 % sample and 90 % PTFE. A detailed description of the production process and the results is shown in Appendix B. Before the pellets were placed in the sample holder on a 2 mm thick HRFZ silicon window, a baseline measurement in vacuum with only the silicon window was acquired. This way, any effects of the silicon window can be calibrated. A reference measurement of a pure PTFE pellet was also taken. All pellets were scanned in 2D and then spatially averaged to compensate for inhomogeneities. Any Fabry-Pérot oscillations, caused by trailing echoes, were windowed out in time domain. We use Equation 5.9 and Equation 5.10, derived by Leung et al. to calculate the effective optical properties for each pellet (Leung et al., 2025):

$$n(f) = n_{\text{ref}}(f) + \frac{c\Delta\phi(f)}{2\pi f d} \tag{5.9}$$

$$k(f) = -\frac{c}{2\,\pi f d} \ln\left(\frac{E_{\text{sample}}(f)}{E_{\text{ref}}(f)}\,\frac{(n(f)+n_{\text{ref}}(f))^2}{4\,n(f)\,n_{\text{ref}}(f)}\right) \tag{5.10}$$

where $\Delta\phi(f)$ is the phase difference of the baseline and the pellet measurement, d is the thickness of the pellet, c is the speed of light in vacuum and $n_{\text{ref}}(f) = 1$ as the measurements are taken in vacuum. The refractive index $n(f)$ and extinction coefficient $k(f)$ can now be combined to form the complex refractive index $\tilde{n}(f)$

$$\tilde{n} = n - i\,k,$$

and this further leads to the dielectric constant $\tilde{\varepsilon}(f)$

$$\tilde{\varepsilon}(f) = \tilde{n}(f)^2$$

After obtaining the dielectric constant of the pure PTFE pellet $\tilde{\varepsilon}_(f)$ and the effective dielectric constants of the remaining mixture pellets $\tilde{\varepsilon}_{\text{eff}}(f)$, we can use Effective Medium Theory (EMT), to calculate the true absorption coefficient and refractive index of the sample at different porosities. We used the ***Bruggeman*** method (Markel, 2016), presented in Equation 5.11,

$$\mathbf{v}_h \frac{\tilde{\varepsilon}_h(\omega) - \tilde{\varepsilon}_{\text{eff}}(\omega)}{\tilde{\varepsilon}_h(\omega) + 2\,\tilde{\varepsilon}_{\text{eff}}(\omega)} = -\sum_{i=1}^{n} \mathbf{v}_i \frac{\tilde{\varepsilon}_i(\omega) - \tilde{\varepsilon}_{\text{eff}}(\omega)}{\tilde{\varepsilon}_i(\omega) + 2\,\tilde{\varepsilon}_{\text{eff}}(\omega)}, \tag{5.11}$$

where $\tilde{\varepsilon}_h(\omega)$ is the permittivity and $\mathbf{v}_h$ the volumetric ratio of the host material and $\tilde{\varepsilon}_i(\omega)$ the respective permittivities and $\mathbf{v}_i$ the volumetric ratios of the sample materials. While the samples were produced with a specific mass ratio, we used the density of each sample to calculate the volumetric ratios, as described in Appendix B. We solve the binary case of Equation 5.11 for $\tilde{\varepsilon}_i(\omega)$ in Equation 5.12.

$$\tilde{\varepsilon}(\omega)_i = 2\,\tilde{\varepsilon}(\omega)_{\text{eff}} \frac{\tilde{\varepsilon}(\omega)_{\text{eff}} + \tilde{\varepsilon}(\omega)_h(\mathbf{v}_i - 1)}{\tilde{\varepsilon}(\omega)_h - \tilde{\varepsilon}(\omega)_{\text{eff}}(1 - 3\,\mathbf{v}_i)} \tag{5.12}$$

From the permittivity $\tilde{\varepsilon}_i(\omega)$, we can extract the complex refractive index $\tilde{n}(\omega)$,

$$\tilde{n}(\omega) = \sqrt{\tilde{\varepsilon}_i(\omega)}$$

and ultimately, the frequency dependent real part of the refractive index $n(f)$, extinction coefficient $k(f)$ and absorption coefficient $\alpha(f)$ using Equation 5.13 - Equation 5.15 (Leung et al., 2025).

$$n(f) = \text{Re}\left(\tilde{n}(2\,\pi f)\right), \tag{5.13}$$

$$k(f) = \text{Im}\left(\tilde{n}(2\,\pi f)\right), \tag{5.14}$$

$$\alpha(f) = \frac{4\,\pi f k(f)}{c}, \tag{5.15}$$

The extracted refractive indices and absorption coefficients for kuniper charcoal, activated charcoal, SiO_2, forsterite, carbonaceous chondrite (CI) and our cometary dust analogues CoDA-Tx are shown in Figure 5.8. Individual plots of each of the stated materials here and further materials are noted in Appendix B.

To circumvent the problem of ejecting dust, we introduce CoDA-T3. CoDA-T3 is a mixture of commercially available CI (Britt et al., 2019)[2] and SiO_2[3]. It was designed to match the absorption behavior of CoDA-T2 in the THz range. To calculate the optimal volumetric ratio of the two components, we used Effective Medium Theory (EMT), specifically the ***Bruggeman*** method, already presented in Equation 5.11. In the simplified case of a binary mixture, we can reduce Equation 5.11 to Equation 5.16,

$$\mathbf{v}_{\text{CI}} \frac{\tilde{\varepsilon}_{\text{CI}}(\omega) - \tilde{\varepsilon}_{\text{eff}}(\omega)}{\tilde{\varepsilon}_{\text{CI}}(\omega) + 2\,\tilde{\varepsilon}_{\text{eff}}(\omega)} = -(1 - \mathbf{v}_{\text{CI}}) \frac{\tilde{\varepsilon}_{\text{SiO}_2}(\omega) - \tilde{\varepsilon}_{\text{eff}}(\omega)}{\tilde{\varepsilon}_{\text{SiO}_2}(\omega) + 2\,\tilde{\varepsilon}_{\text{eff}}(\omega)}, \tag{5.16}$$

and set the imaginary part of the square root of the effective primitivity $\tilde{\varepsilon}_{\text{eff}}(f)$, which is proportional to the absorption coefficient, to that of CoDA-T2 and solved for $\mathbf{v}_{\text{CI}}$. This volumetric ratio is then converted to the mass ratio listed in Table 5.6. CoDA-T3 forms agglomerates,

---

[2] CI-E, obtained from Space Resource Technologies (SRT)

[3] Silicon dioxide, obtained from Sigma Aldrich

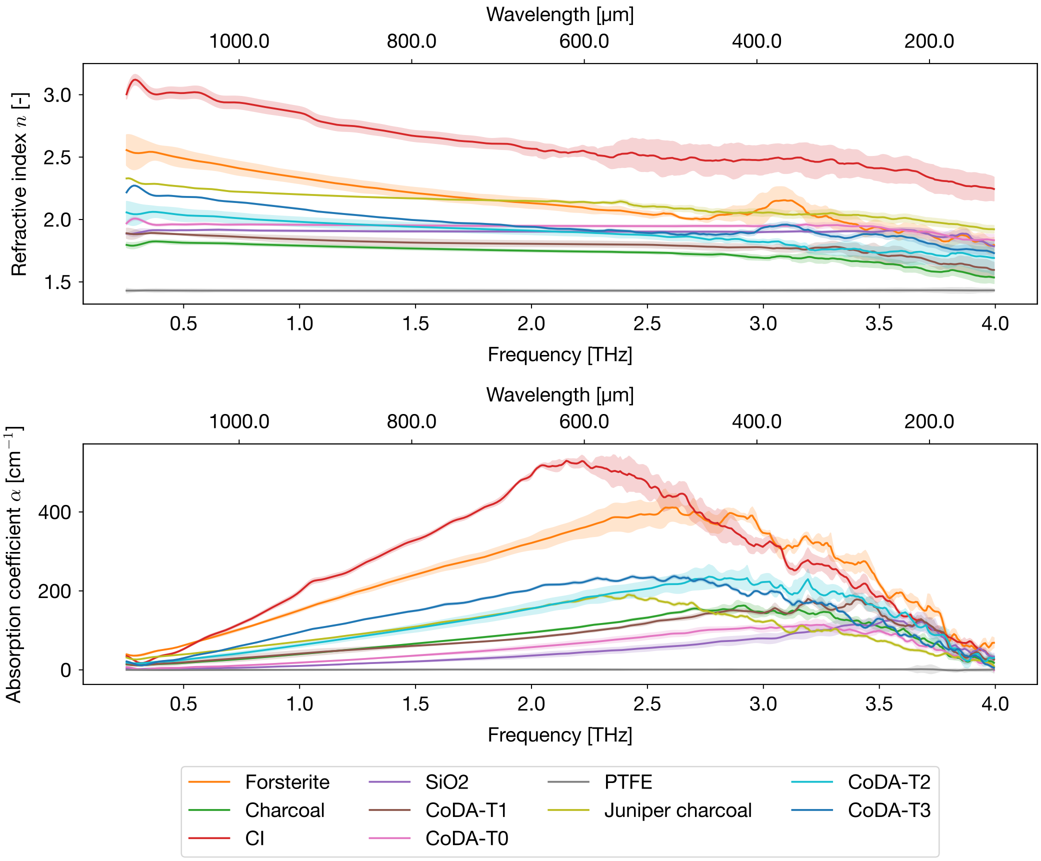

Figure 5.8: Optical properties of different dust components measured with pellets. The absorption of CoDA-T3 is slightly higher than CoDA-T2 which is likely caused by an overcompensation of spillage when mixing the samples.

matches the absorption of CoDA-T2 and has a density of $\rho = 0.374\,\mathrm{g/cm^3}$, and thus poses an excellent cometary dust analogue for experiments in the THz frequency range.

Table 5.3: CoDA-T0 contents with C/Si = 0.55 and a bulk density of approximately $\rho = 0.25\,\mathrm{g/cm^3}$

Component	Mass %	Formula	Molar Mass [g/mol]	Si [mol]	C [mol]
Charcoal	10.0	C	12.01	0.0	0.0083
SiO_2	90.0	SiO_2	60.08	0.0150	0.0
Total	**100.00**	—	—	**0.0083**	**0.0150**

Table 5.4: CoDA-T1 contents with C/Si = 5.5 and a bulk density of approximately $\rho = 0.42\,\mathrm{g/cm^3}$

Component	Mass %	Formula	Molar Mass [g/mol]	Si [mol]	C [mol]
Charcoal	52.37	C	12.01	0.0	0.0436
SiO_2	47.63	SiO_2	60.08	0.0079	0.0
Total	**100.00**	—	—	**0.0079**	**0.0436**

Table 5.5: CoDA-T2 contents with C/Si = 5.5, bulk density of approximately $\rho = 0.43\,\mathrm{g/cm^3}$

Component	Mass %	Formula	Molar Mass [g/mol]	Si [mol]	C [mol]
Charcoal	37.34	C	12.01	0.0	0.0311
SiO_2	12.58	SiO_2	60.08	0.0021	0.0
Forsterite	50.08	Mg_2SiO_4	140.69	0.0036	0.0
Total	**100.00**	—	—	**0.0057**	**0.0311**

Table 5.6: CoDA-T3 contents, bulk density of approximately $\rho = 0.37\,\mathrm{g/cm^3}$

Component	Mass %	Formula	Molar Mass [g/mol]	Si [mol]	C [mol]
CI	34.01	N/A	N/A	N/A	N/A
SiO_2	65.99	SiO_2	60.08	0.011	0.0
Total	**100.00**	—	—	**N/A**	**N/A**

5.4 Results

5.4.1 Surface Extraction

The resolution of the surface extraction was first characterized by scanning resolution targets that were 3D printed with Cyclic Olefin Copolymer (COC). The scans were obtained with a pixel size of 0.25 mm × 0.25 mm. The surface was then extracted according to the method described in Subsection 5.3.1 and then compared to the original 3D mesh file with *CloudCompare*. The color coded point cloud, where the color corresponds to the distance to the nearest point of the mesh file, is shown in Figure 5.12.

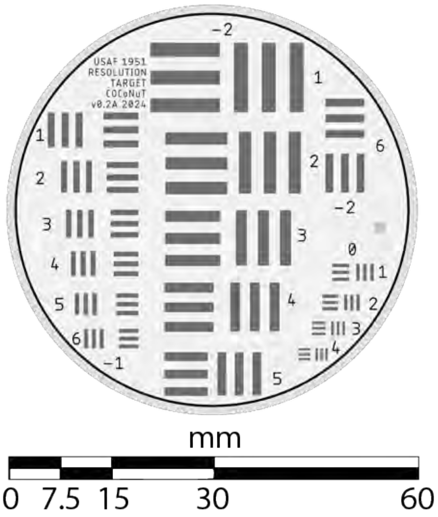

Figure 5.9: Top view of the CAD representation of the COCoNuT resolution target v0.2 (2024) (Stöckli et al., 2025), modified for a 3D implementation in which the bars are extruded into cuboids with identical width and height.

Table 5.7: COCoNuT 3D resolution target based on the USAF 1951 resolution target (2D). The resolution is given in bar-pairs per mm (bp/mm).

Element	**Group Number**	**Group Number**	**Group Number**
	-2	-1	0
1	0.250	0.500	1.00
2	0.281	0.561	1.12
3	0.315	0.630	1.26
4	0.354	0.707	1.41
5	0.397	0.794	1.59
6	0.445	0.891	1.78

We then repeated the measurements for the surface imprinted in cometary dust analogue. We chose 50 % activated charcoal and 50 % SiO_2 as a simulant to provide a lower limit, since a higher amount of charcoal will lead to a lower reflection than SiO_2. This is shown in Figure 5.10.

The accuracy μ, precision σ and root-mean-square error (RMSE), shown in Table 5.8, are obtained from the Gaussian fit with

$$\text{RMSE} = \sqrt{\mu^2 + \sigma^2}$$

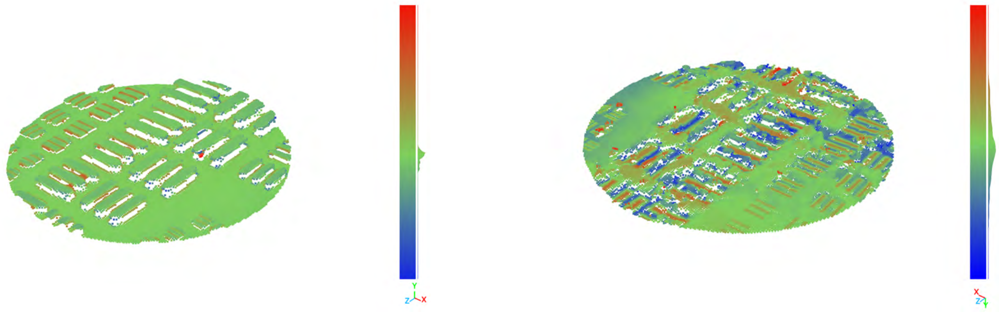

(a) Plain target (b) Negative imprinted in Dust

Figure 5.10: Point-clouds of the extracted surface from the 3D resolution targets, color coded according to the distance of each point to the closest point on the 3D mesh of the scanned object.

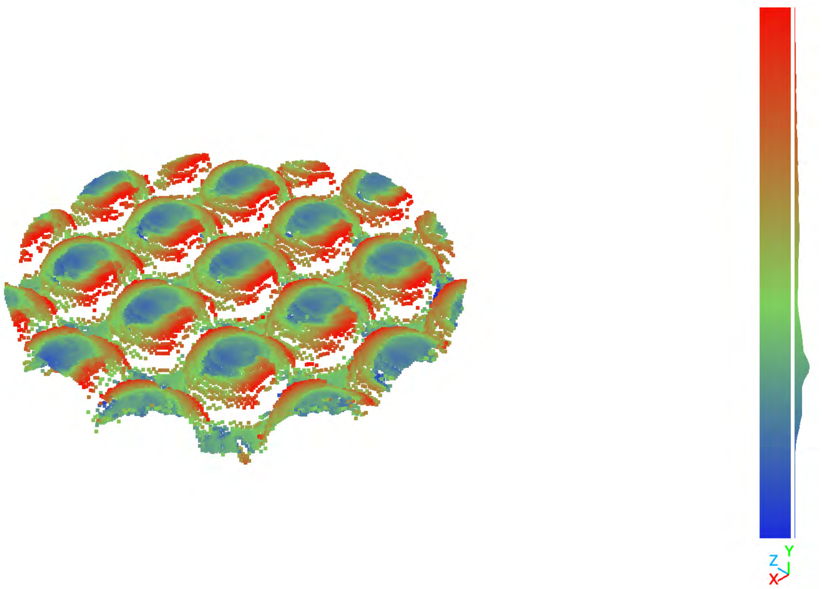

Figure 5.11: Point-clouds of the extracted surface from the 10 mm spheres target, color coded according to the distance of each point to the closest point on the 3D mesh of the scanned object.

Label	Accuracy [mm]	Precision [mm]	RMSE [mm]
Resolution Target	0.01	0.03	0.03
Dust Resolution Target	-0.02	0.22	0.22
10 mm Spheres	-0.06	0.35	0.36
Gaussian Surface 1.0 mm	0.01	0.18	0.18
Gaussian Surface 1.5 mm	0.00	0.16	0.16
Gaussian Surface 2.0 mm	0.07	0.25	0.26
Gaussian Surface 2.5 mm	0.04	0.20	0.20
Gaussian Surface 5.0 mm	0.04	0.10	0.11

Table 5.8: Gaussian fit results for point cloud histograms.

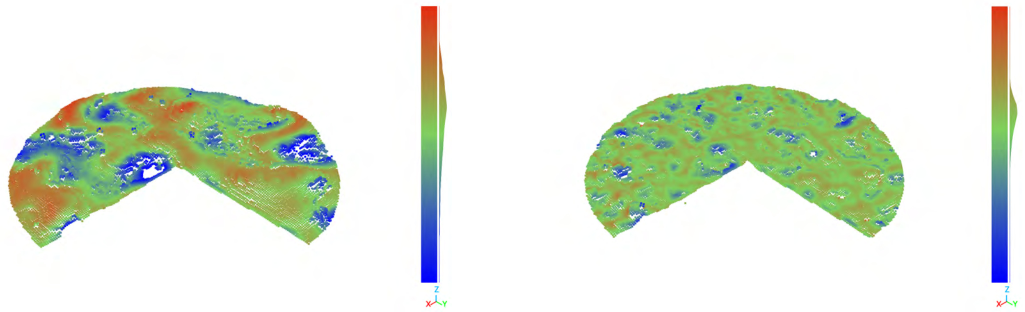

(a) Gaussian 5 mm

(b) Gaussian 2 mm

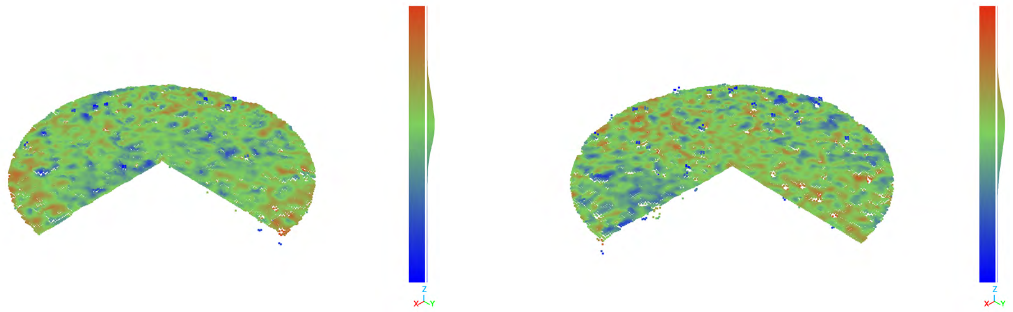

(c) Gaussian 1.5 mm

(d) Gaussian 1 mm

Figure 5.12: Point-clouds of the extracted surface from the Gaussian surface samples, color coded according to the distance of each point to the closest point on the 3D mesh of the scanned object.

While the accuracy primarily reflects the quality of alignment with the 3D model, the RMSE serves as an overall indicator of measurement performance.

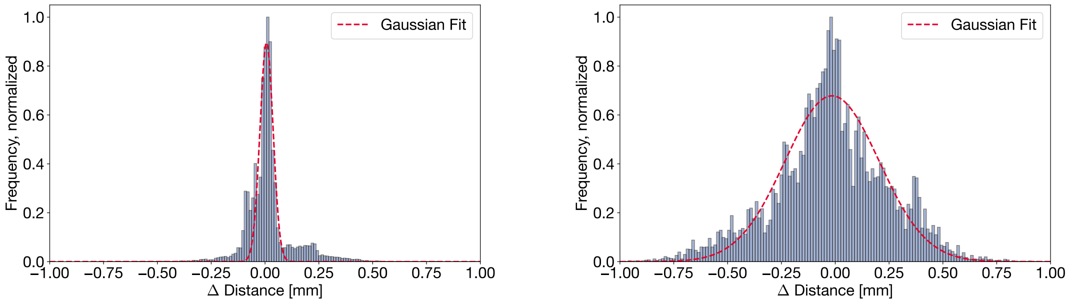

(a) Plain Resolution Target (b) Resolution Target in Dust

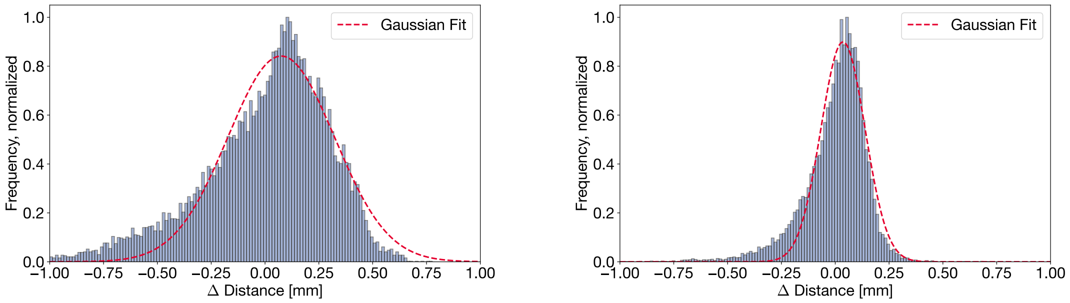

(c) Gaussian 5.0 mm (d) Gaussian 2.0 mm

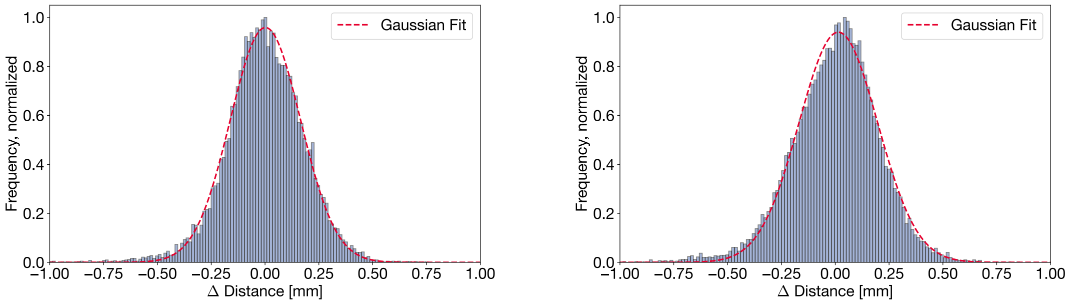

(e) Gaussian 1.5 mm (f) Gaussian 1.0 mm

Figure 5.13: Binned distances of all points of the point-cloud to the closest point on the 3D mesh of the scanned object, including a Gaussian fit and FWHM.

5.4.2 Layer Detection

To observe different layers, we placed a slab (ice/COC cube with side length of 10 mm) under a dust layer. The flat top and bottom surface of the slab create significantly stronger and more distinct reflection signals than the numerous interfaces between the dust grains. The deconvolution discussed in Chapter 3 was first applied to the acquired data. Similar to data representations in ground-penetrating radar (radargrams) or ultrasound imaging (sonograms), THz-TDS measurements can also be visualized using B-scans (a 2D slice along the x-axis). In the B-scan of a COC cube shown in Figure 5.14, as well as in that of a solid ice cube in Figure 5.15, the top and bottom interfaces are clearly distinguishable. If the ice cube is rotated by 45°, the signal is deflected away from the receiver and thus no longer visible.

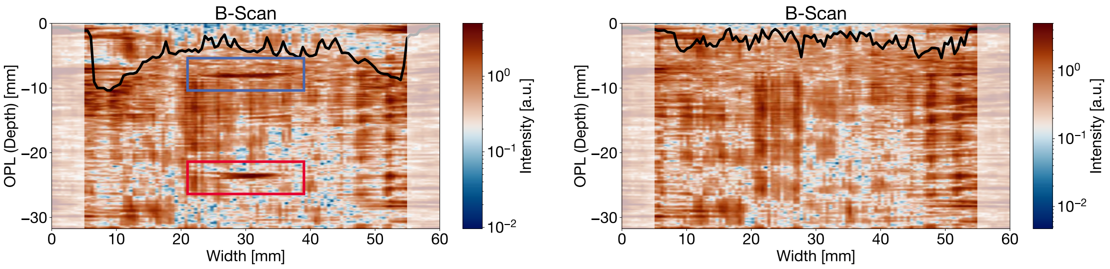

(a) COC, Flat

(b) COC, 45° Tilted

Figure 5.14: B-Scans of a 10 mm × 10 mm × 10 mm COC cube covered with CoDA-T3 dust. The depth depends on the refractive index n and is given as Optical Path Length (OPL). The top surface of the cube is indicated with a blue rectangle, the bottom surface with a red rectangle. The extracted surface of the dust is indicated with a black line, the rims of the sample holder are marked with a lower saturation.

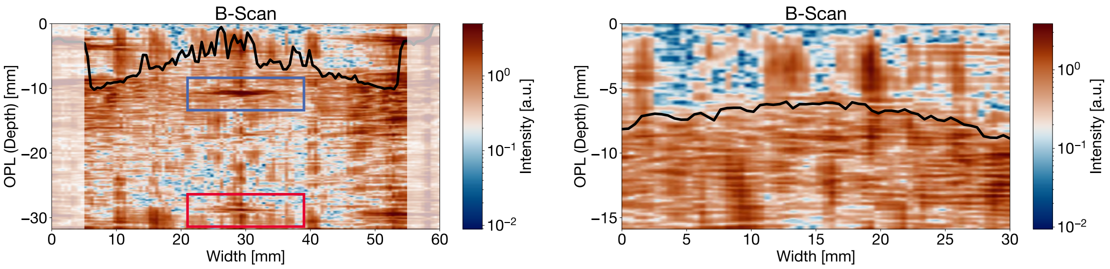

(a) Ice, Flat

(b) Ice, 45° Tilted, zoomed

Figure 5.15: B-Scans of a 10 mm × 10 mm × 10 mm COC cube covered with CoDA-T3 dust. The depth depends on the refractive index n and is given as Optical Path Length (OPL). The top surface of the cube is indicated with a blue rectangle, the bottom surface with a red rectangle. The extracted surface of the dust is indicated with a black line, the rims of the sample holder are marked with a lower saturation.

5.4.3 Resolving Pebbles

Solid ice and SPIPA-B pebble simulants were prepared in the lab, put in the sample holder and covered with CoDA-T3 dust as shown in Figure 5.16.

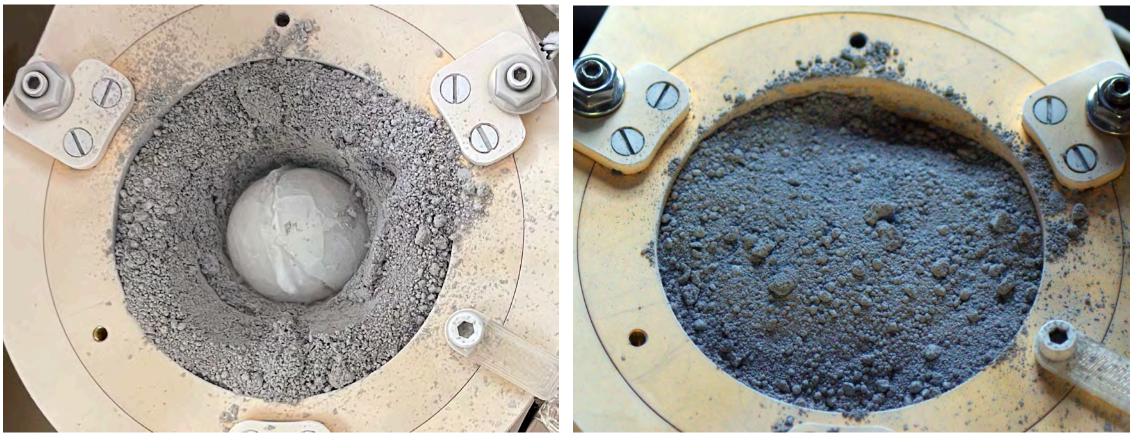

(a) Preparation

(b) Covered

Figure 5.16: Pebble simulant made of solid ice, before and after being covered with CoDA-T3. The picture to the left was taken outside of the vacuum chamber at ambient pressure and the picture to the right was taken inside the vacuum chamber shortly before the scan began, hence the larger amount of frost on the cold surfaces in the left picture.

After applying the filtering pipeline the solid ice pebble becomes visible in the B-Scan, whereas the SPIPA-B pebble does not exceed the noise level, see Figure 5.17.

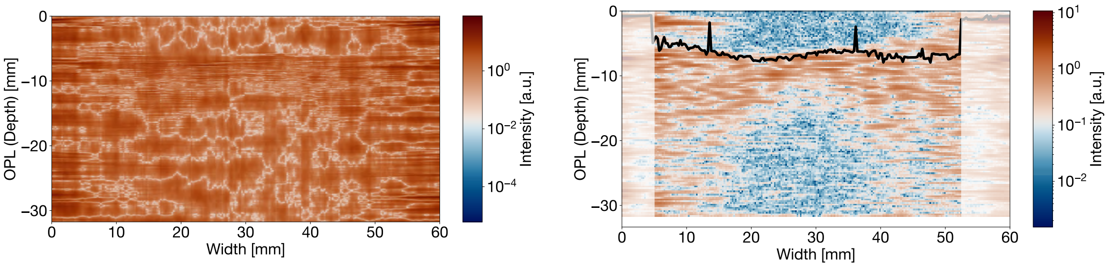

(a) Solid ice, raw (b) Solid ice, filtered

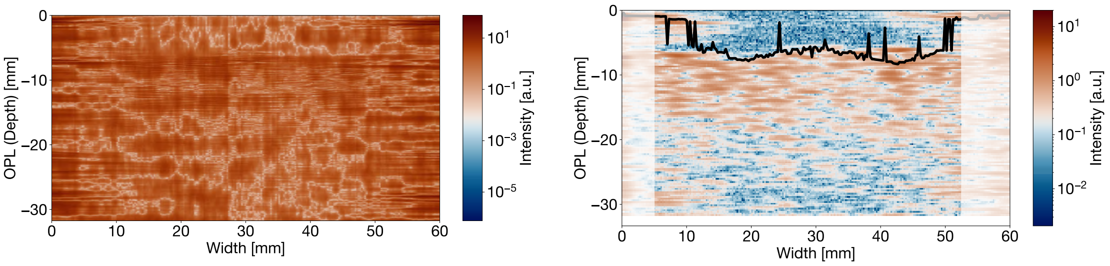

(c) SPIPA-B, raw (d) SPIPA-B, filtered

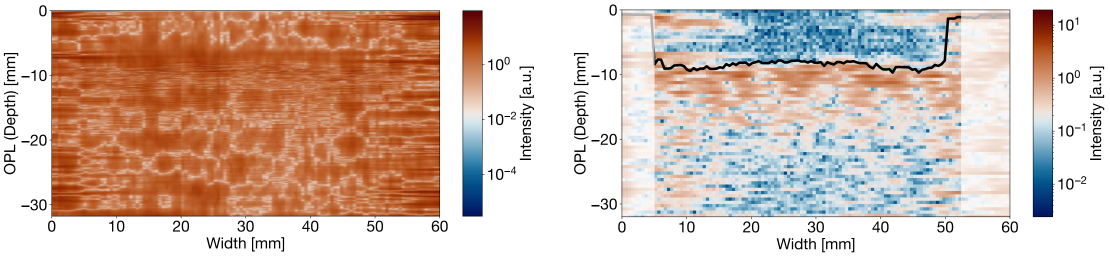

(e) Empty, raw (f) Empty, filtered

Figure 5.17: Raw (a,c,e) and filtered (b,d,f) B-Scans of the solid ice pebble and SPIPA-B ice pebble as well as the empty control scan. The raw plots show the absolute value of the recorded signal. The filtered plots show the data after a band-pass of 0.2 THz to 0.5 THz, de-convolution, downsampling and a ball-kernel smoothing is applied. The extracted surface is indicated as a black line.

The data was then further processed to extract the pebble as a 3D structure. A masked B-scan as well as the full 3D plot including the extracted surface are shown in Figure 5.18.

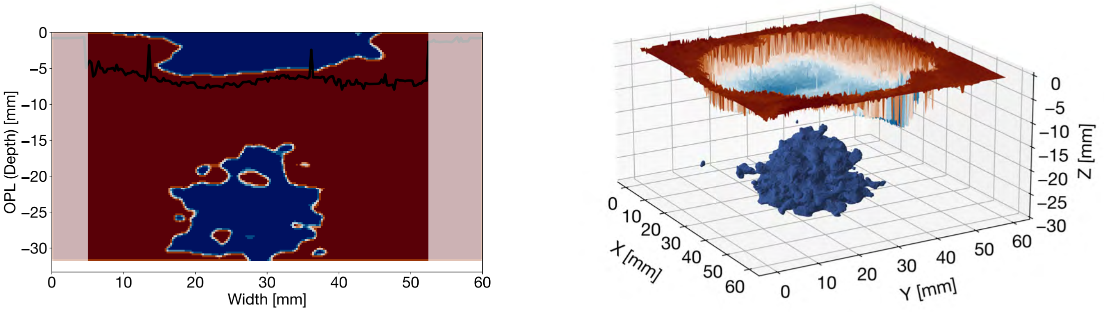

(a) Solid ice, mask

(b) Solid ice, 3D

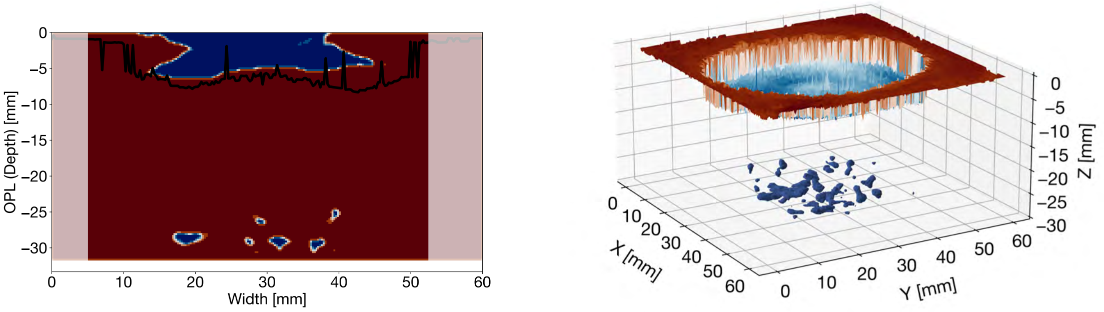

(c) SPIPA-B, mask

(d) SPIPA-B, 3D

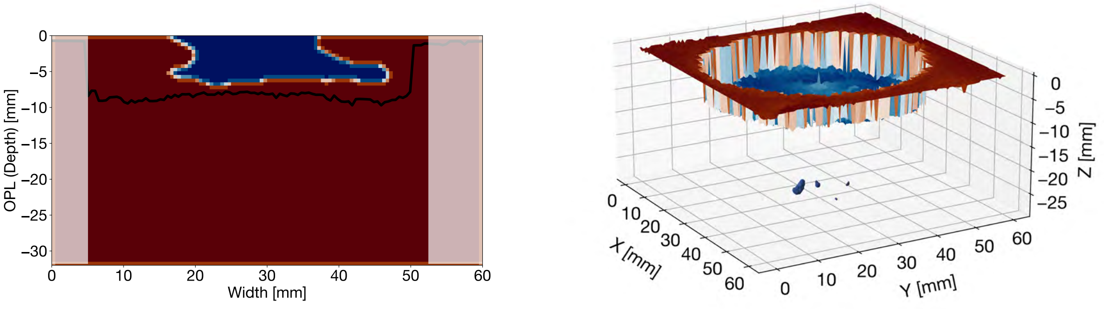

(e) Empty, mask

(f) Empty, 3D

Figure 5.18: A mask with a threshold of 0.08 is applied to the data do extract sub-surface pebbles. A B-Scan is shown on the left side with the extracted surface indicated as a black line. To the left, the 3D plots show the extracted surface and the extracted sub-surface features. Solid ice presents itself as a void inside the 3D voxel plot, due to the lack of interfaces and thus lack of reflected pulses. SPIPA-B is virtually indistinguishable from pure dust sample, due to the comparable amount of interfaces.

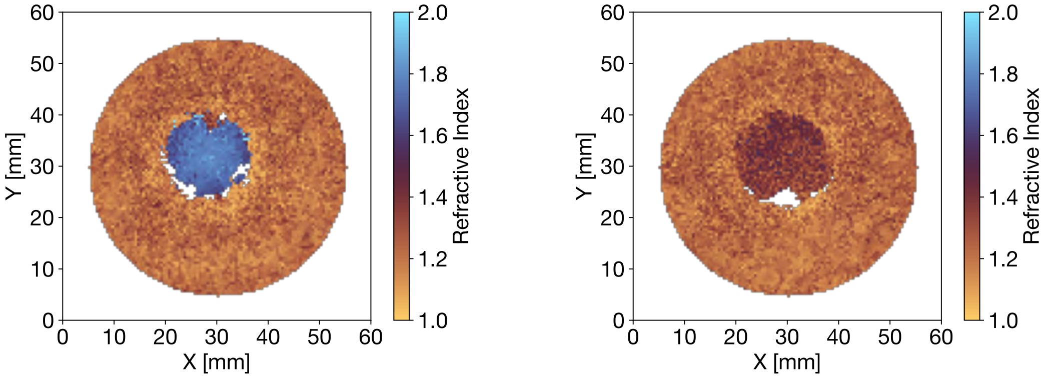

(a) Solid ice pebble

(b) SPIPA-B ice pebble

Figure 5.19: Refractive Index maps of two circular ice pebbles measured in transmission. The white spots around the pebble are invalid values due to strong scattering of the pulse at the edge. The refractive index was calculated for a thickness of 11.5 mm (radius of the spherical pebble).

Finally, the dust covered pebbles were recorded in transmission. The averaged refractive index $\overline{n(\omega)}$ is plotted for each pixel in Figure 5.19.

Discussion

In the course of our experiments, several dust analogues were investigated and a stable and representative formulation, referred to as CoDA-T3, was successfully developed. Its composition is derived from the current understanding of cometary dust. As new insights into cometary material are expected in the near future, further refinement and iteration of this analogue are anticipated. Although the absorption of CoDA-T3 is slightly higher than anticipated, likely due to inaccuracies in the mixing process, it serves as an upper limit. Experiments with samples like CoDA-T2 are expected to yield a stronger signal, as it absorbs less.

Our experiments have shown that we can resolve the surface down to a RMSE < 0.4 mm for different surface targets with smooth surfaces. This performance will decrease for more porous materials, as this leads to broadening of the reflected THz pulse. This is evident from the scan of the 3D resolution target imprinted in porous CI dust. The distribution is broader than the 3D resolution target printed out of COC. This is largely attributed to the higher porosity, though also due to imperfections in the dust surface that resulted from the surface preparation method which use the resolution target stamp. These imperfections are shown in Figure 6.1. The 3D point-cloud scans show that elevated features such as hills or valleys tend to be less accurate than flatter areas, which is especially noticeable in the Gaussian surface with 5 mm sized features. This is likely caused by valleys and hills being further away from the focal point of the off-axis parabolic mirrors. This issue could be eliminated by using collimated beams instead of focused beams. The scan of the spherical target shows a clear asymmetry in the x/y plane, which we suppose is caused by the beam being aligned in along the x-axis. We expect no asymmetry for a 0° setup, where receiver and transmitter are at a 0° phase angle.

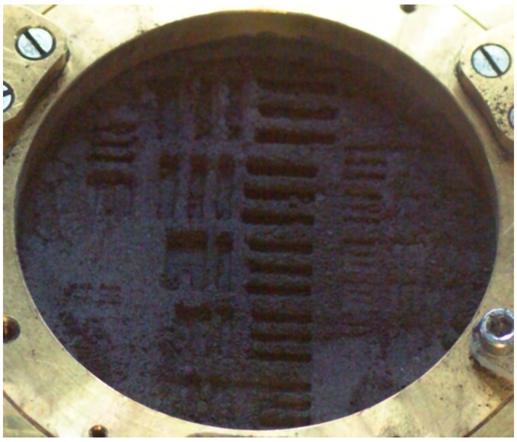

Figure 6.1: The 3D resolution target imprinted in CI dust. Minor imperfections due to walls collapsing when removing the stamp can be seen.

Overall, the surface extraction, based on the log-norm distributions of noise and signal, works well. However, this method breaks down if multiple peaks with significantly different magnitudes are present in the recorded time domain signal. The method could be adapted by using the Bayesian Information Criterion (BIC) to estimate the number of log-norm distributions. Such an implementation would however result in a large increase in computational cost.

We have been able to show that ice slabs can be detected using THz-TDS beneath a dust layer with a thickness at the millimeter scale. Figure 5.15a and Figure 5.14a show that the thickness of the slab can be accurately extracted from the optical path length (OPL) scale by dividing it by the refractive index of the material. In both cases (COC cube and solid ice cube) this yields the expected value of approximately 10 mm. While flat surfaces lead to a strong, distinct reflection, this is not the case for tilted faces which reflect almost all of the signal away from the receiver and appear to be virtually invisible in the data. However, if the object itself is solid and covered with a porous medium, like dust, it appears as a void in the dataset, since the lack of interfaces of a solid object will result in a lack of reflected signal, whereas dust grains lead to many diffuse reflections. We have presented a filtering pipeline that lets us extract such a solid object as a 3D shape from the dataset. This is shown in Figure 5.17 and Figure 5.18. While this works well for solid objects like a solid, dense ice sphere, resembling a Water-ice Enriched Block (WEB), it breaks down when trying to resolve porous ice spheres made from SPIPA-B, as this results in a very similar reflection behavior as the surrounding porous dust. In our setup, the penetration depth in reflection mode is mainly limited by the location of the focal point along the z axis. This could be adapted by either moving the optical setup on a linear stage along the z-axis, thereby moving the focal point to different depths, or by transitioning to a 0° setup, possibly even with a collimated beam.

These findings indicate that reflection based THz spectroscopy might be limited to resolving solid ice and not porous ice. However, both solid ice and SPIPA-B pebble simulants have been measured in transmission. Solid ice has an approximate refractive index of $n_{\text{ice}} \approx 1.8$ and SPIPA-B of $n_{\text{SPIPA-B}} \approx 1.5$, which differs from the refractive index of the dust $n_{\text{CoDA-T3}} \approx 1.2$ and is thus well detectable even when surrounded by dust. These findings are shown in Figure 5.19. We note that even though the half-spherical pebbles have a non uniform thickness along the z-direction, their refractive index appears to be constant throughout the cross-section even though a constant thickness was assumed. This is likely attributed due to the lensing effect of the curved surface, which refracts the THz pulse, altering its path length inside the ice.

An additional limiting factor for the penetration depth is the absorption and scattering of the dust, the sensitivity of the receiver (Rx), and the output power of the transmitter (Tx). Prior to establishing definitive requirements for a future flight instrument, additional investigations involving cometary dust analogues are essential. The pebble simulants utilized in this study represent a deliberately simplified model of structurally and compositionally complex pebbles, for which our current understanding remains limited. Advancing this line of research will require the development and characterization of more representative and physically realistic pebble analogues.

In addition to mineral studies, spectra of L-alanine, pyrene, anthracene and NH_4Cl were analyzed. We have discovered that while the studied amino-acids show distinct absorption features in the THz regime, they can only be detected in their crystalline form and are not visible when studied as a porous powder. Additionally, broad absorption of our dust samples and water ice is more dominant and shadows these features. NH_4Cl also has a broad absorption behavior, which is indistinguishable from the dust samples. These results are included in Appendix B.

Conclusion and Outlook

In this work, we have presented our laboratory setup, COCoNuT, in Chapter 2. We further established a frequency dependent deconvolution algorithm to post process THz-TDS measurements in Chapter 3. We have implemented this algorithm in an interactive, cross-platform GUI application presented in Chapter 4. Furthermore, we have presented our analysis of the measurements of cometary analogues in Chapter 5 and have set out to lay the ground work for the possible development of a THz spectrometer to perform in-situ studies on comets.

7.1 THz Time-Domain Spectroscopy in Space

Broadband THz Time-Domain Spectroscopy (THz-TDS) has proven to be a promising technology to resolve centimeter sized structures in sub-surface layers using the lower frequencies and to resolve the surface topology with the higher frequencies. However, the question of the lower limit of the detectable pebble-size is still unanswered and requires further investigations. While the main limitation remains the scattering of the THz beam on the dust and ice grains, these factors are much less dominant in transmission. On the other hand, reflection measurements are simpler to conduct on in-situ exploration missions. While the technology also provides the possibility to study the absorption features of different materials in the range from 0.1 THz to 5.0 THz in laboratory conditions, e.g. clean pressed pellets, the application for in-situ measurements in space is more difficult. The main challenges are the broad absorption features of salts, ice, and minerals, and the scattering of agglomerates of porous dust. While transmission measurements are less susceptible to the latter, it is more difficult to perform transmission spectroscopy in-situ of the surface, as this requires either drilling two boreholes or to excavate the material. Furthermore, comets may have a dust layer with a local thickness in the meter range. Our proof-of-concept setup is not able to penetrate meters into the sample. It is uncertain if this is due to the dominating scattering effect or the absorption of the dust, which could be mitigated with a higher transmitting power. However, drilling a borehole into this thick dust layer and inserting a THz probe would be a plausible approach to resolve the surface structure underneath the dust layer in either case. Such a concept is discussed in Subsection 7.2.1.

7.2 Outlook

While our proof-of-concept studies have delivered promising results and lay the groundwork for THz time-domain spectroscopy for in-situ measurements in space, there are still unanswered questions about its implementation and application. Our experiments were conducted with a focused beam which is very sensitive to the vertical position of the sample since only one point can be fully in focus. A 0° setup could mitigate this and deliver more precise measurements. The main challenge is the loss of signal due to a beam splitter (Yoo et al., 2023), or the more complex integration of a THz transceiver antenna (Busch et al., 2014). This setup would however be more compact and if combined with an unfocused, collimated beam, could possibly penetrate deeper into the sample at the cost of a reduced spatial resolution, because of the larger beam diameter.

Further challenges include the absorption and scattering effects of cometary dust, which is not yet known. While we have based our dust simulants on previously reported measurements of cometary dust, the exact absorption and scattering properties in the THz frequency range of dust found on a comet's nucleus are still unknown. The amount of signal loss and the maximum power of the transmitting antenna directly determine the maximum penetration depth into the sub-surface layers. The exact requirements for a mission-certified instrument have yet to be determined, but clearly, the work presented here can inform this definition.

The distinct fingerprint absorption features of water vapor make THz-TDS a valuable option of measuring the H_2O concentration in the atmosphere. However, preliminary tests with COCoNuT have shown that the SNR of our setup is too low to resolve these absorption features at pressures below 1 mbar, which makes it unsuitable for cometary applications. Nevertheless, on other planetary bodies with higher atmospheric pressures, such as Mars, the application of THz-TDS to detect the abundance of water vapor should be investigated. It is also important to note that deuterium oxide (D_2O, or heavy water) exhibits distinct absorption features in the terahertz range compared to ordinary water (H_2O) (Yu et al., 2006). This distinction is particularly relevant in the context of the ongoing debate about the origin of Earth's water, specifically whether comets contributed significantly during the Late Heavy Bombardment. A key parameter in this discussion is the deuterium-to-hydrogen (D/H) ratio (Altwegg et al., 2015; Mandt et al., 2024).

7.2.1 Future Mission

This work was part of the SUBICE project, which investigates the overall application of THz-TDS in space and build a foundation for the miniaturization of the instrument. A potential idea for an implementation is illustrated in Figure 7.1. The THz spectrometer is mounted on top of a hollow drill, which is based on the drill used on the Rosalind Franklin Rover (Altieri et al., 2023). The optics is set up in a 0° configuration with a beam splitter. A collimated beam is guided through the drill and focused by an off-axis parabolic mirror at the bottom of the drill. By slowly moving the drill in the vertical and rotational axes, the entire bore hole could be imaged. The main advantage of this setup is the decoupling of the sensitive spectrometer and antenna to the drill. There is no need for optical and electrical feed-throughs and/or slip-rings. Challenges for the development of a space-grade THz time-domain spectrometer are the power consumption of the laser and delay line, although the latter could be mitigated by using a dual comb laser (Willenberg et al., 2024). A further obstacle is the production of space-grade Photoconductive Antennas (PCA), which need to withstand larger temperature ranges and radiation doses than the commercial antennas used in this work.

Alternatively, designs based on transmission measurements with two drills, one housing the transmitter and one housing the receiver, could be investigated further. The ORIGO proposal for ESA's M8 call intended to include a THz time domain tomograph based on the findings in this work (Marschall et al., 2023).

We conclude that given the findings presented in this work, we are confident that a mission carrying a THz spectrometer has potential to gain new insights about the interior structure of comets and its implications for planetary formation.

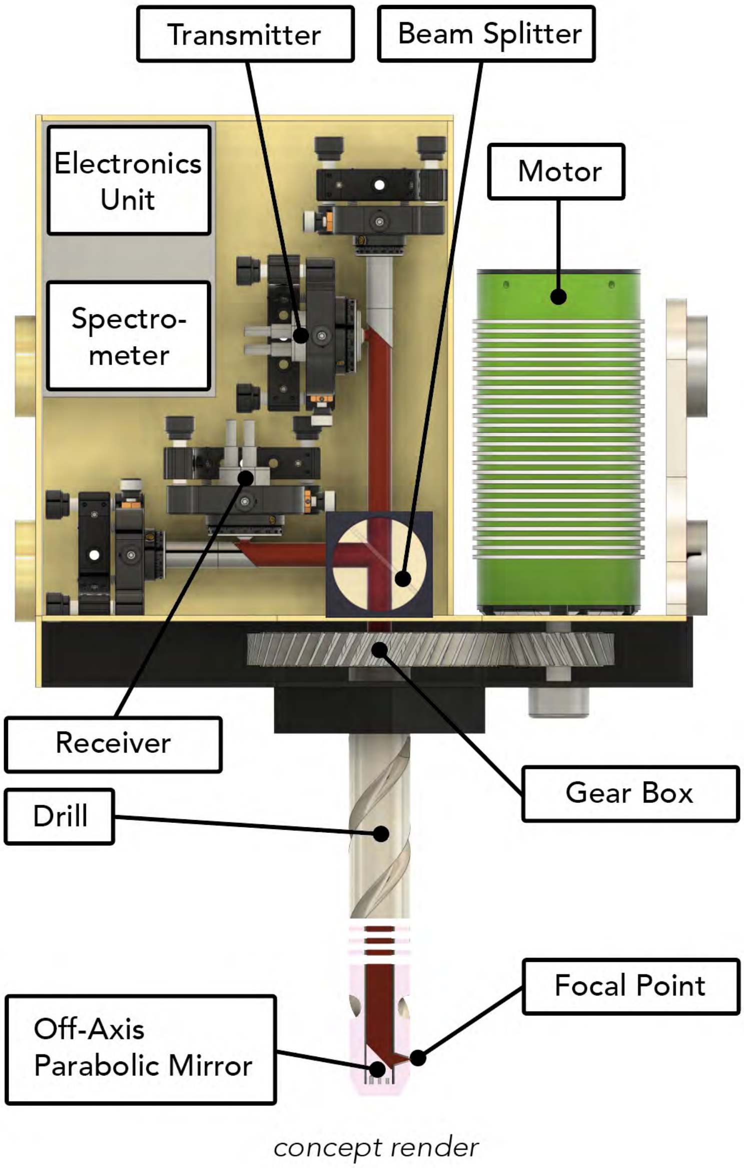
Transmitter
Beam Splitter
Electronics Unit
Motor
Spectro-meter
Receiver
Drill
Gear Box
Focal Point
Off-Axis Parabolic Mirror
concept render

Figure 7.1: Concept of the instrument with one mirror and a window inside the drill. The optical setup and antennas are decoupled from the drill.

Cryo Cooler Performance

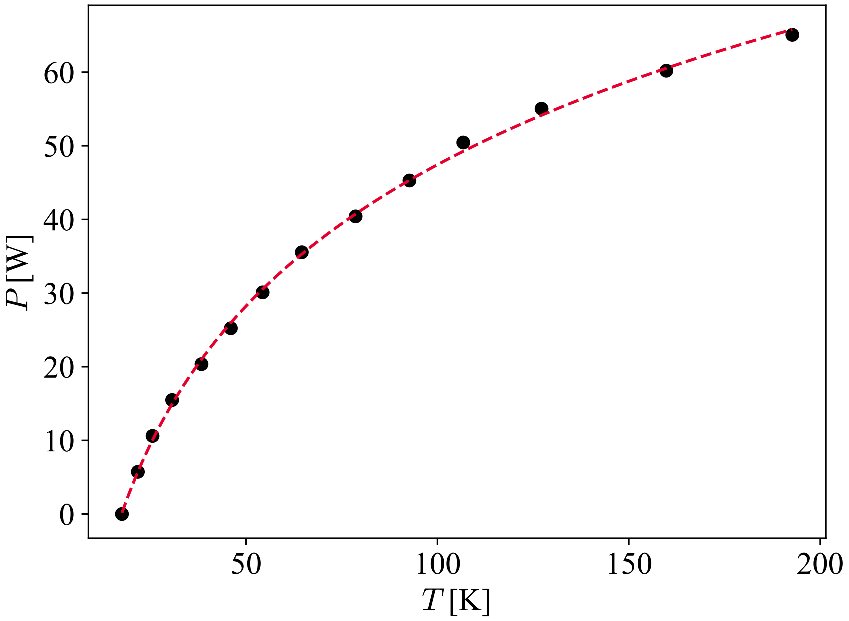

Figure A.1: The temperature dependent cooling power of the CH-104 cryo-cooler by *SHI Cryogenics Group* as specified in the data-sheet.

Spectroscopic Analysis of Amino Acids, Salts and Minerals

The samples have been prepared by Hervé Girard from HES-SO. To press pellets, different methods were explored:

A PTFE was used as matrix material. Dry powders were mixed and then pressed with a ***Carver*** hydraulic press with a 15 mm die and with a force of 90 kN, yielding a compression pressure of about 500 MPa.

B PTFE was used as matrix material. Sample powder is dissolved in water, then mixed with dry PTFE powder and then dried. The obtained powder is then pressed with a ***Carver*** hydraulic press with a 15 mm die and with a force of 90 kN, yielding a compression pressure of about 500 MPa.

A detailed description of all individual sample components is given in Table B.1.

These samples have been measured in transmission at room temperature and in vacuum (1×10^{-1} mbar).

Effective Medium Theory (EMT) was used to determine the refractive index and absorption coefficients of the material. At first, the pellets were measured in transmission and averaged over different points in the xy-plane in time-domain. The complex refractive index of the matrix material PTFE was determined using Equation B.1 - Equation B.3 and a reference measurement in clear space $n_{\text{ref}} = 1$.

$$n(f) = n_{\text{ref}}(f) + \frac{c\Delta\phi(f)}{2\,\pi f d} \tag{B.1}$$

$$\alpha(f) = -\frac{2}{d}\ln\left(\frac{E_{\text{sample}}(f)}{E_{\text{ref}}(f)}\,\frac{(n(f)+n_{\text{ref}}(f))^2}{4\,n(f)\,n_{\text{ref}}(f)}\right) = \frac{4\,\pi f k(f)}{c} \tag{B.2}$$

$$\tilde{n} = n - i\,k = \sqrt{\tilde{\varepsilon}} \tag{B.3}$$

Where $\Delta\phi(f) = \phi_{\text{ref}}(f) - \phi_{\text{sample}}(f)$ is the phase difference obtained from the FFT, d is the thickness of the sample and c is the speed of light. The remaining pellets were measured and the optical properties were determined again using Equation B.1 - Equation B.3 but this time with the previously mentioned PTFE measurement as a reference set, thus $n_{\text{ref}} = n_{\text{PTFE}}(f)$. Using the ***Bruggeman*** equation (Markel, 2016) given in Equation B.4.

$$\mathbf{v}_h \frac{\tilde{\varepsilon}_h(\omega) - \tilde{\varepsilon}_{\text{eff}}(\omega)}{\tilde{\varepsilon}_h(\omega) + 2\,\tilde{\varepsilon}_{\text{eff}}(\omega)} = -\sum_{i=1}^{n} \mathbf{v}_i \frac{\tilde{\varepsilon}_i(\omega) - \tilde{\varepsilon}_{\text{eff}}(\omega)}{\tilde{\varepsilon}_i(\omega) + 2\,\tilde{\varepsilon}_{\text{eff}}(\omega)}, \tag{B.4}$$

Where $\mathbf{v}_i$ is the volumetric ratio of the component. We can solve for the permittivity $\tilde{\varepsilon}_i(\omega)$. The volumetric ratios $\mathbf{v}_i$ were calculated by measuring the mass m_{total} and volume V_{total} of

Sample	CAS	Manufacturer	Description
PTFE	9002-84-0	unbranded	1.6 µm particle size
Anthracene	120-12-7	Sigma Aldrich	
L-alanine	56-41-7	Sigma Aldrich	
Pyrene	129-00-0	Sigma Aldrich	
NH_4Cl	12125-02-9	Sigma Aldrich	
SiO_2	14808-60-7	Sigma Aldrich	0.5 – 10 µm particle size
Activated charcoal	7440-44-0	Sigma Aldrich	untreated powder, 100 – 400 mesh
Juniper charcoal	7440-44-0	CoPhyLab/Werth-Metall	UN-Nr.: 1361, Lagerklasse 4.2, $<$ 100 µm particle size
CI-E	-	Space Resource Technologies (SRT)	Carbonaceous chondrite (CI-E) high-fidelity asteroid regolith simulant, 003-15-001-0823
Forsterite	-	Reade Advanced Materials	15 µm particle size
Fayalite	-	Reade Advanced Materials	15 µm particle size

Table B.1: Description of the individual components.

the pellet. The pellets were produced with a fixed mass-ratio of 1:9.

$$\mathbf{v}_i = \frac{V_{\text{total}} - V_{\text{PTFE}}}{V_{\text{total}}}, \qquad V_{\text{PTFE}} = \frac{m_{\text{PTFE}}}{\rho_{\text{PTFE}}}, \qquad m_{\text{PTFE}} = 0.9\, m_{\text{total}} \tag{B.5}$$

The refractive index and absorption coefficient can be extracted from the obtained permittivity as shown in Equation B.6 - Equation B.8.

$$n(f) = \text{Re}\left(\tilde{n}(f)\right) = \text{Re}\left(\sqrt{\tilde{\varepsilon}(f)}\right) \tag{B.6}$$

$$\alpha(f) = \text{Im}\left(\tilde{n}(f)\right) = \text{Im}\left(\sqrt{\tilde{\varepsilon}(f)}\right) \tag{B.7}$$

$$k(f) = \frac{4\,\pi\,\alpha(f)\,f}{c} \tag{B.8}$$

The pellets are documented in Table B.2 - Table B.17.

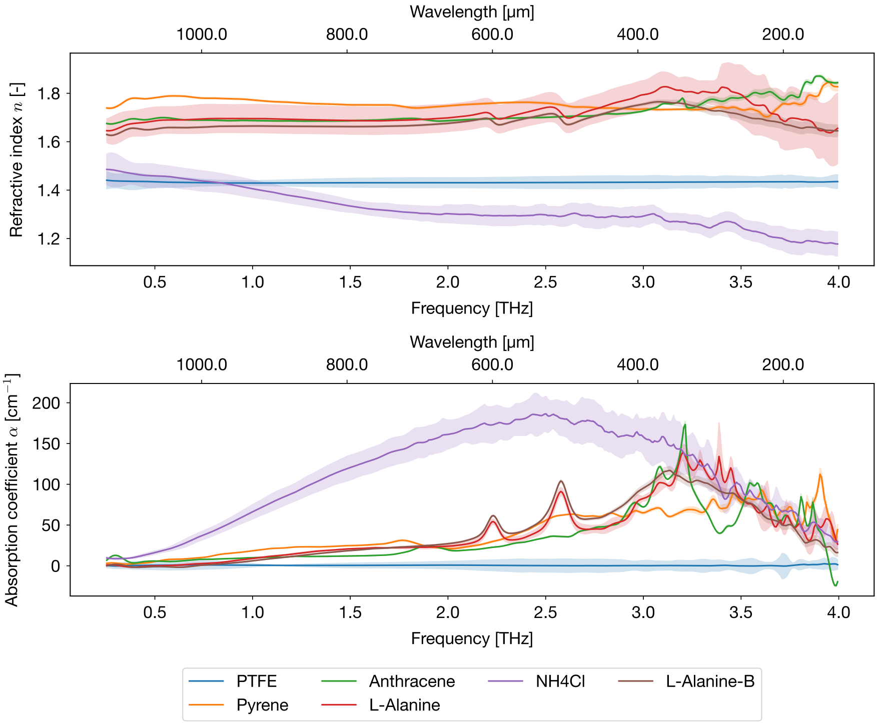

Figure B.1: Optical properties extracted from the pellets from batch # 1 using EMT.

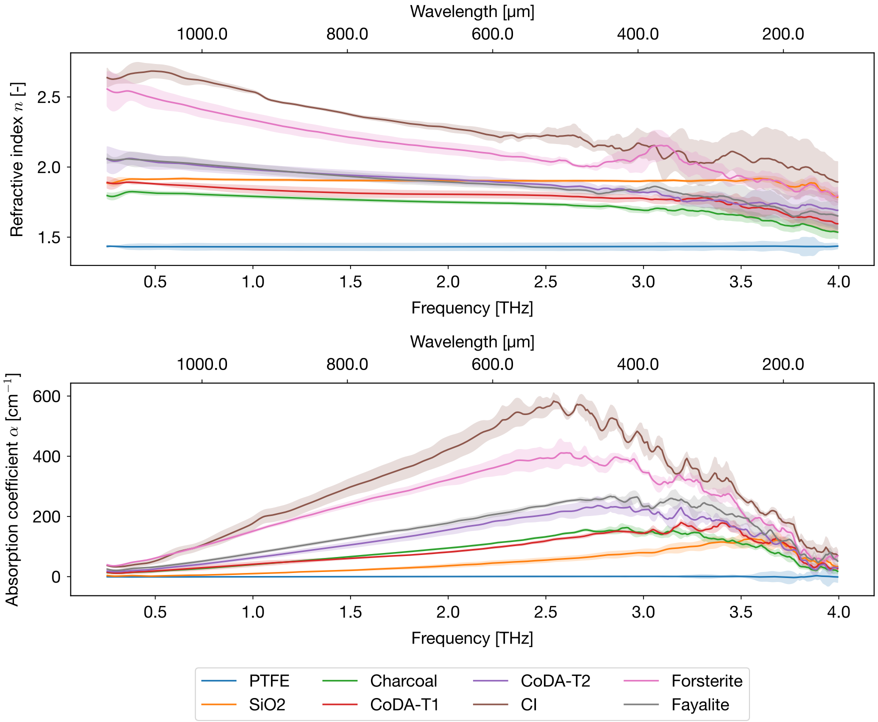

Figure B.2: Optical properties extracted from the pellets from batch # 2 using EMT.

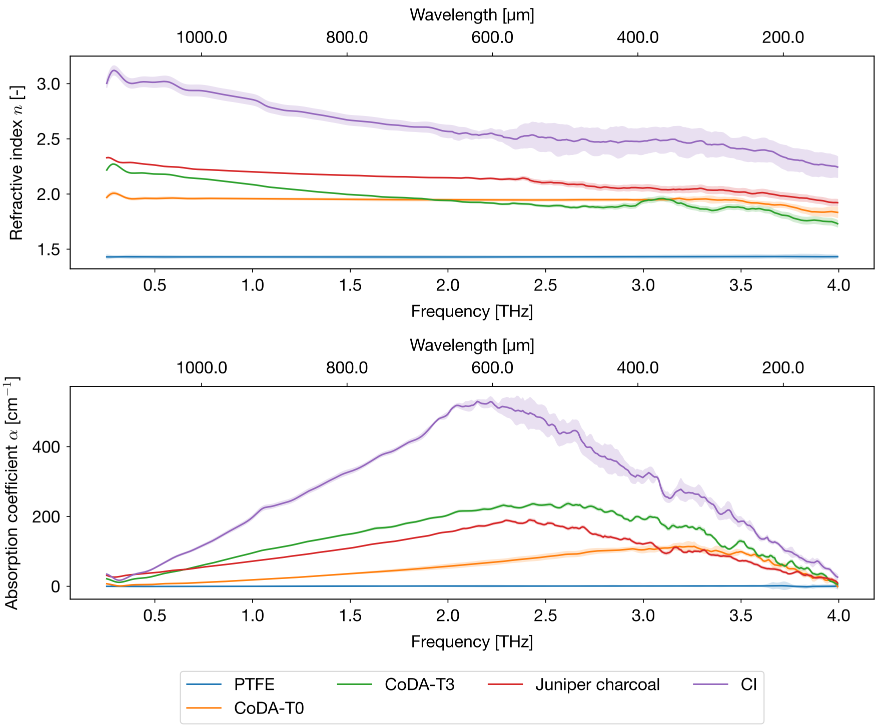

Figure B.3: Optical properties extracted from the pellets from batch # 3 using EMT.

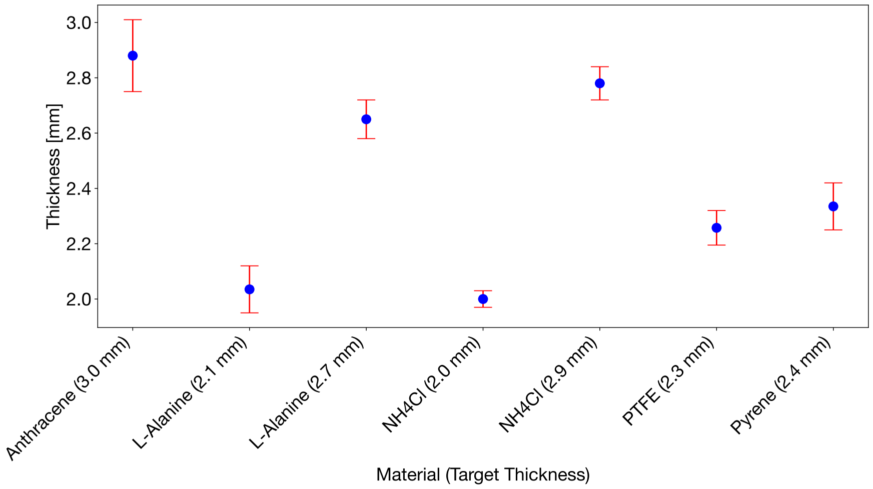

Figure B.4: Thickness range for each pellet of the batch # 1.

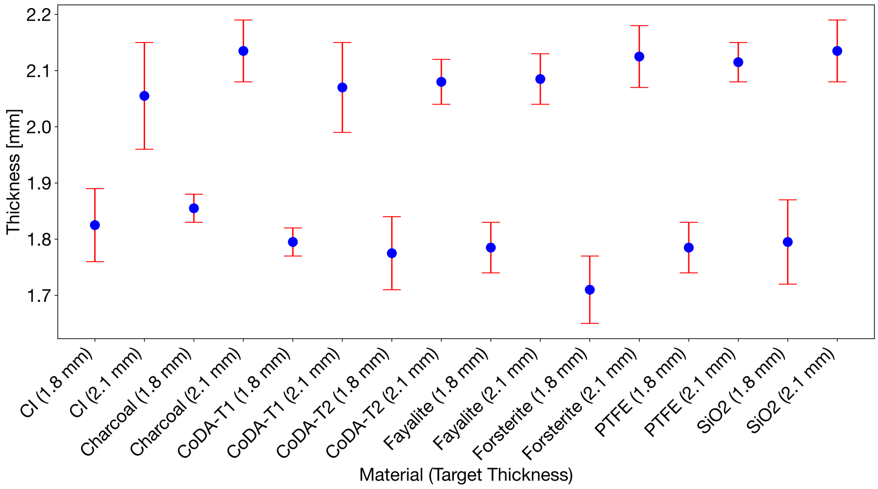

Figure B.5: Thickness range for each pellet of the batch # 2.

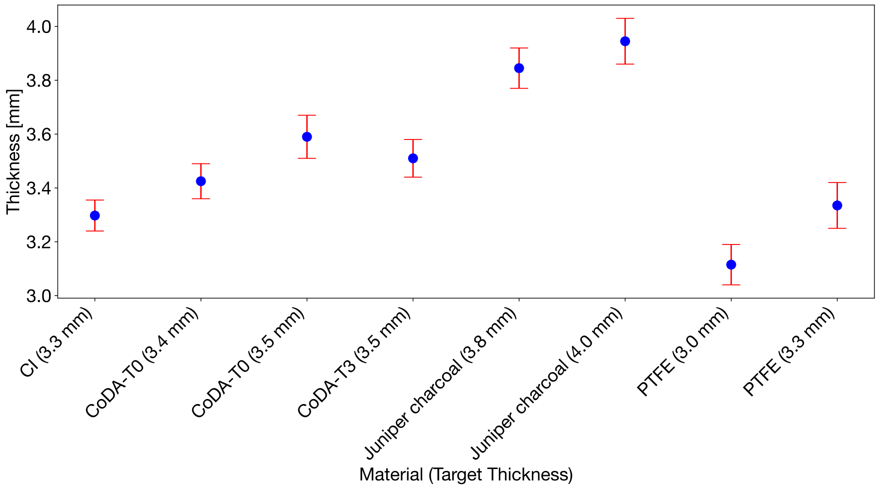

Figure B.6: Thickness range for each pellet of the batch # 3.

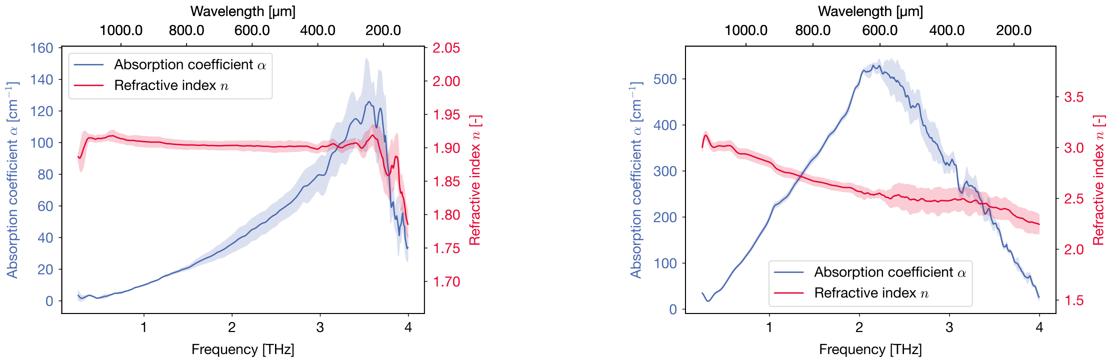

(a) SiO_2

(b) CI

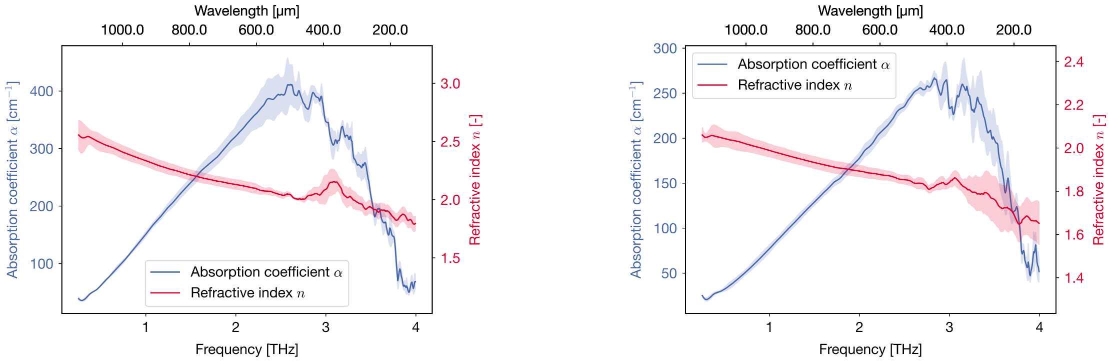

(c) Forsterite

(d) Fayalite

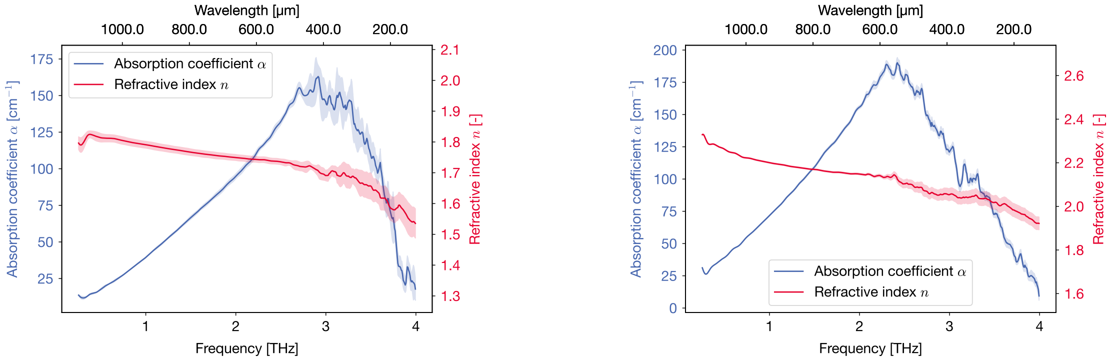

(e) Charcoal

(f) Juniper charcoal

Figure B.7: Refractive indices and absorption coefficients of different dust samples.

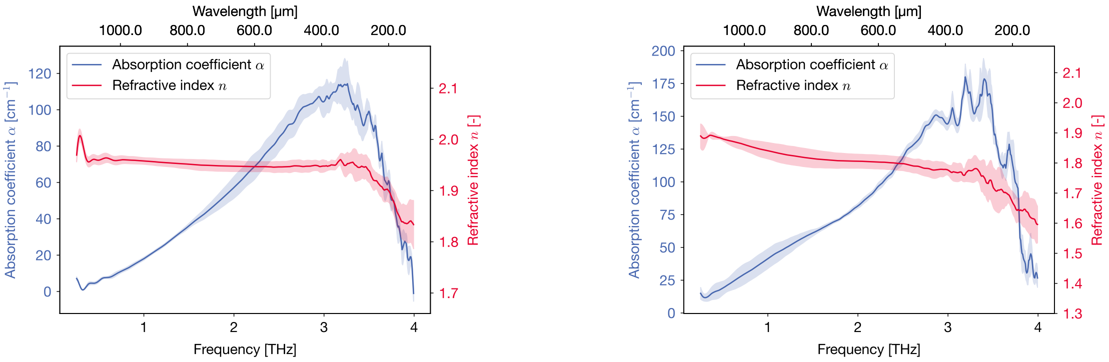

(a) CoDA-T0

(b) CoDA-T1

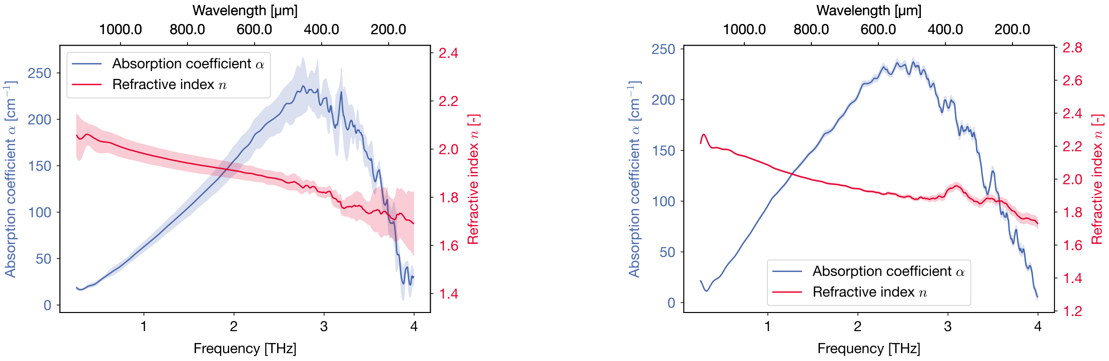

(c) CoDA-T2

(d) CoDA-T3

Figure B.8: Refractive indices and absorption coefficients of different dust analogues.

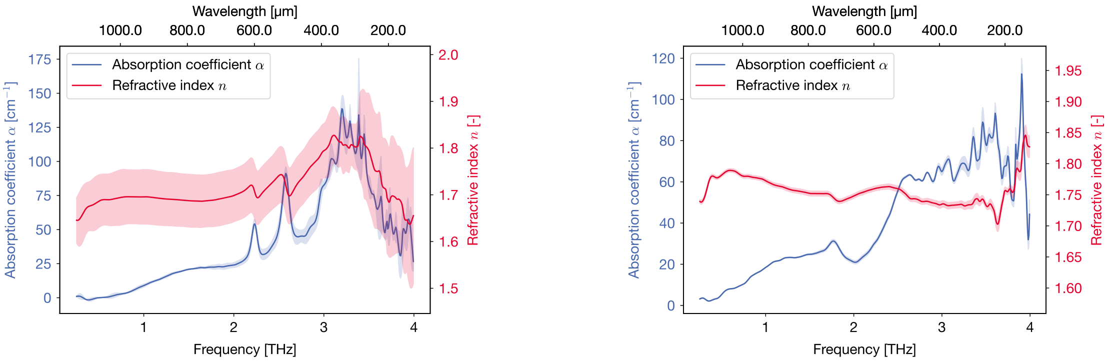

(a) L-alanine

(b) Pyrene

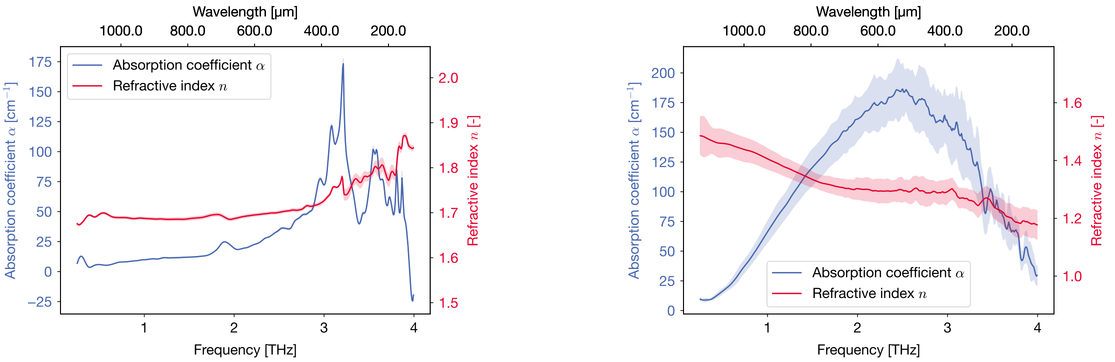

(c) Anthracene

(d) NH_4Cl

Figure B.9: Refractive indices and absorption coefficients of different amino acid and NH_4Cl samples.

Parameter	
Name	**Pellet 1**
Material	**PTFE**
Production Method	*A*
Target thickness	1.8 mm
Mass	(0.672 ± 0.005) g
Measured thickness	(1.79 ± 0.04) mm
Calculated sample density	(2.16 ± 0.63) g/cm^3
Sample volumetric ratio	1.0

Table B.2: Pellet with 100% PTFE – Target 1.8 mm

Parameter	
Name	**Pellet 2**
Material	**PTFE**
Production Method	*A*
Target thickness	2.1 mm
Mass	(0.797 ± 0.005) g
Measured thickness	(2.12 ± 0.03) mm
Calculated sample density	(2.19 ± 0.48) g/cm^3
Sample volumetric ratio	1.0

Table B.3: Pellet with 100% PTFE – Target 2.1 mm

Parameter	
Name	**Pellet 3**
Material	**SiO2**
Production Method	*A*
Target thickness	1.8 mm
Mass	(0.682 ± 0.005) g
Measured thickness	(1.79 ± 0.08) mm
Calculated sample density	(2.38 ± 1.15) g/cm^3
Sample volumetric ratio	0.09 ± 0.04

Table B.4: Pellet with 90% PTFE and 10% SiO2 – Target 1.8 mm

Parameter	
Name	**Pellet 4**
Material	**SiO2**
Production Method	*A*
Target thickness	2.1 mm
Mass	(0.812 ± 0.005) g
Measured thickness	(2.13 ± 0.06) mm
Calculated sample density	(2.41 ± 0.77) g/cm^3
Sample volumetric ratio	0.09 ± 0.03

Table B.5: Pellet with 90% PTFE and 10% SiO2 – Target 2.1 mm

Parameter	
Name	**Pellet 5**
Material	**Charcoal**
Production Method	*A*
Target thickness	1.8 mm
Mass	(0.619 ± 0.005) g
Measured thickness	(1.85 ± 0.02) mm
Calculated sample density	(0.95 ± 0.11) g/cm^3
Sample volumetric ratio	0.20 ± 0.02

Table B.6: Pellet with 90% PTFE and 10% Charcoal – Target 1.8 mm

Parameter	
Name	**Pellet 6**
Material	**Charcoal**
Production Method	*A*
Target thickness	2.1 mm
Mass	(0.715 ± 0.005) g
Measured thickness	(2.13 ± 0.06) mm
Calculated sample density	(0.97 ± 0.15) g/cm^3
Sample volumetric ratio	0.20 ± 0.03

Table B.7: Pellet with 90% PTFE and 10% Charcoal – Target 2.1 mm

Parameter	
Name	**Pellet 7**
Material	**CoDA-T1**
Production Method	*A*
Target thickness	1.8 mm
Mass	(0.642 ± 0.005) g
Measured thickness	(1.79 ± 0.03) mm
Calculated sample density	(1.42 ± 0.22) g/cm^3
Sample volumetric ratio	0.15 ± 0.02

Table B.8: Pellet with 90% PTFE and 10% CoDA-T1 – Target 1.8 mm

Parameter	
Name	**Pellet 8**
Material	**CoDA-T1**
Production Method	*A*
Target thickness	2.1 mm
Mass	(0.736 ± 0.005) g
Measured thickness	(2.07 ± 0.08) mm
Calculated sample density	(1.36 ± 0.38) g/cm^3
Sample volumetric ratio	0.15 ± 0.04

Table B.9: Pellet with 90% PTFE and 10% CoDA-T1 – Target 2.1 mm

Parameter	
Name	**Pellet 9**
Material	**CoDA-T2**
Production Method	*A*
Target thickness	1.8 mm
Mass	(0.635 ± 0.005) g
Measured thickness	(1.77 ± 0.07) mm
Calculated sample density	(1.42 ± 0.40) g/cm^3
Sample volumetric ratio	0.15 ± 0.04

Table B.10: Pellet with 90% PTFE and 10% CoDA-T2 – Target 1.8 mm

Parameter	
Name	**Pellet 10**
Material	**CoDA-T2**
Production Method	*A*
Target thickness	2.1 mm
Mass	(0.746 ± 0.005) g
Measured thickness	(2.08 ± 0.04) mm
Calculated sample density	(1.45 ± 0.25) g/cm^3
Sample volumetric ratio	0.14 ± 0.02

Table B.11: Pellet with 90% PTFE and 10% CoDA-T2 – Target 2.1 mm

Parameter	
Name	**Pellet 11**
Material	**CI**
Production Method	*A*
Target thickness	1.8 mm
Mass	(0.700 ± 0.005) g
Measured thickness	(1.82 ± 0.06) mm
Calculated sample density	(2.65 ± 1.22) g/cm^3
Sample volumetric ratio	0.08 ± 0.04

Table B.12: Pellet with 90% PTFE and 10% CI – Target 1.8 mm

Parameter	
Name	**Pellet 12**
Material	**CI**
Production Method	*A*
Target thickness	2.1 mm
Mass	(0.777 ± 0.005) g
Measured thickness	(2.05 ± 0.10) mm
Calculated sample density	(2.26 ± 1.13) g/cm^3
Sample volumetric ratio	0.10 ± 0.05

Table B.13: Pellet with 90% PTFE and 10% CI – Target 2.1 mm

Parameter	
Name	**Pellet 13**
Material	**Forsterite**
Production Method	*A*
Target thickness	1.8 mm
Mass	(0.635 ± 0.005) g
Measured thickness	(1.71 ± 0.06) mm
Calculated sample density	(1.90 ± 0.65) g/cm^3
Sample volumetric ratio	0.11 ± 0.04

Table B.14: Pellet with 90% PTFE and 10% Forsterite – Target 1.8 mm

Parameter	
Name	**Pellet 14**
Material	**Forsterite**
Production Method	*A*
Target thickness	2.1 mm
Mass	(0.794 ± 0.005) g
Measured thickness	(2.12 ± 0.06) mm
Calculated sample density	(2.01 ± 0.55) g/cm^3
Sample volumetric ratio	0.11 ± 0.03

Table B.15: Pellet with 90% PTFE and 10% Forsterite – Target 2.1 mm

Parameter	
Name	**Pellet 15**
Material	**Fayalite**
Production Method	*A*
Target thickness	1.8 mm
Mass	(0.655 ± 0.005) g
Measured thickness	(1.79 ± 0.04) mm
Calculated sample density	(1.72 ± 0.42) g/cm^3
Sample volumetric ratio	0.12 ± 0.03

Table B.16: Pellet with 90% PTFE and 10% Fayalite – Target 1.8 mm

Parameter	
Name	**Pellet 16**
Material	**Fayalite**
Production Method	*A*
Target thickness	2.1 mm
Mass	(0.761 ± 0.005) g
Measured thickness	(2.08 ± 0.04) mm
Calculated sample density	(1.65 ± 0.34) g/cm^3
Sample volumetric ratio	0.13 ± 0.03

Table B.17: Pellet with 90% PTFE and 10% Fayalite – Target 2.1 mm

Parameter	
Name	**Pellet 17**
Material	**CoDA-T0**
Production Method	*A*
Target thickness	3.5 mm
Mass	(1.365 ± 0.005) g
Measured thickness	(3.59 ± 0.08) mm
Calculated sample density	(2.08 ± 0.51) g/cm^3
Sample volumetric ratio	0.11 ± 0.03

Table B.18: Pellet with 90% PTFE and 10% CoDA-T0 – Target 3.5 mm

Parameter	
Name	**Pellet 18**
Material	**CoDA-T0**
Production Method	*A*
Target thickness	3.4 mm
Mass	(1.301 ± 0.005) g
Measured thickness	(3.42 ± 0.07) mm
Calculated sample density	(2.06 ± 0.45) g/cm^3
Sample volumetric ratio	0.11 ± 0.02

Table B.19: Pellet with 90% PTFE and 10% CoDA-T0 – Target 3.4 mm

Parameter	
Name	**Pellet 19**
Material	**CoDA-T3**
Production Method	*A*
Target thickness	3.5 mm
Mass	(1.342 ± 0.005) g
Measured thickness	(3.50 ± 0.07) mm
Calculated sample density	(2.26 ± 0.55) g/cm^3
Sample volumetric ratio	0.10 ± 0.02

Table B.20: Pellet with 90% PTFE and 10% CoDA-T3 – Target 3.5 mm

Parameter	
Name	**Pellet 20**
Material	**CoDA-T3**
Production Method	*A*
Target thickness	3.5 mm
Mass	(1.344 ± 0.005) g
Measured thickness	(3.52 ± 0.07) mm
Calculated sample density	(2.17 ± 0.50) g/cm^3
Sample volumetric ratio	0.10 ± 0.02

Table B.21: Pellet with 90% PTFE and 10% CoDA-T3 – Target 3.5 mm

Parameter	
Name	**Pellet 21**
Material	**Juniper charcoal**
Production Method	*A*
Target thickness	4.0 mm
Mass	(1.416 ± 0.005) g
Measured thickness	(3.95 ± 0.08) mm
Calculated sample density	(1.33 ± 0.21) g/cm^3
Sample volumetric ratio	0.16 ± 0.02

Table B.22: Pellet with 90% PTFE and 10% Juniper charcoal – Target 4.0 mm

Parameter	
Name	**Pellet 22**
Material	**Juniper charcoal**
Production Method	*A*
Target thickness	3.8 mm
Mass	(1.379 ± 0.005) g
Measured thickness	(3.84 ± 0.08) mm
Calculated sample density	(1.33 ± 0.20) g/cm^3
Sample volumetric ratio	0.16 ± 0.02

Table B.23: Pellet with 90% PTFE and 10% Juniper charcoal – Target 3.8 mm

Parameter	
Name	**Pellet 23**
Material	**CI**
Production Method	*A*
Target thickness	3.3 mm
Mass	(1.272 ± 0.005) g
Measured thickness	(3.28 ± 0.06) mm
Calculated sample density	(2.55 ± 0.65) g/cm^3
Sample volumetric ratio	0.09 ± 0.02

Table B.24: Pellet with 90% PTFE and 10% CI – Target 3.3 mm

Parameter	
Name	**Pellet 24**
Material	**CI**
Production Method	*A*
Target thickness	3.3 mm
Mass	(1.292 ± 0.005) g
Measured thickness	(3.31 ± 0.06) mm
Calculated sample density	(2.71 ± 0.69) g/cm^3
Sample volumetric ratio	0.08 ± 0.02

Table B.25: Pellet with 90% PTFE and 10% CI – Target 3.3 mm

Parameter	
Name	**SUBALA 28**
Material	**PTFE**
Production Method	*B*
Target thickness	2.3 mm
Mass	(0.813 ± 0.005) g
Measured thickness	(2.22 ± 0.08) mm
Calculated sample density	(1.87 ± 0.62) g/cm^3
Sample volumetric ratio	1.0

Table B.26: Pellet with 100% PTFE – Target 2.3 mm

Parameter	
Name	**SUBALA 29**
Material	**PTFE**
Production Method	*B*
Target thickness	2.3 mm
Mass	(0.861 ± 0.005) g
Measured thickness	(2.29 ± 0.05) mm
Calculated sample density	(2.49 ± 0.77) g/cm^3
Sample volumetric ratio	1.0

Table B.27: Pellet with 100% PTFE – Target 2.3 mm

Parameter	
Name	**SUBALA 30**
Material	**Pyrene**
Production Method	*B*
Target thickness	2.4 mm
Mass	(0.838 ± 0.005) g
Measured thickness	(2.33 ± 0.08) mm
Calculated sample density	(1.61 ± 0.50) g/cm^3
Sample volumetric ratio	0.13 ± 0.04

Table B.28: Pellet with 90% PTFE and 10% Pyrene – Target 2.4 mm

Parameter	
Name	**SUBALA 31**
Material	**Anthracene**
Production Method	*B*
Target thickness	3.0 mm
Mass	(1.037 ± 0.005) g
Measured thickness	(2.88 ± 0.13) mm
Calculated sample density	(1.65 ± 0.63) g/cm^3
Sample volumetric ratio	0.13 ± 0.05

Table B.29: Pellet with 90% PTFE and 10% Anthracene – Target 3.0 mm

Parameter	
Name	**SUBALA 32**
Material	**L-alanine**
Production Method	*B*
Target thickness	2.1 mm
Mass	(0.692 ± 0.005) g
Measured thickness	(2.04 ± 0.08) mm
Calculated sample density	(1.18 ± 0.22) g/cm^3
Sample volumetric ratio	0.22 ± 0.04

Table B.30: Pellet with 90% PTFE and 10% L-alanine – Target 2.1 mm

Parameter	
Name	**SUBALA 33**
Material	**L-alanine**
Production Method	*B*
Target thickness	2.7 mm
Mass	(0.909 ± 0.005) g
Measured thickness	(2.65 ± 0.07) mm
Calculated sample density	(1.18 ± 0.22) g/cm^3
Sample volumetric ratio	0.17 ± 0.03

Table B.31: Pellet with 90% PTFE and 10% L-alanine – Target 2.7 mm

Parameter	
Name	**SUBALA 34**
Material	**NH_4Cl**
Production Method	*B*
Target thickness	2.0 mm
Mass	(0.693 ± 0.005) g
Measured thickness	(2.00 ± 0.03) mm
Calculated sample density	(1.26 ± 0.19) g/cm^3
Sample volumetric ratio	0.16 ± 0.02

Table B.32: Pellet with 90% PTFE and 10% NH_4Cl – Target 2.0 mm

Parameter	
Name	**SUBALA 35**
Material	**NH_4Cl**
Production Method	*B*
Target thickness	2.9 mm
Mass	(0.953 ± 0.005) g
Measured thickness	(2.78 ± 0.06) mm
Calculated sample density	(1.18 ± 0.19) g/cm^3
Sample volumetric ratio	0.17 ± 0.03

Table B.33: Pellet with 90% PTFE and 10% NH_4Cl – Target 2.9 mm

Electronics

As part of this project, I have designed, assembled and programmed various PCBs (Printed Circuit Boards). An overview is shown in Table C.1 and Figure C.1. Most of these boards are part of the COCoNuT Electronics Unit (ELU), which is shown in Figure C.2. A second ELU unit is part of the WEEVIL (Water Emission of Vapour from Ice in the Laboratory) laboratory setup. The prototype of the ELU is used in another lab setup called SCITEAS 2 (Simulation Chamber for Imaging the Temporal Evolution of Analogue Samples - Version 2.0). A stepper motor control prototype board is in use in a test setup for the RAMSES/CHANCES camera. The control boards are based around STM microcontrollers. The firmware is written in Rust (Matsakis & Klock II, 2014; Sharma et al., 2024) and uses a freeRTOS wrapper (Barry, 2023)

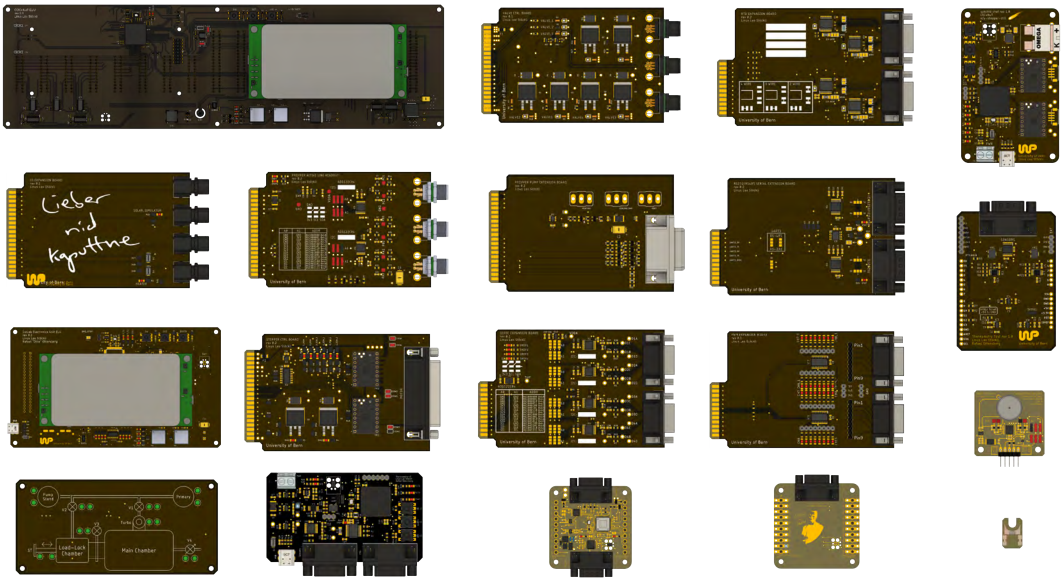

Figure C.1: An overview of the PCBs developed as part of this work.

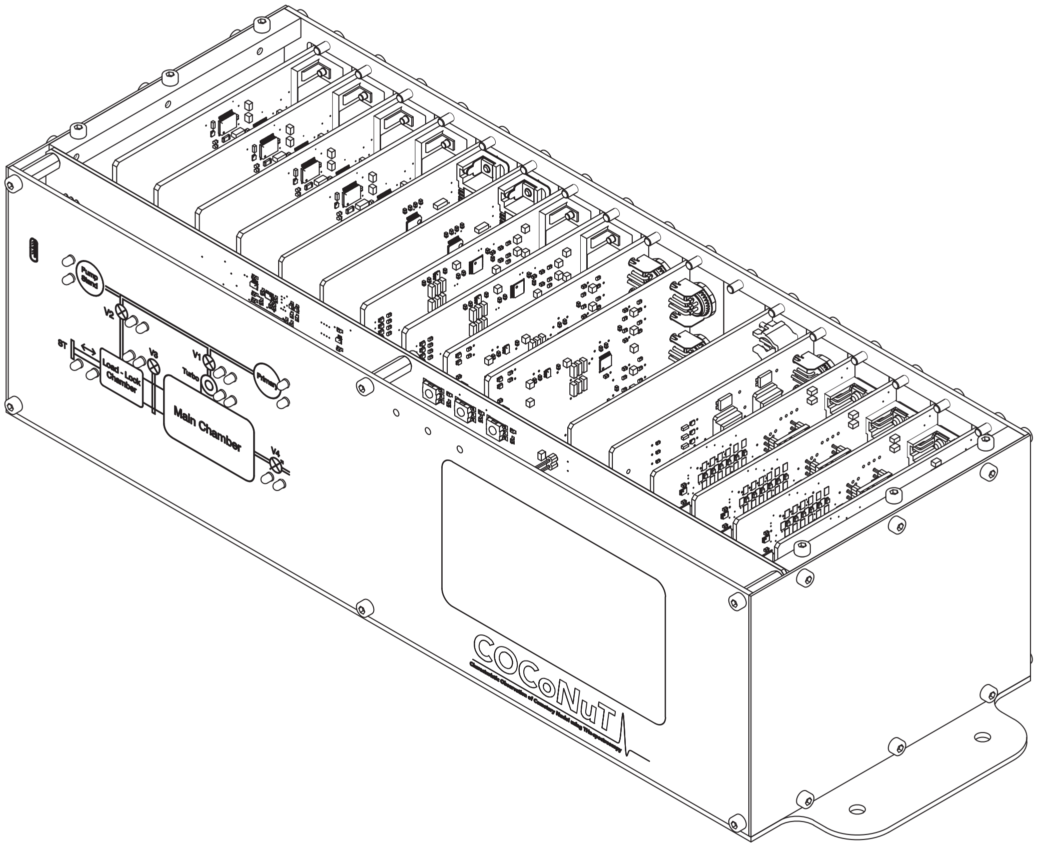
Pump Stand
V2
ST
V3
Load - Lock Chamber
V1
Turbo
Primary
Main Chamber
V4
COCoNuT

Figure C.2: The ELU consists of a large main PCB as a front panel to which many extension boards can be connected in the back using PCB finger connectors. This design is flexible and easily upgradable. The front panel also contains a vacuum display diagram and a touchscreen.

Name	**Description**
ELU Mainboard	Mainboard of the COCoNuT Electronics Unit (ELU), it is built around an STM32F405 microcontroller.
ELU Prototype	Prototype of the ELU mainboard, now full in use with another instrument.
Pressure Readout Board	Extension board to read out up to 3 Pfeiffer pressure gauges.
Valve Control Board	Extension board to control the valves of COCoNuT.
Serial Board	Extension board for RS-232/RS-485 Serial communication with other devices.
IO Board	Extension board for simple IO connections for COCoNuT.
Pfeiffer Pump IO Board	Prototype extension board to interface with Pfeiffer Vacuum pumps.
RTD Readout Board	Extension board to read out up to 4 PT100 or PT1000.
Diode Temperature Readout	Extension board to read out up to 4 diodes (Lakeshore or BAS16).
Stepper Motor Control Board	Extension board to control up to 2 stepper motors.
Servo Motor Control Board	Extension board to control up to 2 servo motors.
PWM Board	Extension board to generate up to 16 PWM signals.
Valve Display Board	Display board to indicate the states of the valves and pumps of COCoNuT.
Vacuum Gateway Unit	Mainboard of the vacuum compatible VGU to serve as a hub inside a vacuum chamber.
Vacuum Gateway Unit Expansion	Vacuum compatible expansion board of the VGU.
Pirani Sensor Mount	Vacuum compatible sensor mount for a Pirani pressure sensor.
”Schlittä Chef”	USB board to control up to 2 stepper motors and read out one thermocouple. Currently used by RAMSES/CHANCES for motor characterization.
Thermometry Arduino Board	Arduino expansion board for simple RTD and diode readout as well as SSR (Solid State Relais) control.
Thermometry Control Board	Full control board for simple RTD and diode readout as well as SSR (Solid State Relais) control.
Sensor Mount	Vacuum compatible temperature sensor mount for RTDs or diodes (Stöckli et al., 2024).

Table C.1: A description of the contribution in the electronics field.

Open Source Contributions

This work has resulted in contributions to multiple open source projects. An overview is provided in Table D.1. The contributions range from minor dependency updates, bug fixes and feature additions to the leading development role for repositories indicated with ”Owner”. Only projects are listed here that are categorized as **Open Source** as per the definition of the Open Source Initiative.

Project	Description	Language	Owner
THz Image Explorer	An interactive THz image explorer. [3]	Rust	X
Serial Monitor	An interactive cross-platform serial monitor and plotter. [1]	Rust	X
TeraFlash Control	An interactive cross-platform control software for the TeraFlash Pro THz spectrometer from Toptica. Reverse Engineered control protocol. [1]	Rust	X
`teraflash-ctrl-python`	A python library to control the TeraFlash Pro THz spectrometer from Toptica. Reverse Engineered control protocol. [1]	Python	X
THz TDS Database	A Django-based web application for managing and serving a database of THz time-domain spectra. [3]	Python	X
`stm32f4xx-hal`	Hardware abstraction layer for STM32F4 micro-controllers. [1]	Rust	
`ads122x04-rs`	Embedded driver for ADS122x04 ADCs. [1]	Rust	X
`mlx9061x-rs`	Embedded driver for MLX9061x IR thermopile. [1]	Rust	
`acs37800-rs`	Embedded driver for ACS37800 ADC. [1]	Rust	X
`tmc5160-rs`	Embedded driver for TMC5160 stepper motor controller. [1]	Rust	
egui	Immediate mode cross-platform GUI library for Rust. [3]	Rust	
`egui_double_slider`	A double slider widget for egui. [1,3]	Rust	X
`egui-file-dialog`	A file dialog for egui. [3]	Rust	
`egui-circular-progress-bar`	A circular progress bar widget for egui. [3]	Rust	X
`bevy_voxel_plot`	A voxel plot for the bevy engine. [3]	Rust	X
`ndarray-ndimage`	A crate for multidimensional image processing based on ndarrays. [3]	Rust	
`shift-register-driver`	An embedded shift register driver. [1]	Rust	
`dotthz-rs`	A library to interface with dotTHz files. [3]	Rust	X
`pydotthz`	A library to interface with dotTHz files. [3]	Python	X
`thzpy`	A library with tools to analyse THz time domain data. [4]	Python	
thz-deconvolution	THz deconvolution implementation in Python. [2]	Python	
HDF5QL	A QuickLook plugin for HDF5 files in macOS Finder. [3]	Swift	X
DotTHzQL	A QuickLook plugin for dotTHz files in macOS Finder. [3]	Swift	X

Table D.1: An overview of Open Source software contributions.

---

[1] In the scope of Chapter 2

[2] In the scope of Chapter 3

[3] In the scope of Chapter 4

[4] In the scope of Chapter 5

Internal Documentation

This work has resulted in various documents. Since they are only intended for internal use as user manuals or procedures, a small overview is available below in Table E.1.

Document	**Description**	**Figures**	**Pages**
IceLab SCITEAS2 Thermal Simulation, *SCITS1, 2022*	Simulation of the SCITEAS2 sample holder and shroud based on ANSYS simulations.	15	19
COCoNuT Sample Holder Thermal Analysis, *CNUT_SHTA01, 2023*	Design evaluation of the thermal components of COCoNuT based on ANSYS simulations.	18	19
COCoNuT Optical Design Evaluation, *CNUT_ODER01, 2023*	Design evaluation for the optical components of COCoNuT based on ANSYS Zemax simulations.	6	8
COCoNuT ELU Documentation, *CNUT_ELDOC, 2024*	Internal user manual of the COCoNuT Electronics Unit (ELU). The COCoNuT ELU performs temperature readout, pressure readout, motor, heating and pump as well as valve control.	11	29
Vacuum Gateway Unit Documentation, *VGU_DOC, 2024*	Internal user manual of the Vacuum Gateway Unit (VGU). The Vacuum Gateway Unit is used as a hub inside a vacuum chamber to read out sensors locally and relay the communication through a RS-232 to the outside.	6	17
COCoNuT Procedures, *CNUT_PROC, 2024*	Internal procedures for the COCoNuT setup.	1	10
COCoNuT Window Scan Report 01, *CNUT_WIN SCAN_REP_01, 2024*	Test report about simple sapphire, silicon and quartz window scans to document an anomaly.	12	11
COCoNuT Antenna Report 01, *CNUT_ATN_ REP_01, 2024*	Test report about an anomaly observed with the transmitter antenna. This report has been shared with the manufacturers and has led to the replacement of the transmitter antenna.	7	12
COCoNuT Beam-Splitter Evaluation, *CNUT_BSEVAL01, 2025*	Evaluation of a beam-splitter design based on ANSYS Zemax simulations.	6	3
COCoNuT Documentation, *CNUT_DOC, 2025*	Detailed internal documentation about the COCoNuT setup.	25	53

Table E.1: An overview of additional internal documents that have been prepared as part of this work.

Improvements in the Lab

Temperature Control

To dimension the thermal system of COCoNuT in the design phase, we have performed thermal simulations with Ansys® Mechanical and Airbus Systema Thermica. To verify these simulations, we have first set up simulations for the already existing SCITEAS2 (Simulation Chamber for Imaging the Temporal Evolution of Analogue Samples - Version 2.0) laboratory setup and verified them with measurements. These investigations have helped gaining a better understanding of the thermal behavior of both the COCoNuT and SCITEAS2 setup. Based on these insights, we have then developed accurate and low-cost temperature measurement techniques (further described in Appendix G) and PID controller based temperature control implementations for both setups. These updates have significantly increased the reliability, temperature range and stability during experiments. The above mentioned improvements have also been essential in the design process of the WEEVIL (Water Emission of Vapour from Ice in the Laboratory) setup.

Web-based Lab Journal

To keep track of the conducted experiments we have set up an internal web-based lab journal. This is based on the Django framework and can be accessed either via a web-browser or through an API (Application Programming Interface). The API access is especially useful for instruments to automatically push a new measurement entry when a measurement routine is started. Images, meta-data and comments can be added to a measurement entry. The path for the saved data and the link to Grafana for the measurement period is automatically added.

THz Database

To easily share THz TDS spectra between research groups and institutes, I have developed an open-source Django based database called THz TDS Database. User can upload dotTHz files containing a ”Sample” and a ”Reference” signal. The database then automatically calculates the refractive index and absorption coefficient and uploads the spectrum along with the metadata. If the user has supplied a valid name or chemical formula, an image will be pulled from Chemspider if available.

Remote Control

The ELU is connected to a computer that manages the network interface. COCoNuT uses a Raspberry Pi for this purpose. A Python script handles the housekeeping data logging to InfluxDB and runs the measurement script. It also hosts a TCP server to allow for remote control over an encrypted protocol. The encryption is based on the Advances Encryption

Standard (AES128). Every message is encrypted using a key (shared between host and client) and an IV (initialization vector) which is built from the TS (current timestamp) plus the RN (random number) as shown in Figure F.1. Every received IV is added to a nonce set, to prevent replay attacks. Since the IVs contain the timestamp, they can be removed from the set once they have expired (time validity is set to 10 seconds) to reduce the memory load.

<table>
<tr><td colspan="3">A multiple of 128-bits</td></tr>
<tr><td colspan="2">128 bits IV</td><td>128 bits payload</td></tr>
<tr><td>64 bits TS</td><td>64 bits RN</td><td>message (padded)</td></tr>
</table>

Figure F.1: The structure of an encrypted message packet. The initialization vector (IV) contains the current timestamp (TS) and a random number (RN). The message is padded to be a multiple of 128 bit as the AES-128 block size is 128 bits. If the message is longer than 128 bits, a second block is attached to the packet.

On the decryption side, the IV is tracked with a nonce set to make sure that every message can only be sent once. This prevents replay attacks. Since the IVs contain the timestamp, they can be removed from the set once they have expired (time validity is set to 10 seconds) to reduce the memory load. To authenticate the connection, the client must first transmit its own IP address, as shown in Figure F.2. This authentication with the IP address prevents relay attacks, where an attacker might intercept a message and transmit it to the host. This will lead to an IP address mismatch in the authentication sequence which will ultimately lead to a termination of the connection. The drawback of this protocol is that the key needs to be shared across all devices which poses a security risk.

This TCP server requires authentication upon connection, otherwise the server drops the connection after 10 seconds with a timeout error.

I implemented this TCP protocol in Python and additionally developed a Graphical User Interface (GUI) for more convenient use. This GUI is cross platform and runs on Linux, macOS, iOS, Android (untested) and Windows. A screenshot of the macOS application is shown in Figure F.3.

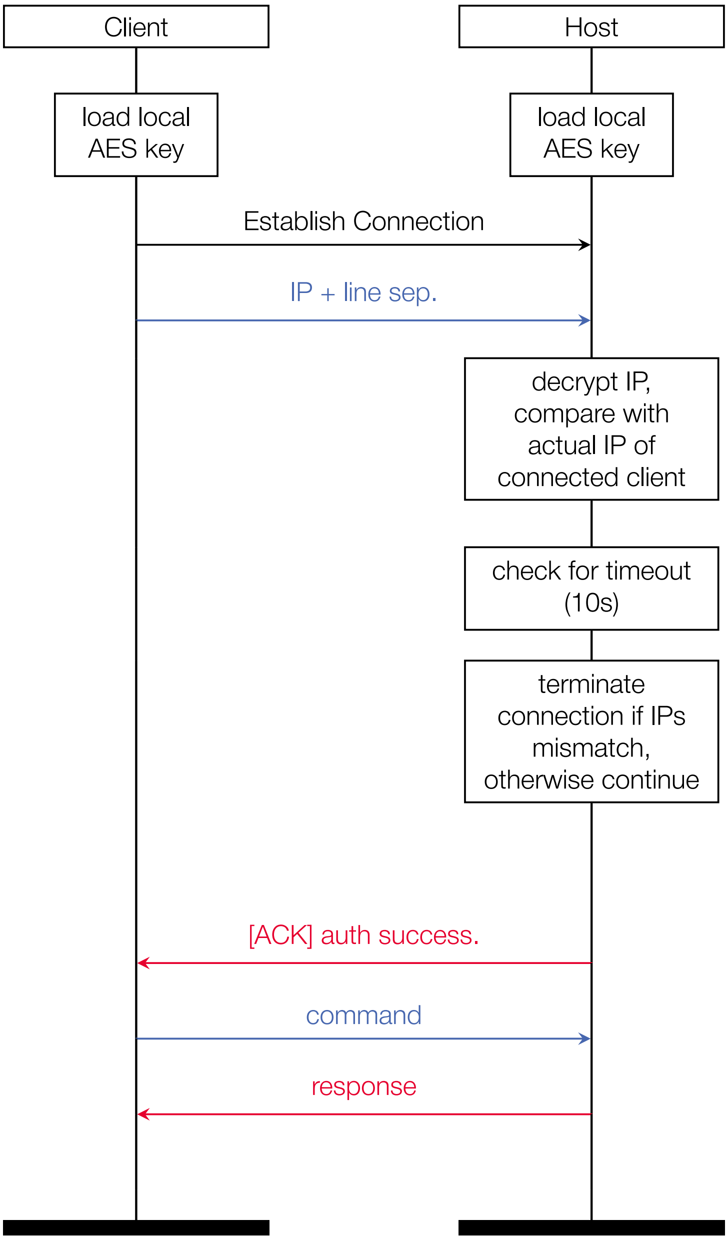
Client
Host
load local AES key
load local AES key
Establish Connection
IP + line sep.
decrypt IP, compare with actual IP of connected client
check for timeout (10s)
terminate connection if IPs mismatch, otherwise continue
[ACK] auth success.
command
response

Figure F.2: High-Level encrypted communication protocol between the client (user) and the host (TCP server running on the Raspberry Pi). Messages in blue are always encrypted, messages in red are not encrypted by default to save computational resources on the host side, but can also be encrypted for maximum security. The connection is left open until either side actively closes it.

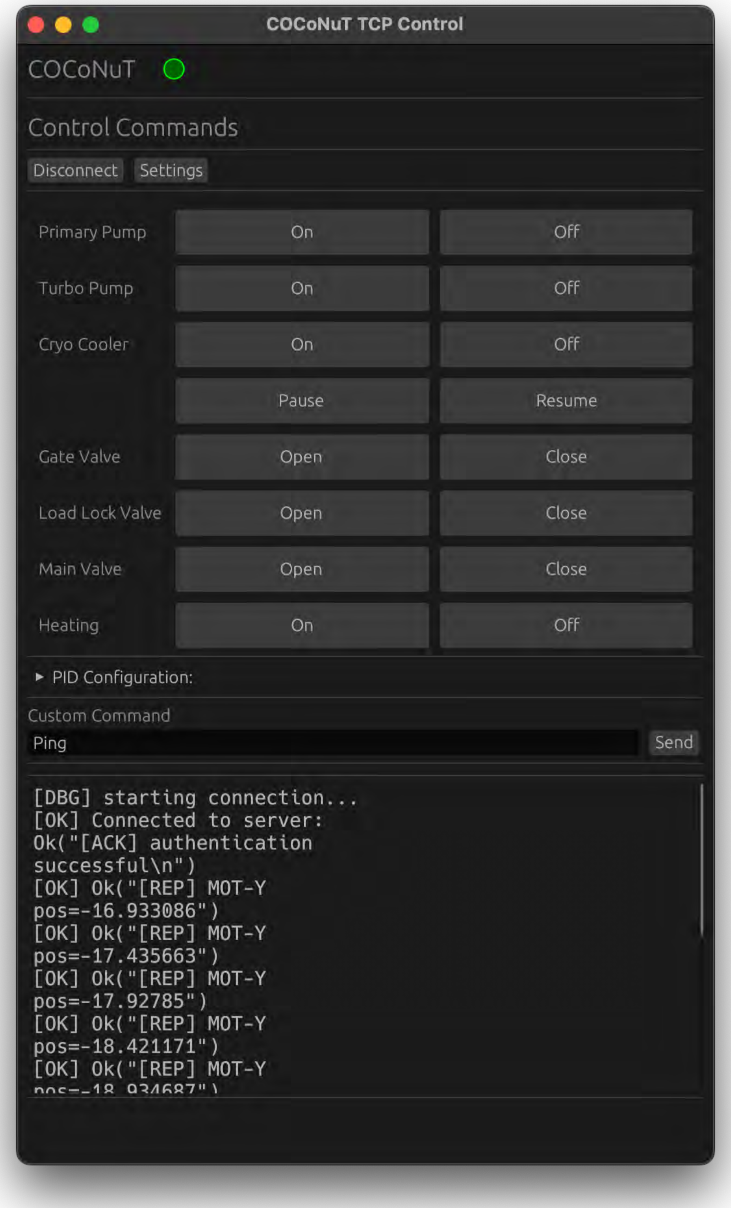
COCoNuT TCP Control
COCoNuT
Control Commands
Disconnect
Settings
Primary Pump
On
Off
Turbo Pump
On
Off
Cryo Cooler
On
Off
Pause
Resume
Gate Valve
Open
Close
Load Lock Valve
Open
Close
Main Valve
Open
Close
Heating
On
Off
▸ PID Configuration:
Custom Command
Send

Ping

```
[DBG] starting connection...
[OK] Connected to server:
Ok("[ACK] authentication
successful\n")
[OK] Ok("[REP] MOT-Y
pos=-16.933086")
[OK] Ok("[REP] MOT-Y
pos=-17.435663")
[OK] Ok("[REP] MOT-Y
pos=-17.92785")
[OK] Ok("[REP] MOT-Y
pos=-18.421171")
[OK] Ok("[REP] MOT-Y
pos=-18.934687")
```

Figure F.3: Screenshot of the COCoNuT remote control GUI. Certain controls have been mapped to buttons but there is a dedicated field for general commands that get relayed to the ELU.

Metal Substrate PCBs as Low-Cost, Robust Temperature Sensor Mounts for Cryogenic Thermometry

***Linus Leo Stöckli**, Rafael Ottersberg, Nicolas Thomas*

Published in *Engineering Research Express*, Vol. 6 (4): 046002, 2024
DOI: https://doi.org/10.1088/2631-8695/ad8ac0

Abstract:

Cryogenic experiments strongly depend on accurate temperature measurements. Many of the sensors used for these purposes are glued to the object to be measured to achieve adequate thermal contact. This calls for a more flexible, long lasting and robust bolt-mounted solution. Therefore, we present a low-cost (< 5$), compact, PCB (printed circuit board) based sensor mount for RTDs (resistance temperature detector) and diodes showing reliable results at temperatures from 50 K to 400 K with possible modifications for an extended range down below 20 K. We anticipate that the robustness and low cost of the reported sensor mount design will strongly enhance the accessibility of reliable temperature measurements at a wide range of temperatures in laboratory applications.

Introduction

Accurate temperature readings are of utmost importance in many laboratories. A temperature sensor usually consists of a Resistance Temperature Detector (RTD), a diode, or a thermocouple. An RTD can have either a positive (PTC) or a negative temperature coefficient (NTC). For both temperature measurements in the cryogenic regime and above 300 K, a platinum sensor is widely regarded as a sensible choice (Lebioda, 2015; Meyers, 1932). Platinum sensors are often marketed as Pt100, Pt500, or Pt1000, where the number corresponds to the resistance value in Ohms at 0 °C. Platinum has a positive temperature coefficient, and thus, excitation with a constant current is the most appropriate measurement setup to read the temperature. Similarly, a constant current can be applied to a silicon diode, and the temperature-dependent forward voltage can be read. A thermocouple relies on the temperature-dependent thermoelectric effect of the junction of two materials. To achieve an accurate measurement, the cables connecting the thermocouple to the readout device must be made of the same materials, which requires special feed-throughs when used in a vacuum chamber. We focus on RTDs and diodes as temperature sensors in this paper.

RTDs are relatively inexpensive and readily available from various manufacturers but are mostly produced in fragile packages with thin wires to reduce thermal flow from the connected cables. They must be glued to the object which needs to be measured. This can provide good thermal contact, but it is not guaranteed to be reproducible. The process is irreversible, as the sensors will likely break upon removal. Special diodes rated for use as cryogenic temperature sensors can be purchased in different packages from manufacturers such as Lake Shore Cryotronics, Inc. (Courts, 2002). They provide excellent thermal contact but are expensive and fragile as they are equipped with very thin leads as well. Lake Shore Cryotronics, Inc. also offers bolt-down Platinum temperature sensors in a similar price range.

Printed circuit boards (PCBs) are commonly used to connect electrical components with a good electrical, thermal, and structural bond. Circuit boards used in commercial applications usually use FR-4, a glass-reinforced epoxy laminate material, as a substrate since this is highly flame-resistant and an insulator (Daghighia et al., 2014). For applications requiring good heat dissipation, other base substrates such as aluminum (Huizhou Green Standard Optoelectronics Technology Co., Ltd., 2010) can be used. This option is readily available among manufacturers. Alternatively, copper substrate offers better heat dissipation but is more expensive and manufacturers currently only offer it in large quantities. Temperature sensors, such as diodes or platinum RTDs, also exist in surface mount device packages (SMD), which can be easily and reliably soldered onto a PCB. This suggests a simple assembly for compact temperature sensor mounts.

We present a relatively inexpensive bolt-down sensor mount that promises good thermal contact, flexibility and robustness. A representation of the assembled sensor mount is shown in Figure G.1.

Method

The sensor mount consists of a PCB with aluminum substrate material. The sensor was designed to be of similar size as the DT-670 BO package from Lake Shore Cryotronics, Inc. (Courts, 2002), due to the constraint of placing solder pads and traces, our sensor mount is wider but thinner. A copper thickness of 0.035 mm (corresponding to 1 oz copper weight) and an insulation layer composed of aluminum hydroxide and silica with a thickness of 0.1 mm and a thermal conductivity of 1 W K/m at room temperature have been selected

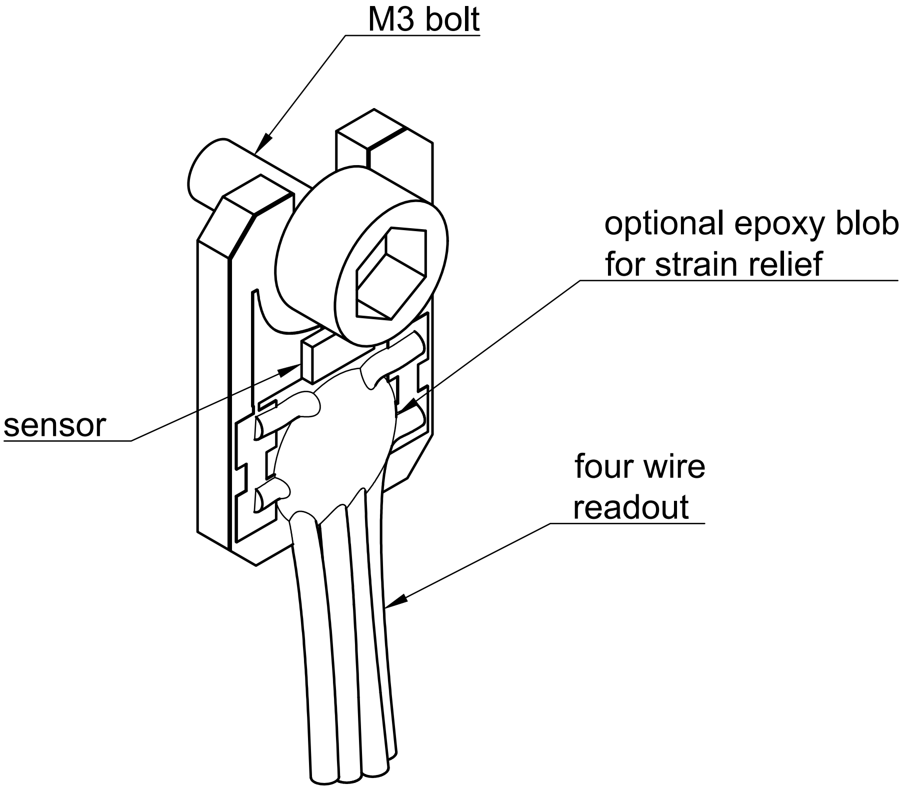

Figure G.1: General overview of the sensor mount with robust AWG24 wires attached and a bolt in place.

(JLCPCB, 2024). No solder mask was applied to prevent out-gassing and, therefore, make it Ultra-High-Vacuum (UHV) compatible. The thermal conductance in Equation G.1 is given by the ratio of heat flow $\dot{Q}(T)$ and temperature difference, ΔT. It can be derived from the definition of the thermal conductivity, $\kappa(T)$, and thus also depends on thickness, d, and area, A.

$$K(T) = \dot{Q}(T)/\Delta T \;=\; \kappa(T)\;/\;d\;\cdot A \tag{G.1}$$

This design aims to guide the thermal flow from the cables directly onto the sample and away from the sensor. Therefore, the thermal flow and, correspondingly, the thermal gradient between the sensor and the sample is minimized, which in turn decreases the systematic error of the measured temperature. This is a key goal in the design of this sensor mount. To reduce the thermal flow through the thermal paths connecting the solder pads of the wires and the sensor, the traces need to have a maximum length, d, and a minimum cross-section area, A, as seen in Equation G.1. The paths connecting the solder pads of the wires to the sink object (sample) need to have maximum cross-sectional area, A, with the thickness, d, set by the thickness of the insulation layer of the PCB. To provide an alternative to the fragile connections of commercial sensors, durable AWG24 wires will be soldered directly to the pads and can, for extra robustness, be epoxied to the sensor mount to provide better strain relief. We focus our work on a robust design that works reliably in thermal equilibrium. We do not characterize the sensor mount's dynamic properties.

Since the temperature-dependent thermal properties of copper, aluminum and epoxy are

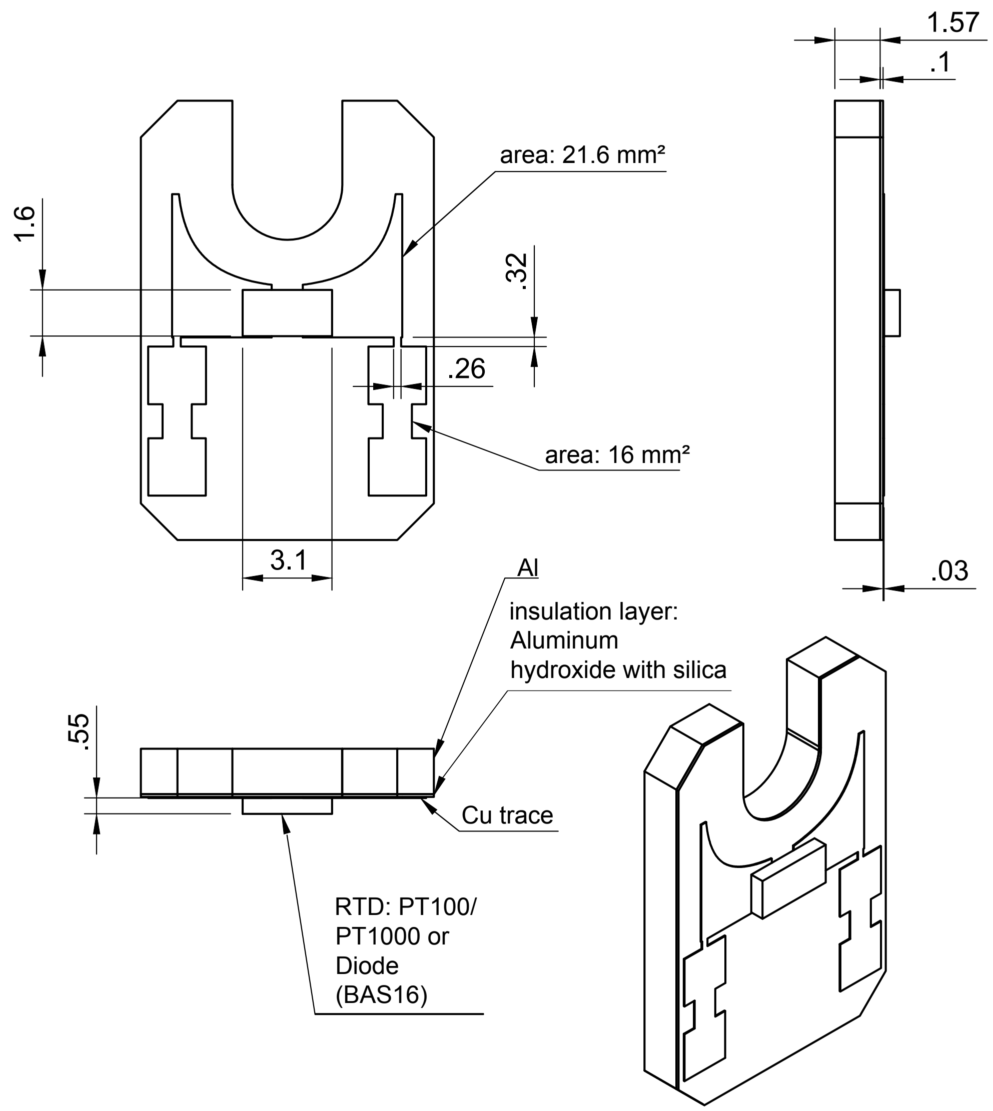
1.57
.1
area: 21.6 mm²
1.6
.32
.26
area: 16 mm²
3.1
Al
.03
insulation layer:
Aluminum
hydroxide with silica
.55
Cu trace
RTD: PT100/
PT1000 or
Diode
(BAS16)

Figure G.2: Drawing of the sensor mount PCB showing the dimensions of the traces and layer thickness. Units are given in [mm].

Width	Length	Height	Mass
10.16 mm	4 mm	2.12 mm	8 g

Table G.1: Specifications of the sensor mount, including the sensor, but without cables.

well documented (Bradley & Radebaugh, 2013; Verma et al., 2017), we performed steady-state simulations with Ansys Mechanical (Ansys®, 2018) for AWG24 copper wires with length of 100 mm. The temperature gradient is shown in Figure G.3. From the simulation, we can see that about 1 W flows through the cables (assuming that the sample is at 23.15 K and the cables are connected to an object at 300 K). Only about 5% flows into the sensor, the rest is directed onto the sample. The simulation has been run for different sample temperatures, which shows the systematic offset we can expect on the sensor as shown in Figure G.4. This simulation shows that while our design is as compact as connecting the wires directly to a sensor without additional external thermal grounding, it still provides excellent results

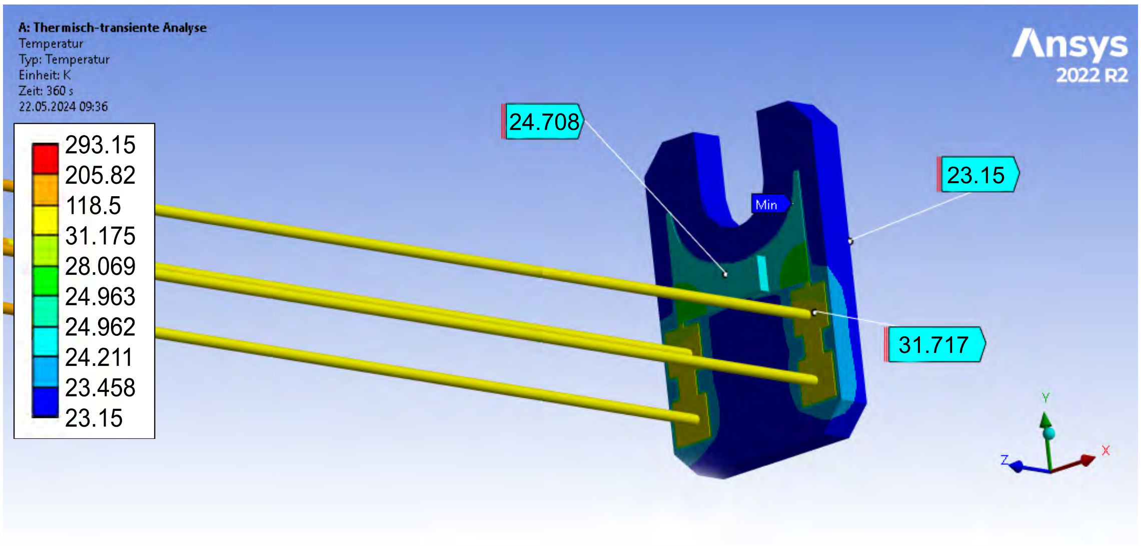
A: Thermisch-transiente Analyse
Temperatur
Typ: Temperatur
Einheit: K
Zeit: 360 s
22.05.2024 09:36
293.15
205.82
118.5
31.175
28.069
24.963
24.962
24.211
23.458
23.15
24.708
Min
23.15
31.717
Ansys
2022 R2
Y
Z
X

Figure G.3: A Thermal simulation run with Ansys Mechanical. The sensor is connected to a sink object (sample) with fixed temperature of 23.15 K. Four simplified AWG24 wires with length of 100 mm are connected to the solder pads and the other end is at a fixed temperature of 300 K. To simplify the simulation, radiation has not been considered.

down to $T = 50\,\mathrm{K}$, with a slight systematic error around $T = 20\,\mathrm{K}$.

The radiation onto the sensor, with the assumptions given in Table G.2, is given in Equation G.2 by the black body radiation (Kreith & Bohn, 2001), assuming that the sensor is a true black body to obtain an upper limit.

$$P_{\text{rad}} = \sigma\, A_{\text{rad}} \cdot (T^4_{\text{amb}} - T^4_{\text{sensor}}) = 2.2\,\text{mW} \tag{G.2}$$

A_{rad}	T_{amb}	T_{sensor}
50 mm^2	298 K	23.15 K

Table G.2: Parameters to calculate the black body radiation of the environment onto the sensor.

By dividing the radiative power input by the minimum thermal conductance $K = 0.04\,\text{W/K}$ of the sensor mount (at 20 K), we measured in Figure G.6, we can estimate an induced temperature change in Equation G.3

$$\Delta T_{\text{rad}} = \frac{P_{\text{rad}}}{K} = 0.055\,\text{K} \tag{G.3}$$

This provides an upper limit to the temperature increase on the sensor, assuming an ideal black body.

Results

For the characterisation of the thermal properties at different temperatures, we used a Pt1000 in a 1206 SMD package from Vishay (Beyschlag, 2024). Two sensor mounts were attached

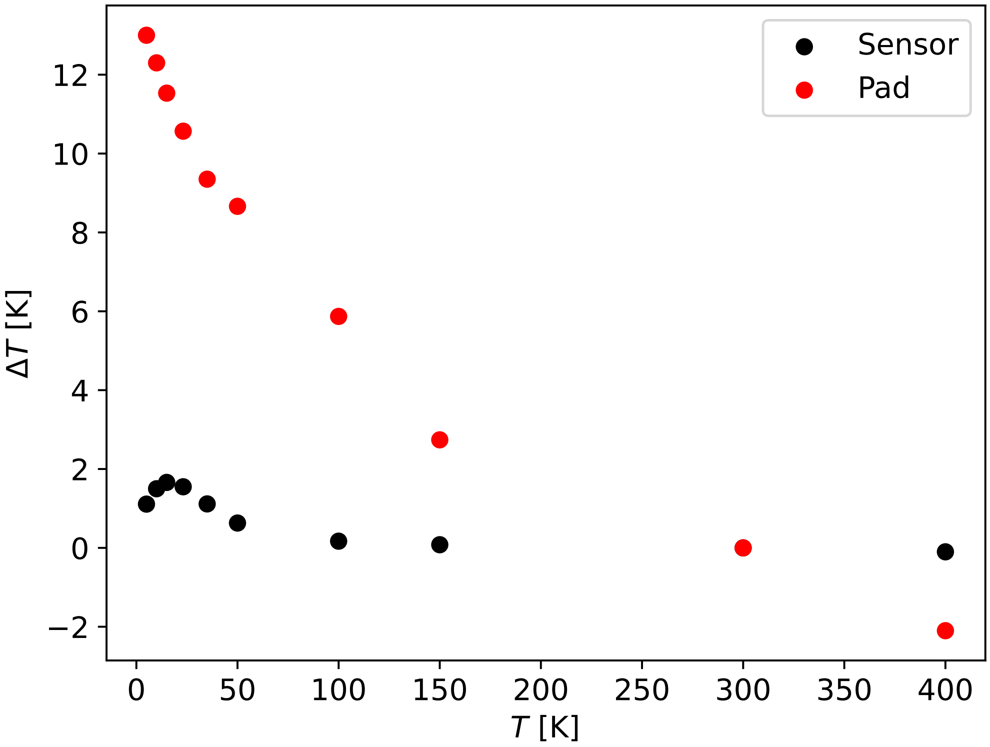

Figure G.4: Simulations run for multiple object temperatures with the temperature offset of the cable pads and the sensor. Four AWG24 copper wires with a length of 100 mm and connected to ambient temperature of 300 K were simulated. The large increase in the offset of the sensor at around $T = 20$ K is mainly caused by the increased thermal conductivity of copper at these temperatures (Bradley & Radebaugh, 2013).

to a copper adapter, which was connected to a cryo-cooler in a vacuum chamber as depicted in Figure G.5. The vacuum pressures ranged from 1×10^{-6} mbar to 1×10^{-5} mbar throughout the tests. One sensor is actively and continuously heated by using a high excitation current (7.5 mA), while the other measures the reference temperature of the copper body with a standard short current pulses (0.1 mA). The high excitation current will result in a temperature difference $\Delta T = T_{\text{excited}} - T_{\text{ref}}$ which can then be used to determine the thermal conductance K using Equation G.4.

$$K \; = \; P \; / \; \Delta T \; = \; R \, I^2 \; / \; \Delta T \tag{G.4}$$

This allows us to characterize the thermal contact between the reference sink copper body and the temperature sensor attached to the sensor mount. A Keithley Model 2450 (Keithley, 2013) was used to supply the heating current and read the resistance of the heated RTD. A Keithley DMM7510 (Keithley, 2024) read out the reference temperature sensor.

We compared the measurement of our sensor mount with a Pt1000 (standard two-lead wire package) epoxied to a copper block with silver epoxy EPO-TEK H20E (EPO-TEK, 2021). The sensor mount with the high excitation current was replaced with the epoxied Pt1000. The results taken at different temperatures are presented in Figure G.6 and show that our sensor mount has comparable thermal conductance K as the Pt1000 glued with silver epoxy.

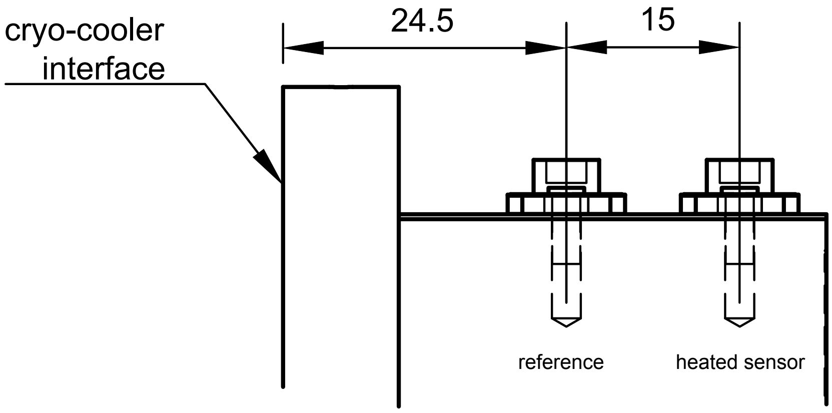

Figure G.5: Side-view of the setup with two sensors screwed down on a copper adapter which is attached to a cryo-cooler. During the measurements the cryo-cooler was turned off, such that the copper block can be assumed to be in thermal equilibrium with no temperature gradient across. Units are given in mm.

Further measurements have been conducted to compare the measured temperature of Pt1000, Pt100 and BAS16 temperature sensors and the measured temperature of a reference Lake Shore Cryotronics, Inc. DT-670 silicon diode (Courts, 2002). A Pt1000 epoxied to the sensor block is also included. The results shown in Figure G.7 confirm the temperature offset obtained from the simulations in Figure G.4 and show reproducible measurements across different sensor mounts with different sensors mounted on.

Conclusion

We have shown the feasibility of aluminum substrate PCBs as low-cost, robust temperature sensor mounts for cryogenic temperatures. The presented sensor mount shows comparable thermal conductance (as shown in Figure G.6) to an epoxied RTD sensor, but with the advantage of flexible bolt-down mounting, more robustness and being more compact as there is no need for thermal grounding of the incoming wires. Durable AWG24 stranded wires can be used, which are more durable than the solid wires attached to commercial sensor packages. The measured temperatures lie within the tolerance bands of the RTD sensors with a slight systematic error of 1 K - 2 K around temperatures of 20 K as shown in Figure G.7.

This sensor mount has been tested with SMD 1206 Pt100, SMD 1206 Pt1000 (Beyschlag, 2024) and SMD SOD123 BAS16 silicon diodes (Rijpma & Ter Brake, 2006) and the temperature measurements remain in the specified tolerance bands.

While commercial sensors along with the attached cables can also be epoxied to an object, this is less compact and only serves as a permanent solution, as the sensor is likely to be damaged upon removal.

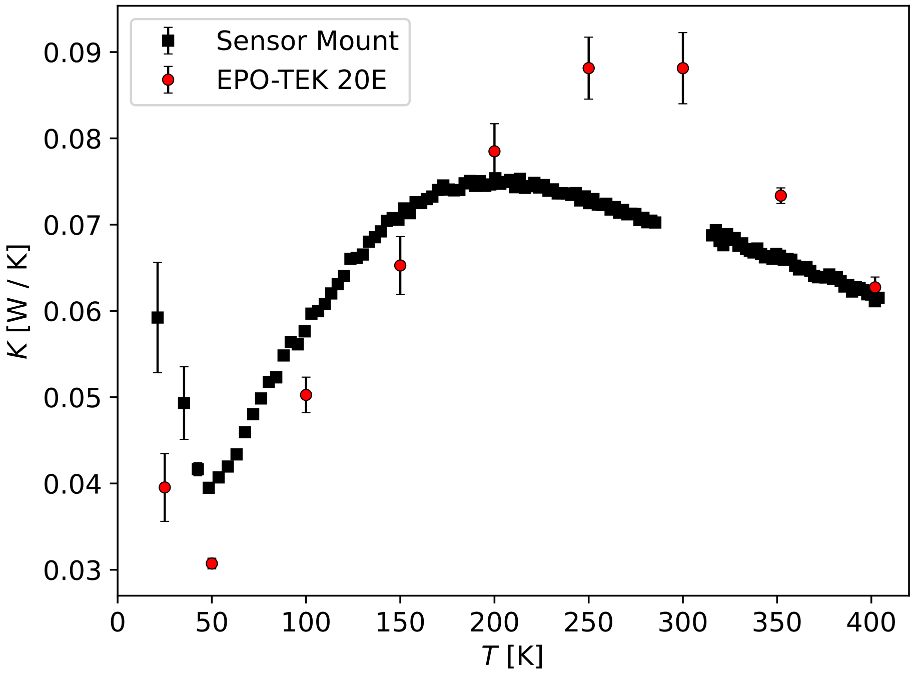

Figure G.6: Thermal contact of a Pt1000 on our sensor mount compared to an epoxied Pt1000 with EPO-TEK H20E. It is important to note that we observe the net thermal conductance which is composed of all different materials (Pt, Cu, Insulator, Al_2O_3) and not the characteristic curve of one single material. The measurements were averaged over four runs.

We thus conclude that the thermal conductance of our sample holder design is sufficient for temperatures in the range of 50 K up to 400 K. The requirements of robustness, mounting flexibility and low cost have been fulfilled. This poses an excellent, low-cost and longer lasting alternative to expensive, fragile commercial products for applications in thermal equilibrium. Concerning reaction time, the sensor mount cannot compete with the much more expensive Lake Shore Cryotronics, Inc. diode, where the silicon wafer has improved thermal contact with the base, allowing for increased responsiveness in dynamic applications.

Outlook

The incoming heat from the wires to the sensor can further be decreased by increasing the length of the connected signal trace between the cable pads and the sensor pads. A possible future iteration is illustrated in Figure G.8. The improved design would decrease the systematic error at temperatures around 20 K.

Acknowledgment

This work was supported through a MARVIS programme of the Swiss Department for Business, Education, and Research (SBFI) called SUBICE. SUBICE is a project of the University of Bern, the University of Applied Sciences and Arts, Western Switzerland (HES-SO), and Thales-Alenia Space Switzerland (TASCH). The contribution of RO has been carried

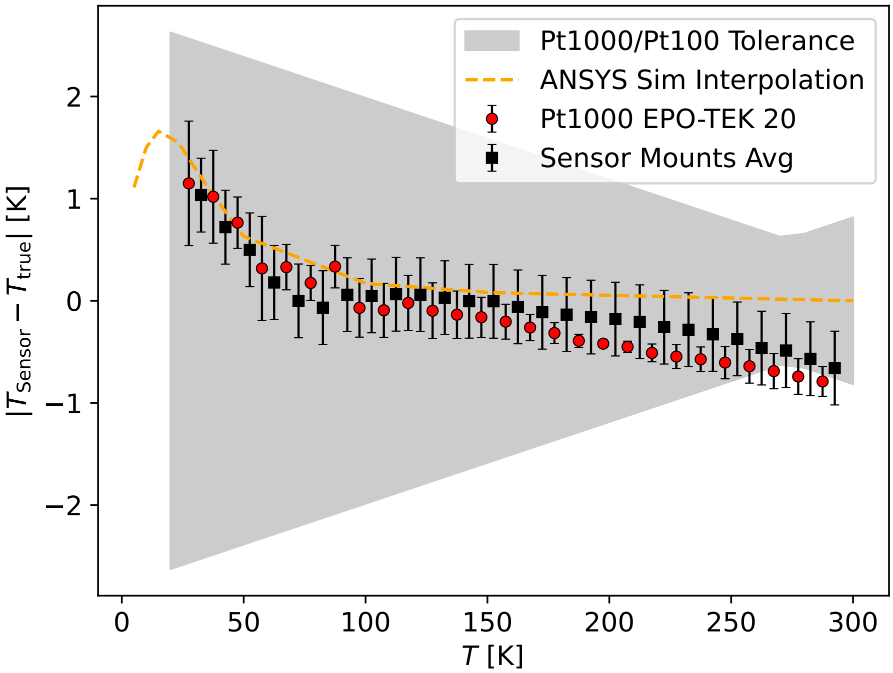

Figure G.7: The Difference of the measured temperature to that of the reference Lake Shore Cryotronics, Inc. DT-670 silicon diode. The Average was taken for four Pt1000 and Pt100 sensors and two thermal cycles each. The result show reproducible and comparable results to a Pt1000 epoxied with EPO-TEK 20 and the cables taped down with aluminum tape for thermal grounding. The thermal grounding with aluminum tape was not required for our sensor mounts. Durable AWG24 wires were used. The simulation discussed in the previous section agrees with the measurements taken.

out within the framework of the NCCR PlanetS supported by the Swiss National Science Foundation under grants 51NF40-182901 and 51NF40-205606.

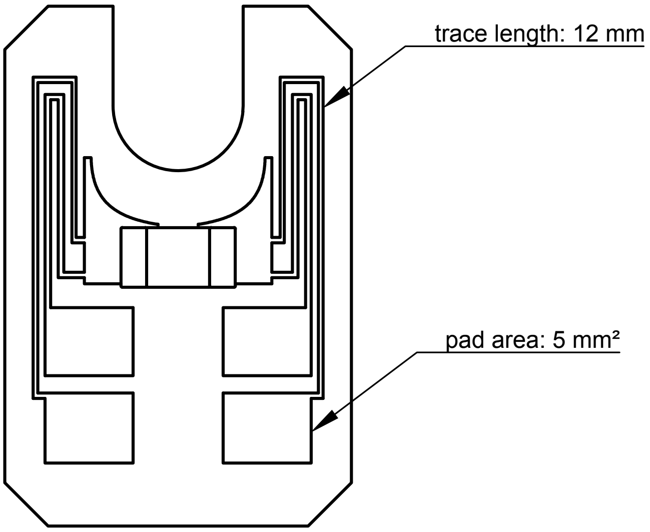
trace length: 12 mm
pad area: 5 mm²

Figure G.8: An adapted design with longer signal traces to decrease further the amount of heat flowing from the wire-pads to the sensor. The four-wire readout is extended up to the pads where the sensor is mounted.

Title Page Design

The title page features a comet aligned towards the center of a Fibonacci spiral, with its tail extending along a second Fibonacci spiral. The accompanying text is arranged according to the golden ratio of the page, while the sun is placed at a distance of 1 page height unit extended from the bottom. The design of the title page is shown in Figure H.1.

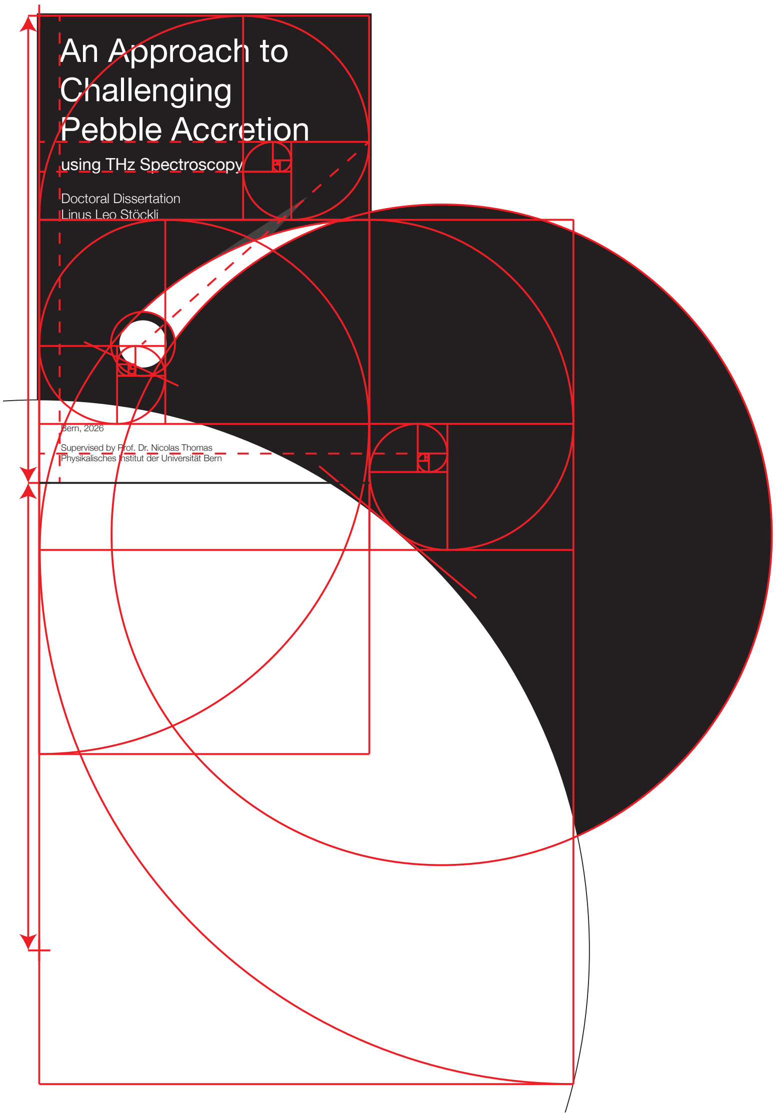
An Approach to
Challenging
Pebble Accretion
using THz Spectroscopy
Doctoral Dissertation
Linus Leo Stöckli
Bern, 2026
Supervised by Prof. Dr. Nicolas Thomas
Physikalisches Institut der Universität Bern

Figure H.1: The design of the title page is based around the Fibonacci spiral. It depicts a comet, with its two tails, approaching the Sun.

Bibliography

A'Hearn, M. F., Belton, M. J. S., Delamere, W. A., Kissel, J., Klaasen, K. P., McFadden, L. A., Meech, K. J., Melosh, H. J., Schultz, P. H., Sunshine, J. M., Thomas, P. C., Veverka, J., Yeomans, D. K., Baca, M. W., Busko, I., Crockett, C. J., Collins, S. M., Desnoyer, M., Eberhardy, C. A., … White, R. L. (2005). Deep Impact: Excavating Comet Tempel 1. *Science*, *310*(5746), 258–264. https://doi.org/10.1126/science.1118923

A'Hearn, M. F., Belton, M. J. S., Delamere, W. A., Feaga, L. M., Hampton, D., Kissel, J., Klaasen, K. P., McFadden, L. A., Meech, K. J., Melosh, H. J., Schultz, P. H., Sunshine, J. M., Thomas, P. C., Veverka, J., Wellnitz, D. D., Yeomans, D. K., Besse, S., Bodewits, D., Bowling, T. J., … Williams, J. L. (2011). EPOXI at Comet Hartley 2. *Science*, *332*(6036), 1396–1400. https://doi.org/10.1126/science.1204054

Ahi, K., Shahbazmohamadi, S., & Asadizanjani, N. (2018). Quality control and authentication of packaged integrated circuits using enhanced-spatial-resolution terahertz time-domain spectroscopy and imaging. *Optics and Lasers in Engineering*, *104*, 274–284. https://doi.org/10.1016/j.optlaseng.2017.07.007

Airbus. (2021). Systema Thermica V4.9.1.

Alibert, Y., Mordasini, C., Benz, W., & Winisdoerffer, C. (2005). Models of giant planet formation with migration and disc evolution. *Astronomy & Astrophysics*, *434*(1), 343–353. https://doi.org/10.1051/0004-6361:20042032

Altieri, F., Frigeri, A., Lavagna, M., Le Gall, A., Yuryevich Nikiforov, S., Stoker, C., Ciarletti, V., Cristina De Sanctis, M., Josset, J.-L., Mitrofanov, I., Sefton-Nash, E., & Vago, J. L. (2023). Investigating the Oxia Planum subsurface with the ExoMars rover and drill. *Advances in Space Research*, *71*(11), 4895–4903. https://doi.org/10.1016/j.asr.2023.01.044

Altwegg, K., Balsiger, H., Bar-Nun, A., Berthelier, J. J., Bieler, A., Bochsler, P., Briois, C., Calmonte, U., Combi, M., De Keyser, J., Eberhardt, P., Fiethe, B., Fuselier, S., Gasc, S., Gombosi, T. I., Hansen, K., Hässig, M., Jäckel, A., Kopp, E., … Wurz, P. (2015). 67P/Churyumov-Gerasimenko, a Jupiter family comet with a high D/H ratio. *Science*, *347*(6220), 1261952. https://doi.org/10.1126/science.1261952

Altwegg, K., Balsiger, H., Bar-Nun, A., Berthelier, J.-J., Bieler, A., Bochsler, P., Briois, C., Calmonte, U., Combi, M. R., Cottin, H., De Keyser, J., Dhooghe, F., Fiethe, B., Fuselier, S. A., Gasc, S., Gombosi, T. I., Hansen, K. C., Haessig, M., Jäckel, A., … Wurz, P. (2016). Prebiotic chemicals—amino acid and phosphorus—in the coma of comet 67P/Churyumov-Gerasimenko. *Science Advances*, *2*(5), e1600285. https://doi.org/10.1126/sciadv.1600285

Andrews, S. M., Huang, J., Pérez, L. M., Isella, A., Dullemond, C. P., Kurtovic, N. T., Guzmán, V. V., Carpenter, J. M., Wilner, D. J., Zhang, S., Zhu, Z., Birnstiel, T., Bai, X.-N., Benisty, M., Hughes, A. M., Öberg, K. I., & Ricci, L. (2018). The Disk Substructures at High Angular Resolution Project (DSHARP). I. Motivation, Sample, Calibration, and Overview. *The Astrophysical Journal Letters*, *869*(2), L41. https://doi.org/10.3847/2041-8213/aaf741

Ansys®. (2018). Mechanical, Release 18.1.

Ansys®. (2019). Zemax OpticStudio 19.4.

Armitage, P. J. (2020). *Astrophysics of planet formation, Second Edition* (2nd ed.). Cambridge University Press.

Barbin, Y., Kofman, W., Nielsen, E., Hagfors, T., Seu, R., Picardi, G., & Svedhem, H. (1999). The CONSERT instrument for the ROSETTA mission. *Advances in Space Research*, *24*(9), 1115–1126. https://doi.org/10.1016/S0273-1177(99)80205-1

Bardyn, A., Baklouti, D., Cottin, H., Fray, N., Briois, C., Paquette, J., Stenzel, O., Engrand, C., Fischer, H., Hornung, K., Isnard, R., Langevin, Y., Lehto, H., Le Roy, L., Ligier, N., Merouane, S., Modica, P., Orthous-Daunay, F.-R., Rynö, J., … Hilchenbach, M. (2017). Carbon-rich dust in comet 67P/Churyumov-Gerasimenko measured by COSIMA/Rosetta. *Monthly Notices of the Royal Astronomical Society*, *469*(Suppl_2), S712–S722. https://doi.org/10.1093/mnras/stx2640

Barry, R. (2023). FreeRTOS. https://www.freertos.org/index.html

Beard, M. C., Turner, G. M., & Schmuttenmaer, C. A. (2002). Terahertz Spectroscopy. *The Journal of Physical Chemistry B*, *106*(29), 7146–7159. https://doi.org/10.1021/jp020579i

Besl, P. J., & McKay, N. D. (1992). A method for registration of 3-D shapes. *IEEE Transactions on Pattern Analysis and Machine Intelligence*, *14*(2), 239–256. https://doi.org/10.1109/34.121791

Bevy Contributors. (2025, May). Bevy Engine. https://github.com/bevyengine/bevy/releases/tag/v0.16.1

Beyschlag, V. (2024). Temperature dependent Platinum thin film chip resistor (RTD).

Biermann, L. F., & Lüst, R. (1958). The Tails of Comets. *Scientific American*, *199*(4), 44–51. Retrieved September 30, 2025, from http://www.jstor.org/stable/24944791

Binzel, R. P. (2004). *Comets II* (M. C. Festou, H. U. Keller, & H. A. Weaver, Eds.). University of Arizona Press. https://doi.org/10.2307/j.ctv1v7zdq5

Blum, J., Bischoff, D., & Gundlach, B. (2022). Formation of Comets. *Universe*, *8*(7), 381. https://doi.org/10.3390/universe8070381

Blum, J., Gundlach, B., Krause, M., Fulle, M., Johansen, A., Agarwal, J., Von Borstel, I., Shi, X., Hu, X., Bentley, M. S., Capaccioni, F., Colangeli, L., Della Corte, V., Fougere, N., Green, S. F., Ivanovski, S., Mannel, T., Merouane, S., Migliorini, A., … Snodgrass, C. (2017). Evidence for the formation of comet 67P/Churyumov-Gerasimenko through gravitational collapse of a bound clump of pebbles. *Monthly Notices of the Royal Astronomical Society*, *469*(Suppl_2), S755–S773. https://doi.org/10.1093/mnras/stx2741

Blum, J., & Wurm, G. (2008). The Growth Mechanisms of Macroscopic Bodies in Protoplanetary Disks. *Annual Review of Astronomy and Astrophysics*, *46*(1), 21–56. https://doi.org/10.1146/annurev.astro.46.060407.145152

Boehnhardt, H., Bibring, J.-P., Apathy, I., Auster, H. U., Ercoli Finzi, A., Goesmann, F., Klingelhöfer, G., Knapmeyer, M., Kofman, W., Krüger, H., Mottola, S., Schmidt, W., Seidensticker, K., Spohn, T., & Wright, I. (2017). The Philae lander mission and science overview. *Philosophical Transactions of the Royal Society A: Mathematical, Physical and Engineering Sciences*, *375*(2097), 20160248. https://doi.org/10.1098/rsta.2016.0248

Bond, P. (2020). *Rosetta: The Remarkable Story of Europe's Comet Explorer*. Springer International Publishing. https://doi.org/10.1007/978-3-030-60720-3

Bouchard, J., Eichmann, S. L., Ow, H., Poitzsch, M., & Petkie, D. T. (2022). Terahertz imaging for non-destructive porosity measurements of carbonate rocks. *Scientific Reports*, *12*(1), 18018. https://doi.org/10.1038/s41598-022-22535-z

Bradley, P. E., & Radebaugh, R. (2013). ***Properties of selected materials at cryogenic temperatures***. CRC Press, Boca Raton, FL. https://tsapps.nist.gov/publication/get_pdf.cfm?pub_id=913059

Brandt, J. C., Niedner, M. B., & Rosenvinge, T. v. (1985). The ICE project. ***Advances in Space Research***, ***5***(12), 3–16. https://doi.org/10.1016/0273-1177(85)90062-6

Britt, D. T., Cannon, K. M., Donaldson Hanna, K., Hogancamp, J., Poch, O., Beck, P., Martin, D., Escrig, J., Bonal, L., & Metzger, P. T. (2019). Simulated asteroid materials based on carbonaceous chondrite mineralogies. ***Meteoritics & Planetary Science***, ***54***(9), 2067–2082. https://doi.org/10.1111/maps.13345

Brownlee, D., Tsou, P., Aléon, J., Alexander, C. M. O., Araki, T., Bajt, S., Baratta, G. A., Bastien, R., Bland, P., Bleuet, P., Borg, J., Bradley, J. P., Brearley, A., Brenker, F., Brennan, S., Bridges, J. C., Browning, N. D., Brucato, J. R., Bullock, E., … Zolensky, M. (2006). Comet 81P/Wild 2 Under a Microscope. ***Science***, ***314***(5806), 1711–1716. https://doi.org/10.1126/science.1135840

Brügger, N., Burn, R., Coleman, G. A. L., Alibert, Y., & Benz, W. (2020). Pebbles versus planetesimals: The outcomes of population synthesis models. ***Astronomy & Astrophysics***, ***640***, A21. https://doi.org/10.1051/0004-6361/202038042

Burford, N. M., & El-Shenawee, M. O. (2017). Review of terahertz photoconductive antenna technology. ***Optical Engineering***, ***56***(1), 010901. https://doi.org/10.1117/1.OE.56.1.010901

Busch, S., Probst, T., Schwerdtfeger, M., Dietz, R., Palací, J., & Koch, M. (2014). Terahertz transceiver concept. ***Optics Express***, ***22***(14), 16841. https://doi.org/10.1364/OE.22.016841

Chambers, J. (2001). Making More Terrestrial Planets. ***Icarus***, ***152***(2), 205–224. https://doi.org/10.1006/icar.2001.6639

Chen, Y., Huang, S., & Pickwell-MacPherson, E. (2010). Frequency-wavelet domain deconvolution for terahertz reflection imaging and spectroscopy. ***Opt. Express***, ***18***(2), 1177–1190. https://doi.org/10.1364/OE.18.001177

Chopra, N., & Lloyd-Hughes, J. (2023). Optimum Optical Designs for Diffraction-Limited Terahertz Spectroscopy and Imaging Systems Using Off-Axis Parabolic Mirrors. ***Journal of Infrared, Millimeter, and Terahertz Waves***, ***44***(11-12), 981–997. https://doi.org/10.1007/s10762-023-00949-8

Choukroun, M., Altwegg, K., Kührt, E., Biver, N., Bockelée-Morvan, D., Drążkowska, J., Hérique, A., Hilchenbach, M., Marschall, R., Pätzold, M., Taylor, M. G. G. T., & Thomas, N. (2020). Dust-to-Gas and Refractory-to-Ice Mass Ratios of Comet 67P/Churyumov-Gerasimenko from Rosetta Observations. ***Space Science Reviews***, ***216***(3), 44. https://doi.org/10.1007/s11214-020-00662-1

Ciarniello, M., Fulle, M., Raponi, A., Filacchione, G., Capaccioni, F., Rotundi, A., Rinaldi, G., Formisano, M., Magni, G., Tosi, F., De Sanctis, M. C., Capria, M. T., Longobardo, A., Beck, P., Fornasier, S., Kappel, D., Mennella, V., Mottola, S., Rousseau, B., & Arnold, G. (2022). Macro and micro structures of pebble-made cometary nuclei reconciled by seasonal evolution. ***Nature Astronomy***, ***6***(5), 546–553. https://doi.org/10.1038/s41550-022-01625-y

Courts, S. S. (2002). A new cryogenic diode thermometer. ***AIP Conference Proceedings***, ***613***, 1620–1627. https://doi.org/10.1063/1.1472198

Crété-Roffet, F., Dolmière, T., Ladret, P., & Nicolas, M. (2007). The Blur Effect: Perception and Estimation with a New No-Reference Perceptual Blur Metric. ***Human Vision and Electronic Imaging***, ***12***. https://doi.org/10.1117/12.702790

Cui, H., Zhang, X., Su, J., Yang, Y., Fang, Q., & Wei, X. (2015). Vibration–rotation absorption spectrum of water vapor molecular in frequency selector at 0.5–2.5 THz range. ***Optik***, ***126***(23), 3533–3537. https://doi.org/10.1016/j.ijleo.2015.08.066

Daghighia, H. M., Bir, S. C., & Babel, G. D. (2014). ***Hybrid printed circuit board construction*** (US20150289368A1). Sunnyvale, CA, USA.

Dai, J., Zhang, J., Zhang, W., & Grischkowsky, D. (2004). Terahertz time-domain spectroscopy characterization of the far-infrared absorption and index of refraction of high-resistivity, float-zone silicon. ***Journal of the Optical Society of America B***, ***21***(7), 1379. https://doi.org/10.1364/JOSAB.21.001379

Davidsson, B. J. R., Sierks, H., Güttler, C., Marzari, F., Pajola, M., Rickman, H., A'Hearn, M. F., Auger, A.-T., El-Maarry, M. R., Fornasier, S., Gutiérrez, P. J., Keller, H. U., Massironi, M., Snodgrass, C., Vincent, J.-B., Barbieri, C., Lamy, P. L., Rodrigo, R., Koschny, D., … Tubiana, C. (2016). The primordial nucleus of comet 67P/Churyumov-Gerasimenko. ***Astronomy & Astrophysics***, ***592***, A63. https://doi.org/10.1051/0004-6361/201526968

De Araújo, M. A., Silva, R., De Lima, E., Pereira, D. P., & De Oliveira, P. C. (2009). Measurement of Gaussian laser beam radius using the knife-edge technique: Improvement on data analysis. ***Applied Optics***, ***48***(2), 393. https://doi.org/10.1364/AO.48.000393

De Niem, D., Kührt, E., Hviid, S., & Davidsson, B. (2018). Low velocity collisions of porous planetesimals in the early solar system. ***Icarus***, ***301***, 196–218. https://doi.org/10.1016/j.icarus.2017.09.024

Demion, A., Stöckli, L. L., Thomas, N., & Zahno, S. (2025). Frequency-Dependent Deconvolution for Enhanced THz-TDS Scans: Accounting for Beam Width Variations in Time Traces. ***IEEE Transactions on Terahertz Science and Technology***, ***15***(3), 505–513. https://doi.org/10.1109/TTHZ.2025.3546756

Department of Defense. (1959). Military Standard, Photographic Lenses. [MIL-STD-150A].

Dhillon, S. S., Vitiello, M. S., Linfield, E. H., Davies, A. G., Hoffmann, M. C., Booske, J., Paoloni, C., Gensch, M., Weightman, P., Williams, G. P., Castro-Camus, E., Cumming, D. R. S., Simoens, F., Escorcia-Carranza, I., Grant, J., Lucyszyn, S., Kuwata-Gonokami, M., Konishi, K., Koch, M., … Johnston, M. B. (2017). The 2017 terahertz science and technology roadmap. ***Journal of Physics D: Applied Physics***, ***50***(4), 043001. https://doi.org/10.1088/1361-6463/50/4/043001

Ding, S.-H., Li, Q., Yao, R., & Wang, Q. (2010). High-resolution terahertz reflective imaging and image restoration. ***Appl. Opt.***, ***49***(36), 6834–6839. https://doi.org/10.1364/AO.49.006834

Domingues, A., Martínez-Carboneres, A., & Carlson, S. (2025). Evaluation of 3D-printed plastics for Ultra-High Vacuum applications: Outgassing, and residual gas analysis. ***Vacuum***, ***233***, 113970. https://doi.org/10.1016/j.vacuum.2024.113970

Drs, J., Modsching, N., Paradis, C., Kränkel, C., Wittwer, V., Razskazovskaya, O., & Südmeyer, T. (2019). Optical rectification of ultrafast Yb lasers: Pushing power and bandwidth of terahertz generation in GaP. ***Journal of the Optical Society of America B***, ***36***, 3039. https://doi.org/10.1364/JOSAB.36.003039

Duchêne, G., Ménard, F., Stapelfeldt, K. R., Villenave, M., Wolff, S. G., Perrin, M. D., Pinte, C., Tazaki, R., & Padgett, D. L. (2024). JWST Imaging of Edge-on Protoplanetary Disks. I. Fully Vertically Mixed 10 μm Grains in the Outer Regions of a 1000 au Disk. ***The Astronomical Journal***, ***167***(2), 77. https://doi.org/10.3847/1538-3881/acf9a7

Duncan, M. (2009). Re-viewing an Old Comet Reservoir. ***Science***, ***325***(5945), 1211–1212. https://doi.org/10.1126/science.1177312

Duncan, M. J., & Levison, H. F. (1997). A Disk of Scattered Icy Objects and the Origin of Jupiter-Family Comets. ***Science***, ***276***(5319), 1670–1672. https://doi.org/10.1126/science.276.5319.1670

El-Maarry, M. R., Groussin, O., Keller, H. U., Thomas, N., Vincent, J.-B., Mottola, S., Pajola, M., Otto, K., Herny, C., & Krasilnikov, S. (2019). Surface Morphology of Comets and Associated Evolutionary Processes: A Review of Rosetta's Observations of 67P/Churyumov–Gerasimenko. ***Space Science Reviews***, ***215***(4), 36. https://doi.org/10.1007/s11214-019-0602-1

Engrand, C., Lasue, J., Wooden, D. H., & Zolensky, M. E. (2024). Chemical and physical properties of cometary dust. In ***Comets III*** (pp. 577–620). University of Arizona Press. Retrieved May 29, 2024, from http://www.jstor.org/stable/jj.21819446.24

EPO-TEK. (2021). EPO-TEK® H20E.

Feng, Z., Qiu, H., Wang, D., Zhang, C., Sun, S., Jin, B., & Tan, W. (2021). Spintronic terahertz emitter. ***Journal of Applied Physics***, ***129***(1), 010901. https://doi.org/10.1063/5.0037937

Fernández, J. A. (2008). Origin of Comet Nuclei and Dynamics. ***Space Science Reviews***, ***138***(1-4), 27–42. https://doi.org/10.1007/s11214-007-9274-3

Filacchione, G., Groussin, O., Herny, C., Kappel, D., Mottola, S., Oklay, N., Pommerol, A., Wright, I., Yoldi, Z., Ciarniello, M., Moroz, L., & Raponi, A. (2019). Comet 67P/CG Nucleus Composition and Comparison to Other Comets. ***Space Science Reviews***, ***215***(1), 19. https://doi.org/10.1007/s11214-019-0580-3

Fletcher, L. N., Cavalié, T., Grassi, D., Hueso, R., Lara, L. M., Kaspi, Y., Galanti, E., Greathouse, T. K., Molyneux, P. M., Galand, M., Vallat, C., Witasse, O., Lorente, R., Hartogh, P., Poulet, F., Langevin, Y., Palumbo, P., Gladstone, G. R., Retherford, K. D., … Costa, M. (2023). Jupiter Science Enabled by ESA's Jupiter Icy Moons Explorer. ***Space Science Reviews***, ***219***(7), 53. https://doi.org/10.1007/s11214-023-00996-6

Fulle, M., Della Corte, V., Rotundi, A., Rietmeijer, F. J. M., Green, S. F., Weissman, P., Accolla, M., Colangeli, L., Ferrari, M., Ivanovski, S., Lopez-Moreno, J. J., Epifani, E. M., Morales, R., Ortiz, J. L., Palomba, E., Palumbo, P., Rodriguez, J., Sordini, R., & Zakharov, V. (2016). Comet 67P/Churyumov–Gerasimenko preserved the pebbles that formed planetesimals. ***Monthly Notices of the Royal Astronomical Society***, ***462***(Suppl_1), S132–S137. https://doi.org/10.1093/mnras/stw2299

Garg, D., Bandyopadhyay, A., & Sengupta, A. (2022). Critical spectroscopic considerations towards reliable detection of material using terahertz time-domain spectroscopy. ***Spectrochimica Acta Part A: Molecular and Biomolecular Spectroscopy***, ***268***, 120632. https://doi.org/10.1016/j.saa.2021.120632

Giuliano, B. M., Gavdush, A. A., Müller, B., Zaytsev, K. I., Grassi, T., Ivlev, A. V., Palumbo, M. E., Baratta, G. A., Scirè, C., Komandin, G. A., Yurchenko, S. O., & Caselli, P. (2019). Broadband spectroscopy of astrophysical ice analogues: I. Direct measurement of the complex refractive index of CO ice using terahertz time-domain spectroscopy. ***Astronomy & Astrophysics***, ***629***, A112. https://doi.org/10.1051/0004-6361/201935619

Gladman, B. (2005). The Kuiper Belt and the Solar System's Comet Disk. ***Science***, ***307***(5706), 71–75. https://doi.org/10.1126/science.1100553

Glassmeier, K.-H., Boehnhardt, H., Koschny, D., Kührt, E., & Richter, I. (2007). The Rosetta Mission: Flying Towards the Origin of the Solar System. ***Space Science Reviews***, ***128***(1-4), 1–21. https://doi.org/10.1007/s11214-006-9140-8

Glavin, D. P., Dworkin, J. P., & Sandford, S. A. (2008). Detection of cometary amines in samples returned by Stardust. ***Meteoritics & Planetary Science***, ***43***(1-2), 399–413. https://doi.org/10.1111/j.1945-5100.2008.tb00629.x

Gombosi, T. I., & Houpis, H. L. F. (1986). An icy-glue model of cometary nuclei. ***Nature***, ***324***(6092), 43–44. https://doi.org/10.1038/324043a0

Gomez-Sepulveda, A. M., Hernandez-Serrano, A. I., Radpour, R., Koch-Dandolo, C. L., Rojas-Landeros, S. C., Ascencio-Rojas, L. F., Zarate, A., Hernandez, G., Gonzalez-Tirado, R. C., Insaurralde-Caballero, M., & Castro-Camus, E. (2017). History of Mexican Easel Paintings from an Altarpiece Revealed by Non-invasive Terahertz Time-Domain Imaging. ***Journal of Infrared, Millimeter, and Terahertz Waves***, ***38***(4), 403–412. https://doi.org/10.1007/s10762-016-0346-x

Gueckstock, O., Stojanovic, N., Ha, Y., Hagelschuer, T., Denker, A., Kourkafas, G., Seifert, T. S., Kampfrath, T., & Gensch, M. (2024). Radiation hardness of ultrabroadband spintronic terahertz emitters: En-route to a space-qualified terahertz time-domain gas spectrometer. ***Applied Physics Letters***, ***124***(14), 141103. https://doi.org/10.1063/5.0196951

Guillet, J. P., Recur, B., Frederique, L., Bousquet, B., Canioni, L., Manek-Hönninger, I., Desbarats, P., & Mounaix, P. (2014). Review of Terahertz Tomography Techniques. ***Journal of Infrared, Millimeter, and Terahertz Waves***, ***35***(4), 382–411. https://doi.org/10.1007/s10762-014-0057-0

Gulkis, S., Frerking, M., Crovisier, J., Beaudin, G., Hartogh, P., Encrenaz, P., Koch, T., Kahn, C., Salinas, Y., Nowicki, R., Irigoyen, R., Janssen, M., Stek, P., Hofstadter, M., Allen, M., Backus, C., Kamp, L., Jarchow, C., Steinmetz, E., … Spilker, T. (2007). MIRO: Microwave Instrument for Rosetta Orbiter. ***Space Science Reviews***, ***128***(1-4), 561–597. https://doi.org/10.1007/s11214-006-9032-y

Hamran, S.-E., Paige, D. A., Allwood, A., Amundsen, H. E. F., Berger, T., Brovoll, S., Carter, L., Casademont, T. M., Damsgård, L., Dypvik, H., Eide, S., Fairén, A. G., Ghent, R., Kohler, J., Mellon, M. T., Nunes, D. C., Plettemeier, D., Russell, P., Siegler, M., & Øyan, M. J. (2022). Ground penetrating radar observations of subsurface structures in the floor of Jezero crater, Mars. ***Science Advances***, ***8***(34), eabp8564. https://doi.org/10.1126/sciadv.abp8564

Harker, D. E., Wooden, D. H., Kelley, M. S. P., & Woodward, C. E. (2023). Dust Properties of Comets Observed by Spitzer. ***The Planetary Science Journal***, ***4***(12), 242. https://doi.org/10.3847/PSJ/ad0382

Herique, A., Kofman, W., Zine, S., Blum, J., Vincent, J.-B., & Ciarletti, V. (2019). Homogeneity of 67P/Churyumov-Gerasimenko as seen by CONSERT: Implication on composition and formation. ***Astronomy & Astrophysics***, ***630***, A6. https://doi.org/10.1051/0004-6361/201834865

Herrmann, M., & Sakai, K. (2000). Objects in powders detected and imaged with THz radiation. ***Conference on Lasers and Electro-Optics (CLEO 2000). Technical Digest. Postconference Edition. TOPS Vol.39 (IEEE Cat. No.00CH37088)***, 479. https://doi.org/10.1109/CLEO.2000.907279

Heshmat, B., Andrews, G. M., Naranjo-Montoya, O. A., Castro-Camus, E., Ciceri, D., Sanchez, A. R., Allanore, A., Kmetz, A. A., Eichmann, S. L., Poitzsch, M. E., & Raskar, R. (2017). Terahertz scattering and water absorption for porosimetry. ***Optics Express***, ***25***(22), 27370. https://doi.org/10.1364/OE.25.027370

Hsieh, H. H., & Jewitt, D. (2006). A Population of Comets in the Main Asteroid Belt. ***Science***, ***312***(5773), 561–563. https://doi.org/10.1126/science.1125150

Hu, J., Xu, Z., Li, M., He, Y., Sun, X., & Liu, Y. (2021). Detection of Foreign-Body in Milk Powder Processing Based on Terahertz Imaging and Spectrum. ***Journal of Infrared,*** *Millimeter, and Terahertz Waves*, *42*(8), 878–892. https://doi.org/10.1007/s10762-021-00802-w

Huizhou Green Standard Optoelectronics Technology Co., Ltd. (2010). *Aluminium base copper-clad plate* (CN201947540U) [CN201947540U].

Ioppolo, S., McGuire, B. A., Allodi, M. A., & Blake, G. A. (2014). THz and mid-IR spectroscopy of interstellar ice analogs: Methyl and carboxylic acid groups. *Faraday Discuss.*, *168*, 461–484. https://doi.org/10.1039/C3FD00154G

Jepsen, P. U. (2019). Phase Retrieval in Terahertz Time-Domain Measurements: A "how to" Tutorial. *Journal of Infrared, Millimeter, and Terahertz Waves*, *40*(4), 395–411. https://doi.org/10.1007/s10762-019-00578-0

Jewitt, D. (2005). A First Look at the Damocloids. *The Astronomical Journal*, *129*(1), 530–538. https://doi.org/10.1086/426328

Jewitt, D., & Hsieh, H. H. (2024). The Asteroid-Comet Continuum. In *Comets III* (pp. 767–798). University of Arizona Press. Retrieved September 19, 2025, from http://www.jstor.org/stable/jj.21819446.29

Jiang, H., & Ormel, C. W. (2022). Efficient planet formation by pebble accretion in ALMA rings. *Monthly Notices of the Royal Astronomical Society*, *518*(3), 3877–3900. https://doi.org/10.1093/mnras/stac3275

Jiang, H., Mei, H., Bian, X., Li, L., Wang, L., & Wang, L. (2021). Detection of Double-layer Air Gap Defects Based on Terahertz Imaging Method. *2021 IEEE International Instrumentation and Measurement Technology Conference (I2MTC)*, 1–5. https://doi.org/10.1109/I2MTC50364.2021.9459793

Jin, Y.-S., Kim, G.-J., Jeon, S.-G., Shon, C.-H., & Jung, S.-S. (2006). Experimental Measurement of the 3D Spatio-Temporal Profile of a Pulsed Terahertz Wave. *Journal of the Korean Physical Society*, *48*(4), 603–606.

JLCPCB. (2024). JLCPCB Capabilities. https://jlcpcb.com/capabilities/pcb-capabilities

Johansen, A., Blum, J., Tanaka, H., Ormel, C., Bizzarro, M., & Rickman, H. (2014). The Multifaceted Planetesimal Formation Process. In *Protostars and Planets VI*. University of Arizona Press. https://doi.org/10.2458/azu_uapress_9780816531240-ch024

Johansen, A., Oishi, J. S., Low, M.-M. M., Klahr, H., Henning, T., & Youdin, A. (2007). Rapid planetesimal formation in turbulent circumstellar disks. *Nature*, *448*(7157), 1022–1025. https://doi.org/10.1038/nature06086

Jones, G. H., Snodgrass, C., Tubiana, C., Küppers, M., Kawakita, H., Lara, L. M., Agarwal, J., André, N., Attree, N., Auster, U., Bagnulo, S., Bannister, M., Beth, A., Bowles, N., Coates, A., Colangeli, L., Corral van Damme, C., Da Deppo, V., De Keyser, J., … Ji, H. (2024). The Comet Interceptor Mission. *Space Science Reviews*, *220*(1), 9. https://doi.org/10.1007/s11214-023-01035-0

Jutzi, M., Benz, W., Toliou, A., Morbidelli, A., & Brasser, R. (2017). How primordial is the structure of comet 67P?: Combined collisional and dynamical models suggest a late formation. *Astronomy & Astrophysics*, *597*, A61. https://doi.org/10.1051/0004-6361/201628963

Kaluza, M., Walczakowski, M., & Siemion, A. (2024). Exploring the Impact of 3D Printing Parameters on the THz Optical Characteristics of COC Material. *Materials*, *17*(20), 5104. https://doi.org/10.3390/ma17205104

Kanda, N., Konishi, K., Nemoto, N., Midorikawa, K., & Kuwata-Gonokami, M. (2017). Real-time broadband terahertz spectroscopic imaging by using a high-sensitivity terahertz camera. *Scientific Reports*, *7*(1), 42540. https://doi.org/10.1038/srep42540

Karpowicz, N., Zhong, H., Xu, J., Lin, K.-I., Hwang, J.-S., & Zhang, X.-C. (2005). Comparison between pulsed terahertz time-domain imaging and continuous wave terahertz imaging. *Semiconductor Science and Technology*, *20*(7), S293–S299. https://doi.org/10.1088/0268-1242/20/7/021

Kataoka, A., Tanaka, H., Okuzumi, S., & Wada, K. (2013). Fluffy dust forms icy planetesimals by static compression. *Astronomy & Astrophysics*, *557*, L4. https://doi.org/10.1051/0004-6361/201322151

Keithley. (2013). Keithley Model 2450 Datasheet.

Keithley. (2024). Keithley DMM7510 Datasheet.

Keller, H. U., Arpigny, C., Barbieri, C., Bonnet, R. M., Cazes, S., Coradini, M., Cosmovici, C. B., Delamere, W. A., Huebner, W. F., Hughes, D. W., Jamar, C., Malaise, D., Reitsema, H. J., Schmidt, H. U., Schmidt, W. K. H., Seige, P., Whipple, F. L., & Wilhelm, K. (1986). First Halley Multicolour Camera imaging results from Giotto. *Nature*, *321*(S6067), 320–326. https://doi.org/10.1038/321320a0

Keller, H. U., Barbieri, C., Lamy, P., Rickman, H., Rodrigo, R., Wenzel, K.-P., Sierks, H., A'Hearn, M. F., Angrilli, F., Angulo, M., Bailey, M. E., Barthol, P., Barucci, M. A., Bertaux, J.-L., Bianchini, G., Boit, J.-L., Brown, V., Burns, J. A., Büttner, I., … Zaccariotto, M. (2007). OSIRIS – The Scientific Camera System Onboard Rosetta. *Space Science Reviews*, *128*(1-4), 433–506. https://doi.org/10.1007/s11214-006-9128-4

Koch, M., Mittleman, D. M., Ornik, J., & Castro-Camus, E. (2023). Terahertz time-domain spectroscopy. *Nature Reviews Methods Primers*, *3*(1), 48. https://doi.org/10.1038/s43586-023-00232-z

Koch-Dandolo, C. L., Filtenborg, T., Fukunaga, K., Skou-Hansen, J., & Jepsen, P. U. (2015). Reflection terahertz time-domain imaging for analysis of an 18th century neoclassical easel painting. *Applied Optics*, *54*(16), 5123–5123. https://doi.org/10.1364/ao.54.005123

Kofman, W., Herique, A., Barbin, Y., Barriot, J.-P., Ciarletti, V., Clifford, S., Edenhofer, P., Elachi, C., Eyraud, C., Goutail, J.-P., Heggy, E., Jorda, L., Lasue, J., Levasseur-Regourd, A.-C., Nielsen, E., Pasquero, P., Preusker, F., Puget, P., Plettemeier, D., … Van Zyl, J. (2015). Properties of the 67P/Churyumov-Gerasimenko interior revealed by CONSERT radar. *Science*, *349*(6247), aab0639. https://doi.org/10.1126/science.aab0639

Kofman, W., Zine, S., Herique, A., Rogez, Y., Jorda, L., & Levasseur-Regourd, A.-C. (2020). The interior of Comet 67P/C–G; revisiting CONSERT results with the exact position of the Philae lander. *Monthly Notices of the Royal Astronomical Society*, *497*(3), 2616–2622. https://doi.org/10.1093/mnras/staa2001

Kohlhaas, R. B., Nellen, S., Liebermeister, L., Breuer, S., & Globisch, B. (2018). Monolithically Integrated THz Transceiver for 1550 nm Excitation [Journal Abbreviation: CLEO_SI]. *Conference on Lasers and Electro-Optics*, STu3D.5. https://doi.org/10.1364/CLEO_SI.2018.STu3D.5

Kreith, F., & Bohn, M. (2001). *Principles of Heat Transfer* (6th ed.). Brooks/Cole Pub.

Kretke, K. A., & Levison, H. F. (2014). CHALLENGES IN FORMING THE SOLAR SYSTEM'S GIANT PLANET CORES VIA PEBBLE ACCRETION. *The Astronomical Journal*, *148*(6), 109. https://doi.org/10.1088/0004-6256/148/6/109

Kretke, K., & Levison, H. (2015). Evidence for pebbles in comets. *Icarus*, *262*, 9–13. https://doi.org/10.1016/j.icarus.2015.08.017

Kreuzig, C., Kargl, G., Pommerol, A., Knollenberg, J., Lethuillier, A., Molinski, N. S., Gilke, T., Bischoff, D., Feller, C., Kührt, E., Sierks, H., Hänni, N., Capelo, H., Güttler, C., Haack, D., Otto, K., Kaufmann, E., Schweighart, M., Macher, W., … Blum, J. (2021). The CoPhyLab comet-simulation chamber. *Review of Scientific Instruments*, *92*(11), 115102. https://doi.org/10.1063/5.0057030

Kubiczek, T., Kolpatzeck, K., Schultze, T., & Balzer, J. C. (2024). A Highly Frequency-Selective 3D-Printed Dielectric Structure for the Terahertz Range. *Journal of Infrared, Millimeter, and Terahertz Waves*, *45*(3-4), 322–336. https://doi.org/10.1007/s10762-024-00973-2

Lambrechts, M., & Johansen, A. (2012). Rapid growth of gas-giant cores by pebble accretion. *Astronomy & Astrophysics*, *544*, A32. https://doi.org/10.1051/0004-6361/201219127

Lambrechts, M., & Johansen, A. (2014). Forming the cores of giant planets from the radial pebble flux in protoplanetary discs. *Astronomy & Astrophysics*, *572*, A107. https://doi.org/10.1051/0004-6361/201424343

Lebioda, M. (2015). Dynamic properties of cryogenic temperature sensors. *Przegląd Elektrotechniczny*, *1*(2), 227–229. https://doi.org/10.15199/48.2015.02.51

Lecar, M., Podolak, M., Sasselov, D., & Chiang, E. (2006). On the Location of the Snow Line in a Protoplanetary Disk. *The Astrophysical Journal*, *640*(2), 1115–1118. https://doi.org/10.1086/500287

Lee, J., Leung, C. K., Ma, M., Ward-Berry, J., Santitewagun, S., & Zeitler, J. A. (2023). The dotTHz Project: A Standard Data Format for Terahertz Time-Domain Data. *Journal of Infrared, Millimeter, and Terahertz Waves*, *44*(11-12), 795–813. https://doi.org/10.1007/s10762-023-00947-w

Leitenstorfer, A., Moskalenko, A. S., Kampfrath, T., Kono, J., Castro-Camus, E., Peng, K., Qureshi, N., Turchinovich, D., Tanaka, K., Markelz, A. G., Havenith, M., Hough, C., Joyce, H. J., Padilla, W. J., Zhou, B., Kim, K.-Y., Zhang, X.-C., Jepsen, P. U., Dhillon, S., … Cunningham, J. (2023). The 2023 terahertz science and technology roadmap. *Journal of Physics D: Applied Physics*, *56*(22), 223001. https://doi.org/10.1088/1361-6463/acbe4c

Lethuillier, A., Feller, C., Kaufmann, E., Becerra, P., Hänni, N., Diethelm, R., Kreuzig, C., Gundlach, B., Blum, J., Pommerol, A., Kargl, G., Kührt, E., Capelo, H., Haack, D., Zhang, X., Knollenberg, J., Molinski, N. S., Gilke, T., Sierks, H., … Jäggi, N. (2022). Cometary dust analogues for physics experiments. *Monthly Notices of the Royal Astronomical Society*, *515*(3), 3420–3438. https://doi.org/10.1093/mnras/stac1734

Leung, C. K., Ward-Berry, J. N., Wanvig I Dot, E., Lee, J., & Zeitler, J. A. (2025). Tutorial: Accurate Determination of Refractive Index and Absorption Coefficient in Terahertz Time-Domain Spectroscopy. *Journal of Infrared, Millimeter, and Terahertz Waves*, *46*(9), 59. https://doi.org/10.1007/s10762-025-01070-8

Levasseur-Regourd, A. C., Mukai, T., Lasue, J., & Okada, Y. (2007). Physical properties of cometary and interplanetary dust. *Planetary and Space Science*, *55*(9), 1010–1020. https://doi.org/10.1016/j.pss.2006.11.014

Li, M. (2001). Measurement of the dielectric constant of thin films using goniometric time-domain spectroscopy [ISSN: 0094243X]. *AIP Conference Proceedings*, *550*, 392–396. https://doi.org/10.1063/1.1354430

Li, X., Danell, R. M., Pinnick, V. T., Grubisic, A., Van Amerom, F., Arevalo, R. D., Getty, S. A., Brinckerhoff, W. B., Southard, A. E., Gonnsen, Z. D., & Adachi, T. (2017). Mars Organic Molecule Analyzer (MOMA) laser desorption/ionization source design and performance characterization. *International Journal of Mass Spectrometry*, *422*, 177–187. https://doi.org/10.1016/j.ijms.2017.03.010

Liebendorfer, A. (2020). New deconvoluting algorithm offers new approach for mass spectrometry data compression. *Scilight*, *2020*(1), 011103. https://doi.org/10.1063/10.0000540

Ljubenovic, M., Artesani, A., Bonetti, S., & Traviglia, A. (2022). Beam-Shape Effects and Noise Removal From THz Time-Domain Images in Reflection Geometry in the 0.25–6 THz Range. *IEEE Transactions on Terahertz Science and Technology*, *12*(6), 574–586. https://doi.org/10.1109/TTHZ.2022.3196191

Llorca, J. (2005). Organic matter in comets and cometary dust. *International microbiology : the official journal of the Spanish Society for Microbiology*, *8*(1), 5–12.

Loaiza, J. P., Higuera-Quintero, S., Noori, A., Mohtashemi, L., Hall, R. P., Yimam, N. A., & Dodge, J. S. (2024). THzTools: Data analysis software for terahertztime-domain spectroscopy. *Journal of Open Source Software*, *9*(104), 7542. https://doi.org/10.21105/joss.07542

Lorek, S., Gundlach, B., Lacerda, P., & Blum, J. (2016). Comet formation in collapsing pebble clouds: What cometary bulk density implies for the cloud mass and dust-to-ice ratio. *Astronomy & Astrophysics*, *587*, A128. https://doi.org/10.1051/0004-6361/201526565

Mandt, K. E., Lustig-Yaeger, J., Luspay-Kuti, A., Wurz, P., Bodewits, D., Fuselier, S. A., Mousis, O., Petrinec, S. M., & Trattner, K. J. (2024). A nearly terrestrial D/H for comet 67P/Churyumov-Gerasimenko. *Science Advances*, *10*(46), eadp2191. https://doi.org/10.1126/sciadv.adp2191

Mannel, T., Bentley, M. S., Boakes, P. D., Jeszenszky, H., Ehrenfreund, P., Engrand, C., Koeberl, C., Levasseur-Regourd, A. C., Romstedt, J., Schmied, R., Torkar, K., & Weber, I. (2019). Dust of comet 67P/Churyumov-Gerasimenko collected by Rosetta/MIDAS: Classification and extension to the nanometer scale. *Astronomy & Astrophysics*, *630*, A26. https://doi.org/10.1051/0004-6361/201834851

Markel, V. A. (2016). Introduction to the Maxwell Garnett approximation: Tutorial. *Journal of the Optical Society of America A*, *33*(7), 1244. https://doi.org/10.1364/JOSAA.33.001244

Marschall, R., Thomas, N., Ulamec, S., Hviid, S., Mottola, S., Vincent, J.-B., Ferri, F., Herique, A., Plettemeier, D., Kereszturi, A., Lavagna, M. R., Prinetto, J., Dottori, A., Falke, A., & Da Silva Pais Cabral, F. (2023). ORIGO: A mission concept to challenge planetesimal formation theories. *Frontiers in Space Technologies*, *3*, 1054360. https://doi.org/10.3389/frspt.2022.1054360

Matsakis, N. D., & Klock II, F. S. (2014). The rust language. *ACM SIGAda Ada Letters*, *34*, 103–104. https://doi.org/10.1145/2692956.2663188

Mazaheri, Z., Koral, C., & Andreone, A. (2022). Accurate THz ellipsometry using calibration in time domain. *Scientific Reports*, *12*(1), 7342. https://doi.org/10.1038/s41598-022-10804-w

Mei, H., Jiang, H., Yin, F., Li, L., & Wang, L. (2020). Detection of Small Defects in Composite Insulators Using Terahertz Technique and Deconvolution Method. *IEEE Transactions on Instrumentation and Measurement*, *69*(10), 8146–8155. https://doi.org/10.1109/TIM.2020.2987407

Mei, H., Jiang, H., Yin, F., Wang, L., & Farzaneh, M. (2021). Terahertz Imaging Method for Composite Insulator Defects Based on Edge Detection Algorithm. *IEEE Transactions on Instrumentation and Measurement*, *70*, 1–10. https://doi.org/10.1109/TIM.2021.3075031

Meyers, C. (1932). Coiled filament resistance thermometers. *Bureau of Standards Journal of Research*, *9*(6), 807. https://doi.org/10.6028/jres.009.058

Michal, V., & Radek, S. (2015). PID control parameters optimization for temperature calibration laboratory. *17th International Congress of Metrology*. https://doi.org/10.1051/metrolo/gy2015510111

Misra, P., & Nagaraju, J. (2010). Thermal gap conductance at low contact pressures (<1 MPa): Effect of gold plating and plating thickness. *International Journal of Heat and Mass Transfer*, *53*(23-24), 5373–5379. https://doi.org/10.1016/j.ijheatmasstransfer.2010.06.052

Morbidelli, A., Kleine, T., & Nimmo, F. (2025). Did the terrestrial planets of the solar system form by pebble accretion? *Earth and Planetary Science Letters*, *650*, 119120. https://doi.org/10.1016/j.epsl.2024.119120

Mordasini, C., Alibert, Y., & Benz, W. (2009). Extrasolar planet population synthesis: I. Method, formation tracks, and mass-distance distribution. *Astronomy & Astrophysics*, *501*(3), 1139–1160. https://doi.org/10.1051/0004-6361/200810301

Murphy, K. N., Markl, D., Nordon, A., & Naftaly, M. (2023). Observation of Spurious Spectral Features in Mixed-Powder Compressed Pellets Measured by Terahertz Time-Domain Spectroscopy. *IEEE Transactions on Terahertz Science and Technology*, *13*(5), 569–572. https://doi.org/10.1109/TTHZ.2023.3290118

Murphy, K. N., Naftaly, M., Nordon, A., & Markl, D. (2022). Polymer Pellet Fabrication for Accurate THz-TDS Measurements. *Applied Sciences*, *12*(7), 3475. https://doi.org/10.3390/app12073475

Murray, C. D., & Dermott, S. F. (2000). *Solar System Dynamics*. Cambridge University Press. https://doi.org/10.1017/CBO9781139174817

Naftaly, M., Vieweg, N., & Deninger, A. (2019). Industrial Applications of Terahertz Sensing: State of Play. *Sensors*, *19*(19), 4203. https://doi.org/10.3390/s19194203

NASA. (2007). *NASA Systems Engineering Handbook* (Vol. NASA/SP-2007-6105).

National Institute of Standards and Technology (US). (2001). *Advanced Encryption Standard (AES)* (tech. rep. No. NIST FIPS 197-upd1). National Institute of Standards and Technology (U.S.) Washington, D.C. https://doi.org/10.6028/NIST.FIPS.197-upd1

Neu, J., & Schmuttenmaer, C. A. (2018). Tutorial: An introduction to terahertz time domain spectroscopy (THz-TDS). *Journal of Applied Physics*, *124*(23), 231101. https://doi.org/10.1063/1.5047659

Ning, W., Qi, F., Zhaoyang, L., Wang, Y., Wu, H., & Wang, J. (2019). Resolution Enhancement in Terahertz Imaging via Deconvolution. *IEEE Access*, *7*, 65116–65121. https://doi.org/10.1109/ACCESS.2019.2917531

Öberg, K. I., Murray-Clay, R., & Bergin, E. A. (2011). THE EFFECTS OF SNOWLINES ON C/O IN PLANETARY ATMOSPHERES. *The Astrophysical Journal*, *743*(1), L16. https://doi.org/10.1088/2041-8205/743/1/L16

Oort, J. H. (1950). The structure of the cloud of comets surrounding the Solar System and a hypothesis concerning its origin. *Bulletin of the Astronomical Institutes of the Netherlands*, *11*(11), 91–110. https://ui.adsabs.harvard.edu/abs/1950BAN....11...91O

Öpik, E. (1973). Comets and the formation of planets. *Astrophysics and Space Science*, *21*(2), 307–398. https://doi.org/10.1007/BF00643104

Orieux, F., Giovannelli, J.-F., & Rodet, T. (2010). Bayesian estimation of regularization and point spread function parameters for Wiener–Hunt deconvolution. *J. Opt. Soc. Am. A*, *27*(7), 1593–1607. https://doi.org/10.1364/JOSAA.27.001593

Ormel, C. W., & Klahr, H. H. (2010). The effect of gas drag on the growth of protoplanets: Analytical expressions for the accretion of small bodies in laminar disks. *Astronomy and Astrophysics*, *520*, A43. https://doi.org/10.1051/0004-6361/201014903

Ormel, C. W. (2017). The Emerging Paradigm of Pebble Accretion. In M. Pessah & O. Gressel (Eds.), *Formation, Evolution, and Dynamics of Young Solar Systems* (pp. 197–228, Vol. 445). Springer International Publishing. Retrieved October 15, 2025, from http://link.springer.com/10.1007/978-3-319-60609-5_7

Ottersberg, R., Pommerol, A., Stöckli, L. L., Obersnel, L., Galli, A., Murk, A., Wurz, P., & Thomas, N. (2025). Evolution of granular salty ice analogs for Europa: Sublimation and Irradiation. ***Icarus***, ***439***, 116590. https://doi.org/10.1016/j.icarus.2025.116590

Pajola, M., Lucchetti, A., Fulle, M., Mottola, S., Hamm, M., Da Deppo, V., Penasa, L., Kovacs, G., Massironi, M., Shi, X., Tubiana, C., Güttler, C., Oklay, N., Vincent, J. B., Toth, I., Davidsson, B., Naletto, G., Sierks, H., Barbieri, C., … Thomas, N. (2017). The pebbles/boulders size distributions on Sais: Rosetta's final landing site on comet 67P/Churyumov–Gerasimenko. ***Monthly Notices of the Royal Astronomical Society***, ***469***(Suppl_2), S636–S645. https://doi.org/10.1093/mnras/stx1620

Park, S.-H., Jang, J.-W., & Kim, H.-S. (2015). Non-destructive evaluation of the hidden voids in integrated circuit packages using terahertz time-domain spectroscopy. ***Journal of Micromechanics and Microengineering***, ***25***(9), 095007. https://doi.org/10.1088/0960-1317/25/9/095007

Pätzold, M., Andert, T., Hahn, M., Asmar, S. W., Barriot, J.-P., Bird, M. K., Häusler, B., Peter, K., Tellmann, S., Grün, E., Weissman, P. R., Sierks, H., Jorda, L., Gaskell, R., Preusker, F., & Scholten, F. (2016). A homogeneous nucleus for comet 67P/Churyumov–Gerasimenko from its gravity field. ***Nature***, ***530***(7588), 63–65. https://doi.org/10.1038/nature16535

Pawar, A. Y., Sonawane, D. D., Erande, K. B., & Derle, D. V. (2013). Terahertz technology and its applications. ***Drug Invention Today***, ***5***(2), 157–163. https://doi.org/10.1016/j.dit.2013.03.009

Pearson, J. C., Drouin, B. J., & Yu, S. (2021). Instrumentation for THz Spectroscopy in the Laboratory and in Space. ***IEEE Journal of Microwaves***, ***1***(1), 43–54. https://doi.org/10.1109/JMW.2020.3032454

Peretti, R., Mitryukovskiy, S., Froberger, K., Mebarki, M. A., Eliet, S., Vanwolleghem, M., & Lampin, J.-F. (2019). THz-TDS Time-Trace Analysis for the Extraction of Material and Metamaterial Parameters. ***IEEE Transactions on Terahertz Science and Technology***, ***9***(2), 136–149. https://doi.org/10.1109/TTHZ.2018.2889227

Phing, S. H., Mazhorova, A., Shalaby, M., Peccianti, M., Clerici, M., Pasquazi, A., Ozturk, Y., Ali, J., & Morandotti, R. (2015). Sub-wavelength terahertz beam profiling of a THz source via an all-optical knife-edge technique. ***Scientific Reports***, ***5***(1), 8551. https://doi.org/10.1038/srep08551

Piesiewicz, R., Kleine-Ostmann, T., Krumbholz, N., Mittleman, D., Koch, M., & Kürner, T. (2005). Terahertz characterisation of building materials. ***Electronics Letters***, ***41***(18), 1002–1004. https://doi.org/10.1049/el:20052444

Plancherel, M., & Leffler, M. (1910). Contribution à l'étude de la représentation D'une fonction arbitraire par des intégrales définies. ***Rendiconti del Circolo Matematico di Palermo (1884-1940)***, ***30***(1), 289–335. https://doi.org/10.1007/BF03014877

Pollack, J. B., Hubickyj, O., Bodenheimer, P., Lissauer, J. J., Podolak, M., & Greenzweig, Y. (1996). Formation of the Giant Planets by Concurrent Accretion of Solids and Gas. ***Icarus***, ***124***(1), 62–85. https://doi.org/10.1006/icar.1996.0190

Pommerol, A., Jost, B., Poch, O., Yoldi, Z., Brouet, Y., Gracia-Berná, A., Cerubini, R., Galli, A., Wurz, P., Gundlach, B., Blum, J., Carrasco, N., Szopa, C., & Thomas, N. (2019). Experimenting with Mixtures of Water Ice and Dust as Analogues for Icy Planetary Material: Recipes from the Ice Laboratory at the University of Bern. ***Space Science Reviews***, ***215***(5), 37. https://doi.org/10.1007/s11214-019-0603-0

Poulet, F., Lucchetti, A., Bibring, J.-P., Carter, J., Gondet, B., Jorda, L., Langevin, Y., Pilorget, C., Capanna, C., & Cremonese, G. (2016). Origin of the local structures at the Philae landing site and possible implications on the formation and evolution of 67P/Churyumov–Gerasimenko. *Monthly Notices of the Royal Astronomical Society*, *462*(Suppl_1), S23–S32. https://doi.org/10.1093/mnras/stw1959

Rasmussen, M., Nagy, O., Skupin, S., Stathopulos, A., Bergé, L., Jepsen, P., & Zhou, B. (2023). Frequency-resolved characterization of broadband two-color air-plasma terahertz beam profiles. *Optics Express*, *31*. https://doi.org/10.1364/OE.482995

Rezac, L., Zhao, Y., Hartogh, P., Ji, J., Marshall, D., & Shi, X. (2019). Three-dimensional analysis of spatial resolution of MIRO/Rosetta measurements at 67P/Churyumov-Gersimenko. *Astronomy & Astrophysics*, *630*, A34. https://doi.org/10.1051/0004-6361/201935389

Rijpma, A., & Ter Brake, H. (2006). Cryogenic thermometry with a common diode: Type BAS16. *Cryogenics*, *46*(1), 68–69. https://doi.org/10.1016/j.cryogenics.2005.11.009

Roehle, H., Dietz, R. J. B., Hensel, H. J., Böttcher, J., Künzel, H., Stanze, D., Schell, M., & Sartorius, B. (2010). Next generation 15 µm terahertz antennas: Mesa-structuring of InGaAs/InAlAs photoconductive layers. *Optics Express*, *18*(3), 2296. https://doi.org/10.1364/OE.18.002296

Rogalin, V. E., Kaplunov, I. A., & Kropotov, G. I. (2018). Optical Materials for the THz Range. *Optics and Spectroscopy*, *125*(6), 1053–1064. https://doi.org/10.1134/S0030400X18120172

Roskos, H., Thomson, M., Kreß, M., & Löffler, T. (2007). Broadband THz emission from gas plasmas induced by femtosecond optical pulses: From fundamentals to applications. *Laser & Photonics Reviews*, *1*(4), 349–368. https://doi.org/10.1002/lpor.200710025

Rottländer, H., Umrath, W., & Voss, G. (2016). Fundamentals of leak detection.

Rotundi, A., Sierks, H., Della Corte, V., Fulle, M., Gutierrez, P. J., Lara, L., Barbieri, C., Lamy, P. L., Rodrigo, R., Koschny, D., Rickman, H., Keller, H. U., López-Moreno, J. J., Accolla, M., Agarwal, J., A'Hearn, M. F., Altobelli, N., Angrilli, F., Barucci, M. A., … Zarnecki, J. C. (2015). Dust measurements in the coma of comet 67P/Churyumov-Gerasimenko inbound to the Sun. *Science*, *347*(6220), aaa3905. https://doi.org/10.1126/science.aaa3905

Safronov, V. S., & Zvjagina, E. V. (1969). Relative sizes of the largest bodies during the accumulation of planets. *Icarus*, *10*(1), 109–115. https://doi.org/10.1016/0019-1035(69)90013-X

Saunders, R. S., & Pettengill, G. H. (1991). Magellan: Mission Summary. *Science*, *252*(5003), 247–249. https://doi.org/10.1126/science.252.5003.247

Schulz, R., Hilchenbach, M., Langevin, Y., Kissel, J., Silen, J., Briois, C., Engrand, C., Hornung, K., Baklouti, D., Bardyn, A., Cottin, H., Fischer, H., Fray, N., Godard, M., Lehto, H., Le Roy, L., Merouane, S., Orthous-Daunay, F.-R., Paquette, J., … Zaprudin, B. (2015). Comet 67P/Churyumov-Gerasimenko sheds dust coat accumulated over the past four years. *Nature*, *518*(7538), 216–218. https://doi.org/10.1038/nature14159

Seidensticker, K. J., & Kochan, H. (1995). The DLR small simulation chamber: A tool for cometary research in the lab. *Advances in Space Research*, *15*(10), 29–34. https://doi.org/10.1016/0273-1177(94)00147-S

Seu, R., Phillips, R. J., Biccari, D., Orosei, R., Masdea, A., Picardi, G., Safaeinili, A., Campbell, B. A., Plaut, J. J., Marinangeli, L., Smrekar, S. E., & Nunes, D. C. (2007). SHARAD sounding radar on the Mars Reconnaissance Orbiter. *Journal of Geophysical Research: Planets*, *112*(E5), 2006JE002745. https://doi.org/10.1029/2006JE002745

Sharma, A., Sharma, S., Torres-Arias, S., & Machiry, A. (2024). Rust for Embedded Systems: Current State, Challenges and Open Problems. *Association for Computing Machinery*, 2296–2310. https://doi.org/10.1145/3658644.3690275

Siegel, P. H. (2010). THz for space: The golden age. *2010 IEEE MTT-S International Microwave Symposium*, 816–819. https://doi.org/10.1109/MWSYM.2010.5515761

Sierks, H., Barbieri, C., Lamy, P. L., Rodrigo, R., Koschny, D., Rickman, H., Keller, H. U., Agarwal, J., A'Hearn, M. F., Angrilli, F., Auger, A.-T., Barucci, M. A., Bertaux, J.-L., Bertini, I., Besse, S., Bodewits, D., Capanna, C., Cremonese, G., Da Deppo, V., … Pätzold, M. (2015). On the nucleus structure and activity of comet 67P/Churyumov-Gerasimenko. *Science*, *347*(6220), aaa1044. https://doi.org/10.1126/science.aaa1044

Simon, M., Dütsch, C., Schieferdecker, J., Storck, K., Völklein, F., & Grau, M. (2012). 1.1.4 MEMS Pirani type vacuum sensor with extended sensitivity range, 42–47. https://doi.org/10.5162/sensoren2012/1.1.4

Slocum, D. M., Slingerland, E. J., Giles, R. H., & Goyette, T. M. (2013). Atmospheric absorption of terahertz radiation and water vapor continuum effects. *Journal of Quantitative Spectroscopy and Radiative Transfer*, *127*, 49–63. https://doi.org/https://doi.org/10.1016/j.jqsrt.2013.04.022

Smith, D. E., Zuber, M. T., Frey, H. V., Garvin, J. B., Head, J. W., Muhleman, D. O., Pettengill, G. H., Phillips, R. J., Solomon, S. C., Zwally, H. J., Banerdt, W. B., Duxbury, T. C., Golombek, M. P., Lemoine, F. G., Neumann, G. A., Rowlands, D. D., Aharonson, O., Ford, P. G., Ivanov, A. B., … Sun, X. (2001). Mars Orbiter Laser Altimeter: Experiment summary after the first year of global mapping of Mars. *Journal of Geophysical Research: Planets*, *106*(E10), 23689–23722. https://doi.org/10.1029/2000JE001364

Smith, D. E., Zuber, M. T., Neumann, G. A., Lemoine, F. G., Mazarico, E., Torrence, M. H., McGarry, J. F., Rowlands, D. D., Head, J. W., Duxbury, T. H., Aharonson, O., Lucey, P. G., Robinson, M. S., Barnouin, O. S., Cavanaugh, J. F., Sun, X., Liiva, P., Mao, D.-d., Smith, J. C., & Bartels, A. E. (2010). Initial observations from the Lunar Orbiter Laser Altimeter (LOLA). *Geophysical Research Letters*, *37*(18), 2010GL043751. https://doi.org/10.1029/2010GL043751

Spencer, Z. R., Heligman, D., & Mendis, R. (2024). Terahertz Imaging Through Dust. *2024 IEEE Research and Applications of Photonics in Defense Conference (RAPID)*, 1–2. https://doi.org/10.1109/RAPID60772.2024.10646952

Šroubek, F., Kerepecký, T., & Kamenický, J. (2019). Iterative Wiener Filtering for Deconvolution with Ringing Artifact Suppression. *2019 27th European Signal Processing Conference (EUSIPCO)*, 1–5. https://doi.org/10.23919/EUSIPCO.2019.8903114

Stöckli, L. L., Brändli, M., Piazza, D., Ottersberg, R., Pommerol, A., Murk, A., & Thomas, N. (2025). Design and commissioning of a THz time-domain spectro-goniometer in a cryogenic comet simulation chamber [_eprint: https://pubs.aip.org/aip/rsi/article-pdf/doi/10.1063/5.0252742/20446261/034502_1_5.0252742.pdf]. *Review of Scientific Instruments*, *96*(3), 034502. https://doi.org/10.1063/5.0252742

Stöckli, L. L., Ottersberg, R., & Thomas, N. (2024). Metal substrate printed circuit boards as low-cost, robust temperature sensor mounts for cryogenic thermometry. *Engineering Research Express*, *6*(4), 046002. https://doi.org/10.1088/2631-8695/ad8ac0

Strohaber, J., Kaya, G., Kaya, N., Hart, N., Kolomenskii, A., Paulus, G., & Schuessler, H. (2011). In situ tomography of femtosecond optical beams with a holographic knife-edge. *Optics Express*, *19*, 14321–14334. https://doi.org/10.1364/OE.19.014321

Su, W.-T., Hung, Y.-C., Yu, P.-J., Yang, S.-H., & Lin, C.-W. (2023). Making the Invisible Visible: Toward High-Quality Terahertz Tomographic Imaging via Physics-Guided Restoration. ***International Journal of Computer Vision***, ***131***(9), 2388–2407. https://doi.org/10.1007/s11263-023-01812-y

Sunshine, J. M., A'Hearn, M. F., Groussin, O., Kissel, J., Klaasen, K. P., McFadden, L. A., Meech, K. J., Melosh, H. J., Schultz, P. H., Thomas, P. C., Veverka, J., Yeomans, D. K., Busko, I. C., Desnoyer, M., Farnham, T. L., Feaga, L. M., Hampton, D. L., Lindler, D. J., Lisse, C. M., & Wellnitz, D. D. (2006). Exposed Water Ice Deposits on the Surface of Comet 9P/Tempel 1. ***Science***, ***311***, 1453–1455. https://doi.org/10.1126/science.1123632

Tao, Y. H., Dai, X., Moggach, S. A., Clode, P. L., Fitzgerald, A. J., Hodgetts, S. I., Harvey, A. R., & Wallace, V. P. (2024). The spectrum of Ih ice using terahertz time-domain spectroscopy. ***The Journal of Chemical Physics***, ***160***(21), 214503. https://doi.org/10.1063/5.0193458

TEC-SHS. (2008). Technology Readiness Levels Handbook for Space Applications. https://connectivity.esa.int/sites/default/files/TRL_Handbook.pdf

Thomas, N., Cremonese, G., Ziethe, R., Gerber, M., Brändli, M., Bruno, G., Erismann, M., Gambicorti, L., Gerber, T., Ghose, K., Gruber, M., Gubler, P., Mischler, H., Jost, J., Piazza, D., Pommerol, A., Rieder, M., Roloff, V., Servonet, A., … Wray, J. J. (2017). The Colour and Stereo Surface Imaging System (CaSSIS) for the ExoMars Trace Gas Orbiter. ***Space Science Reviews***, ***212***(3-4), 1897–1944. https://doi.org/10.1007/s11214-017-0421-1

Thomas, N., Davidsson, B., El-Maarry, M. R., Fornasier, S., Giacomini, L., Gracia-Berná, A. G., Hviid, S. F., Ip, W.-H., Jorda, L., Keller, H. U., Knollenberg, J., Kührt, E., La Forgia, F., Lai, I. L., Liao, Y., Marschall, R., Massironi, M., Mottola, S., Pajola, M., … Tubiana, C. (2015). Redistribution of particles across the nucleus of comet 67P/Churyumov-Gerasimenko. ***Astronomy & Astrophysics***, ***583***, A17. https://doi.org/10.1051/0004-6361/201526049

Thomas, N., Hussmann, H., Spohn, T., Lara, L. M., Christensen, U., Affolter, M., Bandy, T., Beck, T., Chakraborty, S., Geissbuehler, U., Gerber, M., Ghose, K., Gouman, J., HosseiniArani, S., Kuske, K., Peteut, A., Piazza, D., Rieder, M., Servonet, A., … Metz, B. (2021). The BepiColombo Laser Altimeter. ***Space Science Reviews***, ***217***(1), 25. https://doi.org/10.1007/s11214-021-00794-y

Thomas, N. (2020). ***An Introduction to Comets*** (N. Thomas, Ed.). Springer International Publishing. https://doi.org/10.1007/978-3-030-50574-5_2

Thommes, E., Duncan, M., & Levison, H. (2003). Oligarchic growth of giant planets. ***Icarus***, ***161***(2), 431–455. https://doi.org/10.1016/S0019-1035(02)00043-X

Toptica. (2014). Toptica TeraFlash Pro Datasheet.

True, J., Xi, C., Jessurun, N., Ahi, K., & Asadizanjani, N. (2021). Review of THz-based semiconductor assurance. ***Optical Engineering***, ***60***(6), 060901. https://doi.org/10.1117/1.OE.60.6.060901

van Exter, M., Fattinger, C., & Grischkowsky, D. (1989). Terahertz time-domain spectroscopy of water vapor. ***Optics Letters***, ***14***(20), 1128. https://doi.org/10.1364/OL.14.001128

Verma, R., Shivaprakash, N. C., Kasthurirengan, S., & Behera, U. (2017). Optimization of epoxy-aluminium composites used in cryosorption pumps by thermal conductivity studies from 4.5 K to 300 K. ***IOP Conference Series: Materials Science and Engineering***, ***278***, 012158. https://doi.org/10.1088/1757-899X/278/1/012158

Wahlberg Jansson, K., & Johansen, A. (2014). Formation of pebble-pile planetesimals. ***Astronomy & Astrophysics***, ***570***, A47. https://doi.org/10.1051/0004-6361/201424369

Walker, G. C., Bowen, J. W., Labaune, J., Jackson, J.-B., Hadjiloucas, S., Roberts, J., Mourou, G., & Menu, M. (2012). Terahertz deconvolution. ***Optics Express***, ***20***(25), 27230. https://doi.org/10.1364/OE.20.027230

Wang, Q., Xie, L., & Ying, Y. (2022). Overview of imaging methods based on terahertz time-domain spectroscopy. ***Applied Spectroscopy Reviews***, ***57***(3), 249–264. https://doi.org/10.1080/05704928.2021.1875480

Wang, S. (2024). Terahertz Emission Modeling of Lunar Regolith. ***Remote Sensing***, ***16***(21), 4037. https://doi.org/10.3390/rs16214037

Wang, S., & Hiramatsu, K. (2024). Experimental Analysis of Terahertz Wave Scattering Characteristics of Simulated Lunar Regolith Surface. ***Remote Sensing***, ***16***(20), 3819. https://doi.org/10.3390/rs16203819

Weidenschilling, S. J. (1977). The Distribution of Mass in the Planetary System and Solar Nebula. ***Astrophysics and Space Science***, ***51***(1), 153–158. https://doi.org/10.1007/BF00642464

Weissman, P. R. (1986). Are cometary nuclei primordial rubble piles? ***Nature***, ***320***(6059), 242–244. https://doi.org/10.1038/320242a0

Wetherill, G. W., & Stewart, G. R. (1989). Accumulation of a swarm of small planetesimals. ***Icarus***, ***77***(2), 330–357. https://doi.org/10.1016/0019-1035(89)90093-6

Whipple, F. L. (1950). A comet model. I. The acceleration of Comet Encke. ***The Astrophysical Journal***, ***111***, 375. https://doi.org/10.1086/145272

Willenberg, B., Phillips, C. R., Pupeikis, J., Camenzind, S. L., Liebermeister, L., Kohlhass, R. B., Globisch, B., & Keller, U. (2024). THz-TDS with gigahertz Yb-based dual-comb lasers: Noise analysis and mitigation strategies. ***Applied Optics***, ***63***(15), 4144. https://doi.org/10.1364/AO.522802

Williams, J. P., & Cieza, L. A. (2011). Protoplanetary Disks and Their Evolution. ***Annual Review of Astronomy and Astrophysics***, ***49***(1), 67–117. https://doi.org/10.1146/annurev-astro-081710-102548

Woolfson, M. M. (1969). The evolution of the solar system. ***Reports on Progress in Physics***, ***32***(1), 303. https://doi.org/10.1088/0034-4885/32/1/303

Xu, L.-M., Fan, W.-H., & Liu, J. (2014). High-resolution reconstruction for terahertz imaging. ***Appl. Opt.***, ***53***(33), 7891–7897. https://doi.org/10.1364/AO.53.007891

Yoo, H., Kim, J., & Ahn, Y. H. (2023). High-Speed THz Time-of-Flight Imaging with Reflective Optics. ***Sensors***, ***23***(2), 873. https://doi.org/10.3390/s23020873

Youdin, A. N., & Goodman, J. (2005). Streaming Instabilities in Protoplanetary Disks. ***The Astrophysical Journal***, ***620***(1), 459–469. https://doi.org/10.1086/426895

Yu, B., Yang, Y., Zeng, F., Xin, X., & Alfano, R. (2006). Terahertz absorption spectrum of D2O vapor. ***Optics Communications***, ***258***(2), 256–263. https://doi.org/10.1016/j.optcom.2005.07.078

Zdanevičius, J., Bauer, M., Boppel, S., Palenskis, V., Lisauskas, A., Krozer, V., & Roskos, H. G. (2015). Camera for High-Speed THz Imaging. ***Journal of Infrared, Millimeter, and Terahertz Waves***, ***36***(10), 986–997. https://doi.org/10.1007/s10762-015-0169-1

Zhang, Y., Zhang, L., Sun, P., He, Y., Zou, Y., & Deng, Y. (2016). Extracting Complex Refractive Index from Polycrystalline Glucose with Self-Referenced Method for Terahertz Time-Domain Reflection Spectroscopy. ***Applied Spectroscopy***, ***70***(7), 1102–1108. https://doi.org/10.1177/0003702816652318

Curriculum Vitae

Name:	Linus Leo Stöckli
Date of Birth:	13 December 1994
Nationality:	Swiss

2022 – 2026 **Doctoral Dissertation in Physics**, University of Bern

Thesis: *An Approach to Challenging Pebble Accretion using THz-Spectroscopy*

Supervised by Prof. Dr. Nicolas Thomas

2020 – 2021 **Master of Science**, University of Bern

Major in Physics, *Summa Cum Laude*

Akademische Raumfahrt Initiative Schweiz (ARIS), 2019 – 2021

– Electrical and Structural Engineer (Recovery)

Thesis: *Investigations into the Filter-Wheel of the CoCa Experiment on the Comet Interceptor Mission*

Supervised by Prof. Dr. Nicolas Thomas

2015 – 2019 **Bachelor of Science**, University of Zurich

Major in Physics

Minor in Computational Science

Board Member, Physics Students' Association (FPU)

– President (2019 – 2020)

– Treasurer (2018 – 2019)

Concurrent Engineering Challenge at ESA, 2019

Thesis: *Building a Temperature Model for the CaSSIS Experiment on the ExoMars Trace Gas Orbiter*

Supervised by Prof. Dr. Nicolas Thomas

List of Publications

- **Linus Leo Stöckli**, Arnaud Demion, and Nicolas Thomas. THz Image Explorer - An Interactive Cross-Platform Open-Source THz Image Analysis Tool. *Journal of Open Source Software* (2025).
- Arnaud Demion, **Linus Leo Stöckli**, Nicolas Thomas, and Silvan Zahno. Frequency-Dependent Deconvolution for Enhanced THz-TDS Scans: Accounting for Beam Width Variations in Time Traces, *IEEE Transactions on Terahertz Science and Technology* (2025).
- **Linus Leo Stöckli**, Mathias Brändli, Daniele Piazza, Rafael Ottersberg, Antoine Pommerol, Axel Murk, and Nicolas Thomas. Design and Commissioning of a THz Time Domain Spectro-Goniometer in a Cryogenic Comet Simulation Chamber. *Review of Scientific Instruments* (2025).
- Rafael Ottersberg, Antoine Pommmerol, **Linus Leo Stöckli**, Lorenzo Obersnel, André Galli, Axel Murk, Peter Wurz, and Nicolas Thomas. Evolution of granular salty ice analogs for Europa: Sublimation and Irradiation. *Icarus* (2025).
- **Linus Leo Stöckli**, Rafael Ottersberg, and Nicolas Thomas. Metal substrate printed circuit boards as low-cost, robust temperature sensor mounts for cryogenic thermometry. *Engineering Research Express* (2024).
- Holly L. Capelo, Jean-David Bodénan, Martin Jutzi, Jonas Kühn, Romain Cerubini, Bernhard Jost, **Linus Leo Stöckli**, Stefano Spadaccia, Clemence Herny, Bastian Gundlach, Günter Kargl, Clément Surville, Lucio Mayer, Maria Schönbächler, Nicolas Thomas, and Antoine Pommerol. Gas permeability and mechanical properties of dust grain aggregates at hyper- and zero-gravity, *Monthly Notices of the Royal Astronomical Society* (2024).

Peer Review Contributions

Peer Reviews

- Reviewer for *JGR Planets*, 2025.
- Contributed feedback to editors on manuscript transfer and revision processes for *Icarus*, 2025.

Scholarly Contribution

- Identified and reported inaccuracies in a published paper; submitted a detailed derivation of the equations in question to the author, 2025

Conference Contributions

- **Europlanet Science Congress (EPSC) 2025**
  Helsinki, Finnland, September 2025.
  oral presentation
- **European Geoscience Union (EGU) 2025**
  Vienna, Austria, May 2025.
  oral presentation
- **International Symposium on Space Terahertz Technology (ISSTT) 2025**
  Berlin, Germany, April 2025.
  oral presentation
- **Europlanet Science Congress (EPSC) 2024**
  Berlin, Germany, September 2024.
  oral presentation
- **International Conference on Infrared, Millimeter, and Terahertz Waves (IRMMW-THz) 2023**
  Montréal, Canada, September 2023.
  poster presentation

Colophon

This document was typeset according to the principles of Swiss Design. Emerging as a distinct movement in the mid-twentieth century, Swiss Design was shaped by the modernist ethos that also informed earlier design schools such as the Bauhaus. While the Bauhaus emphasized functionalism, reduction, and the integration of art, craft, and technology, Swiss designers built upon these foundations to develop a uniquely systematic and typographically driven visual language. This design tradition reinforces the document's commitment to clarity, structure, and rational visual organization.

Helvetica Neue has been chosen as the primary typeface for this document due to its simplicity, typographic precision, and enduring association with the ideals of modernism. Its even spacing and clean letterforms make it particularly well-suited for academic writing, where legibility and neutrality are paramount. This minimalist design choice is intended not only to maintain the reader's focus on the scientific content, but also to align the work with a design tradition that prioritizes clarity and visual coherence.

In the visual documentation of experimental setups, technical drawings have been preferred over photographs. This decision reflects the same principles of clarity and reduction that underlie Swiss Design. Unlike photographs, which may include extraneous details, inconsistent lighting, or distracting background elements, technical drawings allow for a distilled representation of only the essential components of the apparatus. This visual approach aligns the supporting material of the thesis with its broader design philosophy.

Introduction Header Image: `N20141003T092026594ID30F22`
Copyright: European Space Agency & MPS for OSIRIS Team
MPS/UPD/LAM/IAA/SSO/INTA/UPM/DASP/IDA

Declaration of the use of AI-based Tools

AI-based tools, including ChatGPT and GitHub Copilot, were used to support this work. These tools assisted with code generation, language refinement, and structural suggestions but did not replace the author's critical thinking or original contributions in any way. All content has been reviewed and validated by the author to ensure accuracy and integrity.

The utilized models are described in the table below, alongside with the scope of their application in this work.

AI-based tool	**Model**	**Use Case**	**Scope**	**Remarks**
ChatGPT	GPT-3 GPT-4 GPT-4o GPT-5	Code generation Language Refinement Structural evaluations	Chapter 1 Chapter 2 Chapter 3 Chapter 4 Chapter 5	Python Rust LaTeX
GitHub Copilot	GPT-4o GPT-5 Claude Sonnet 3.5 Claude Sonnet 3.7 Gemini 2.5	Code generation	Chapter 4 Chapter 5	Python Rust Swift
Overleaf AI Assist	Writefull	Language Refinement	General	

Declaration of Originality

Last name, first name: Stöckli, Linus Leo

Matriculation number: 15-706-518

I hereby declare that this thesis represents my original work and that I have used no other sources except as noted by citations.
All data, tables, figures and text citations which have been reproduced from any other source, including the internet, have been explicitly acknowledged as such.
I am aware that in case of non-compliance, the Senate is entitled to withdraw the doctorate degree awarded to me on the basis of the present thesis, in accordance with the “Statut der Universität Bern (Universitätsstatut; UniSt)”, Art. 69, of 7 June 2011.

Bern, January 29, 2026

Linus Leo Stöckli